ParisTech
INSTITUT DES SCIENCES ET TECHNOLOGIES
PARIS INSTITUTE OF TECHNOLOGY

MINES ParisTech

Ecole doctorale n°364: Sciences Fondamentales et Appliquées

Doctorat ParisTech

T H È S E

pour obtenir le grade de docteur délivré par

l'École nationale supérieure des mines de Paris

Spécialité "Mécanique Numérique"

présentée et soutenue publiquement par

Vũ Thư PHẠM

le 17 février 2012

Mixed Velocity-Displacement Formulation for Modeling of Complex Behavior of Polymer

Directeur de thèse : **Thierry COUPEZ**
Co-directrice de thèse : **Noëlle BILLON**
Co-encadrement de thèse : **Luisa Alexandra ROCHA DA SILVA**

Encadrement industriel : **Jérôme BIKARD**

Jury

M. Amine AMMAR, Professeur, Arts et Métiers ParisTech, ENSAM Angers, France	Président
M. Luc CHEVALIER, Professeur, MSME, Université Paris-Est, France	Rapporteur
M. Steven LE CORRE, Professeur, Polytech Nantes, France	Rapporteur
M. Thierry COUPEZ, Professeur, CEMEF, MINES ParisTech, France	Examinateur
Mme Noëlle BILLON, Professeur, CEMEF, MINES ParisTech, France	Examinateur
Mme Luisa SILVA, Docteur, CEMEF, MINES ParisTech, France	Examinateur
M. Jérôme BIKARD, Docteur, R&D Rhodia Engineering Plastics, Rhodia, France	Examinateur

MINES ParisTech
Centre de Mise en Forme des Matériaux
Rue Claude Daunesse - BP 207, 06904 Sophia Antipolis Cedex

T H E S E

Acknowledgements

Ce travail de thèse a été réalisé au sein du Centre de Mise en Forme des Matériaux de l'Ecole des Mines de Paris, à Sophia Antipolis dans le cadre du Consortium Rem3D qui regroupe les entreprises Arkema, DOW Chemicals, Rhodia, Schneider Electric, Snecma Propulsion Solide et Transvalor. Je les remercie pour leur soutien financier qui a permis de mener à bien mes travaux.

Je suis très reconnaissant envers le Professeur Amine Ammar qui a bien voulu accepter la présidence de mon jury de thèse. Je remercie chaleureusement le Professeur Luc Chevalier et le Professeur Steven Le Corre d'avoir accepté de juger mon travail en tant que rapporteurs.

Je tiens à exprimer une profonde reconnaissance à mon Directeur de Thèse Thierry Coupez pour sa disponibilité, son encadrement scientifique rapproché et ses remarques critiques. Mes remerciements vont ensuite tout naturellement à ma Co-Directrice Noëlle Billon pour avoir suivi mon travail avec intérêt, ses conseils constructifs et précis, ainsi que pour son enthousiasme pour la recherche et ses explications scientifiques. Je tiens à remercier mon encadrant industriel Jérôme Bikard pour avoir suivi ce travail de près et qui a donné lieu à de nombreux échanges. Et sans oublier d'exprimer ma profonde gratitude à Luisa Silva, ma chère Co-Encadrante, pour le soutien, la contribution et la confiance inconditionnelle qu'elle m'a accordée durant ces années.

Je tiens à remercier tous les collèges et encadrants qui ont collaboré avec moi sur certains aspects de ce travail. Je tiens à exprimer ma gratitude à Hugues Digonnet, un génie de l'informatique, pour le développement d'un nouveau solveur éléments finis hors norme dans Cimlib. Un grand merci à Patrice Laure et Elie Hachem pour les discussions sur la stabilisation et les nombreux échanges sur les méthodes numériques. Un grand merci aussi à Christelle Combeaud et Aurélien Maurel pour leur aide sur les essais expérimentaux et l'implémentation de la loi de comportement hyper-visco-élastique ainsi qu'à Andri Andriyana pour ses premiers cours de polymère et de viscoélasticité.

Je ne saurais oublier la disponibilité, la bonne humeur de l'ensemble des permanents, de l'ensemble du personnel administratif, de la bibliothèque de l'ENSMP et du groupe EII qui rendent la vie plus facile. Qu'ils en soient remerciés. Un grand merci à Patrick Coels et Marie Françoise pour leur disponibilité et leur grande gentillesse.

Je voulais finir par un merci général. J'ai passé trois ans au Cemef dans une ambiance toujours amusante et chaleureuse, merci à la bande libanaise: Karim, Nadine, Pamela, Stéphanie…; à la bande française: Laurence, Guillaume, Grégory P., Audrey, Trystan, Jef, Sylvain…; à la bande internationale: Esteban, Koffi, Okba, Ala… pour tous ces bons moments. Et mon cher Grégory pour l'occupation de la moitié du bureau et tous les moments passés ensemble. Cuối cùng là lời cảm ơn đến hội ăn trưa Ceram : Châu béo, Vân, Kim Anh, cu Sơn, chị Hà, a Trọng và những người bạn. Sẽ nhớ mãi những tiếng cười, những buổi tọa đàm trên sân cỏ Ceram và những cuộc tranh luận long trời lở đất mà diễn viên chính ít khi đổi vai :)). Hi vọng những kí ức tươi đẹp ấy mãi là một phần trên con đường mọi người đã và sẽ đi.

Je pense également aux amis que j'ai eu la chance de côtoyer durant ces années passées dans le sud, plein de soleil, de vent et de sable.

Finalement, et non la moindre, a very special thanks to my family pour tous.

… to my family and …

Contents

1 Introduction 9

1.1 Injection molding process 11

1.1.1 Description of injection molding process 11

1.1.2 Simulation of injection molding 12

1.2 Context, objectives and outline 13

1.2.1 Context and objectives 13

1.2.2 A short literature review and outline 14

1.3 Résumé du chapitre en français 16

2 Viscoelasticity and Fluid Structure Interaction (FSI) 17

2.1 Characteristics, applications and properties of polymers 19

2.1.1 An introduction to viscoelasticity 20

2.1.2 Isochronous modulus vs. temperature behavior 21

2.1.3 Phenomenological mechanical models 22

2.2 Fluid structure interaction (FSI) numerical approaches review 26

2.2.1 Fluid-Structure formulation 26

2.2.2 Fluid-structure coupling: monolithic vs. partitioned coupling 27

2.2.2.1 FSI resolution 28

2.2.3 Summary 33

2.3 Monolithic approach for the resolution of the extended Navier-Stokes equations with an extra-stress tensor: behavior point of view 35

2.3.1 Motion description 35

2.3.2 Strain and strain rate description 36

2.3.3 Internal forces and stress description 37

2.3.4 Equilibrium equation 38

2.3.5 Large deformations and used models: hyper-elastic and visco-hyper-elastic 38

2.3.6 Small deformation and used models: elastic and viscoelastic 42

2.3.7 Modeling a viscoelastic behavior 42

2.3.8 Resolution and introduced errors 45

2.4 Résumé du chapitre en français 49

3 Numerical resolution of the two phase problem through a mixed finite element method in (*v, p, u*) 51

3.1 Description of the numerical test benchmarks 53
3.1.1 Simple tensile test benchmark 53
3.1.2 Flow between two rigid solid particles 54
3.2 Mixed finite elements with Mini-Element P1+/P1 55
3.2.1 Numerical resolution 55
3.3 Application for the tensile test case by a Lagrangian approach 62
3.3.1 Single time step resolution for the tensile test case with an elastic behavior 62
3.3.2 Incremental time step resolution for the tensile test case with an elastic behavior 67
3.3.3 Incremental time step resolution for the tensile test case with an viscoelastic behavior 71
3.3.4 Instability problems in the tensile test by Lagrangian approach 73
3.4 Application for the tensile test case by Eulerian approach 76
3.4.1 Immersed volume method 76
3.4.2 Eulerian method for the incompressible elastic tensile test 79
3.4.3 Numerical results 83
3.5 Application in flow between two rigid particles 85
3.5.1 Formulation for a rigid solid 85
3.5.2 Numerical results 87
3.5.3 Concluding remarks 89
3.6 Résumé du chapitre en français 90

4 Stabilized Mixed Finite Elements 91

4.1 Improvement on the mixed velocity-pressure-displacement formulation through a complete solver 93
4.1.1 Stabilized mixed finite elements 95
4.1.2 Comparison between the old solver NSTC and the new SMC 103
4.1.3 Application in the elasticity case: comparison with the old solver 105
4.1.4 Application: flow between two rigid solid particles 115
4.2 Improving stabilization through the bubble viscosity modification 121
4.2.1 A novel formulation with modification of bubble's viscosity 121
4.2.2 Application 123
4.2.3 Concluding remarks 132
4.3 Improving stabilization through Elastic Viscous Split Stress (EVSS) 133
4.3.1 Short review on computational methods used in viscoelastic flow 133
4.4 Résumé du chapitre en français 136

5 Modeling of Viscoelastic, Hyperelastic and Visco-Hyper-Elastic Model 139

5.1 Experimental tensile tests 141

5.1.1 Experimental data base....141
5.1.2 Experimental results analysis....145
5.2 Numerical-experimental comparison....151
5.3 Modeling visco-hyper-elastic behavior....154
5.4 Application of the EVSS stabilized solver to viscoelastic, hyperelastic and visco-hyper-elastic behaviors....157
5.4.1 Kelvin-Voigt viscoelastic model....157
5.4.2 Neo-Hookean viscoelastic model....159
5.4.3 Visco-hyper-elastic model....165
5.5 Résumé du chapitre en français....170

6 Conclusions and Perspectives 173
6.1 Synthesis and conclusion....173
6.2 Perspectives....176

Nomenclature 179

Appendix 182
A. Modeling visco-hyper-elastic behavior....182

List of Figures 193

List of Tables 198

Bibliography 199

Chapter 1

1 Introduction

---

1 Introduction 9

1.1 Injection molding process 11

1.1.1 Description of injection molding process 11

1.1.2 Simulation of injection molding 12

1.2 Context, objectives and outline 13

1.2.1 Context and objectives 13

1.2.2 A short literature review and outline 14

1.3 Résumé du chapitre en français 16

The widespread application of polymers in almost every area of modern industry results in an increasing need for injection molding, one of the most important technologies for forming polymeric material components. Actually, this process is highly automated and can be manufactured in large-scale. However, controlling final properties in polymer processing is complex as induced rheology and developed microstructure highly depends on no trivial local mechanical and thermal conditions experienced by the material. Consequently, the quality and properties of final molded pieces are strongly related to process parameters and to the geometry of the mold. The influence of these parameters on the final properties is far from obvious. Therefore, to guarantee the quality of the final part a precise characterization and monitoring of the injection molding process is required. Numerical tools can speed up product innovation, reduce the associated costs, and help us to understand the material behavior all along the process.

This chapter will introduce a brief description of the injection process, the identification of the main computational needs and the context of the project.

1.1 Injection molding process

The work developed in this study is part of a more general study that intend proposing a complete modeling of injection molding of polymers starting from the filling of the mold to the final part and its properties.

Our main goal is proposing some general numerical tools that allow to account for the viscoelastic behavior of polymers and for the progressive change from a “fluid” to a “solid” philosophy. This should allow a better and simpler accounting for residual stresses development and prediction of end use properties.

Before describing our main results let’s first briefly described the context to introduce the general frame in which our development must be introduced.

1.1.1 Description of injection molding process

Injection molding is the most commonly used polymer processing operation for the fabrication of plastic parts. The injection process allows the manufacture of great range of products which vary in their size, complexity, and application, at high production rates and with a large degree of automation, in a single operation. An injection machine is basically composed of two mains parts: an injection molding machine, where polymer is molten in a screw – barrel system after having be introduced in the granule form through a hopper, and a mold.

General frame of our studies is modeling of the way in which the molten polymer is enforced under high pressure into the mold cavity and then solidifies. This step is very short, ranging typically between 2 seconds and 2 minutes, and is characterized by four sub phases:

- Filling

  The hot molten polymer is pushed through a thin gate inside the cold mold cavity. This step intend in filling the mold but combines quenching on the mold surface and viscous flow in the fluid channel.

- Packing/holding

  After filling the mold, a holding pressure (a few hundreds of bar) is applied to compensate for volume change due to solidification as polymers cools down as soon as it contacts the mold..

- Cooling

  When the mold is filled and packed polymer is cooled down to a temperature that enable manipulating the part.

- Ejection

  After sufficient cooling time, the mold opens and the part is ejected by the ejection system, which is attached to the rear half of the mold. Once the part is ejected, the mold is clamped and the injection cycle starts again.

1.1.2 Simulation of injection molding

Injection molding processing involves then the non isothermal flow of a viscous molten polymer, a solidification phase, the flow of a semi solid material during solidification and stress relaxation in the solid. In any case, thermomechanical models have to be developed that should account for specificity of properties of polymers. In particular, the visco elastic behavior of both the molten and the solid material should be accounted for.

To guarantee the quality of the final parts, a precise characterization and monitoring of the injection molding process is essential. Using analytical solutions is limited due to the complexities of the governing equations, of the material behavior and of the cavity geometry. Therefore, numerical tools are a good solution to get useful results. To achieve such code governing equations are solved by the computational algorithms in a discretized form. In the literature, a variety of numerical methods were developed such as the finite element method, the finite difference method, the meshless particle method, and the boundary element method [1]. Each method has some advantages in a certain class of problems.

It is now well accepted that more valuable models are three-dimensional (3D) analysis rather than initial 2.5D model based on the Hele-Shaw approximation. Indeed, 3D simulation is an important improvement to accurately predict some features of injection molding which are difficult to capture through a Hele-Shaw model: complex geometries, complex flow, fiber and molecular orientation, etc. Starting in the 1970s, 3D simulation of the filling stage leads to a few developments during the past years. A brief review is given by Cardozo [2]. To summarize, first attempt was made by Hétu et al. [3] [4] using a finite element method. In the parallel, the MINI-element was applied to 3D injection molding by Pichelin and Coupez [5]. Later, Zhou et al [6] integrated a mathematical model and numeric method based on 3D model to perform simulations of a fully flows.

However, up to this moment each stage (filling, packing etc.) of the process was considered independently from each other. More recently a continuous computation using a single compressible viscoelastic constitutive model was developed by Silva et al. [7] [8]. This work made it possible modeling from the filling to the post-filling stage using one unique constitutive frame, and allows describing the thermodynamical state of the material at each instant of the injection molding cycle.

In parallel, important thermal gradient across the thickness during processing implied additional sophistication for a correct simulation. In example 3D tetrahedral, unstructured and anisotropic mesh generator that enables a refined discretization throughout the thickness direction was proposed by Coupez [9] [10] to alleviate the problem.

The next session is devoted to the context, objectives and outline of the present study.

1.2 Context, objectives and outline

1.2.1 Context and objectives

This work was performed within the **REM3D®** project context, which includes the following members:

- Arkema (www.arkema.com): French petro-chemical group
- DOW Chemicals (www.dow.com): Polymer producer
- Rhodia (www.rhodia.com) : Chemical producer
- Schneider Electric (www.schneider.fr): Electrical parts distribution, plastic equipment
- Snecma Propulsion Solide (www.snecma.fr): Aeronautic equipment
- Transvalor (www.transvalor.com): Software editor in material forming
- Cemef (www.cemef.mines-paristech.fr): centre for material forming, research laboratory of Mines ParisTech

Rem3D® is the leading 3D Finite Element software that provided the first 3D results in plastic injection molding. Rem3D® is based on the finite element library CimLib® [11] [12] [13] [14] which provides:

- FE solvers only based on the implementation of a local solver interface,
- fully automatic parallel remeshing with integrated transport,
- output results.

The software performed the full 3D simulation of the injection molding process through the combination of different FE equation solvers. The challenge is to deal with the following scientific issues:

- anisotropy induced by the injection molding process (e.g.: fiber orientation…),
- amorphous/semi-crystalline matrix, thermosets, elastomers,
- phase change, crystallization, chemical reaction,
- mechanical prediction, optical prediction…

The present version allows to correctly predicting the thickness distribution of the finished part and an estimate for the local final thermo elastic properties (isotropic and not isotropic). It accounts for crystallization and orientation processes.

Nevertheless it failed predicting completely residual stress and warpage. To adequately describe the whole process, a time dependent solid behavior, namely visco elastic, must be introduced to model post solidification behavior.

Therefore, to extend the Rem3D® software, one has to implement a more generic behavior for the matrix. More precisely, the objectives of this work are to implement and/or use numerical approaches which will make it possible to deal on the future with viscoelasticity, fluid-structure coupling and structure-structure coupling, multi-body contact or high speed solicitations (inertia), and provide its numerical simulation with the finite element method (FEM) of three-dimensional

structures of viscoelastic substances. We will focus on the development of new numerical techniques to treat viscoelastic modeling.

1.2.2 A short literature review and outline

Viscoelastic materials are materials whose behavior is thermodynamically irreversible but geometrically reversible. Main effect is that behavior of such material sounds time dependent.

Roughly speaking, visco elastic bodies are often considered as combining the characteristics of elastic and of viscous bodies. Analogical models consist then in combining springs and dashpots. The simplest approaches are Kelvin-Voigt's model or Zener's model [15] in case of solids and Maxwell's model for fluid. In both cases, at the numerical level, viscoelastic simulation requires solving of two different types of equation: an elliptic problem that characterizes the conservation of momentum and a hyperbolic problem linked to the constitutive equation. Many numerical schemes are studied to deal with the two types of problem, especially at high Weissenberg numbers (*We*) which represents the case of viscous fluids. The most commonly method used is based on a mixed finite element formulation [16]. To deal with the momentum balance, several algorithms such as Elastic Viscous Split Stress (EVSS) [17] [18] were used. Guenette and Fortin [19] introduced a modification of the EVSS formulation, known as the Discrete EVSS method (D.E.V.S.S.). This is one of the most robust formulations currently available due to its simplicity and its stability. It can easily be applied to a variety of constitutive equations. All these methods may be coupled to SU (Streamline-Upwind), SUPG (Streamline-Upwind–Petrov–Galerkin) or DG (Discontinuous-Galerkin) techniques for FEM [7] [16] [20] [21] to stabilize the solving of the viscoelastic constitutive equation and, therefore, overcome the HWNP (High Weissenberg Number Problem).

To study the numerical modeling of viscoelastic fluid as far as fluid flow, only a few attempts have been made in the context of Lagrangian framework where the strategy for remeshing is required to deal with mesh distortion [22]. Harlen et al. [23] developed remeshing technology and combined an Eulerian calculation of the velocity to a Lagrangian calculation of the stress. Recently, Moresi and co-workers [24] have developed a Lagrangian integration point finite element formulation designed to account for large deformation of a viscoelastic material. More precisely, an Eulerian mesh and embedded Lagrangian integration points or particles were used. Un-known variables were computed at the mesh nodes and the Lagrangian integration points or particles carried history variables during the deformation process. Alternatively, an arbitrary Lagrangian Eulerian finite element method (ALE), popular in applications where interaction between fluid and structures are important, has been recently adopted to deal with the viscoelastic problem [25] [26]. The ALE benefits the advantages of both Lagrangian and Eulerian frameworks by allowing the computational mesh to move in an arbitrary manner, independent of the material motion.

However, the mechanical behavior of viscoelastic solid represents another aspect of computational modeling compared with that of viscoelastic fluid where the FEM or the BEM may be applied. In spite of the advantage of dimension reduction, the use of BEM remains little [27]. Concerning the FEM on the modeling of viscoelastic solid, early work was proposed by Holzapfel and Reiter [28] who introduced a fully coupled thermomechanical formulation of the viscoelastic four-parameter material model undergoing small deformations. Hasanpour and co-workers [29] have recently presented the numerical modeling by FE a large deformation framework for compressible viscoelastic solid. Their main purpose is to formulate constitutive equations related to the compressible viscoelastic model which is inspired by the work of Huber and Tsakmakis

[30]. The viscoelastic response of materials and structures under impact loading has been also investigated in the work of many authors as Assie et al [31] [32], and Qian and Demao [33]. The dynamic analysis are numerically treated by FE where Maxwell, Kelvin-Voigt, three parameters and generalized standard linear solid (Wiechert) model have been used for describing the viscoelastic behavior of materials.

After all, for the numerical modeling of viscoelasticity solid, simple Eulerian framework was not widely used because of the need of an advection schemes with low numerical diffusion. This latter generally uses high-order interpolated functions that cause unwanted oscillations. However, the approach is attractive for large deformation of solids [34] which justifies a recent interest in developing Eulerian strategies for viscoelastic problems through different phases of materials.

Parallel to previous attempts, our approach intends at modeling the viscoelastic behavior of polymers from the solid state to the liquid state via a multiphase approach, which is largely used for fluid structure interaction (FSI) [35]. The main idea is to use a mixed formulation of three fields *(u, v, p) (displacement, velocity, pressure),* where *u* and *v* represent the primary variables of a strain and of a strain rate formulation resp., assuming that a closure model exists:

$$f(\frac{du}{dt}, v) = 0 \tag{1.1}$$

This latter represents a hyperbolic equation. The problem can, in this case, be described as the classical Navier-Stokes problem, in which an extra-stress tensor related to the elastic part of the strain is considered. Compared to classical methods using of the mixed method, first introduced in the 1960s, our approach represents an innovative route that will be described and validated in this document.

Finishing this introduction, chapter 2 presents this proposed resolution (monolithic approach) after a brief reminder of needed knowledge about viscoelasticity, fluid-structure interaction and an overall summary of the continuum mechanics in large deformation together with the isotropic viscoelastic, hyperelastic and visco-hyper-elastic behavior.

Chapter 3 is devoted to preliminary validation in a purely elastic frame which enlightens some sources of instability making it necessary the definition of stabilization steps that are described in chapter 4. Investigation of stabilized methods with the governing equations of the Navier-Stokes problem with extra-stress and some numerical illustrations of the capabilities of the approach are also summarized.

In chapter 5 our approach applied to a simple Kelvin Voigt model is compared to some experimental tests. Efficiencies within Lagrangian and Eulerian frames are discussed. The last section demonstrates feasibility for a more realistic visco-hyper-elastic model on the finite elements library CimLib®.

It is the scope of chapter 6 to offer an overall summary of the work together with conclusions which open the discussion to the perspectives. Within the appendix *A* some further information on modeling of the visco-hyper-elastic model.

1.3 Résumé du chapitre en français

Le but de ce chapitre est de présenter nos objectifs généraux et nos choix de méthodologie de résolution. Ce travail s'insère dans une étude plus globale visant à proposer une modélisation intégrée, de la mise en œuvre aux propriétés d'usage, fiable du procédé d'injection des polymères.

Le cadre du projet est le consortium REM3D® auquel participent plusieurs entreprises industrielles intéressées au développement d'une simulation 3D par éléments finis du procédé d'injection. La version actuelle a montré son efficacité dans la prédiction des distributions d'épaisseur dans la pièce finie et une première estimation des propriétés thermoélastiques (isotropes et anisotropes) locales. La cristallisation éventuelle et les phénomènes d'orientation de fibres sont aussi reproduits. Néanmoins, l'absence de prise en compte des effets viscoélastiques dans le lit solide reste un frein à une bonne estimation des contraintes résiduelles et effet de gauchissement.

Notre objectif est de proposer un outil générique qui permettrait de prendre en compte aussi bien la viscoélasticité du polymère fondu pendant les phases de remplissage et de compactage que de celle du polymère solide pendant et après le refroidissement. L'idée est d'utiliser une formulation mixte à trois champs (*u, v, p*) *(déplacement, vitesse, pression)*, où u et v représentent les variables principales "déformation" et "vitesse de déformation". Le problème exprimé ainsi se réduit au problème classique de Navier-Stokes dans lequel un tenseur "extra-contrainte" lié à la partie élastique de la déformation est pris en compte.

Cette approche inhabituelle dans ce contexte représente une réelle innovation.

Chapter 2

2 Viscoelasticity and Fluid Structure Interaction (FSI)

2 Viscoelasticity and Fluid Structure Interaction (FSI) 17

2.1 Characteristics, applications and properties of polymers 19

2.1.1 An introduction to viscoelasticity 20

2.1.2 Isochronous modulus vs. temperature behavior 21

2.1.3 Phenomenological mechanical models 22

2.2 Fluid structure interaction (FSI) numerical approaches review 26

2.2.1 Fluid-Structure formulation 26

2.2.2 Fluid-structure coupling: monolithic vs. partitioned coupling 27

2.2.2.1 FSI resolution 28

2.2.3 Summary 33

2.3 Monolithic approach for the resolution of the extended Navier-Stokes equations with an extra-stress tensor: behavior point of view 35

2.3.1 Motion description 35

2.3.2 Strain and strain rate description 36

2.3.3 Internal forces and stress description 37

2.3.4 Equilibrium equation 38

2.3.5 Large deformations and used models: hyper-elastic and visco-hyper-elastic 38

2.3.6 Small deformation and used models: elastic and viscoelastic 42

2.3.7 Modeling a viscoelastic behavior 42

2.3.8 Resolution and introduced errors 45

2.4 Résumé du chapitre en français 49

The purpose of this chapter is firstly to provide a description of the viscoelastic mechanical behavior by summarizing the needed concepts. To achieve this, a short bibliographic survey of viscoelastic approaches in injection molding, followed by the description of characteristics and properties related to memory dependent materials is discussed.

Analogy with FSI (Fluid Structure Interaction) and its relevance for the treatment of viscoelasticity are discussed in a second part. We show the selected methodology for a FSI problem, treated in this case by using the numerical tools developed in the library FE CimLib®.

The last part offers an overall summary of continuum mechanics in large deformations together with the isotropic viscoelastic, hyperelastic and visco-hyper-elastic behavior. By linearizing, assumption of small perturbations is finally taken into account to introduce our choice in terms of numerical resolution. A simple Kelvin-Voigt viscoelastic model is used to explain and validate the approach as it allows justifying all the numerical developments.

2.1 Characteristics, applications and properties of polymers

With the aim to illustrate a new approach to take into account a viscoelastic behavior using a monolithic approach, the viscoelastic Kelvin-Voigt's model [15] [36] (see Figure 2-3) is chosen as an application that is simple enough whilst it will enlighten all potential difficulties and allow objective validation of the approach. Despite its physical simplicity it involves a combination, in the same system, of strain (elastic part) and strain rate (viscous part) that allows us to test our methodology: a monolithic approach resolution, which can be analogically used for a viscoelastic problem and a classical fluid-structure interaction one being the main purpose of this work implementation of a solver that can treat both case. Moreover, with this model, elasticity is perfectly preserved, meaning that a deformed object must return to its original position upon unloading which can provide us relatively simple benchmarks.

Using the viscoelastic Kelvin-Voigt model, the stress tensor is defined as:

$$\sigma_{ve} = \sigma_v + \sigma_e \tag{2.1}$$

where σ_e and σ_v are the elastic and viscous stresses, respectively. In the simple linear case:

$$\sigma_v = 2\eta_v \varepsilon(v) - pI \tag{2.2}$$

$$\sigma_e = 2\mu_e \varepsilon(u) + \lambda_e tr\varepsilon(u) I \tag{2.3}$$

where η_v and p are the viscosity and the hydrostatic pressure, $tr(.)$ is the trace operator, I is the identity tensor, $\varepsilon(u)$ and $\varepsilon(v)$ are the strain and the strain rate tensors, with $\varepsilon(\cdot)$ hdefined, in the linear case, as $\varepsilon(\cdot) = \frac{1}{2}\left(\nabla(\cdot) + \nabla^t(\cdot)\right)$

The Lamé's coefficients are defined as:

$$\mu_e = \frac{E}{2(1+\nu_e)} \tag{2.4}$$

and

$$\lambda_e = \frac{E\nu_e}{(1+\nu_e)(1-2\nu_e)} \tag{2.5}$$

with E the Young's modulus, ν_e is the Poisson's ratio.

Since the viscoelastic model contains a "solid" behavior, so-called the elastic part and a "fluid" behavior, so-called the viscous part, the resolution of this system is similar to the resolution of a twophase problem, like in classical Fluid-Structure Interaction. Therefore, a brief introduction of viscoelasticity and FSI in the literature will enlighten our choice and our approach for its resolution.

2.1.1 An introduction to viscoelasticity

The properties (mechanical, electrical, optical, etc.) of polymers are often time dependent and cannot be treated mathematically by the simplest usual constitutive laws of either solids or fluids [15]. According to Rosen [37], two simple experiments allow illustrating viscoelasticity:

- Silly Putty: As bouncing putty, the material bounces when dropped but flow like a liquid when lying stationary. It has some characteristics of an elastic solid and some of a viscous fluid
- Weissenberg Effect: known also as rod-climbing experiment, this is a common phenomenon that occurs when a rod rotated into a solution of liquid polymer. In a visco elastic fluid the material climbs up the rod whereas in a Newtonian fluid dominating inertia effects would move the material away from the rod.

Another way of describing viscoelasticity is the fact that under a constant loading (resp. stretching) strain (resp. stress) depends upon time, which is often described as the fact that mechanical characteristics depend upon time. Specifically, the time dependent behavior of polymers is due to their molecular structure and the fact any deformation would involve conformational changes at different levels. This introduces a kind of memory effects which creates the need to characterize engineering properties in a manner different than those used for other structural materials.

A discussion of physically based approaches for visco elasticity is out of the scope of the present study. Let's start at the point where mechanical effects of viscoelasticity have to be accounted for. The simplified vision according which deformation of polymers combines some reversible phenomena that are equivalent to those existing in an elastic solid and some others, time dependent and irreversible, that exist in a viscous fluid, is then good starting point.

In consequence, models are often depicted through simple analogical systems consisting of elastic elements (springs, which represent the elastic reversible part) and viscous elements (dashpots, which account for time dependent irreversible part). If one considers that global strain results from addition of individual strains, which are associated to the two contributions, serial models are proposed. If one assumes that global stress results from addition of individual stresses, parallel models are used.

Models are then built up via an a priori decomposition of the strain (resp. stress) into contributions that are either reversible or not and a combination of either the elementary strains or stresses.
Additionally to that, one can distinguish two main levels, linear and not linear, of viscoelasticity.
In the linear approaches the Boltzmann superposition principle [15] [38] is valid. It is usually applicable for small strains. However, the superposition principle often provides a useful first order approximation.

The non-linear viscoelasticity usually occurs when the deformations are large or when the properties of the material vary upon deformations. Two types of nonlinearities are to be distinguished: the material nonlinearities and the geometric nonlinearities. Material nonlinearities refer to nonlinear stress strain response that occurs due to the inherent constitutive response of the material, while geometric nonlinearities refer to mathematical issues that arise when displacements and strains become large and when the linearized definitions of stress and strain become irrelevant.

The isochronous response is linear for linear viscoelastic materials, but the stress-strain curves at different times are separated from one another. When a viscoelastic material behaves nonlinearly, the isochronous stress-strain curves begin to deviate from linearity at a certain stress level. In our work, even if starting with simple Kelvin-Voigt model to treat viscoelasticity, we here began to work on the implementation of a nonlinear model, by considering visco-hyper-elasticity.

2.1.2 Isochronous modulus vs. temperature behavior

The temperature plays an important role on the mechanical behavior of polymers. Two important temperatures are the glass transition temperature *Tg* (or second order transition temperature) and *Tm*, the melt temperature (or first order transition temperature) for semicrystalline material or the flowing temperature for amorphous materials. The need of an isochronous modulus-temperature curve as shown in Figure 2-1 is essential to determine the *Tm* and *Tg*. This figure illustrates the variation of the 10 second relaxation modulus with temperature for amorphous, crystalline and cross-linked polymers [15]. Usually, we distinguish four zones: glassy, transition, rubbery and flow regions.

- In the glassy state, polymers are rigid with high modules that can reach 1 *GPa*. The behavior of the polymer is slightly visco elastic and there is often evidence for visco plasticity at higher strains. At the lower temperatures the material become brittle.
- In the glass transition zone, viscoelastic effects become predominant, plastic processes disappear progressively and hyper elasticity progressively takes place. The transition temperature *Tg* corresponding to the limit between glassy and rubbery state.
- In the rubbery state, the stiffness modulus reaches a lower limit, and rupture deformations are larger. In this phase, strain is mainly reversible though not totally elastic when polymer is not crosslinked. In any case elastic part is rather representative for not linear hyper elasticity than glassy enthalpy elasticity.

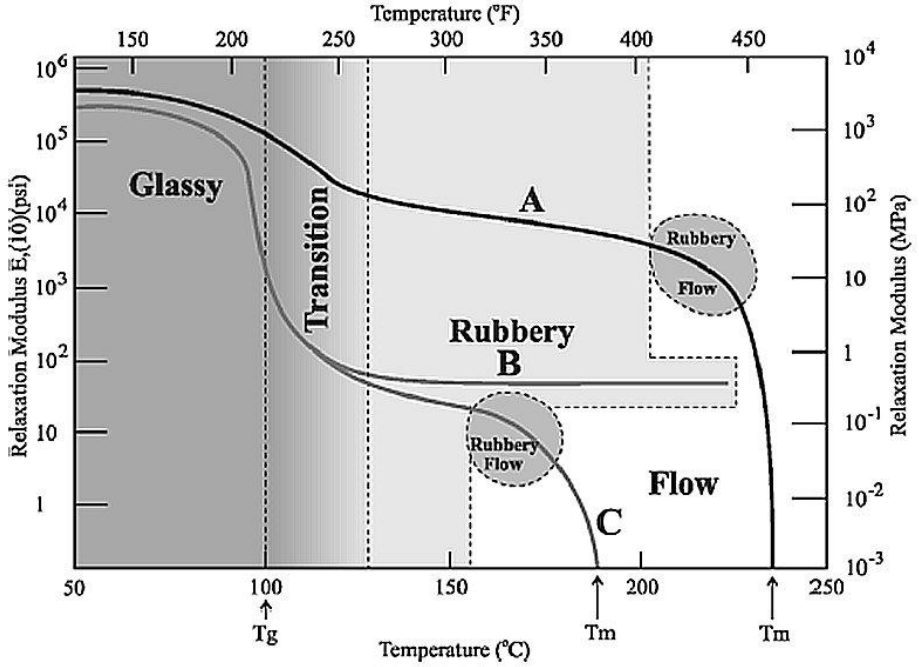


Figure 2-1: E (10 Sec.) for a crystalline polystyrene (A), a lightly cross-linked polystyrene (B), and amorphous polystyrene (C) [15].

The *Tg* is an important descriptor of polymer thermo-mechanical response. This factor is a fundamental measurement of the molecular mobility, and of the effect such as effect of absorbed diluents, expansive stress states, and lack of bulky molecular groups.

2.1.3 Phenomenological mechanical models

The time dependence of viscoelastic response is analogous to the time dependence of reactive electrical circuits, and both can be described by identical ordinary differential equations in time. A convenient way to develop these relations is by employing "spring-dashpot" models. In the following section, we will see the simplest "spring-dashpot" models.

2.1.3.1 Linear viscoelasticity

We remind briefly in the following the three simplest linear viscoelastic models: the Maxwell's model, the Kelvin-Voigt's model and the Zener's model [39]. We start with the Maxwell model, represented by a purely viscous damper and a purely elastic spring connected in series, as shown in the Figure 2-2:

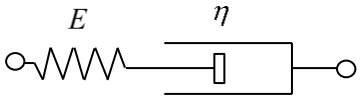


Figure 2-2: Schematic representation of Maxwell model.

At time t the strain in the spring is ε_1 and that of the dashpot ε_2, while the stress on each element is the same and equal to the imposed stress:

$$\sigma = \sigma_2 = \sigma_1 = E\varepsilon_1 = \eta\frac{d\varepsilon_2}{dt} = \eta\frac{d\left(\varepsilon - \varepsilon_1\right)}{dt} \tag{2.6}$$

since the total strain is the sum of the strain in each element:

$$\dot{\varepsilon} = \dot{\varepsilon}_1 + \dot{\varepsilon}_2 = \frac{\dot{\sigma}}{E} + \frac{\sigma}{\eta}t \tag{2.7}$$

This model is able to reproduce partly the relaxation. In that case for a given constant strain, ε:

$$\sigma = E\varepsilon\exp\left(-\frac{t}{t_r}\right) \tag{2.8}$$

with $t_r = \frac{\eta}{E}$, a relaxation time.

However, Maxwell model cannot predict creep, which can be partly reproduced using Kelvin–Voigt's model, also known as the Voigt model (Figure 2-3). In that case stress results from the addition of individual stress in each branch:

$$\sigma = \sigma_1 + \sigma_2 \tag{2.9}$$

with

$$\sigma_1 = \eta \frac{d\varepsilon}{dt} \text{ and } \sigma_2 = E\varepsilon \tag{2.10}$$

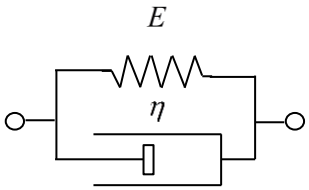


Figure 2-3: Schematic representation of the Kelvin–Voigt model.

In the case of a creep test (stress kept constant at σ):

$$\varepsilon = \frac{\sigma}{E}\left(1 - \exp\left(-\frac{t}{t_r}\right)\right) \tag{2.11}$$

Contrary to Maxwell's model, Kelvin-Voigt's model is not relevant in case of relaxation.

To model more than one viscoelastic phenomenon authors generally combine those simple or those generalized models. Amongst simplest approach, let's quote *Burgers'* model (Figure 2-4) as an example that involves a spring E_1, in series with a Kelvin-Voigt's element with E_2 and η_2, and with a dashpot η_1, as shown in the following Figure 2-6.

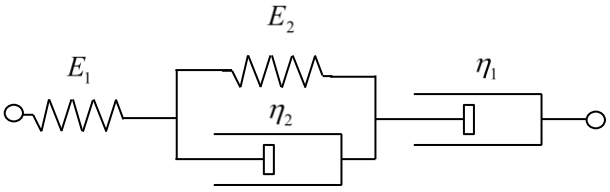


Figure 2-4: Schematic representation of the Burgers model.

Under a constant stress σ left the spring account for a strain:

$$\varepsilon_1 = \frac{\sigma}{E_1} \tag{2.12}$$

At the same time the strain in the Kelvin-Voigt element is:

$$\varepsilon_2 = \frac{\sigma}{E_2}\left(1 - \exp\left(-\frac{E_2 t}{\eta_2}\right)\right) \tag{2.13}$$

Finally strain of the right dashpot is:

$$\varepsilon_3 = \frac{\sigma t}{\eta_1} \tag{2.14}$$

The total strain is then:

$$\varepsilon = \sigma\left[\underbrace{\frac{1}{E_1}}_{elastic} + \underbrace{\frac{1}{E_2}\left(1-\exp\left(-\frac{t}{t_r}\right)\right)}_{delayed\ elastic} + \underbrace{\frac{t}{\eta_1}}_{flow}\right] \tag{2.15}$$

with $t_r = \frac{\eta_2}{E_2}$

which means

- spontaneous elastic deformation,
- delayed elastic deformation, or reversible creep,
- irreversible creep (flow)

Parallel to that, both the two approaches allow defining one unique relaxation time. Due to the complexity of the polymers structure, especially semi-crystalline, one unique relaxation time is not enough to represent all the observed viscoelastic phenomena. Combining several of these elementary models in a parallel (in case of Maxwell's model) or in a serial (in case of Voigt's model) manner defines so-called generalized Maxwell (Figure 2-5) or generalized Kelvin-Voigt (Figure 2-6) models and allow reproducing time relaxation distribution, $t_{r,i}$.

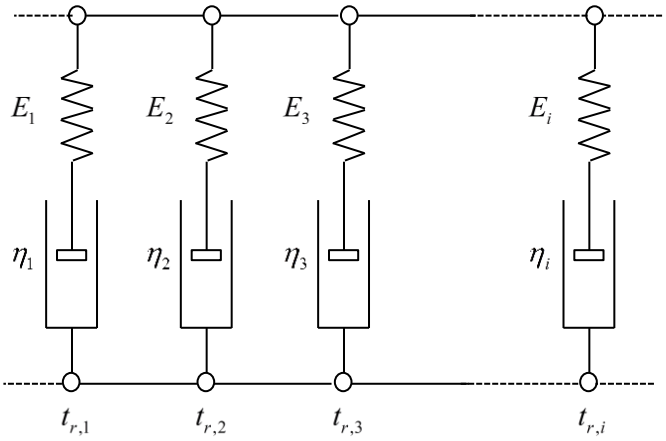


Figure 2-5: Generalized Maxwell model.

In case of genberalized Maxwelle model one can reproduce relaxation as:

$$\sigma = \varepsilon\left[E_1\exp\left(-\frac{t}{t_{r,1}}\right) + E_2\exp\left(-\frac{t}{t_{r,2}}\right) + \cdots + E_i\exp\left(-\frac{t}{t_{r,i}}\right)\right] \tag{2.16}$$

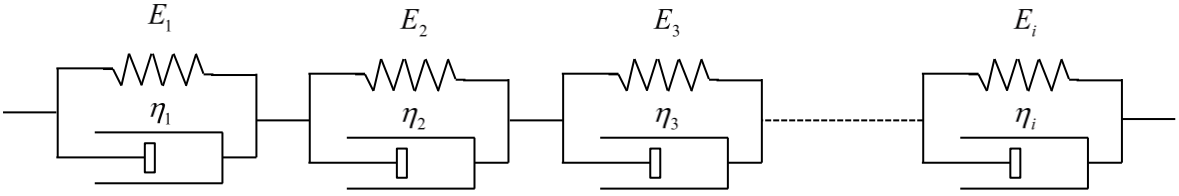


Figure 2-6: Generalized Kelvin-Voigt model.

Whilst creep can be reproduced using generalized Voigt model.

$$\varepsilon = \sigma\left[\frac{1}{E_1}\left(1-\exp\left(-\frac{t}{t_{r,1}}\right)\right)+\frac{1}{E_2}\left(1-\exp\left(-\frac{t}{t_{r,2}}\right)\right)+\cdots+\frac{1}{E_i}\left(1-\exp\left(-\frac{t}{t_{r,i}}\right)\right)\right] \tag{2.17}$$

To be complete let's also emphasize that this review is far from complete. Authors often combine those basic concepts (generalization and combination of Maxwell and Voigt elements) to reproduce experimental observations.

Introducing nonlinear springs or dashpot at one level or another allows accounting for material nonlinearity. Some physically based approaches also exist. Built up within the frame of chain statistic elastic dumbbell strategy leads to results equivalent to Maxwell's model. Network and reptation theories lead to more complex model [40]. Those models manipulate different parameters, namely entanglements density, chain length instead of modulus and viscosity. Obviously one has also to keep in mind that all involves parameters should depend on temperature. Nevertheless, at this stage simple models are rich enough to enlighten numerical difficulties and to validate feasibility of our proposal, and that is why the Kelvin-Voigt model is chosen to illustrate our numerical even it is going to be applied to

- elastic or hyper-elastic,
- viscous,
- viscoelastic,
- visco-hyper-elastic,

simple test cases. In the following, combination of viscous and elastic scheme through a FSI approach in the literature will be summarized.

2.2 Fluid structure interaction (FSI) numerical approaches review

Fluid-structure interaction phenomena are present in many domains of modern engineering such as nuclear, aerospace, civil engineering, shipbuilding and biomechanics domains. In the last three decades, there has been an increasing interest for the simulation of these problems. Nevertheless, the purpose of this literature review is to focus on FSI problem between an incompressible Newtonian fluid and a compressible elastic structure to study efficient numerical methods to model the viscoelastic behavior.

Firstly, we present the FSI problem in a general context. Afterwards, we introduce the numerical methods to solve this problem with its advantages and disadvantages.

2.2.1 Fluid-Structure formulation

We consider a homogeneous linear elastic solid Ω_s, immerged in a computational domain Ω and surrounded by a fluid domain Ω_f, assumed to be incompressible Newtonian.

2.2.1.1 Mechanical characteristics in the solid

The local formulation of the problem is:

$$\begin{cases} \nabla \cdot \sigma_s + f_s = \rho_s \dfrac{d^2 u}{dt^2} & \text{in } \Omega_s \\ u_s = u_{imposed} \quad or \quad \sigma_s . n_s = f_{imposed} & \text{in } \Gamma_{f/s} \end{cases} \tag{2.18}$$

where u, ρ_s and f_s are the displacement of point in the solid, the density and the exterior force applied to the solid, respectively. σ_s is described as the Cauchy stress tensor $\sigma_e = 2\mu_e \varepsilon(u) + \lambda_e tr\varepsilon(u) I$, related to the displacement by a constitutive model (linear elastic).

$\Gamma_{f/s}$, $f_{imposed}$ and $u_{imposed}$ represent the fluid-solid interface, the boundary force and the boundary displacement. n_s is the vector normal to the solid interface.

2.2.1.2 Mechanical characteristics in the fluid

The fluid is assumed to be homogeneous, Newtonian and incompressible. The local formulation of the problem is described by the Navier-Stokes equations below:

$$\begin{cases} \rho_f \left(\dfrac{\partial v}{\partial t} + v \cdot \nabla v\right) - \nabla \cdot \sigma_f = f_f & in\ \Omega_f \\ \nabla \cdot v = 0 & in\ \Omega_f \\ v = v_{imposed} \quad or \quad \sigma_f . n_f = \sigma_{imposed} . n_f & in\ \Gamma_{f/s} \end{cases} \tag{2.19}$$

where v, ρ_f and f_f are the velocity, the fluid density and the exterior force in the fluid. The stress tensor in the fluid is defined as:

$$\sigma_f = 2\eta_f \varepsilon(v) - pI \tag{2.20}$$

2.2.1.3 Fluid-Structure interface conditions

The coupling of the structure and the fluid occurs at the interface $\Gamma_{f/s}$. Therefore, the interface conditions are needed to ensure the continuity of velocity and of the interface force. These conditions can be resumed as following:

$$\begin{cases} \dfrac{du}{dt} = v \\ \sigma_f . n_f = \sigma_s . n_s \end{cases} \quad \text{in } \Gamma_{f/s} \tag{2.21}$$

The fluid-structure interactions are part of the simulation of the behavior where the environment contains two phases. Indeed, the simulation of this environment type requires defining a behavior for the fluid, another for the structure and an interaction model between the two phases.

2.2.2 Fluid-structure coupling: monolithic vs. partitioned coupling

Coupling is the energy conservative transfer between two systems through an interface. In the literature, two coupling types are suggested: the monolithic coupling and the partitioned coupling.

In a monolithic coupling, fluid and structure equations are solved in the same system, it means that the mechanical problems in the fluid and in the solid are simultaneously computed. This method was applied, by Walhorn et al. [41] [42] to FSI problems involving free surface waves using a space-time finite element discretization. It was used also to solve a multiphase problem [43] with pretty good results in the case of a two phases problem (fluid-fluid or fluid-rigid). This coupling gives unconditional stability of the coupling scheme, the time step is limited only by the required accuracy, therefore convergence to the solution is optimal [44] [45] [46].

This method consists of a fully explicit coupling with an alternative exchange between the fluid and the structure solver in each instant via the boundary conditions. The partitioned coupling allows using the computation specific to each environment. However, this method may induce problems in controlling interface and in precision and stability of the calculation [44] [46] [47]. Let us emphasize that a partitioned coupling is not necessarily a weak coupling since the continuity conditions can be strengthened. Recently, a strong partitioned coupling FSI [48] [49] has been developed to solve the problem keeping the robustness and effectiveness of the original approach.

Monolithic coupling for large-displacement FSI problems is often thought to be more robust than the partitioned coupling, but often too expensive both in terms of memory and in terms of CPU time requirements. However, Heil and co-workers [44] demonstrated these beliefs to be at least sometimes unjustified. They studied the relative efficiencies of the partitioned and of the monolithic coupling in the case where the fluid is Newtonian and incompressible. First, results showed that the monolithic solver performs better when the coupling is strong and the partitioned solver performs better for a weak coupling. Nevertheless, for the steady solutions computed here, both methods are competitive. Heil [44] demonstrated that monolithic solvers are competitive even for problems in which the fluid–solid coupling is weak. When the fluid-structure is strong, severe convergence problems appear with the partitioned solvers and the monolithic solvers are advantageous. However, for large problems, particularly in 3D, the effective use of monolithic solvers requires efficient preconditioning of the iterative solving of the large linear systems associated to the fully coupled system of nonlinear algebraic equations by the Newton's method.

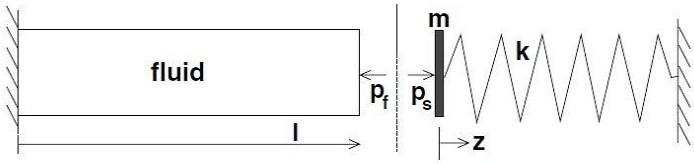


Figure 2-7: The piston problem (interface region expanded for clarity) [46].

Moreover, for a 1D model of a piston interacting with a fluid (Figure 2-7), Hulshoff and al. [46] made a comparison of the two types of coupling in terms of stability, accuracy and computational cost. They demonstrated that the time step controls the stability of the partitioned method. On the other hand, no restriction exists for the monolithic method so that the time step is only limited by the wished accuracy of the calculation. However, for a given accuracy [46] time steps required by the partitioned method are smaller than those of the monolithic method. Consequently, for a certain level of accuracy, a monolithic approach can be a reasonable solution. Furthermore, there is a potential for reducing their computational cost (the monolithic method is still three to four times higher than the one of the partitioned method), which only needs a single fluid-structure iteration per time step in this simulation.

Choosing between partitioned and monolithic approaches is then not a simple task and may depend on the context. The monolithic approach is often more robust and more accurate than the partitioned method and ensures unconditional stability. However, this method is costly in terms of memory and computing time. So, there is an intermediate strategy to combine the benefits (and to avoid the disadvantages) of these two extreme cases. A possible technique is to choose a partitioned explicit algorithm and to make it more robust and less restrictive towards the time step criteria by using an iterative predictor-corrector type. However, a key issue of the FSI problem is the interfaces treatment, the difficulty being to ensure the conditions described in section 2.2.1.3, especially on moving interfaces. The next section will concern the resolution of this problem.

2.2.2.1 FSI resolution

In most cases, FSI is solved using the finite element or the finite volume method. However, meshless methods are also used. Like the SPH method (Smooth Particle Hydrodynamics) developed by Gingold et al. [50] and the PFEM method (Particle Finite Element Method, considered as a special class of meshless methods) [51] [52]. Recently, several studies used the XFEM (eXtended Finite Element Method) method which revealed advantages but also weaknesses in comparison with FEM [53].

In general, meshless methods have considerable flexibility regarding the easiness to add or to remove particles following the evolution of the simulation, without updating the data structure. In addition, as the shape functions are less dependent on the disposal of discretization points, problems due to large deformations are less sensitive in that case. However, whatever the method is, searching for the nearest neighbors is an expensive process, to be performed at all integration points in the numerical integration of the variational problem. The FEM is much less costly thanks to the exact integration in the space of polynomial function. Then, the integration error is zero. Integration points are placed regularly in each finite element. Conversely, the notion of element does not exist in the meshfree methods. Same formulas can be used for integration, but due to a lack of accuracy more integration points are needed to minimize the error. For convenience, we will not use these meshless methods, only the FEM is considered. The fluid problem is generally solved in the literature by an Eulerian formulation where the computational domain remains fixed over time, while a Lagrangian formulation with the deformation of structure domain is used for

the structure problem. However, in a FSI problem which combines the whole fluid and structure problem in a same system, an adaptive approach which satisfies and takes the advantages of the two methods is of prime interest. Whatever the chosen method for fluid-structure coupling, the difficulties are related to the prediction of fluid-structure interface. In practice, authors use a fixed or mobile mesh techniques.

2.2.2.2 Dynamic mesh

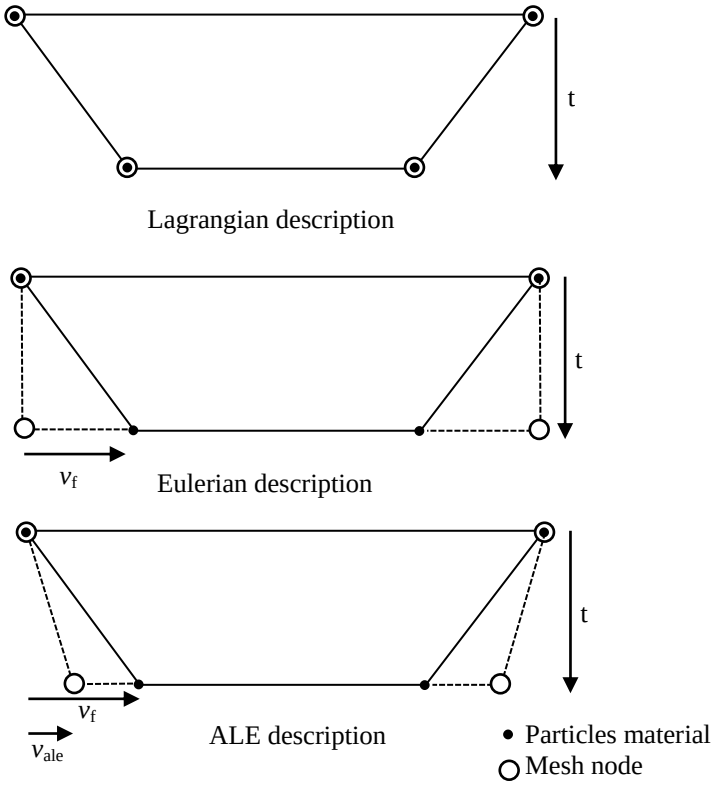


Figure 2-8: Referential Lagrangian, Eulerian and ALE [54].

2.2.2.2.1 Moving mesh

The domain is discretized by a moving mesh in order to follow the motion of the fluid-structure interface. In this context, we can use a Lagrangian formulation where the bodies motion is considered as volume elements which are carried along with the body in a known reference. The reference system is attached to the volume elements.

In the Lagrangian formulation (Figure 2-8), each node is linked to the same material particle throughout the deformation process. An interesting numerical advantage of this approach is the negligible convective terms in the integrated constitutive equations. Moreover, following the boundary becomes easier than in the case of the Eulerian formulation. However, in the large deformations, the mesh can be largely distorted and lead to inaccurate results, or endanger the simulation. In this case, remeshing is required but this step is usually expensive.

Among existing numerical methods, Arbitrary Eulerian-Lagrangian method (ALE) is widely used as an alternative solution. Full explanation can be found in [54] [55] [56] [57] [58]. The ALE formulation (Figure 2-8) combines the advantages of the Lagrangian formulation (accurate

boundary representation, easiness to impose boundary conditions) and those of the Eulerian formulation (for large distortion case). The principle of the ALE formulation is to describe the fluid equations in an arbitrary reference by introducing an arbitrary velocity of the mesh. This reference is a generalization of the Lagrangian and Eulerian frameworks. The arbitrary velocity can deform the domain according to the mesh node position. Concretely, when the nodes are far from the mobile interface, the arbitrary velocity tends to zero such as in the approach tends to an Eulerian approach. On the other hand, when these nodes are near the interface, the arbitrary velocity tends to the velocity of the interface, which corresponds to Lagrangian approach. In between those two zones, intermediate velocities are applied that ensure the deformation is smooth (Figure 2-9). Applying this approach to the incompressible Newtonian fluid leads to equation (2.22):

$$\begin{cases} \rho_f \left(\frac{\partial v}{\partial t} + (v - v_{ale}) \cdot \nabla v\right) = f_f + \nabla \cdot \sigma_f & \text{in } \Omega_f \\ \nabla \cdot v = 0 & \text{in } \Omega_f \\ v = v_{imposed} \quad et \quad \sigma_f . n_f = \sigma_{imposed} . n_f & \text{in } \Gamma_{f/s} \end{cases} \tag{2.22}$$

where v_{ale} is the arbitrary velocity of the material point, which represents the deformation velocity of the mesh. One can check that $v_{ale} = 0$ corresponds to the Eulerian description and $v_{ale} = v$ to the Lagrangian description.

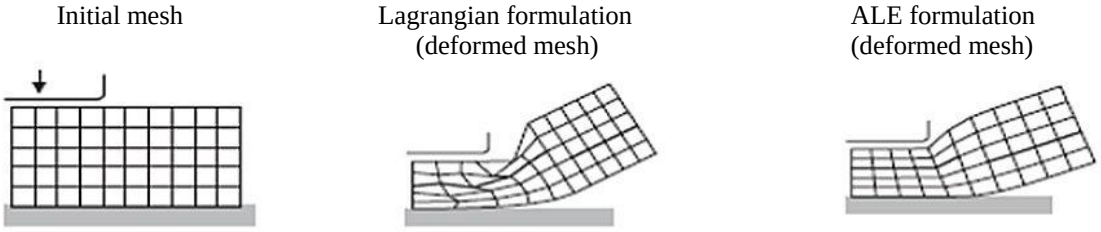


Figure 2-9: Evolution of the mesh following the implemented formulation [58].

The ALE method is quite simple to implement and accurate. However if the deformation, displacement or rotation of the solid is too large, the mesh can be largely distorted, which affects the accuracy of the solution. We can then use mesh adaptation, which causes a significant computational cost.

2.2.2.2.2 Fixed mesh

The computational domain remains fixed, and it is then necessary to model boundaries and boundary conditions to monitor the interface over time within this mesh. Among all numerical method using a fixed mesh, Eulerian formulations are widely used in fluid mechanics or in the stationary materials forming. This method considers volume elements at fixed locations in space, across which material flows. The reference system is fixed. The Eulerian formulation introduces difficulties in problems where the boundaries are variables. It is a great difficulty to take into account the physical boundary conditions and an accurate definition of physical borders when they change over time. In contrast, Eulerian formulations allow a significant distortion of the material.

The Immersed Boundary method (IB) developed by Peskin [59] can also be mentioned. The advantage of this method is to use a fixed Cartesian grid for the fluid domain and a fully

independent structure immersed in the fluid. The fluid-structure interaction is made by the nodal distribution forces and nodal velocity interpolation between Eulerian and Lagrangian domain on the volume using an approximation of the Dirac delta function. The Dirac function is operated in two different stages in the IB algorithm: the first step defines the action-reaction effect, imposing the conservation of forces at the interface, and the second results in the kinematic condition: the structure itself even has to move at the same velocity as the liquid around it. This function shall be continuous to avoid the jump in velocity and in applied forces in the immerged structure or the applied forces. This ensures also that the moment of forces through the interface is maintained.

Several methods based on the IB method have been developed to solve the FSI problem, such as Immersed Finite Element Method (IFEM) [60], Extended Immersed Boundary Method (EIBM) [61], Immersed Interface Method [62] and Fictitious Domain Method [63]. These methods allow large displacements and can be coupled with ALE formulation [64] [65].

Loon and co-workers [66] [67] [68]compared the ALE method and the fictitious domain/ALE coupling in the deformed thin solid case. They concluded that, depending on the problem, the ALE method is probably preferable to other approaches; however, a remeshing tool is required. The algorithm is robust, accurate without excess of degrees of freedom. However, the fictitious domains method is a wise choice when deformation, displacement or rotation of the solid is large. We might choose to use the coupling fictitious domain/adaptation on the required accuracy.

Figure 2-10 shows the results obtained by Van Loon et al. [68] for the pressure drop through a plastic membrane using the fictitious domain with and without mesh adaptation.

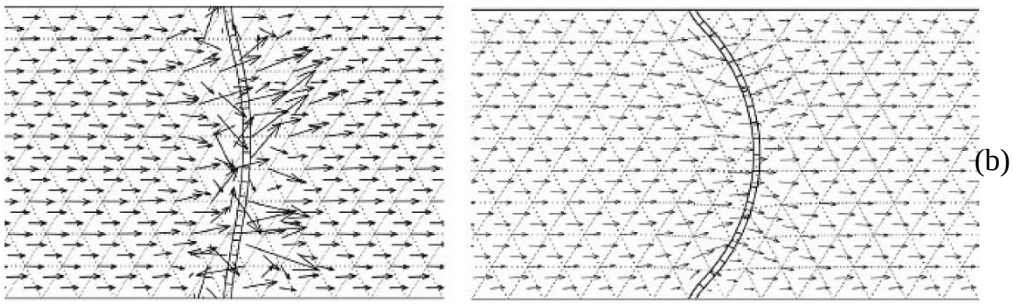
(a)  (b)

Figure 2-10: Pressure drop over a membrane using the fictitious domain method without mesh adaptation (a) and with mesh adaptation (b) (showing the velocity vector field) [68].

2.2.2.3 Determining interfaces

Numerical techniques used in the context of fluid-structure interaction are based on the natural representation of the interface between the two environments, that can be represented through sharp-interface models and diffuse interface models (either two-phase or mixed) (Figure 2-11).

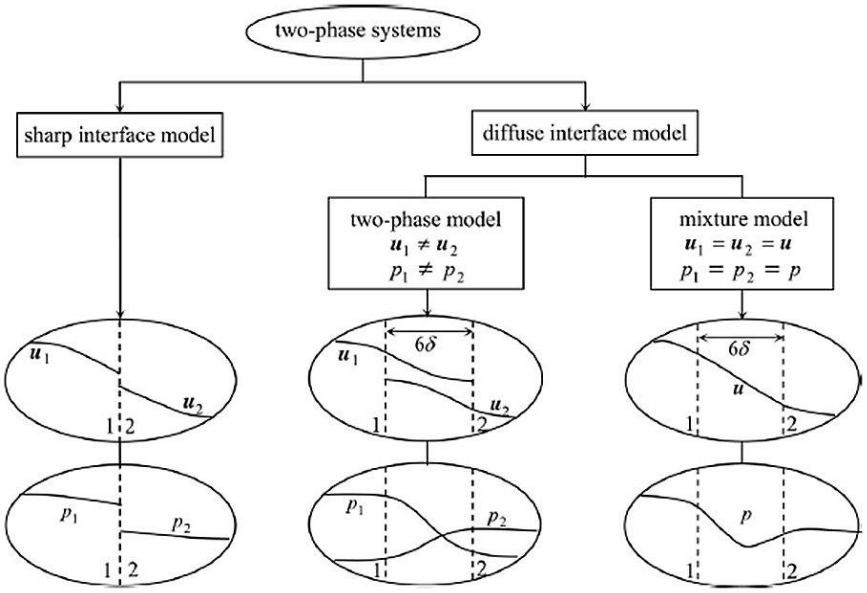


Figure 2-11: Illustration of the sharp-interface, and two-phase and mixture diffuse-interface approaches [69].

In diffuse interface methods, a popular tool for simulation of two-phase flows, interface between the two phases is considered as having a finite width and is characterized by rapid but smooth transitions in the density, viscosity, and other physical quantities. The two-phase model has been discussed in [70] [69], and its performance is compared to those of the mixture model.

If the mesh of the computational domain is fixed, a specific function is required for locating the interface. Two types of computation techniques exist in the literature that are support by the finite elements. The first consists in capturing the geometry of the surface; an example of this type is the level-set method. The second consists on accepting a loss of certain information: such is in the case of volume of fluid method (VOF). The latter methods are sometimes or always associated with diffuse interface approaches.

2.2.2.3.1 Volume of fluid

This method is based on the value of the volume fraction occupied by a phase within an element. This method is considered an ascendant of the earlier MAC methods (Marker and Cell), SLICE method (Simple Line Interface Calculation), or the method PLIC (Piecewise Linear Interface Calculation). A brief idea of these methods is introduced in [56].

2.2.2.3.2 Level-Set

The standard Level-Set method is proposed by Osher and Sethian [71], and it has been used to transport the interfaces between the different phases. Its motion is then described by:

$$\frac{d\alpha(x)}{dt} = 0 \quad x \in \Gamma \tag{2.23}$$

where α is the phase function defined as the distance to the interface:

$$\begin{cases} \alpha(x) = d(x,\Gamma) & x \in \Omega_s \\ \alpha(x) = 0 & x \in \Gamma \\ \alpha(x) = -d(x,\Gamma) & x \in \Omega - \Omega_s \end{cases} \tag{2.24}$$

Γ is the interface and Ω_s represents one of the subdomains, $d(x,\Gamma)$ is the distance between the interface Γ and the coordinate point x, defined by Schneider et al [72]:

$$\left\| d(x,\Gamma) \right\| = \min_{x_\Gamma \in \Gamma} \left\| x - x_\Gamma \right\| \tag{2.25}$$

Then, after extension, generalization to all levels, gives the following evolution equation for α :

$$\frac{d\alpha(x)}{dt} = 0 \quad \forall x \in \Omega \tag{2.26}$$

It is therefore a transport equation where the Level-Set function is updated and the zero level of Level-Set function describes the interface after evolution. Note that only the transport of the zero level of the Level-Set function has a physical sense, the generalization to other levels is only of practical interest.

In an Eulerian framework, the resolution of equation (2.26) returns to the following advection equation:

$$\begin{cases} \frac{\partial \alpha}{\partial t} + v \nabla \alpha = 0 & x \in \Omega \\ \alpha(t=0,x) = \alpha_0(x) & x \in \Omega \\ \alpha(t,x) = g & x \in \partial\Omega \end{cases} \tag{2.27}$$

with $\alpha_0(x)$ is the initial conditions, and g is the boundary condition applied in the upstream border.

2.2.3 Summary

According to our literature review, the partitioned coupling using the ALE formulation for the fluid domain is one of the most common. However, the need to adapt (or to remesh) the fluid domain, and the coupling of the two solvers, requires substantial resources and time. The Immersed Boundary Methods are attractive due to the possible use of a single solver and to the fact that neither remeshing nor choice for coupling with ALE are needed. However, the representation of the fluid-structure interface and the transmitting information from one domain to another is questionable. Among the different available methods to represent the interface, the most accurate method seems to be the Level-Set method which contains the information on the curvature and the normal to the interface.

In this review, an overview of methods and models for FSI has been presented, each has advantages and disadvantages, reliable with an application domain specific and not to another. The goal is to build on these models and their advantage to deal with a behavior that can be representative of a mixture between the solid and liquid phases. It is difficult to circumvent this challenge using a partitioned coupling, thus we have used a monolithic approach with the

treatment of interfaces using the Level-Set method. The idea is to develop a mixed method with three fields *(velocity, displacement and pressure)* which can predict the correct viscoelastic behavior, by the treatment of stable FSI systems. Actually, thanks to a large numbers of modules and of numerical tools developed in the library FE CimLib, we can perform our methodology. Improvement on the representation of the different fields and the numerical results is obtained through the adaptation of meshes near the interface of the involved domains. Developments on the extension of this method for its stabilization are essential to model the complete interaction between the two media.

Numerical methods will be treated on the next chapter, but before that, the next section shows us the material behavior considered in this work in the different examples and benchmarks which our solver is studied: isotropic elastic, viscoelastic, hyperelastic and visco-hyper-elastic.

2.3 Monolithic approach for the resolution of the extended Navier-Stokes equations with an extra-stress tensor: behavior point of view

Firstly, an introduction of elasticity, viscoelasticity, hyper-elasticity and hyper-visco-elasticity will be presented by a brief reminder of the continuum mechanics in large deformations.

Describing the evolution of a deformable solid over time is to know at each moment all the physical quantities characterizing the state of the system (material point position, velocity, temperature, mass volume, strain, stress, etc...). It is important to distinguish the initial configuration and the current configuration, thus two approaches are possible: a Lagrangian description, compared to the initial configuration (or reference to *t=0*), or Eulerian description compared to the current configuration (at time *t*) (Figure 2-12) [73] [74] [75].

2.3.1 Motion description

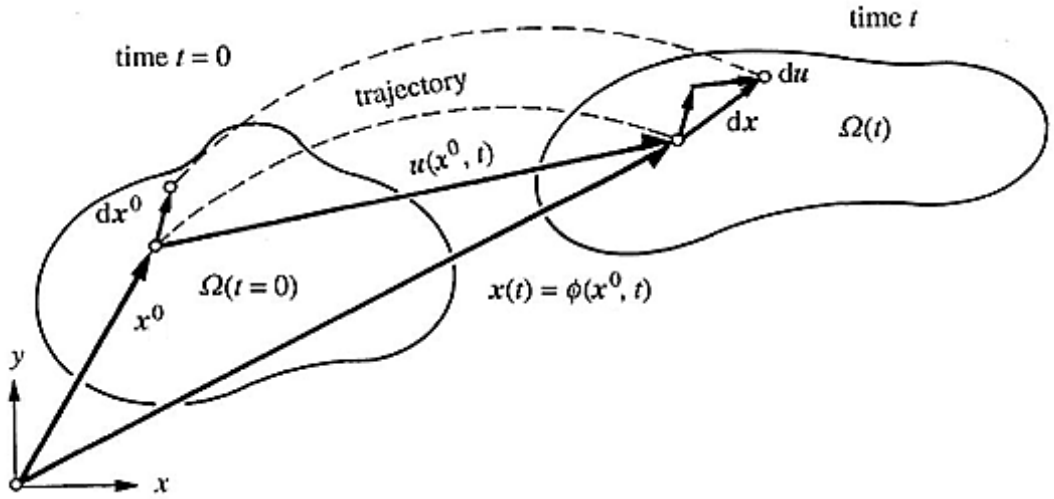


Figure 2-12: Two-dimensional representation of the displacements [76].

In Lagrangian coordinates, the motion of the material is described by the set of trajectories of all the points in the material:

$$x(t) = \phi(x^0, t) \tag{2.28}$$

where x_0 is the initial position of a point at time *t=0* (Figure 2-12). The displacement of a point x^0 at time *t* is naturally defined as the difference between its position at time *t* and its initial position:

$$u(x^0, t) = x(t) - x^0 = \phi(x^0, t) - x^0 \tag{2.29}$$

The displacement field *u* includes the transition, rotation and deformation of the material. The strain can be isolated by considering the displacement of a point neighboring x^0 (Figure 2-12). Differentiating (2.29) at a given time *t*, the new position of a point initially at $v + \Delta x^0$ is given by:

$$x + dx = x^0 + dx^0 + \left(u + du\right) = \left(x^0 + u\right) + dx^0 + \frac{\partial u}{\partial x^0} dx^0 \tag{2.30}$$

From which we obtain:

$$dx = dx^0 + \frac{\partial u}{\partial x^0} dx^0 \tag{2.31}$$

This equation defines the gradient tensor of the transformation *F* or simply the deformation gradient which characterizes the local deformation at *x:*

$$F = \frac{dx}{dx^0} = \frac{dx^0}{dx^0} + \frac{\partial u}{\partial x^0}\frac{dx^0}{dx^0} = I + \nabla_{x^0} u \tag{2.32}$$

where ∇_{x^0} is the gradient operator in the initial configuration x^0.

2.3.2 Strain and strain rate description

The measurement of the form change between the configurations x^0 and $x(t)$. Thus, according to the privileged configuration, several measures of deformations are possible.

2.3.2.1 Lagrangian description (x^0 configuration)

In a Lagrangian framework, we define the right Cauchy-Green strain tensor or Cauchy's dilatation tensor as:

$$C = F^t F = I + \nabla_{x^0} u + \nabla_{x^0} u^t + \nabla_{x^0} u^t \nabla_{x^0} u \tag{2.33}$$

Note that the last term of the Cauchy-Green strain tensor is nonlinear in the displacement. We establish the Green-Lagrange strain tensor, *E*, is defined as:

$$E = \frac{1}{2}\left(C - I\right) = \frac{1}{2}\left(\nabla_{x^0} u + \nabla_{x^0} u^t + \nabla_{x^0} u^t . \nabla_{x^0} u\right) \tag{2.34}$$

We remind that *E* is also a symmetric second order tensor and has the same principal directions as *C* but does not take into account the rigid body motions.

2.3.2.2 Eulerian description ($x(t)$ configuration)

By the same way, in an Eulerian framework, we define the left Cauchy-Green strain tensor $B = FF^t$, symmetric and positive definite. The associated strain tensor is the Euler-Almansi tensor:

$$A = \frac{1}{2}\left(I - B^{-1}\right) = \frac{1}{2}\left(\nabla_x u + \nabla_x u^t + \nabla_x u^t . \nabla_x u\right) \tag{2.35}$$

where ∇_x is, in this case, the gradient operator in the current configuration.

2.3.3 Internal forces and stress description

In fact, the measurement of stress is characterized by the internal force through an element area on a given configuration. Therefore, depending on the choice of configuration, we can have an Eulerian stress, or a Lagrangian stress description.

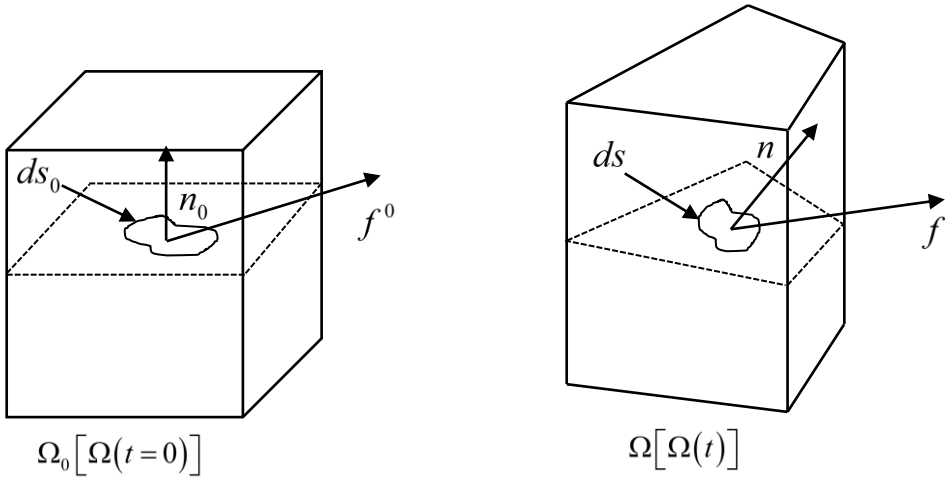


Figure 2-13: Stress description in the different configuration (Lagrangian and Eulerian).

2.3.3.1 Eulerian description

The described stress, in this context, is the Cauchy stress tensor σ, which is a symmetric Eulerian stress tensor:

$$f = \sigma \cdot n \tag{2.36}$$

where n is the normal vector and f is the force, measured in the unit area in the actual configuration. The force in the surface ds can be expressed as:

$$df = \sigma \cdot n \cdot ds \tag{2.37}$$

Numerically, we introduce also the Kirchhoff tensor:

$$\tau^* = J\sigma \tag{2.38}$$

where $J = \det(F)$ represents the changes in volume between a configuration and the other. This stress tensor does not have a physical sense but it is useful to the numerical calculation.

2.3.3.2 Lagrangian description

Since, in a Lagrangian framework, the whole measurement is described in the initial configuration, the force df, measured in the actual configuration, will be transported to the initial configuration as follows:

$$df^0 = F^{-1} \cdot df \tag{2.39}$$

Thus, we define the second Piola-Kirchhoff tensor S as:

$$df^0 = S \cdot n_0 \cdot ds_0 \tag{2.40}$$

S does not have a physical sense but it is described purely in the Lagrangian context and is symmetric. It can be related to the Cauchy tensor by the following relation:

$$\Pi = J\sigma \cdot F^{-t} = F \cdot S \tag{2.41}$$

or

$$\tau^* = J\sigma = F \cdot S \cdot F^t \tag{2.42}$$

with Π is the first Piola-Kirchhoff tensor which relates forces in the current configuration with areas in the initial ("material") configuration.

2.3.4 Equilibrium equation

Equilibrium equations are obtained from the balance of momentum. In a formulation in large deformations, distinction between the initial and current configurations is required.

2.3.4.1 Eulerian description

The balance of momentum in the current configuration can be written:

$$\int_\Omega \rho f_i d\Omega + \int_{\partial\Omega} df_i ds = \int_\Omega \rho\gamma_i d\Omega \tag{2.43}$$

Then, using the definition of the vector forces, and the divergence theorem, we obtain the equilibrium equation in the current configuration:

$$\begin{cases} \rho \dfrac{dv}{dt} - \nabla_x \cdot \sigma = \rho f_i \\ + Boundary\ conditions \end{cases} \tag{2.44}$$

2.3.4.2 Lagrangian description

In a Lagrangian framework, the balance of momentum in the initial configuration can be written:

$$\int_{\Omega_0} \rho f_i^0 d\Omega_0 + \int_{\partial\Omega_0} df_i^0 ds_0 = \int_{\Omega_0} \rho\gamma_i d\Omega_0 \tag{2.45}$$

We obtain the equilibrium equation in the initial configuration:

$$\begin{cases} \rho \dfrac{dv}{dt} - \nabla_{x^0} \cdot \Pi = \rho f_i^0 \\ + Boundary\ conditions \end{cases} \tag{2.46}$$

2.3.5 Large deformations and used models: hyper-elastic and visco-hyper-elastic

Note that the constitutive law must allow us to link the stress tensor with the strain tensor at any point of the solid, regardless of the time *t*. In general, the constitutive law is expressed as a

functional response that depends on the deformation gradient tensor *F*, and must be invariant in any configuration change. Considering a thermodynamic potential, derived from state laws, the specific free energy w which depends on the observable variables and internal variables, and we write in the general case:

$$w = w(F, T, ...) \tag{2.47}$$

For a better detail of the thermodynamic potential, we advise the reader to consult the Appendix or [77]. As example that will be used within this work, in solid behavior laws are written with/without small deformation approaches. Elastic and viscoelastic behavior have been detailed before were written in small deformations as we will show in the following. On the other hand, polymer real behavior should be described in large deformations. Thus hyper-elastic and visco-hyper-elastic laws are firstly written, being the last one the most studied at our lab in what concerns polymers.

2.3.5.1 Modeling of an isotropic hyperelastic material

An elastic material is called hyperelastic if the stress tensor is derived from an energy function of the material. This implies that the work from one state to another does not depend on the path followed. If the material is isotropic (the law of behavior must be invariant under rotation of the reference configuration), we can express w in terms of invariant tensors of C or B, measures of strain defined before. This energy is also called "strain energy". A behavior law in the context of isotropic hyperelastic material can then be written:

$$S = 2\frac{\partial w}{\partial C} \tag{2.48}$$

for 2ème Piola-Kirchhoff tensor or:

$$\sigma = \frac{2}{J}\frac{\partial w}{\partial B}B \tag{2.49}$$

for Cauchy stress tensor.

If the material is isotropic, the energy strain can be also expressed by the invariants I_1, I_2 and I_3 (see Appendix) where *B* and *C* have the same eigenvalues values. Thus, the equation (2.48) can be rewritten as follows [78] [79]:

$$\begin{cases} S = 2\dfrac{\partial w}{\partial C} = 2\left[\left(\dfrac{\partial w}{\partial I_1} + \dfrac{\partial w}{\partial I_2}I_1\right)I - \dfrac{\partial w}{\partial I_2}C + I_3\dfrac{\partial w}{\partial I_3}C^{-1}\right] \\ \sigma = \dfrac{2}{J}\dfrac{\partial w}{\partial B}B = \dfrac{2}{J}\left[\left(\dfrac{\partial w}{\partial I_1} + \dfrac{\partial w}{\partial I_2}I_1\right)B - \dfrac{\partial w}{\partial I_2}B^2 + I_3\dfrac{\partial w}{\partial I_3}I\right] \end{cases} \tag{2.50}$$

2.3.5.1.1 Strain energy

Many forms of the strain energy have been proposed in the literature. Some are based on statistical theory, others are purely phenomenological. There are several ways to classify the different energies of deformation [75]. We present, in this part, the polynomial strain energy. They are among the most used deformation energy. In the polynomial laws, the strain energy depends linearly on the parameters of the constitutive law, and it is expressed in terms of the

invariants I_1 and I_2. They provide a good general smoothing of the experimental results up to moderate strain rates. For higher strain rates, we often increase the order of the polynomial.

The generalized Rivlin model, used in most finite element codes, is given by the following series expansion:

$$w = \sum_{i+j=1}^{N} C_{ij} \left(I_1 - 3\right)^i \left(I_2 - 3\right)^j \tag{2.51}$$

The strain energy is developed to an order proportional to the desired range of deformation (for *N = 3*, there is generally a good correlation with experimental measurements). Practically, most used polynomial corresponds to a particular development Rivlin. For example, keeping only the first term, we obtain the Neo-Hookean law:

$$w = C_{10}\left(I_1 - 3\right) \tag{2.52}$$

The Neo-Hookean model provides a good correlation for moderate strain rates (up to 50%), but is not suitable for the consideration of large deformations.

$$\begin{cases} S = 2\dfrac{\partial w}{\partial C} = 2C_{10}I \\ \sigma = \dfrac{2}{J}\dfrac{\partial w}{\partial B}B = \dfrac{2}{J}C_{10}B \end{cases} \tag{2.53}$$

2.3.5.2 Modeling of an isotropic visco-hyper-elastic material

Billon has recently developed a visco-hyper-elastic model which allows reproducing a wide range of the thermomechanical behavior of materials [80] [81] [82] [83] [84]. Derived from the network model from Vilgis Edwards [38] [85] [86], this new approach leads to a strongly coupled thermal three-dimensional constitutive model [77] detailed in the Appendix. Later in this text, we will deal with its numerical modeling and its implementation in CimLib®, after the validation by comparison with the mechanical tests performed by Baquet E. [77].

Considering the material as incompressible, stress derives from an energy potential as:

$$\begin{cases} S = 2\left[\left(\dfrac{\partial w}{\partial I_{1e}} + I_{1e}\dfrac{\partial w}{\partial I_{2e}}\right)I - \dfrac{\partial w}{\partial I_{2e}}C_e + I_{3e}\dfrac{\partial w}{\partial I_{3e}}C_e^{-1}\right] \\ \sigma = \dfrac{2}{J}\left[\left(\dfrac{\partial w}{\partial I_{1e}} + I_{1e}\dfrac{\partial w}{\partial I_{2e}}\right)C_e - \dfrac{\partial w}{\partial I_{2e}}C_e^{\,2} + I_{3e}\dfrac{\partial w}{\partial I_{3e}}I\right] \end{cases} \tag{2.54}$$

with *w* is based on the Edwards-Vilgis's potential:

$$w=\left[\begin{array}{l}\frac{1}{2}kTN_c\left(\frac{\left(1-\alpha^2\right)I_1^e}{\left(1-\alpha^2 I_1^e\right)}+\ln\left(1-\alpha^2 I_1^e\right)\right)+\frac{1}{2}kTN_s\left(\begin{array}{l}\frac{\left(1+\eta\right)\left(1-\alpha^2\right)}{\left(1-\alpha^2 I_1^e\right)}\frac{I_1^e+2\eta I_2^e+3\eta^2 I_3^e}{1+\eta I_1^e+\eta^2 I_2^e+\eta^3 I_3^e}\\ +\ln\left(1-\alpha^2 I_1^e\right)+\ln\left(1+\eta I_1^e+\eta^2 I_2^e+\eta^3 I_3^e\right)\end{array}\right)\end{array}\right]$$

In fact, the presented thermodynamic model is based on a description of the energy behavior. The potential energy is used from statistical models of the chain. This choice allowed maintaining a strong physical sense while minimizing the number of parameters. For one condition, five principal parameters of materials (N_c, N_s, α, Z_p, β) have been introduced, which are sufficient to reproduce experimental observations with a good agreement.

Apart from E-factors that are thermodependent modules-like parameters *w* depends upon four material parameters:

- N_c the density of cross-links,
- N_s the density of slip-links or the entanglement density,
- α the inextensibility parameter, which account for the fact that polymer chains have a limited extensibility,
- η the slipperiness factor, which is an indirect trace of the freedom of entanglement. If $\eta=0$ entanglements act as permanent nodes and if $\eta=1$, they do not contribute to the elasticity of the network,

Remark: attention, with respect to the notation in the literature, we kept the notation of slippage parameter as η in this case which is different with the viscosity.

For their part I^e are the invariants of right and left elastic Cauchy-Green tensor, C_e, related with the Cartesian components of the elastic stretch ratios λ_i.

Anelasticity results from additional freedom in entanglements (i.e., de entanglement), which is accounted for by an increase in η factor whose kinetics, $\dot{\eta}$, depends on the stored elastic energy:

$$\dot{\eta}=Z_p\left(e^{\Delta w}-1\right) \tag{2.55}$$

where z_p is a material parameter depending upon strain rate and temperature.

Δw is the stored entropic energy due to entanglements if w_s represents the component of w depending upon entanglements:

$$\Delta w=w_s\left(I_1^e,I_2^e,\eta\right)-w_s\left(I_1^e=3,I_2^e=3,\eta\right) \tag{2.56}$$

The anelastic strain rate tensor D_{an} is related to a kinetics as follows:

$$D_{an}=\frac{3}{2}\frac{1}{\left(1-\beta\right)}\frac{\left(S\right)^D}{\left(\sigma_{eq}\right)^2}\frac{\partial w}{\partial\eta}\dot{\eta}\quad\text{with}\quad trace\left(D_{an}\right)=0 \tag{2.57}$$

and obey the Clausius Duhem rule. In this equation $(S)^D$ is the stress in the intermediate configuration and σ_{eq} is the Von Mises stress. Notice that β is the Taylor-Quinney coefficient which represents the proportion of anelastic energy converted into heating.

2.3.6 Small deformation and used models: elastic and viscoelastic

If the material deformations are small, small deformation theory may be used. The strain tensors used before:

$$\begin{cases} E = \frac{1}{2}(C - I) \\ A = \frac{1}{2}(I - B^{-1}) \end{cases} \tag{2.58}$$

can be reduced to:

$$\varepsilon(u) = \frac{1}{2}(\nabla_{x^0} u + \nabla_{x^0} u^t) \tag{2.59}$$

Similarly, stress tensors S or Π are reduced in small perturbations to the Cauchy stress tensor σ. There is this no sense in distinguishing initial and final configurations.

2.3.6.1 Modeling of an isotropic elastic material

We assume then that the deformations are small and the Hooke's law can be used. The isotropic linear elastic is characterized by a strain energy density w, quadratic positive definite [87], which depends only on the invariants of $\varepsilon(u)$:

$$w = \frac{1}{2}(2\mu_e \varepsilon_{II} + \lambda_e \theta^2) \tag{2.60}$$

where

$$\begin{cases} \varepsilon_{II} = tr(\varepsilon^2) \\ \theta = tr(\varepsilon) \end{cases} \tag{2.61}$$

In the context of isotropic linear elasticity, the constitutive law is deduced by the derivation of the strain energy density. We obtain the following relationship:

$$\sigma = \frac{1}{J} F \cdot S \cdot F^t = \frac{2}{J} \frac{\partial w}{\partial \varepsilon} B \approx S = 2\mu_e \varepsilon + \lambda_e tr(\varepsilon) I \tag{2.62}$$

2.3.7 Modeling a viscoelastic behavior

Let us consider equation (2.1), which represents the stress tensor using the viscoelastic Kelvin-Voigt model. First, considering small deformations, the elastic stress is defined as:

$$\sigma_e = 2\mu_e \varepsilon(u) - p_e I \tag{2.63}$$

with $p_e = -\lambda_e tr\varepsilon(u)$, named the "elastic pressure term". Due to the simplification, with the "elastic pressure term" $p_e = -\lambda_e tr\varepsilon(u)$, the elastic problem can be rewritten as:

$$\begin{cases} \sigma_e = 2\mu_e \varepsilon(u) - p_e \\ \nabla \cdot u + \dfrac{1}{\lambda_e} p_e = \nabla \cdot u + \chi_{p_e} p_e = 0 \end{cases} \tag{2.64}$$

with $\chi_{p_e} = \dfrac{1}{\lambda_e} = \dfrac{(1+\nu_e)(1-2\nu_e)}{E\nu_e}$.

Note that in the incompressible elastic case ($\nu_e = 0{,}5$), this is equivalent to the problem:

$$\begin{cases} \sigma_e = 2\mu_e \varepsilon(u) \\ \nabla \cdot u = 0 \end{cases} \tag{2.65}$$

By the same way, if we consider that the material behaves like a purely viscous fluid, the most general behavior law is described:

$$\sigma_v = 2\eta_v \varepsilon(v) - \lambda_v tr\varepsilon(v) I - pI \tag{2.66}$$

Considering the second viscosity $\lambda_v = -\dfrac{2}{3}\eta_v$ as a function of the dynamic viscosity (Stokes fluid), the general viscous problem can be rewritten as:

$$\begin{cases} \sigma_v = 2\eta_v \varepsilon(v) - \dfrac{2\eta_v}{3} tr\varepsilon(v) I - pI = 2\eta_v \varepsilon(v) - p_v I \\ \nabla \cdot v + \chi_{p_v} \dfrac{dp_v}{dt} = 0 \\ p_v = \dfrac{2\eta_v}{3} tr\varepsilon(v) I + pI \end{cases} \tag{2.67}$$

with

$$\begin{cases} \chi_{p_v} = \dfrac{1}{1 - \dfrac{2\eta_v}{3}} \chi_p \\ \chi_p = \dfrac{1}{\rho(p_v)} \dfrac{d\rho(p_v)}{dp_v} \end{cases} \tag{2.68}$$

where χ_p has a physical sense and represents the isothermal compressibility, typical of each material. This last expression is the form of the conservation of mass.

Assuming small strains, the compressible viscoelastic Kelvin-Voigt model can be deduced to system from equations:

$$\begin{cases} \dfrac{du}{dt} = v \\ \sigma_{ve} = 2\eta_v \varepsilon(v) + 2\mu_e \varepsilon(u) - p_e I - p_v I \\ \nabla \cdot u + \dfrac{1}{\lambda_e} p_e = 0 \\ \nabla \cdot v + \chi_{p_v} \dfrac{dp_v}{dt} = 0 \end{cases} \tag{2.69}$$

Therefore, the strong formulation for the compressible viscoelastic behavior can be deduced to the Navier-Stokes system:

$$\begin{cases} \left[\rho \left(\dfrac{\partial v}{\partial t} + v \cdot \nabla v \right) \right] - \left[\nabla \cdot 2\eta_v \varepsilon(v) + \nabla \cdot 2\mu_e \varepsilon(u) - \nabla p_e - \nabla p_v \right] = f \\ \nabla \cdot u + \dfrac{1}{\lambda_e} p_e = 0 \\ \nabla \cdot v + \chi_{p_v} \dfrac{dp_v}{dt} = 0 \\ \dfrac{du}{dt} = v \end{cases} \tag{2.70}$$

where ρ is specific mass and f is the body force vector.

Now, by a matter of simplicity, our methodology will be illustrated, first by the resolution of the incompressible viscoelastic Kelvin-Voigt model:

$$\begin{cases} \left[\rho \left(\dfrac{\partial v}{\partial t} + v \cdot \nabla v \right) \right] - \left[\nabla \cdot 2\eta_v \varepsilon(v) + \nabla \cdot 2\mu_e \varepsilon(u) - \nabla p_v \right] = f \\ \nabla \cdot v = 0 \\ \dfrac{du}{dt} = v \end{cases} \tag{2.71}$$

From equations (2.71), considering small deformations, the viscoelastic stress tensor $2\eta_v \varepsilon(v) + 2\mu_e \varepsilon(u)$ can be linearized:

$$2\eta_v \varepsilon(v) + 2\mu_e \varepsilon(u + vdt - vdt) = 2\eta_v \varepsilon(v) + 2\mu_e dt \varepsilon(v) + 2\mu_e \varepsilon(u - vdt) \tag{2.72}$$

Then:

$$2\eta_v \varepsilon(v) + 2\mu_e dt \varepsilon(v) \quad \text{can be written as} \quad 2\eta_{ve} \varepsilon(v) \tag{2.73}$$

The terms called "extra-stress" $\tau = -2\mu_e \varepsilon(u - vdt)$, deduced from equation (2.72), can be written by moving then to the right-hand side members of the Navier-Stokes incompressible equations (2.71). We obtain the system of equations to be solved as:

$$\begin{cases} \rho\left(\frac{\partial v}{\partial t} + v\cdot\nabla v\right) - \nabla\cdot 2\eta_{ve}\varepsilon(v) + \nabla p_v = f - \nabla\cdot\tau \\ \tau = 2\mu_e\varepsilon\left(u - vdt\right) \\ \nabla\cdot v = 0 \\ \frac{du}{dt} = \frac{\partial u}{\partial t} + v\nabla u = v \end{cases} \tag{2.74}$$

The system (2.74), a general mechanical system of equations, shows our methodology to solve the classical viscoelastic Kelvin-Voigt model by a monolithic approach. The resolution of this system is equivalent to the resolution of a multiphase problem such as FSI problem. This derives from the fact that viscoelastic models are decomposed into two parts: an elastic one, named “extra-stress” in the right-hand side members and viscous other.

Our main idea is to use a mixed formulation *(u, v, p) (displacement, velocity, pressure)*, where the two fields *u* and *v* represent the primary variables of a strain and a strain rate formulation, assuming a closure model:

$$\frac{du}{dt} = \frac{\partial u}{\partial t} + v\nabla u = v \tag{2.75}$$

With this equation, which is totally objective, we demonstrate that the transport of stress tensor as classical method is unnecessary, mainly in the resolution by Eulerian approach.

As a first approach, we decided to keep only the linear part of the behaviors where the stress-strain relation remains linear. Practically, this is valid only in small deformations. Nevertheless, examples shown in the subsequent chapters evolve towards large deformations. For example we will show tensile tests up to 100% deformation using both an incremental Lagrangian and Eulerian approaches. Thus the last section of this chapter is devoted to reveal some errors introduced, by outlining also the neglected terms in the numerical schemes compared with the complete formulation.

2.3.8 Resolution and introduced errors

In the following test cases, Eulerian or incremental Lagrangian methods are used. In this section, neglected terms in both cases are shown.

2.3.8.1 Incompressible isotropic elastic material

Compared with the isotropic elastic model showed previously in equation (2.62), in large deformation, the relation between the stress and the strain, described in the Lagrangian and Eulerian configuration, can be rewritten as the below equations in the incompressible case:

$$\begin{cases} S = 2\frac{\partial w}{\partial E} = 2\mu_e E \\ \sigma = \frac{1}{J}F\cdot S\cdot F^t = 2\mu_e F\cdot E\cdot F^t \end{cases} \tag{2.76}$$

Firstly, in an Eulerian framework, the equilibrium equation in the current configuration is described in large deformations as:

$$\begin{cases} \rho \dfrac{dv}{dt} + \nabla p - \nabla \cdot \left[2\mu_e F \cdot \left(\nabla_{x^0} u + \nabla_{x^0} u^t + \nabla_{x^0} u^t \nabla_{x^0} u \right) \cdot F^t \right] = \rho f \\ + \textit{Boundary conditions} \end{cases} \tag{2.77}$$

whereas in small deformations:

$$\begin{cases} \rho \dfrac{dv}{dt} + \nabla p - \nabla \cdot 2\mu_e \left(\nabla_x u + \nabla_x u^t \right) = \rho f \\ + \textit{Boundary conditions} \end{cases} \tag{2.78}$$

Therefore, for a better representation of the theory, we need to include the non-linear term $\nabla_x u^t \nabla_x u$ in the strain tensor and transport the stress tensor in the initial configuration by multiplying by B. Nevertheless, it has not been done in this work.

In a Lagrangian framework, for large deformations, the equilibrium equation in the initial configuration is described as:

$$\begin{cases} \rho \dfrac{dv}{dt} + \nabla_{x^0} p - \nabla_{x^0} \cdot \left[F \cdot 2\mu_e \left(\nabla_{x^0} u + \nabla_{x^0} u^t + \nabla_{x^0} u^t \nabla_{x^0} u \right) \right] = \rho f^0 \\ + \textit{Boundary conditions} \end{cases} \tag{2.79}$$

And, as previously, small deformations have been assumed:

$$\begin{cases} \rho \dfrac{dv}{dt} + \nabla_x p - \nabla_x \cdot 2\mu_e \left(\nabla_x u + \nabla_x u^t \right) = \rho f \\ + \textit{Boundary conditions} \end{cases} \tag{2.80}$$

Furthermore, there are the several missing terms when we compute E in the initial configuration, when we know only the current configuration (like in incremental Lagrangian test cases):

$$\begin{aligned} E &= \frac{1}{2}\left(\nabla_{x^0} u + \nabla_{x^0} u^t + \nabla_{x^0} u^t \nabla_{x^0} u \right) \\ &= \frac{1}{2}\left(\nabla_x u \cdot F + \nabla_x u^t \cdot F^t + \nabla_x u^t \cdot F^t \nabla_x u \cdot F \right) \\ &= \varepsilon(u) + \frac{1}{2}\begin{pmatrix} \nabla_x u^t \nabla_x u + \nabla_x u \nabla_{x^0} u + \nabla_{x^0} u^t \nabla_x u^t + \nabla_x u^t \nabla_x u \nabla_{x^0} u \\ + \nabla_{x^0} u^t \nabla_x u^t \nabla_x u + \nabla_{x^0} u^t \nabla_x u^t \nabla_x u \nabla_{x^0} u \end{pmatrix} \end{aligned} \tag{2.81}$$

The resolution by the Lagrangian incremental resolution where the large deformations are decomposed in several small deformations may limit the errors introduced, since, at each time step, the initial configuration is the deformed are. This will be demonstrated later in the chapter 3.

2.3.8.2 Incompressible isotropic Neo-Hookean hyper-elastic material

The stress-strain relation in the incompressible Neo-Hookean hyper-elastic material is written as:

$$\begin{cases} S = 2\dfrac{\partial w}{\partial C} = 2C_{10}I \\ \sigma = \dfrac{2}{J}\dfrac{\partial w}{\partial B}B = 2C_{10}B \end{cases} \tag{2.82}$$

In an Eulerian framework, we perform the complete numerical scheme for large deformations where the equilibrium equation in the current configuration is described as:

$$\begin{cases} \rho\dfrac{dv}{dt} + \nabla p - \nabla \cdot 2C_{10}B = \rho f \\ +Boundary\ conditions \end{cases} \tag{2.83}$$

In the other way, in a Lagrangian framework, the right way to describe the equilibrium equation is in the initial configuration:

$$\begin{cases} \rho\dfrac{dv}{dt} + \nabla_{x^0} p - \nabla_{x^0} \cdot F \cdot 2C_{10}I = \rho f^0 \\ +Boundary\ conditions \end{cases} \tag{2.84}$$

Nevertheless, throughout the shown examples, the divergence operator will be computed in the current configuration

$$\begin{cases} \rho\dfrac{dv}{dt} + \nabla_x p - \nabla_x \cdot 2C_{10}B = \rho f \\ +Boundary\ conditions \end{cases} \tag{2.85}$$

Once more, an incremental resolution where we can consider the current configuration in the previous time step becomes the initial configuration in the actual time step, can lead to introduced errors that can be neglected.

2.3.8.3 Incompressible isotropic visco-hyper-elastic material

For the incompressible isotropic visco-hyper-elastic material, the stress-strain relation in the different configurations is written as:

$$\begin{cases} S = \dfrac{2}{J}F^{-1}\left[\left(\dfrac{\partial w}{\partial I_{1e}} + I_{1e}\dfrac{\partial w}{\partial I_{2e}}\right)B_e - \dfrac{\partial w}{\partial I_{2e}}B_e^{\,2} + I_{3e}\dfrac{\partial w}{\partial I_{3e}}I\right]F^{-t} \\ \quad = 2F_{an}^{\ -1}\left[\left(\dfrac{\partial w}{\partial I_{1e}} + I_{1e}\dfrac{\partial w}{\partial I_{2e}}\right)I - \dfrac{\partial w}{\partial I_{2e}}C_e + I_{3e}\dfrac{\partial w}{\partial I_{3e}}C_e^{\ -1}\right]F_{an}^{\ -t} \\ \sigma = 2\left[\left(\dfrac{\partial w}{\partial I_{1e}} + I_{1e}\dfrac{\partial w}{\partial I_{2e}}\right)B_e - \dfrac{\partial w}{\partial I_{2e}}B_e^{\,2} + I_{3e}\dfrac{\partial w}{\partial I_{3e}}I\right] \end{cases} \tag{2.86}$$

where $F = F_{an} \cdot F_e$ is the multiplicative decomposition (see Appendix A).

Then, in an Eulerian framework, the equilibrium equation in the current configuration is described as:

$$\begin{cases} \rho \dfrac{dv}{dt} + \nabla p - \nabla \cdot 2\left[\left(\dfrac{\partial w}{\partial I_{1e}} + I_{1e}\dfrac{\partial w}{\partial I_{2e}}\right)B_e - \dfrac{\partial w}{\partial I_{2e}}B_e^{\,2} + I_{3e}\dfrac{\partial w}{\partial I_{3e}}I\right] = \rho f \\ + \textit{Boundary conditions} \end{cases} \tag{2.87}$$

In a Lagrangian framework, the equilibrium equation in the initial configuration is described as:

$$\begin{cases} \rho \dfrac{dv}{dt} + \nabla_{x^0} p - \nabla_{x^0} \cdot 2F_{an}^{\,-1}\left[\left(\dfrac{\partial w}{\partial I_{1e}} + I_{1e}\dfrac{\partial w}{\partial I_{2e}}\right)I - \dfrac{\partial w}{\partial I_{2e}}C_e + I_{3e}\dfrac{\partial w}{\partial I_{3e}}C_e^{\,-1}\right]F_{an}^{\,-t} = \rho f^0 \\ + \textit{Boundary conditions} \end{cases} \tag{2.88}$$

But, as for the Neo-Hookean model, we have admired an incremental Lagrangian scheme, where, at each time step, we redefine the initial configuration:

$$\begin{cases} \rho \dfrac{dv}{dt} + \nabla_x p - \nabla_x \cdot 2F_{an}^{\,-1} \cdot \left[\left(\dfrac{\partial w}{\partial I_{1e}} + I_{1e}\dfrac{\partial w}{\partial I_{2e}}\right)I - \dfrac{\partial w}{\partial I_{2e}}C_e + I_{3e}\dfrac{\partial w}{\partial I_{3e}}C_e^{\,-1}\right]F_{an}^{\,-t} = \rho f \\ + \textit{Boundary conditions} \end{cases} \tag{2.89}$$

From all the examples shown in this chapter, we will take the elastic and viscous ones to illustrate the numerical resolution through a mixed finite element, in the first time implementation of Lagrangian or Eulerian approach. Application to all the behaviors given above will come back in chapter 5.

2.4 Résumé du chapitre en français

Une introduction bibliographique sur la modélisation de la viscoélasticité des polymères montre que il est habituel d'admettre que la viscoélasticité peut se traiter comme la coexistence de deux contributions au comportement : une partie "solide", de nature élastique et une partie "fluide" ou "visqueuse".

A partir de cette constatation une méthode permettant de résoudre les problèmes liés à son changement de nature entre l'état liquide et l'état solide est proposée. La résolution du problème viscoélastique est en effet similaire à la résolution d'un problème multiphasique tel que le problème d'interaction fluide-structure (IFS). De plus, il sera impossible de s'affranchir des problèmes liés à la coexistence, physique, de phases solides et liquides dans l'étape de cristallisation. C'est pourquoi une brève revue de l'IFS est présentée. Sa pertinence pour le traitement de la viscoélasticité est discutée et son application à notre travail décrite. Nous choisissons une approche monolithique où l'interface est traitée avec la méthode Level-Set.

La troisième partie rappelle les bases des formulations en grandes transformations appliquées aux comportements viscoélastiques, hyper-élastiques et visco-hyper-élastiques isotrope. Pour simplifier l'approche qui est très ambitieuse nous résoudrons d'abord le problème dans le cadre des petites transformations. De même, un modèle viscoélastique simple de Kelvin-Voigt sera utilisé car il porte toutes les difficultés numériques que nous pouvons craindre. Notre méthodologie pour résoudre le problème IFS est décrite et justifiée en dernière partie. Sa mise en œuvre dans la bibliothèque d'éléments finis CimLib® est enfin précisée.

Le chapitre suivant présentera les premiers développements numériques et leurs ajustements d'abord autour du problème d'élasticité.

Chapter 3

3 Numerical resolution of the two phase problem through a mixed finite element method in (*v, p, u*)

---

3 Numerical resolution of the two phase problem through a mixed finite element method in (*v, p, u*) 51

3.1 Description of the numerical test benchmarks....53

3.1.1 Simple tensile test benchmark....53

3.1.2 Flow between two rigid solid particles....54

3.2 Mixed finite elements with Mini-Element P1+/P1 55

3.2.1 Numerical resolution....55

3.3 Application for the tensile test case by a Lagrangian approach....62

3.3.1 Single time step resolution for the tensile test case with an elastic behavior....62

3.3.2 Incremental time step resolution for the tensile test case with an elastic behavior....67

3.3.3 Incremental time step resolution for the tensile test case with an viscoelastic behavior71

3.3.4 Instability problems in the tensile test by Lagrangian approach....73

3.4 Application for the tensile test case by Eulerian approach....76

3.4.1 Immersed volume method....76

3.4.2 Eulerian method for the incompressible elastic tensile test....79

3.4.3 Numerical results....83

3.5 Application in flow between two rigid particles....85

3.5.1 Formulation for a rigid solid....85

3.5.2 Numerical results....87

3.5.3 Concluding remarks....89

3.6 Résumé du chapitre en français....90

In chapter 2, we have introduced the methodology used for solving viscoelastic problems. To strengthen our methodology, a preliminary work is conducted supposing two-phase flows (solid and fluid) where resolution by a monolithic approach can be performed as two separated or mixed phases. Two different benchmarks will be used throughout this chapter to test the numerical implementations: flow between rigid particles and an elastic test.

After a brief introduction of the two benchmarks, resolution by the mixed finite element based on MINI element P1+/P1 is detailed and applied. Efficiency of our computation is first discussed in the case of the tensile benchmark. Two formulations will be used in our methodology: Lagrangian and Eulerian method, the latter based on the Level-Set method [71] [88] [89] [90]. In a Lagrangian approach, only the solid phase exists, in this case we have considered the simple behavior: elastic. After the tensile test, bending and torsion are also illustrated. In an Eulerian approach, the elastic solid is surrounded by a fluid, using the immersed volume method.

The second test case concerns viscous flow between rigid particles and is studied here to test the capability of the immersed volume method, and of the Eulerian approach in something simple than the elastic tensile test. To impose the rigidity condition, penalization and augmented Lagrangian method with Uzawa algorithm were used.

Last section is dedicated to some unstable problems that appeared during the simulation, followed by a proposal to improve the methodology, that will be detailed in the next chapter.

3.1 Description of the numerical test benchmarks

Even if we wish to address accurate viscoelastic computation, the limiting cases of a purely elastic (Figure 3-1) or rigid bodies, viscous flows (Figure 3-2), simple constitutive models. Two different benchmarks will be used throughout this chapter to test the numerical implementations in these two extreme cases: an elastic tensile test and flow between rigid particles.

The aim of this test is this to illustrate the mixed finite element method used at the beginning of this work in different Lagrangian and Eulerian configurations, enlightening all sources for numerical error that have to be improved. Chapter 4 will detailed how the methodology is adjusted to reduce errors.

3.1.1 Simple tensile test benchmark

Let us consider the case of the simple uniaxial uploading-unloading of a sample that is perfectly clamped on its top edge (Figure 3-1). Bottom edge is, for its part, displaced at a given velocity in order to tension the sample. In this case, one key issue is the reversibility of the strain that, for an elastic behavior, has to be numerically kept during calculation even for large strains. Checking this fundamental characteristic allows us optimizing the solver and its implementation in the CimLib® library.

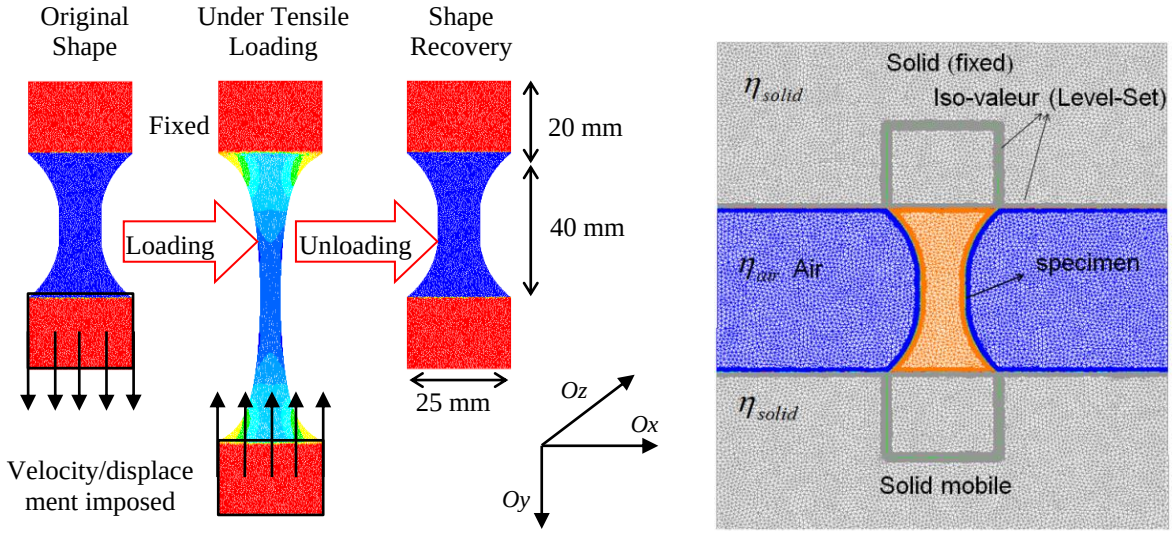


Figure 3-1: Simple uploading-unloading tensile test benchmark by the Lagrangian (left) and Eulerian (right) approach. In the left image, schematic of the original deformed and restored specimen. The image represents the initial, loaded and restored configurations. Remark that the specimen dimensions are in agreement with the real dimension of the specimen in the experimental test, which will be later presented in chapter 5. And the right image represents the schematic of the tensile test using an Eulerian method (detailed later in the section 3.4).

Two methods will be used to validate our methodology: Lagrangian (Figure 3-1 left) and Eulerian (Figure 3-1 right) method, in which we used the mixed finite element solver. Associated strong and discrete problems will be later presented in this chapter. In the Lagrangian approach, the simulation is quite simple and easy to implement. However, problems associated with high distortion in large deformations will limit the capability of simulation as we have described in the previous chapter, since several nonlinear terms are missing in the formulation in this case. Using

an Eulerian approach is thus required. Even if we here showed that the formulation is not complete.

In addition, comparison between the two approaches allows us to predict the capability of our current solver. This also gives a general overview of the errors, the performance and also on the strength and weakness of our numerical methodology.

3.1.2 Flow between two rigid solid particles

Simulation is performed by a two phase approach where the flow (blue zone) circulates through a channel limited by the solid (red zone), supposed rigid. It is a steep case of the two-phase where the elastic behavior degenerates into a rigid one, due to the complexity of the rigid condition in a fluid formulation.

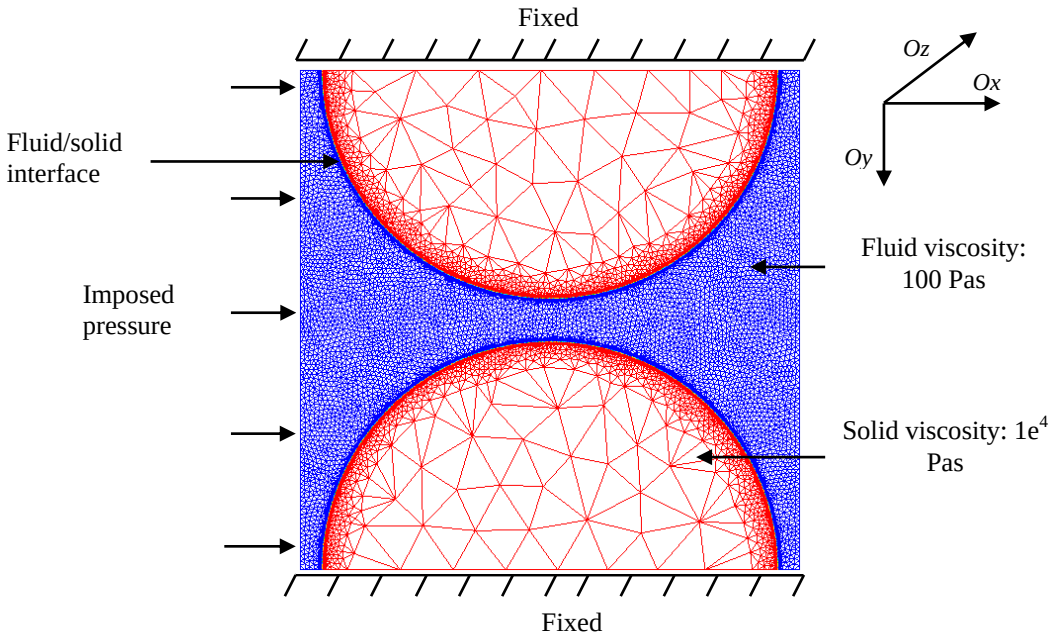


Figure 3-2: Geometry, boundary conditions and mesh representation for the flow between two rigid particles test case.

The simulation is performed by a two phase approach where the flow (blue zone) circulates through a channel limited by two solid particles (red zone), considering as a rigid. In the example displayed in Figure 3-2, a different pressure is imposed on the input and output boundary of the fluid domain. The *y* component of the velocity is zero on the input and output faces of the domain to impose flow in the *x* direction and on the other border sides. Velocity is also imposed to zero on the upper and lower faces. A more detailed description can be found in the study of Puaux G. [91].

Next section is devoted to the resolution of the problem by the mixed velocity-pressure-displacement formulation by the mixed FE method.

3.2 Mixed finite elements with Mini-Element P1+/P1

As detailed in the section 2.3, resolution of an incompressible viscoelastic Kelvin-Voigt model can be performed by a monolithic approach. Therefore, equations can be written:

$$\begin{cases} \rho\left(\frac{\partial v}{\partial t}+v\cdot\nabla v\right)-\nabla\cdot 2\eta_{ve}\varepsilon(v)+\nabla p_v = f-\nabla\cdot\tau \\ 2\eta_{ve}\varepsilon(v)=2\eta_v\varepsilon(v)+2\mu_e dt\varepsilon(v) \\ \tau=2\mu_e\varepsilon\left(u-vdt\right) \\ \nabla\cdot v=0 \\ \frac{du}{dt}=\frac{\partial u}{\partial t}+v\nabla u=v \\ +boundary\ conditions \end{cases} \tag{3.1}$$

In this context, we will first perform the resolution of the simple incompressible elastic tensile test benchmark where the inertia effects and the compressible terms are neglected, as well as the viscous effects:

$$\begin{cases} \nabla\cdot\sigma=\nabla\cdot\left(\sigma_f+\sigma_s\right)=f \\ \sigma_s=\sigma_e=2\mu_e\varepsilon\left(u\right)=2\mu_e\varepsilon\left(u-vdt+vdt\right) \\ \nabla\cdot v=0 \\ \frac{du}{dt}=\frac{\partial u}{\partial t}+v\nabla u=v \\ +boundary\ conditions \end{cases} \tag{3.2}$$

where the solid is considered as a purely elastic ($\sigma_s=\sigma_e$). The above equation (3.2) can be rewritten as follows:

$$\begin{cases} \nabla\cdot 2\eta_{ve}\varepsilon(v)-\nabla p = f-\nabla\cdot\tau \\ \tau=2\mu_e\varepsilon\left(u-vdt\right) \\ 2\eta_{ve}\varepsilon(v)=2\mu_e dt\varepsilon(v) \\ \nabla\cdot v=0 \\ \frac{du}{dt}=\frac{\partial u}{\partial t}+v\nabla u=v \\ +boundary\ conditions \end{cases} \tag{3.3}$$

To solve the above problem in equation (3.3), the mixed finite element based on MINI element P1+/P1 is applied and detailed in the following.

3.2.1 Numerical resolution

For establishing the weak formulation of the problem, we define the functional spaces $V=\left(H^1(\Omega)\right)^d$, $V^0=\left(H_0^1(\Omega)\right)^d$ and $P=L^2(\Omega)$ where $L^2(\Omega)$ is the Lebesgue space of square

assumable functions on Ω, $H^1(\Omega)$ the Sobolev space included in $L^2(\Omega)$, and *d* is the space dimension, and they are all defined as:

$$L^2(\Omega) = \left\{ q, \int_\Omega q^2 dV < \infty \right\} \tag{3.4}$$

$$H^1(\Omega) = \left\{ q \in L^2(\Omega), \nabla q \in \left(L^2(\Omega) \right)^d \right\} \tag{3.5}$$

$$H_0^1(\Omega) = \left\{ q \in H^1(\Omega), q = 0 \text{ sur } \partial\Omega \right\} \tag{3.6}$$

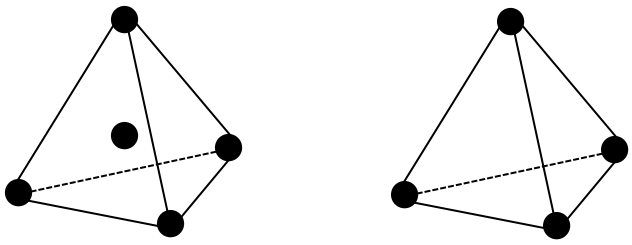
Following equation (3.3), resolution of three fields (*u, v, p*) is performed by the discrete Galerkin method which consists therefore in solving the mixed problem (3.7). The discrete functional spaces V_h, P_h, V_h^0 are built in order to approach V, P and V^0.

Find $(u_h, v_h, p_h) \in (V_h, V_h, P_h)$ such that $\forall (\varsigma_h, w_h, q_h) \in (V_h^0, V_h^0, P_h)$:

$$\begin{cases} 2\mu_e dt \varepsilon(v_h) : \varepsilon(w_h) - (p_h, \nabla \cdot w_h) = (f_h, w_h) - \tau_h : \varepsilon(w_h) \\ \tau_h = 2\mu_e \varepsilon(u_h - v_h dt) \\ (-\nabla \cdot v_h, q_h) = 0 \\ \left(\dfrac{\partial u_h}{\partial t} + v_h \nabla u_h, \varsigma_h \right) = v_h \end{cases} \tag{3.7}$$

For an incompressible elastic problem, finite element approximation (3.7) can generate instabilities because of the compatibility of the *inf-sup* condition (Brezzi-Babuska) [92] [93] [94]. Thus, an appropriate pair of functional spaces for the velocity and the pressure is required to ensure this condition. It verifies the existence and the uniqueness of the solution of this problem. This extreme condition ensures also the convergence of the solution towards the problem solution when the mesh size tends to zero. It should be noted that the order of convergence of the mini-element is *0(h)*, *h* being the mesh size [95].

Therefore, to overcome these conditions, mixed finite element method with the P1+/P1 element (MINI-element), introduced by Fortin et al. [96], may be used for the discretization in velocity and in pressure. A sub-discretization is necessary for the bubble function to ensure its linearity and continue on the sub-elements. The bubble function vanishes at the boundary of elements and is continuous inside the element, and is defined on elements as a polynomial on each of the three sub-triangles:



Velocity interpolation Pressure interpolation

Figure 3-3: Element P1+/P1 (MINI-element) for velocity-pressure interpolation.

The discretization in displacement is also enriched by using element P1+ as velocity in order to stabilize the convection dominated problem appeared in the transport equation of displacement.

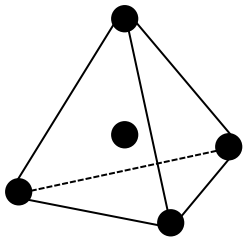


Figure 3-4: Displacement interpolation.

For a better representation of the bubble interpolation function, we can refer to the below figure:

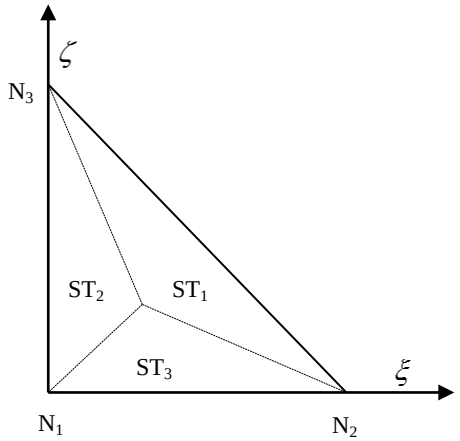


Figure 3-5: Schematic representation of a reference sub-element (ST_i) in two dimensions.

The sub-elements were numerated similar as its opposed nodes, in this way we can resume the bubble interpolation ϕ^b on an element as follows:

$$\phi^b = \begin{cases} \phi^b_{ST_1} = 3(1-\xi-\zeta) & on \quad ST_1 \\ \phi^b_{ST_2} = 3\xi & on \quad ST_2 \\ \phi^b_{ST_3} = 3\zeta & on \quad ST_3 \end{cases} \tag{3.8}$$

The justification of this choice is detailed in [97] [98] [99].

In this context, we consider an overlapping sum decomposition of the displacement, velocity and the pressure fields into coarse-scales and fine-scales, $u = u_h + u_h^b$, $v = v_h + v_h^b$, and $p = p_h$ where u_h, v_h and p_h are the linear part of the displacement, velocity and pressure; u_h^b, v_h^b are the bubble displacement and velocity. Likewise, we keep the same decomposition for the weighting functions $\varsigma = \varsigma_h + \varsigma_h^b$, $w = w_h + w_h^b$ and $q = q_h$.

We can perform the enrichment of the functional spaces as follows:

$$V = V_h \oplus V_h^b,\ V_0 = V_{h,0} \oplus V_{h,0}^b \text{ and } P = P_h \tag{3.9}$$

where the finite element space V_h, V_h^b and P_h defined as:

$$V_h = \left\{ v_h, v_h \in H^1(K), \quad \forall K \in \Omega_K \right\} \tag{3.10}$$

$$V_h^b = \left\{ v_h^b, v_{h|K}^b \in P_k(K_i) \bigcap H_0^1(K_i), i = 1,...D \quad \forall K \in \Omega_K \right\} \tag{3.11}$$

$$P_h = \left\{ p_h, p_h \in H^1(K), \quad \forall K \in \Omega_K \right\} \tag{3.12}$$

The computational domain Ω is decomposed in tetrahedra *K*, a triangulation $T_h(\Omega)$ (or mesh), h is the mesh size related with the diameter of elements by:

$$h = \max_{K \in T_h(\Omega)} diam(K) \tag{3.13}$$

with $P_k(K)$ is the space of polynomials of degree *k* on element *K*. D is the topological dimension and K_i is a decomposition of *K* in D subsimplex (subtriangle in 2D and subtetrahedra in 3D), that have as common vertex the barycentre of *K*. Smaller the mesh size is, more accurate the approximation spaces functional is: $\lim_{h \to 0} U_h = U$, $\lim_{h \to 0} U_h^0 = U^0$, $\lim_{h \to 0} V_h = V$, $\lim_{h \to 0} V_h^0 = V^0$, $\lim_{h \to 0} P_h = P$.

Following the discretization, we have:

$$\Omega_h = \bigcup_{K \in T_h(\Omega)} K \tag{3.14}$$

The discrete variational form for this problem is:

Find $(u_h, v_h, p_h) \in (V_h, V_h, P_h)$ such that $\forall (\varsigma_h, w_h, q_h) \in (V_{h,0}, V_{h,0}, P_h)$:

$$\begin{cases} -\left(p_h, \nabla \cdot \left(w_h + w_h^b\right)\right) + 2\mu_e dt \varepsilon\left(v_h + v_h^b\right) : \varepsilon(w_h + w_h^b) = \left(f_h, w_h + w_h^b\right) - \left(\tau_h + \tau_h^b\right) : \varepsilon(w_h + w_h^b) \\ \tau_h = 2\mu_e \varepsilon\left(u_h - v_h dt\right) \quad and \quad \tau_h^b = 2\mu_e \varepsilon\left(u_h^b - v_h^b dt\right) \\ \left(-\nabla \cdot \left(v_h + v_h^b\right), q_h\right) = 0 \\ \left(\frac{\partial\left(u_h + u_h^b\right)}{\partial t} + \left(v_h + v_h^b\right) \nabla\left(u_h + u_h^b\right), \varsigma_h + \varsigma_h^b\right) = \left(v_h + v_h^b\right) \end{cases} \tag{3.15}$$

Thus, we obtain the system equations which can be split into two sub-problems by separating the two scales, called the coarse-scale problem:

$$\begin{cases} -\left(p_h, \nabla . w_h\right) + 2\mu_e dt \varepsilon\left(v_h\right) : \varepsilon\left(w_h\right) = \left(f_h, w_h\right) - \tau_h : \varepsilon\left(w_h\right) \\ \tau_h = 2\mu_e \varepsilon\left(u_h - v_h dt\right) \\ \left(-\nabla \cdot v_h, q_h\right) = 0 \\ \left(\frac{\partial u_h}{\partial t} + \left(v_h + v_h^b\right) \nabla\left(u_h + u_h^b\right), \varsigma_h\right) = v_h \end{cases} \tag{3.16}$$

and the fine-scale problem:

$$\begin{cases} -\left(p_h, \nabla.w_h^b\right) + 2\mu_e dt\varepsilon\left(v_h^b\right) : \varepsilon\left(w_h^b\right) = \left(f_h, w_h^b\right) - \tau_h^b : \varepsilon\left(w_h^b\right) \\ \tau_h^b = 2\mu_e\varepsilon\left(u_h^b - v_h^b dt\right) \\ \left(-\nabla\cdot v_h^b, q_h\right) = 0 \\ \left(\dfrac{\partial u_h^b}{\partial t} + \left(v_h + v_h^b\right)\nabla\left(u_h + u_h^b\right), \varsigma_h^b\right) = v_h^b \end{cases} \tag{3.17}$$

We remind that at this stage, there are some important remarks and assumptions to be made:

- since the bubble functions vanish on each element boundary, we take into account those unresolvable scales (fine-scales), in which terms involving integrals over the element interior boundaries will be neglected [100],
- by choosing the test function ($w_h = 0$ on $\partial\Omega$), integration by parts (Green's formula) is simplified:

$$\int_\Omega \nabla p.w d\Omega = -\int_\Omega p\nabla\cdot w d\Omega + \int_{\partial\Omega} p.w.n d\Omega = -\int_\Omega p\nabla\cdot w d\Omega$$

- as the fine-scale space is assumed to be orthogonal to the finite element space, the crossed viscous terms vanish in (3.16) and (3.17) [98],
- only Dirichlet boundary conditions are considered,

3.2.1.1 Time scheme

In our context, the fine-scales will also be resolved which cause the complexities of the resolution by three fields $\left(u_h, v_h, p_h\right)$ in the same system. The construction of a system with 5 unknowns u_h, u_h^b, v_h, v_h^b and p_h will be required which considerably increase the computational cost, specifically when the number of unknowns is large. Thus, we introduce a coupling resolution scheme in which the resolution of the displacement (see equations (3.16) and (3.17)) was separated from the resolution of velocity and pressure.

Moreover, for the time-scheme discretization, the general theta-scheme was implemented. We can choose θ = 0.5, this is equivalent to the trapezoidal method of order 2. It can be seen as the average between the patterns of implicit and explicit Euler, themselves obtained respectively when θ = 1 and θ = 0. But for sake of simplicity in the notation and for illustration purposes, we used the implicit Euler time-integration scheme (θ = 1).Therefore, the illustration of the implicit time-scheme discretization for the coarse-scale can read:

$$\begin{cases} -\left(p_h, \nabla.w_h\right)^{n+1} + 2\mu_e\Delta t\varepsilon\left(v_h\right)^{n+1} : \varepsilon\left(w_h\right) = \left(f_h, w_h\right)^{n+1} - \left(\tau_h\right)^n : \varepsilon\left(w_h\right) \\ \left(\tau_h\right)^n = 2\mu_e\varepsilon\left(u_h - v_h\Delta t\right)^{n+1} = 2\mu_e\varepsilon\left(u_h\right)^n \\ \left(-\nabla\cdot\left(v_h\right)^{n+1}, q_h\right) = 0 \end{cases} \tag{3.18}$$

and the fine-scales:

$$\begin{cases} -\left(p_h, \nabla.w_h^b\right)^{n+1} + 2\mu_e \Delta t \varepsilon\left(v_h^b\right)^{n+1} : \varepsilon\left(w_h^b\right) = \left(f_h, w_h^b\right)^{n+1} - \left(\tau_h^b\right)^n : \varepsilon\left(w_h^b\right) \\ \left(\tau_h^b\right)^n = 2\mu_e \varepsilon\left(u_h^b - v_h^b \Delta t\right)^{n+1} = 2\mu_e \varepsilon\left(u_h^b\right)^n \\ \left(-\nabla\cdot\left(v_h^b\right)^{n+1}, q_h\right) = 0 \end{cases} \tag{3.19}$$

Otherwise, the resolution of displacement can be predicted by a resolution in the coarse-scales and the fine-scales:

$$\left(\frac{u_h + u_h^b}{\Delta t}, w_h\right)^{n+1} = \left(\frac{u_h + u_h^b}{\Delta t}, w_h\right)^n + \left(v_h + v_h^b, w_h\right)^{n+1} \tag{3.20}$$

$$\left(\frac{u_h + u_h^b}{\Delta t}, w_h^b\right)^{n+1} = \left(\frac{u_h + u_h^b}{\Delta t}, w_h^b\right)^n + \left(v_h + v_h^b, w_h^b\right)^{n+1} \tag{3.21}$$

Please note that in order to simplify the preliminary work, only the resolution in a Lagrangian framework is taken into account for the displacement formulation. A full discrete stabilized resolution of this displacement equation is further detailed in chapter 4, addressing more property in the Lagrangian approach.

3.2.1.2 Matrix formulation

Let us summarize and rewrite the resulting variational stabilized formulation in the usual matrix scheme (3.22) where the previous scheme in (3.18) and (3.19) can be put naturally under the matrix form to be solved:

$$\begin{pmatrix} A_{vv} & 0 & A_{vp} \\ 0 & A_{v_b v_b} & A_{v_b p} \\ A_{vp}^t & A^t{}_{v_b p} & 0 \end{pmatrix} \begin{pmatrix} v \\ v_b \\ p \end{pmatrix} = \begin{pmatrix} B_v \\ B_{v_b} \\ 0 \end{pmatrix} \tag{3.22}$$

where:

$$A_{vv} = 2\mu_e \Delta t \varepsilon\left(v_h\right)^{n+1} : \varepsilon\left(w_h\right) \qquad A_{v_b v_b} = 2\mu_e \Delta t \varepsilon\left(v_h^b\right)^{n+1} : \varepsilon\left(w_h^b\right)$$

$$A_{vp}^t = -\left(p_h, \nabla\cdot w_h\right)^{n+1} \qquad A^t{}_{v_b p} = -\left(p_h, \nabla\cdot w_h^b\right)^{n+1}$$

and

$$B_v = -2\mu_e \varepsilon\left(u_h - v_h \Delta t\right)^{n+1} : \varepsilon\left(w_h\right) + \left(f_h, w_h\right)^{n+1} \qquad B_{v_b} = -2\mu_e \varepsilon\left(u_h^b - v_h^b \Delta t\right)^{n+1} : \varepsilon\left(w_h^b\right) + \left(f_h, w_h^b\right)^{n+1}$$

Indeed, the resolution of a linear or nonlinear system is performed using an iterative method with preconditioning, in a sequential calculation as well as in a parallel computation [99] [95]. The FE library Cimlib, in which the solver is implemented, uses PETSc (Portable, Extensible Toolkit for Scientific Computation) (http://www.mcs.anl.gov/petsc/petsc-as/) to solve the systems, after linearization. The library PETSc offers interesting solutions in both the sequential and the parallel scientific computing computation which allows solving the partial differential equations and linear algebra problems by iterative methods. In fact, the creation of matrices is performed by

CimLib, and then PETSc is used to do the preconditioning and resolution. So we can use it through the PETSc library for solving the linear system (3.22) resulting from the incompressible elastic problem.

With the sub-discretization elements (Figure 3-5), it is possible to calculate the bubble locally on each element:

$$v_b = \left(A_{v_b v_b}\right)^{-1} \times B_{v_b} - \left(A_{v_b v_b}\right)^{-1} \times A_{v_b p} \times p \tag{3.23}$$

Then, with a condensation technique, the system can be reduced to the matrix form:

$$\begin{pmatrix} A_{vv} & A_{vp} \\ A_{vp}^t & C \end{pmatrix} \begin{pmatrix} v \\ p \end{pmatrix} = \begin{pmatrix} B_v \\ B_{v_b} \end{pmatrix} \tag{3.24}$$

with

$$C = -A_{v_b p} \times A_{v_b v_b}^{-1} \times A_{v_b p} + A_{v_b p}^t \times A_{v_b v_b}^{-1} \times B_{v_b} \tag{3.25}$$

Due to the condensation technique, the fine-scales are unresolved in our previously implemented solver, only their effects remain in the coarse-scales as displayed in the matrix form (3.24). Thus, the "bubble extra-stress" $B_{v_b} = \tau_b$ represents a true difficulty in terms of computer programming. Therefore, as a first attempt, this term was neglected in the numerical resolution.

In order to assess the main characteristics of the formulation previously presented, test its feasibility in the context of a multiphase problem and reveal all sources for numerical error, the two benchmarks are analyzed in the next section.

3.3 Application for the tensile test case by a Lagrangian approach

For the tensile test case, as we intend to deform up to large strains, one may think that an Eulerian approach is the most appropriate. Nevertheless, results on a Lagrangian framework will first be analyzed. Numerical resolution of this case in the context of Lagrangian approach can be performed by two methods: single time step resolution and an incremental time step resolution. Now let us introduce first the resolution by the single time step resolution.

3.3.1 Single time step resolution for the tensile test case with an elastic behavior

From a theoretical point of view, the elasticity problem we wish to solve (load-unload of a sample) in single time step could be solved using two time steps: one between the initial to the loaded configurations and one between the loaded and unloaded configurations (Figure 3-1). Please note that the resolution is carried out directly in the displacement formulation and not that of velocity formulation as usual.

From equation (3.2), since we supposed that the sample behavior is incompressible and elastic, the first step consists in deforming the specimen by a displacement can be described as follows:

$$\begin{cases} \nabla_{x^0} \cdot \sigma_e - \nabla_{x^0} p = 0 \\ \sigma_e = 2\mu_e \varepsilon(u) \\ \nabla_{x^0} \cdot u = 0 \\ u = u_{imposed} \ in \ \Gamma_{\inf} \ and \ u = 0 \ in \ \Gamma_{\sup} \end{cases} \tag{3.26}$$

where $\Gamma_{\inf}$ *and* $\Gamma_{\sup}$ is the boundary interface, in this case, this represents the lower and upper edge of the specimen.

As the calculation is performed in a Lagrangian approach where the domain is deformed, the instantaneous configuration also varies over time. Lector can refer to the previously section 2.3 for a brief reminder of continuum mechanic. In the same manner the equilibrium equation is written in different configurations, since:

$$\nabla_{x^0} \cdot 2\mu_e \varepsilon(u) \neq \nabla_{x^n} \cdot 2\mu_e \varepsilon(u) \tag{3.27}$$

Modeling of the recovery step corresponds to an inverse displacement imposed on $\Gamma_{\inf}$, the lower edge of the loaded configuration:

$$\begin{cases} \nabla_{x^1} \cdot 2\mu_e \varepsilon(u^1) - \nabla_{x^1} p^1 = -\left(\nabla_{x^1} \cdot 2\mu_e \varepsilon(u) + \nabla_{x^1} p\right) \\ \nabla_{x^1} \cdot u^1 = 0 \\ u = -u_{imposed} \ in \ \Gamma_{\inf} \ and \ u = 0 \ in \ \Gamma_{\sup} \end{cases} \tag{3.28}$$

To simplify the expression, the hydrostatic pressure at the right-hand side members of equation (3.28) is moved to that in the left-hand side members, which has no effect on the conservation of the equilibrium equation. One defines p' as:

$$p' = p^1 - p \tag{3.29}$$

From which we obtain:

$$\begin{cases} \nabla_{x^1} \cdot 2\mu_e \varepsilon\left(u^1\right) - \nabla_{x^1} p' = -\nabla_{x^1} \cdot 2\mu_e \varepsilon\left(u\right) \\ \nabla_{x^1} \cdot u^1 = 0 \end{cases} \tag{3.30}$$

In the following, strain will be characterized by ε_{yy}, the nominal strain in the longitudinal direction, in the case of small deformations:

$$\varepsilon_{yy} = \frac{L - L_0}{L_0} = \frac{u_{imposed}}{L_0} \tag{3.31}$$

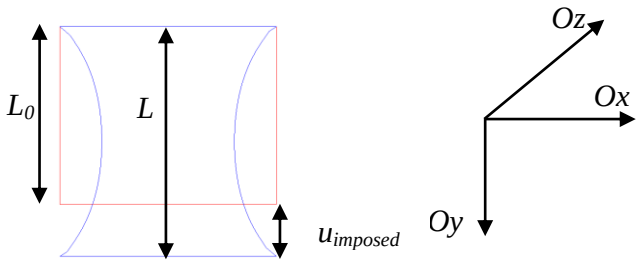


Figure 3-6: Schematic representation of the deformation of specimen, measure of the longitudinal strain. Deformations of the specimen up to two levels of strain are considered: 5 to 10% and 20 to 30% - ε_{yy}.

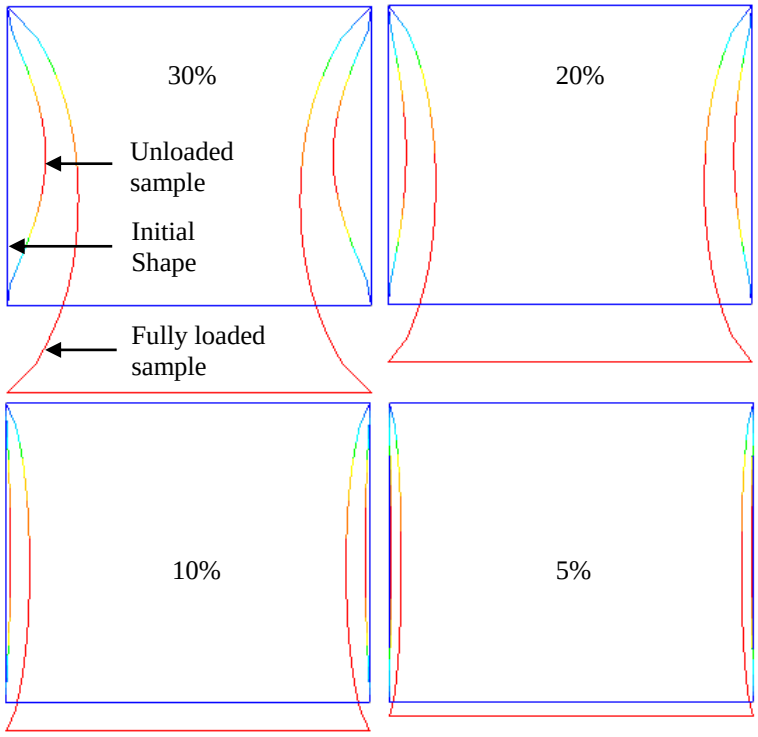


Figure 3-7: Specimen shape under uploading and unloading tensile tests with different levels of strain, for an elastic behavior and resolution on one single step.

Figure 3-7 illustrates the differences in the three computed shapes (initial, loaded and restored). Overall quality of the calculation is illustrated by the global reversibility of the cycle, i.e. the coincidence of restored and initial shapes. Note that in this case, to simplify the error measurement of the sample during the simple uniaxial uploading-unloading, a 10 mm-length square shaped sample was chosen which is quite different with that represented previously in Figure 3-1.

As one could imagine coincidence is acceptable for a global strain of 5 to 10% but reversibility is not numerically achieved for strains of 20 to 30%. This discrepancy is partly due to the abusive uses of small transformation assumptions that have to be further avoided. However, the resolution scheme is not optimal as there are some missing terms in the resolution, which was revealed in the previous section as the "bubble extra-stress" B_{v_b} in the fine-scales resolution (equation (3.24)) or the last term nonlinear of Cauchy-Green strain tensor (equation (2.33)).

At this stage one can also argue that an incremental time step simulation method would be more relevant since it allows considering intermediate current configuration, and will be introduced in section 3.3.2. Before that, let's go on gathering sources of numerical errors by verifying the influence of mesh and geometry.

3.3.1.1 Influence of mesh and geometry

3.3.1.1.1 Influence of mesh

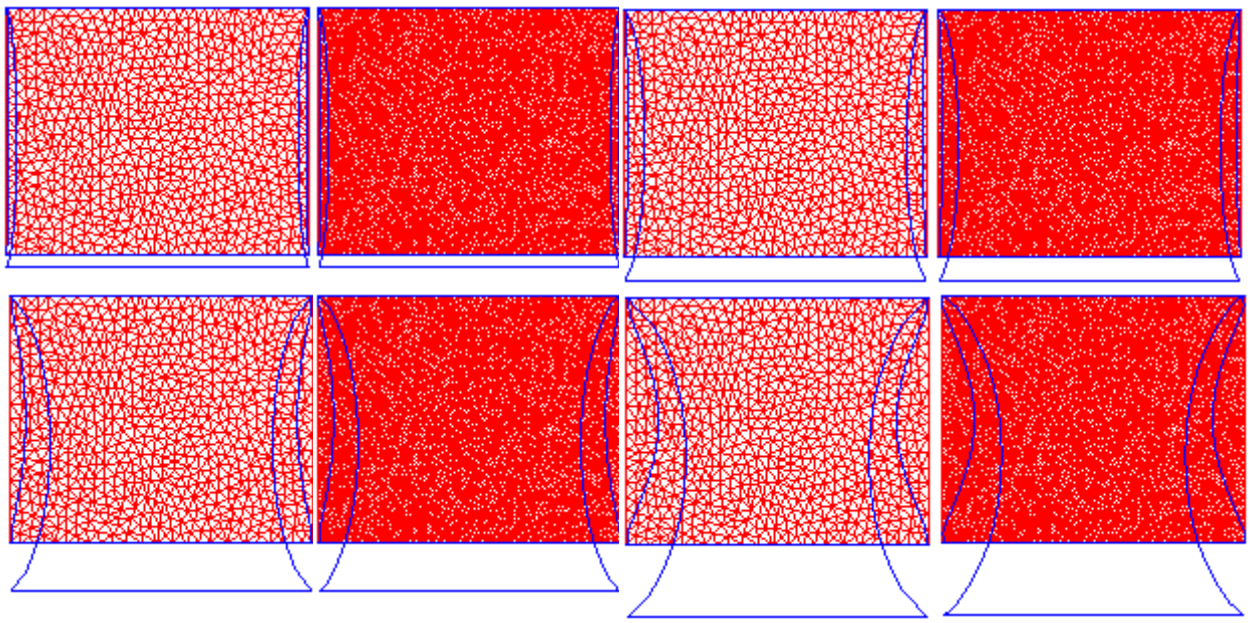


Figure 3-8: Specimen shape under uploading-unloading tensile with different levels of strain and different meshes (5%, 10%, 20% and 30% strain).

Sensitivity to mesh characteristics is obviously a key issue. In Figure 3-8 loss of reversibility is illustrated with two meshes having 8000 and 1000 elements, respectively. Despite the huge different in refinement both the two calculations are equivalent.

3.3.1.1.2 Influence of geometry

Another point is the influence of geometry's shape on accuracy of the results obtained with the numerical simulation. In fact, geometry may also modify the local stress field as displayed in Figure 3-9 where a rectangular or circular hole is drilled in the specimen center. The goal is to see the influence of the geometry compared with the previous results and validate both geometrical and mechanical aspects.

As illustrated in Figure 3-9, this showed a slight difference between the shape recovery and the original shape of the specimen in small deformations. However, in large deformations, the introduced error is large to neglect, and the difference is considerable.

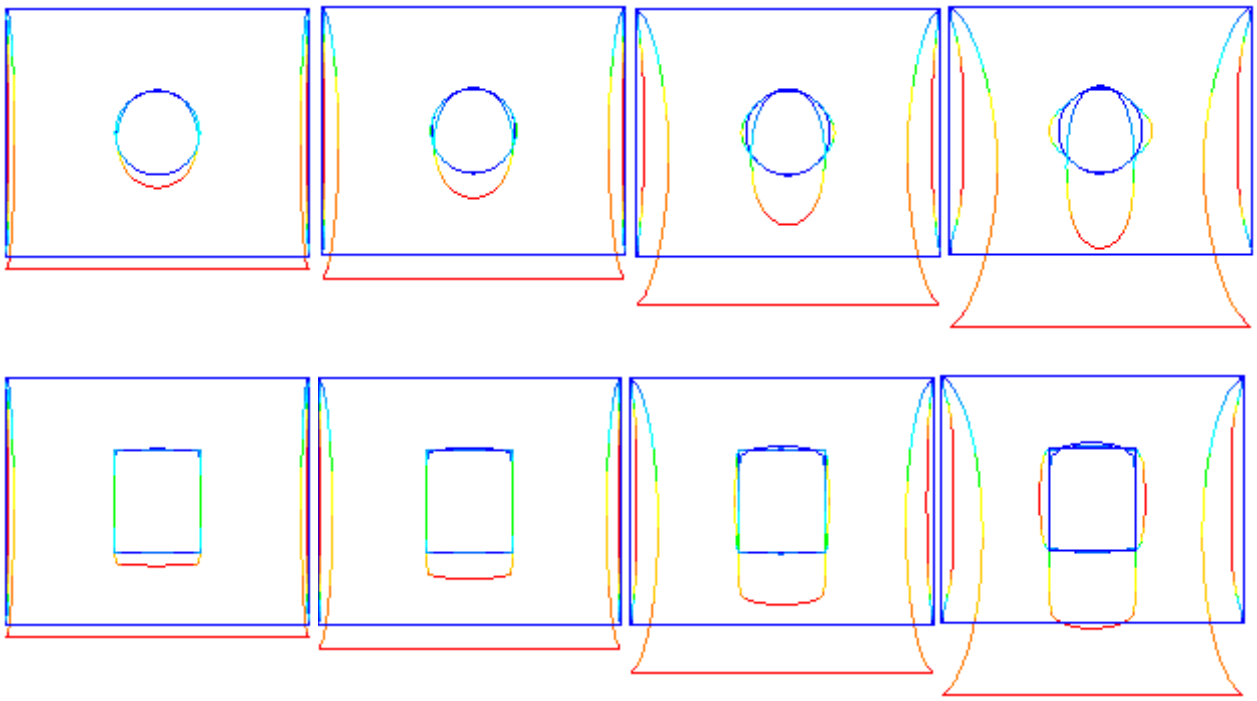


Figure 3-9: Specimen shape (with a rectangular/circular hole) under uploading-unloading tensile with different levels of strain and different meshes (5%, 10%, 20% and 30% strain).

In conclusion, analyzing this tensile test, with an elastic behavior of the sample and a resolution on (u, p) with a single step demonstrates a slight difference between the shape recovered and the original shape of the specimen in small deformations (5% and 10%). However, for higher deformations, the introduced error is far from being neglected, and the differences between initial and recovered shapes are considerable. The numerical results show also that, at this level of deformations there are no visible effects of the mesh and the geometry for our numerical scheme. The 3D case completes our analysis in the next section.

3.3.1.2 Simulation results in 3D

This section will focus on the simulation results for a 3D elastic problem using the described mixed finite element. The specimen shape has been changed and corresponds to a better representation of a real specimen shape in an experimental tensile test described later. The dimension on each side is 1mm x 5mm x 15mm. The deformation varies from 5% strain to 30% strain, different meshes and geometries are also simulated as for the test in 2D.

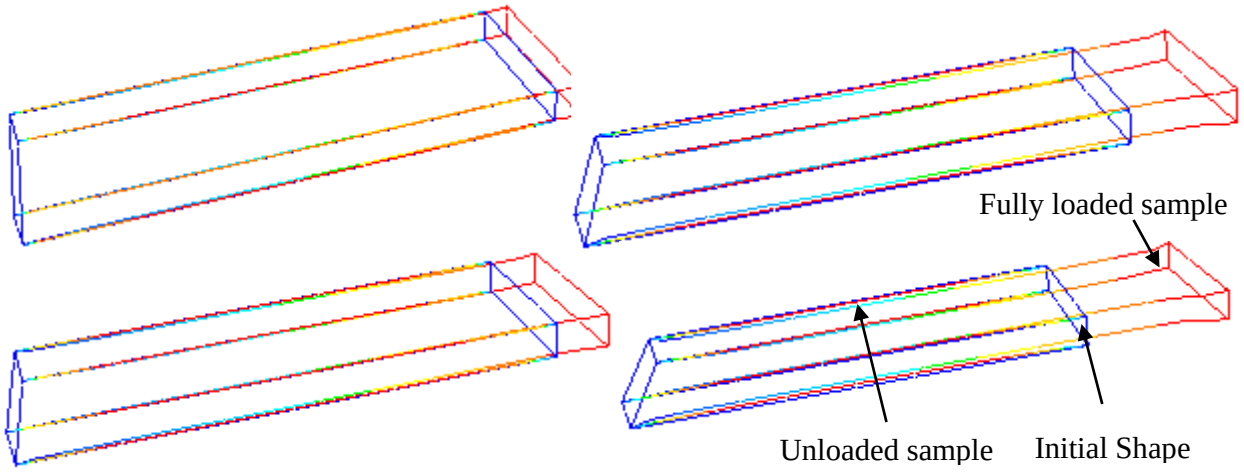


Figure 3-10: Specimen shape (3D) under uploading-unloading tensile with different levels of strain.

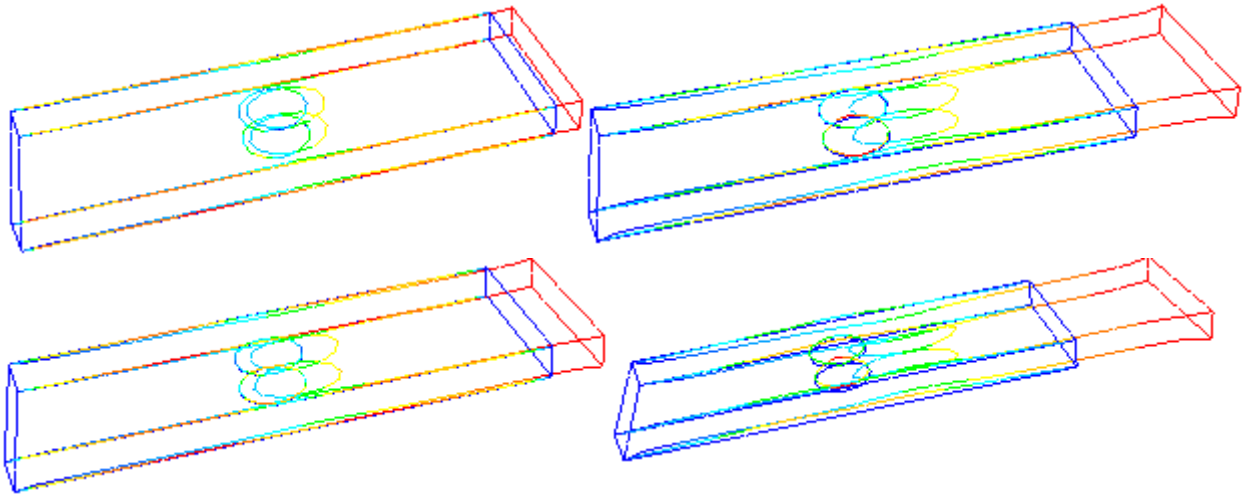


Figure 3-11: Specimen shape (3D with a circular hole) under uploading and unloading tensile with different levels of strain and different meshes (5%, 10%, 20% and 30% strain).

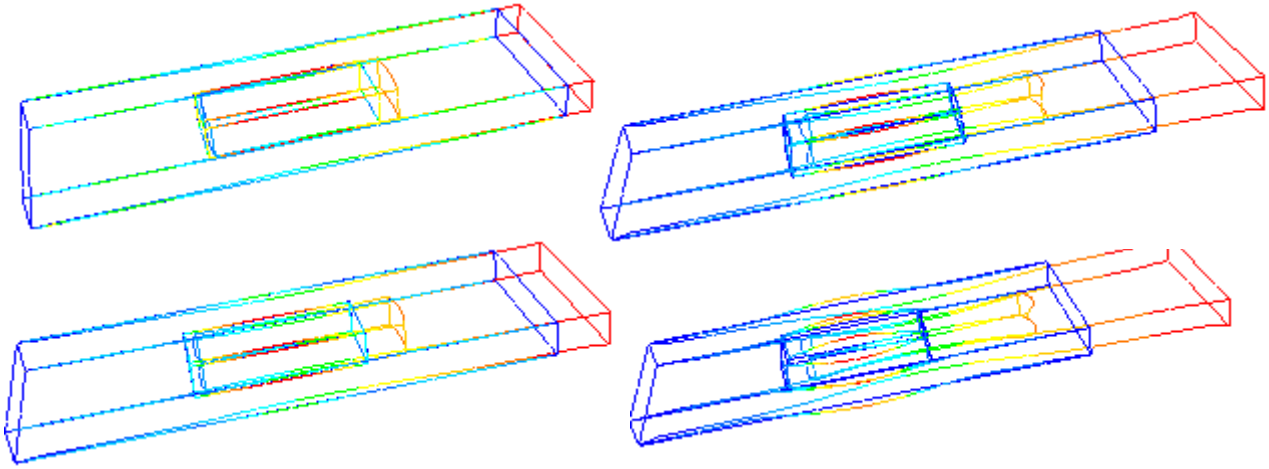


Figure 3-12: Specimen shape (3D with a rectangular hole) under uploading and unloading tensile with different levels of strain and different meshes (5%, 10%, 20% and 30% strain).

Results are given in Figure 3-10 to Figure 3-12 and lead to similar conclusions as the 2D approach. In other words, the errors introduced are neglected in small deformations, but remain important in large deformations, independently of the change of geometry (or mesh).

As mentioned in the previous section, in the context of a Lagrangian approach, the tensile test can also be performed using an incremental time step resolution.

In fact, in the incremental time step resolution method, the displacement is decomposed into several small displacements. By this way, a large deformation calculation can be performed by an assumption of several small deformations by considering the initial configuration as one at each increment of deformation. This which limits the errors introduced.

3.3.2 Incremental time step resolution for the tensile test case with an elastic behavior

When considered an incremental time step method, conservation equations for an incompressible elastic behavior can be rewritten as follows:

$$\nabla_{x^{n+1}}.2\mu_e\varepsilon(u^{n+1})-\nabla_{x^{n+1}}p^{n+1}=0 \tag{3.32}$$

where $\nabla_{x_{n+1}}$ is gradient operator in the configuration x_{n+1} in the time step *n+1*, u^{n+1}, v^{n+1} is displacement and velocity in the time step *n+1*.

The elastic stress in the time step *n+1* may be developed such that:

$$\begin{aligned}
&\nabla_{x^{n+1}}\cdot\tau^{n+1}=\nabla_{x^{n+1}}\cdot 2\mu_e\varepsilon\left(u^{n+1}\right)\\
&=\nabla_{x^{n+1}}\cdot 2\mu_e\varepsilon\left(u^{n+1}-\delta u+\delta u\right)\\
&=\nabla_{x^{n+1}}\cdot 2\mu_e\varepsilon\left(u^{n+1}-\delta u\right)+\nabla_{x^{n+1}}\cdot 2\mu_e\varepsilon\left(\delta u\right)dt\\
&=\nabla_{x^{n+1}}\cdot 2\mu_e\varepsilon\left(u^{n}\right)+\nabla_{x^{n+1}}\cdot 2\mu_e\varepsilon\left(v^{n+1}\right)dt\\
&=\nabla_{x^{n+1}}\cdot\tau^{n}+\nabla_{x^{n+1}}\cdot 2\mu_e\varepsilon\left(v^{n+1}\right)dt
\end{aligned} \tag{3.33}$$

The terms called "extra-stress" $\tau^n=2\mu_e\varepsilon(u^n)$ (see also section 2.3) can be resolved by moving them to the right-hand side member of the equilibrium equation. Thus, in this case, the equilibrium equation is resumed as:

$$\nabla_{x^{n+1}}.2\mu_e\Delta t\varepsilon\left(v^{n+1}\right)-\nabla_{x^{n+1}}p^{n+1}=-\nabla_{x^{n+1}}.2\mu_e\varepsilon\left(u^{n}\right) \tag{3.34}$$

With the incremental method, the calculation of the deformation consists of several calculation steps assuming small strains where the system is nonlinear. Therefore, the problem is solved by splitting the system in two sub-systems:

- knowing the configuration of our computational domain, *v* and *p* is computed by solving conservation equations,
- knowing *v*, we can find *u* which enables the calculation of the extra-stress τ.

The global problem, with a large number of unknowns, and therefore large-consuming memory, is broken up into smaller systems thanks to this technique: a Stokes system augmented with an elastic term and the non-linear evolution equations that allow the determination of τ. Furthermore, each problem can be treated taking into account its mathematical type as the Stokes problem is elliptic and linear, whereas stretch problems involve non-linearities and convection. Consequently, the resolution algorithm is:

Algorithm for an incremental resolution of the incompressible elastic case

For each time step $\left[t^n, t^{n+1}\right]$ for *loading* **do**

Knowing $\left(u^n, v^n, p^n\right)$

1) Compute $\left(v^{n+1}, p^{n+1}\right)$ such that

$$\begin{cases} \nabla_{x^{n+1}}.2\mu_e\Delta t\varepsilon\left(v^{n+1}\right)-\nabla_{x^{n+1}}p^{n+1}=-\nabla_{x^{n+1}}.\tau^n \\ \tau^n=2\mu_e\varepsilon\left(u^n\right) \\ \nabla.v^{n+1}=0 \\ v=v_{imposed}\ in\ \Gamma_{\inf}\ and\ v=0\ in\ \Gamma_{\sup} \end{cases} \tag{3.35}$$

2) Find u^{n+1} by solving

$$u^{n+1}=u^n+v^{n+1}\Delta t \tag{3.36}$$

3) Update the configuration by moving the mesh

$$x^{n+1}+u^{n+1}\Rightarrow x^{n+2} \tag{3.37}$$

4) Compute the extra-stress tensor

$$\tau^{n+1}=2\mu_e\varepsilon\left(u^{n+1}\right) \tag{3.38}$$

End for *loading*

For each time step $\left[t^n, t^{n+1}\right]$ for *unloading* **do**

Knowing $\left(u^n, v^n, p^n\right)$

1) Compute $\left(v^{n+1}, p^{n+1}\right)$ such that

$$\begin{cases} \nabla_{x^{n+1}}.2\mu_e\Delta t\varepsilon\left(v^{n+1}\right)-\nabla_{x^{n+1}}p^{n+1}=-\nabla_{x^{n+1}}.\tau^n \\ \tau^n=2\mu_e\varepsilon\left(u^n\right) \\ \nabla.v^{n+1}=0 \\ v=-v_{imposed}\ in\ \Gamma_{\inf}\ and\ v=0\ in\ \Gamma_{\sup} \end{cases} \tag{3.39}$$

2) Find u^{n+1} by solving

$$u^{n+1}=u^n+v^{n+1}\Delta t \tag{3.40}$$

3) Update the configuration by moving the mesh

$$x^n+u^n\Rightarrow x^{n+1} \tag{3.41}$$

4) Compute the extra-stress tensor

$$\tau^{n+1}=2\mu_e\varepsilon\left(u^{n+1}\right) \tag{3.42}$$

End for *unloading*

Figure 3-13 to Figure 3-16 reproduce the same tests as above and demonstrate that the calculation in several small displacements is a real improvement. As shown in the first image of Figure 3-13 (1 time step), corresponding to the single time step resolution, the introduced errors are important, in opposite to in the two others (10 and 100 time steps), where the difference between the shape recovery and the original shape is quasi-negligible. To verify the effects of the geometry and also the calculation in 3D, the change of specimen shape was performed by the incremental time step resolution, showing slight effects on the final results.

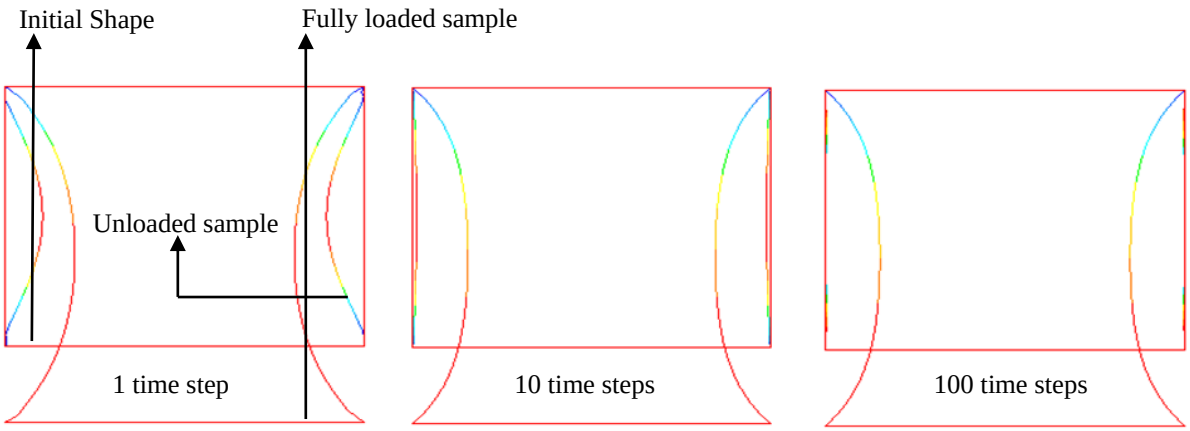


Figure 3-13: Specimen shape under uploading-unloading tensile at 30% strain for different time steps.

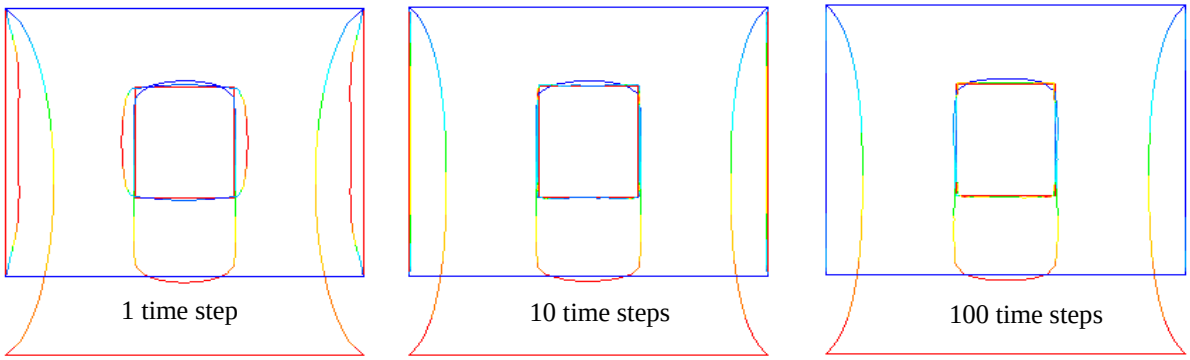


Figure 3-14: Specimen shape (2D with a rectangular hole) under uploading-unloading tensile at 30% strain for different time steps.

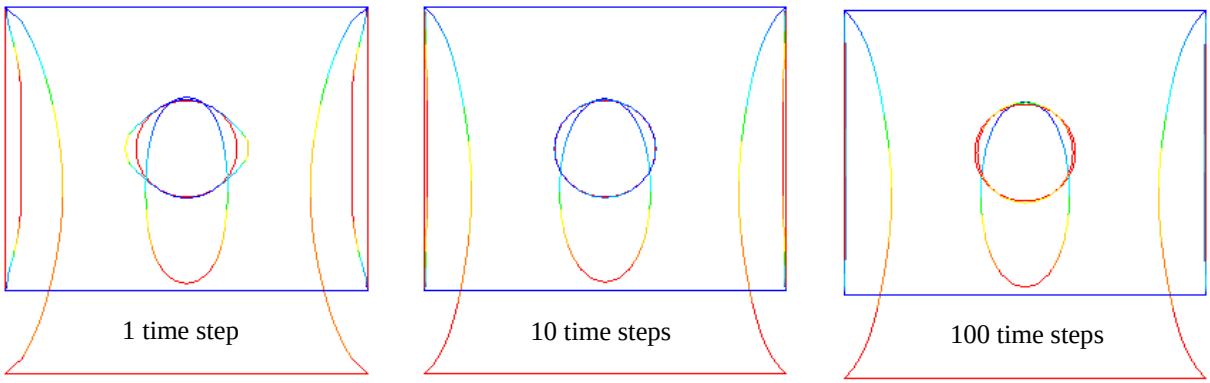


Figure 3-15: Specimen shape (2D with a circular hole) under uploading-unloading tensile at 30% strain for different time steps.

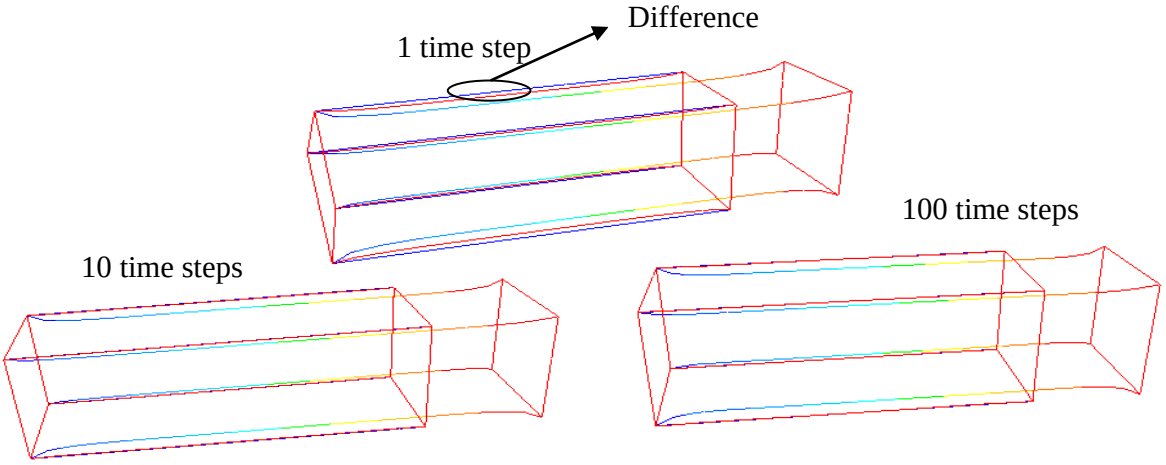


Figure 3-16: Specimen shape (3D with a rectangular/circular hole) under uploading-unloading tensile at 30% strain for a different time steps.

Finally, validation can be extended to the bending test (Figure 3-17 left), the torsion test (Figure 3-17 right), and compression tests (Figure 3-18) in large deformation. The idea is similar as the tensile test where only the boundary conditions were modified to adapt with the test case. For example, the upper edge of the specimen Γ_{sup} is fixed and we impose a velocity in the lower edge Γ_{inf} as follows:

Tensile test:

$$v = v_{imposed} = \begin{pmatrix} 0 \\ v_y \\ 0 \end{pmatrix} \tag{3.43}$$

Compressible tensile test:

$$v = v_{imposed} = \begin{pmatrix} 0 \\ -v_y \\ 0 \end{pmatrix} \tag{3.44}$$

Bending test:

$$v = v_{imposed} = \begin{pmatrix} v_x \\ 0 \\ 0 \end{pmatrix} \tag{3.45}$$

Torsion test:

$$v = v_{imposed} = \begin{pmatrix} \frac{\pi}{2}\left(x - \frac{1}{2}\right) \\ 0 \\ -\frac{\pi}{2}\left(z - \frac{1}{2}\right) \end{pmatrix} \tag{3.46}$$

where x, y and z are the node coordinate of the mesh.

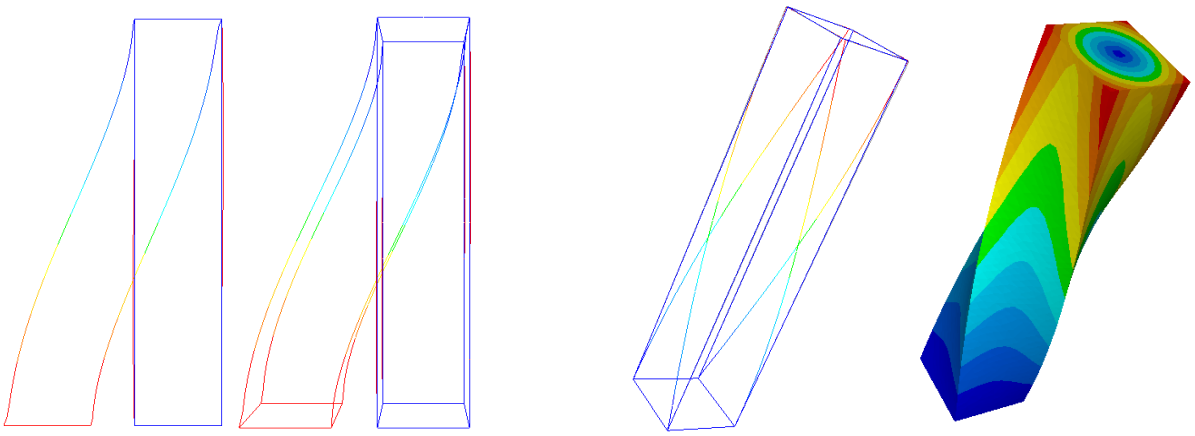


Figure 3-17: Specimen shape (3D) under flexion (left image) and torsion (right image) for 100 time steps.

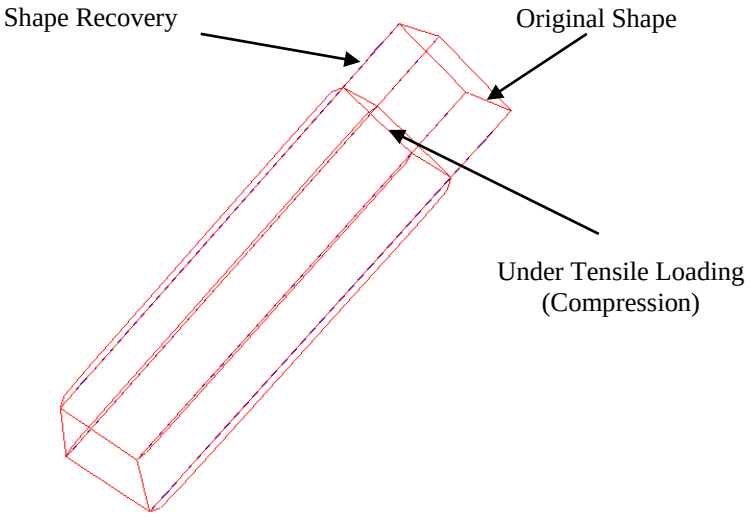


Figure 3-18: Specimen shape (3D) under compression for 100 time steps.

To comfort the use of our methodology, we perform the same test but by considering the viscoelastic Kelvin-Voigt model.

3.3.3 Incremental time step resolution for the tensile test case with an viscoelastic behavior

As we now are able to perform reasonably accurate elastic calculations, let us go further with the chosen viscoelastic Kelvin-Voigt's model (Figure 2-6) by adding the viscous parts in the equilibrium equation (3.32):

$$\nabla_{x^{n+1}}.\left(2\mu_e\varepsilon\left(u^{n+1}\right)+2\eta_v\varepsilon\left(v^{n+1}\right)\right)-\nabla_{x^{n+1}}p^{n+1}=0 \qquad (3.47)$$

where $2\eta_v\varepsilon\left(v^{n+1}\right)$ represents the viscous part in the time step *n+1*. As done for the resolution of an elastic behavior by the incremental method, the resolution algorithm is summarized as follows:

Algorithm for resolution of the viscoelastic Kelvin-Voigt model

For each time step $\left[t^n, t^{n+1}\right]$ for *loading* **do**

Knowing $\left(u^n, v^n, p^n\right)$

1) Compute $\left(v^{n+1}, p^{n+1}\right)$ such that

$$\begin{cases} \nabla_{x^{n+1}}.\left(2\mu_e\Delta t + 2\eta_v\right)\varepsilon\left(v^{n+1}\right) - \nabla_{x^{n+1}} p^{n+1} = -\nabla_{x^{n+1}}.\tau^n \\ \tau^n = 2\mu_e\varepsilon\left(u^n\right) \\ \nabla.v^{n+1} = 0 \\ v = v_{imposed} \ in\ \Gamma_{\inf} \ and\ v = 0 \ in\ \Gamma_{\sup} \end{cases} \tag{3.48}$$

2) Find u^{n+1} by solving

$$u^{n+1} = u^n + v^{n+1}\Delta t \tag{3.49}$$

3) Update the configuration by moving the mesh

$$x^{n+1} + u^{n+1} \Rightarrow x^{n+2} \tag{3.50}$$

4) Compute the extra-stress tensor

$$\tau^{n+1} = 2\mu_e\varepsilon\left(u^{n+1}\right) \tag{3.51}$$

End for *loading*

For each time step for *unloading* **do**

Knowing $\left(u^n, v^n, p^n\right)$

1) Compute $\left(v^{n+1}, p^{n+1}\right)$ such that

$$\begin{cases} \nabla_{x^{n+1}}.\left(2\mu_e\Delta t + 2\eta_v\right)\varepsilon\left(v^{n+1}\right) - \nabla_{x^{n+1}} p^{n+1} = -\nabla_{x^{n+1}}.\tau^n \\ \tau^n = 2\mu_e\varepsilon\left(u^n\right) \\ \nabla.v^{n+1} = 0 \\ v = -v_{imposed} \ in\ \Gamma_{\inf} \ and\ v = 0 \ in\ \Gamma_{\sup} \end{cases} \tag{3.52}$$

2) Find u^{n+1} by solving

$$u^{n+1} = u^n + v^{n+1}\Delta t \tag{3.53}$$

3) Update the configuration by moving the mesh

$$x^{n+1} + u^{n+1} \Rightarrow x^{n+2} \tag{3.54}$$

4) Compute the extra-stress tensor

$$\tau^{n+1} = 2\mu_e\varepsilon\left(u^{n+1}\right) \tag{3.55}$$

End for *unloading*

This algorithm can be used whatever the level of visco elasticity is. Table (Table 3-1), represents the different elastic and viscous modulus values that were chosen to define different viscoelastic behavior ranging from purely elastic to purely viscous behaviors. The time step Δt is fixed at 100 increments of resolution with an equivalent strain-rate of $0{,}003s^{-1}$.

	σ_v =0	σ_v << σ_e (a)	σ_v ~ σ_e (d)	σ_v >> σ_e (b)	σ_e =0 (c)
Young modulus (Pa)	3.3e^4	3.3e^7	6.6e^7	3.3 e^3	0
Viscous modulus (Pas)	0	5.91e^3	3.3e^5	5.91e^7	5.91e^3
Test Case	Pure Elastic Case	Elastic Part Dominates	Elastic and viscous stress have the similar weight	Viscous Part Dominates	Pure Viscous Case
		Viscoelasticity			

Table 3-1: Elastic part (σ_e) in relation to a viscous part (σ_v), in what concerns a Kelvin Voigt law. The time step Δt corresponds to a computation of 100 increments.

We observe that up to a strain of 30 %, the algorithm is performed. Figure 3-19 shows that initial and restored configurations are undistinguishable. Deformed shape presents no instability for all viscous/elastic roles. However, some instabilities have been observed for more important loadings, object of the following discussions.

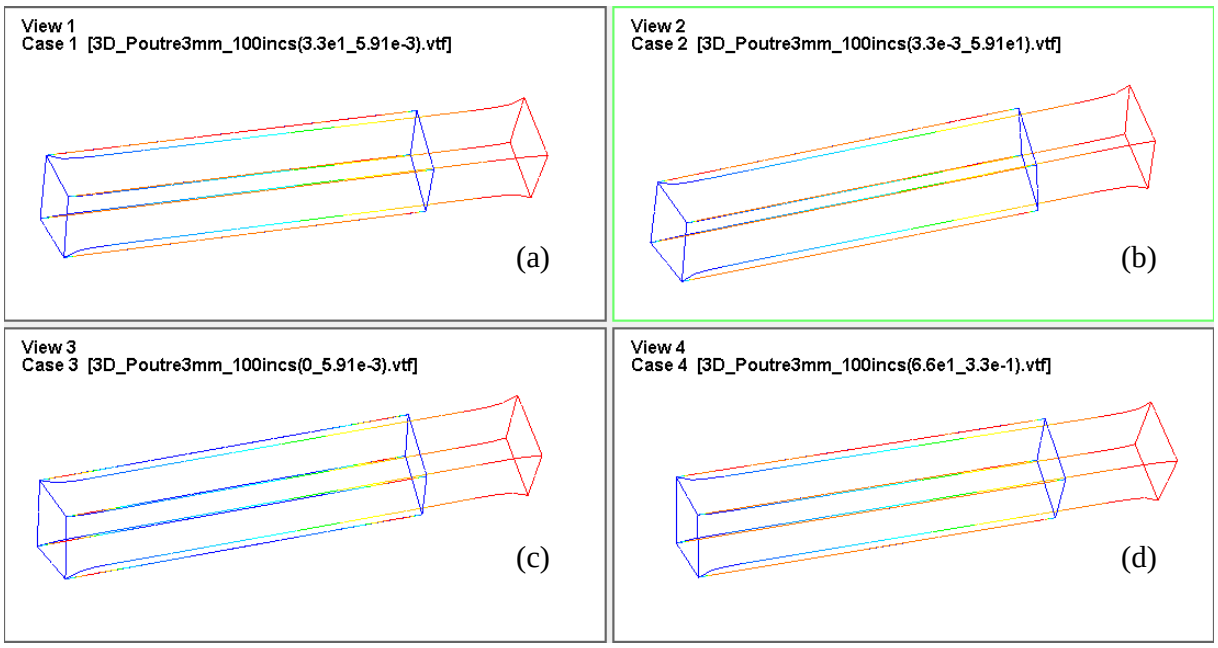


Figure 3-19: Specimen shape under uploading-unloading tensile at 30% strain for 100 time steps with different viscous and elastic factors. (a, b, c, d) correspond to the different cases of Table 3-1.

3.3.4 Instability problems in the tensile test by Lagrangian approach

For the single time step resolution, in spite of the important errors in large deformation, it remains stable in the numerical resolution. However, some instabilities problems occurred in the incremental method for the viscoelastic case (Figure 3-20, Figure 3-21) as well as the elastic case (Figure 3-22).

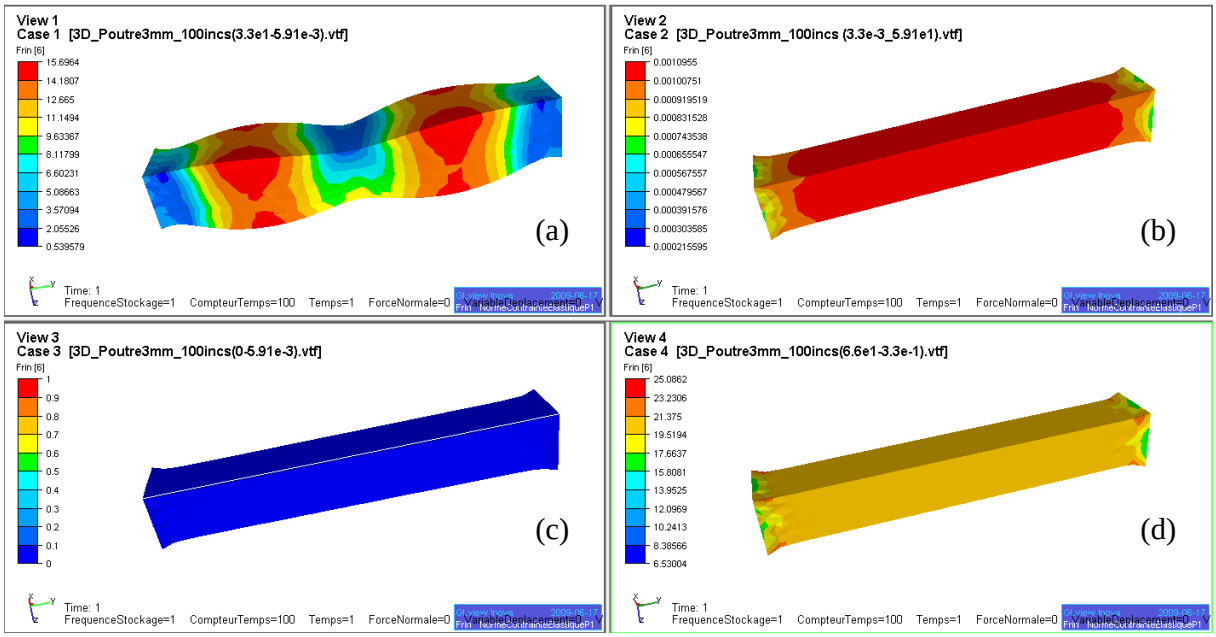


Figure 3-20: Elastic stress under uploading at 35% strain for 100 time steps in the viscoelastic case. (a, b, c, d) refer to the different cases of Table 3-1.

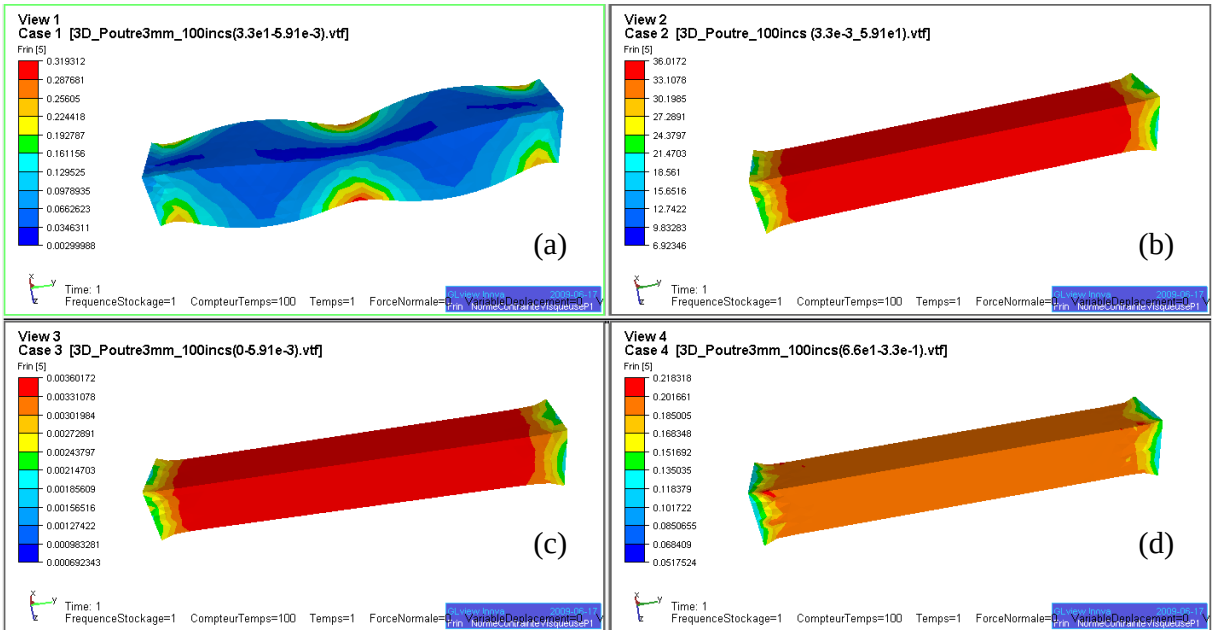


Figure 3-21: Viscous stress under uploading at 35% strain for 100 time steps in the viscoelastic case. (a, b, c, d) refer to the different cases of Table 3-1.

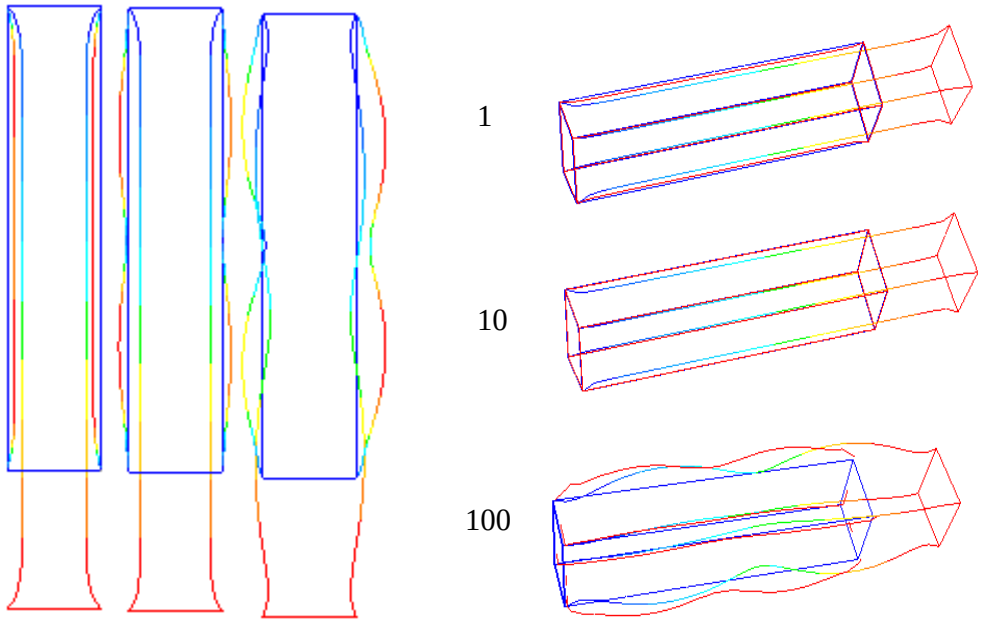


Figure 3-22: Specimen shape (2D-left image and 3D-right image) under tensile test at 35% strain for 1, 10 and 100 time steps in the elastic case.

In fact, the instabilities problems have appeared only in the incremental method when the elastic stress becomes significantly more important than the viscous stress in the viscoelastic case, or when strain is higher than 35% in the elastic case. As appears in the first image of Figure 3-20, where the elastic part dominates in the viscoelastic case (Table 3-1), and the specimen is deformed in a very strange way, resulting in a totally not physical deformation. Otherwise, in the other cases, the deformation of specimen seems normally.

The origin of that problem is the relative magnitude order of the elastic stress, i.e. the elastic stress become very important. If this latter is too high, the extra-stress in the right-hand side members of the equilibrium equation (equation (3.3)) causes some ellipticity loss in the resolution by the mixed finite method [95] [101]. In addition, the schema of resolution in the equilibrium equation is quite sensible due to the explicit calculation of the extra-stress. Moving to an implicit formulation (for this extra-stress) would have been possible but too complex in terms of computer programming and very costly.

Please note that there are also some missing terms in the resolution as mentioned previously (non-linear terms in large deformation or "bubble extra-stress"). Nevertheless, we prefer focusing on the stabilization of the extra stress on the numerical resolution which will be discussed later in chapter 4.

In the following, we will look at the resolution by the Eulerian approach. To model the tensile test by the monolithic approach, we define three different regions with different viscosities which represent three fields in the resolution by the multiphase approach. Firstly, we introduce the immersed volume method which is applied to deal with the problem.

3.4 Application for the tensile test case by Eulerian approach

3.4.1 Immersed volume method

A comprehensive description of the immersed volume method is structured into three subsections. The first one is related to the distance function used within a level-set approach in order to describe, position and immerse the solid object inside the fluid; next the mixing of different physical properties is explained, and finally a brief anisotropic mesh adaptation algorithm is needed to refine at the interface level between the fluid and the solid, which allows us to represent complex objects in a global computational domain.

3.4.1.1 Signed distance function

In the Eulerian test case, the solid interface between the phases is described by a signed distance function $\alpha(x)$ (equation (2.24)), as already presented in section 2.2 through the Level-Set method.

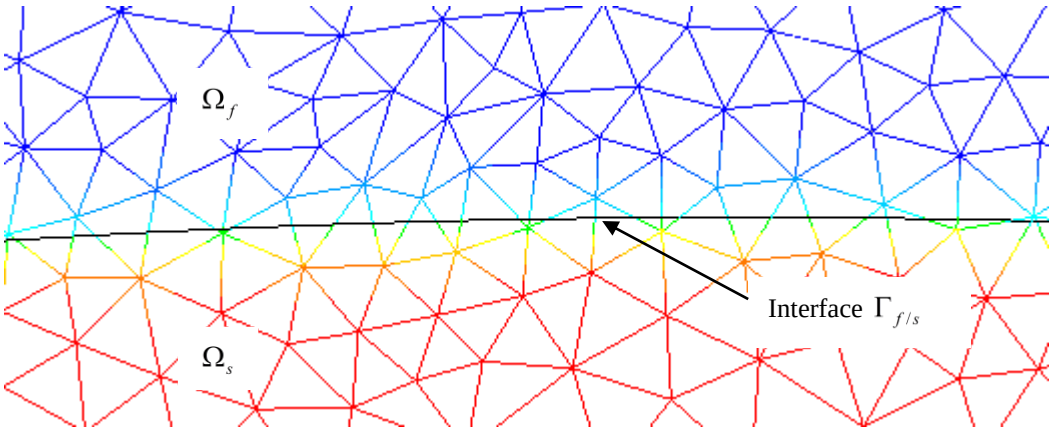


Figure 3-23: Two phases of a single mesh. The interface $\Gamma_{f/s}$ which separates the two phases through the elements is represented by a distance function α.

This function allows us to obtain a viscosity field $\eta(\alpha)$ depending on the position, and allows us to solve the equations throughout the whole computational domain.

$$\eta(\alpha) = \eta_f H(\alpha) + \eta_s (1 - H(\alpha)) \tag{3.56}$$

where $H(\alpha)$ is the characteristic function, so-called the Heaviside function.

3.4.1.2 Diffuse interface

As explained above, the viscosity varies, thanks to the equation (3.56), with the position. Several mixed laws can be used. Some are based on elements, other based on nodes where the viscosity change is not regular. Indeed, on an element crossed by the interface, some nodes are defined as fluid and other as solid. A mixed function based on elements, named here a "P0 mixture law", can be described as:

$$H(\alpha) = \frac{|\Omega_i \cap \kappa|}{|\kappa|} \tag{3.57}$$

where $\Omega_i \cap \kappa$ represents the volume occupied by the domain i on the element κ. Therefore, the mixed viscosity in equation (3.56) can be rewritten in the form:

$$\eta(\alpha) = \frac{\eta_s |\Omega_s \cap \kappa| + \eta_f |\Omega_f \cap \kappa|}{|\kappa|} \tag{3.58}$$

To smooth the variation of viscosity, another mixture law, named "P1 mixed law", consists in that, a smoothed Heaviside function given by:

$$H(\alpha) = \begin{cases} 1 & if \quad \alpha > e \\ \frac{1}{2}\left(1 + \frac{\alpha}{e} + \frac{1}{\pi}\sin\left(\frac{\pi\alpha}{e}\right)\right) & if \quad |\alpha| \le e \\ 0 & if \quad \alpha < -e \end{cases} \tag{3.59}$$

where e is known as the transition interface thickness, and will be related to h, the mesh size.

Figure 3-24 shows an example of the two mixture laws. The first is the discontinues law based on elements (P0) where the change occurs only in the elements crossed by the interface. The second is the continuous linear law. Figure 3-25 shows the mixed viscosity along a vertical section of Figure 3-24.

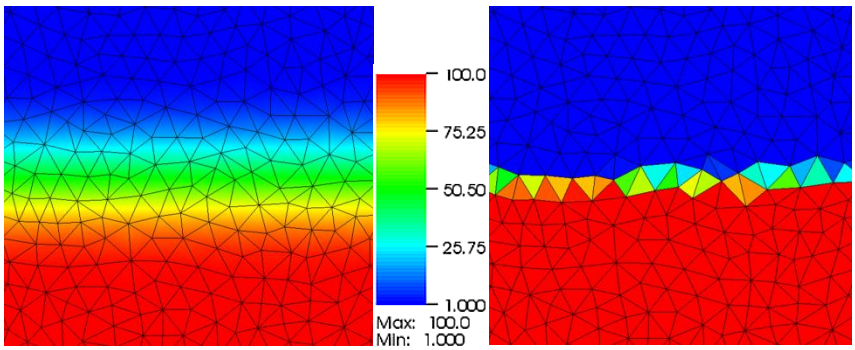


Figure 3-24: Illustration of the viscosity distribution on the mesh for the two mixture laws: P1 on the left and P0 on the right.

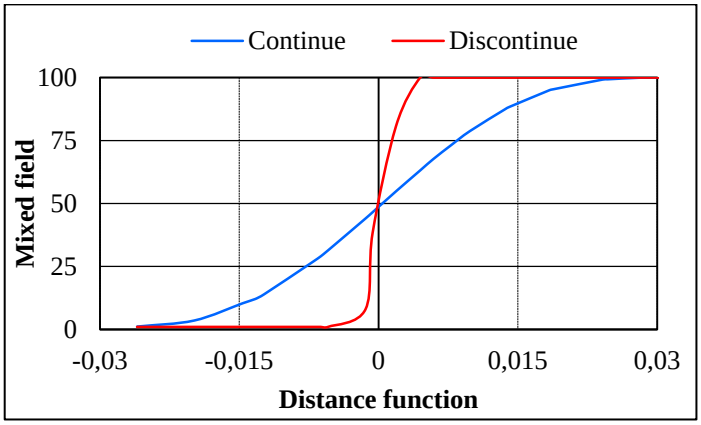


Figure 3-25: Vertical section of Figure 3-24. A good intermediate value of the mixed field for the discontinuous law is corresponding to that in the element crossed by the interface. The two variations of slope for the continue law P1 are due to the mesh.

We highlight that the thickness *e* should be sufficiently thin to limit errors due to the fact that the interface is defined in the volume, but large enough to ensure the representation of interface curvature. Practically, a mixture thickness is chosen arbitrarily several mesh elements. Moreover, an anisotropic mesh adaptation may present a better solution to keep an accurate interface.

3.4.1.3 Anisotropic mesh

Using the monolithic approach makes it is possible to simulate 3D applications involving several objects (i.e. several subdomains). However, due to the discontinuity of the properties of the material across the interface, the velocities, the pressures or the stresses are less accurate. Of course, isotropic refinement of the mesh can be used to reach a desired accuracy in the interface description (for example, to reach a sharp-interface solution) but too many nodes for an implicit three-dimensional finite element solver will lead to a significant increase of the computation cost. An anisotropic mesh adaptation can adequately represent the interfaces without increasing the cost of calculating so substantially with the use of an isotropic mesh. Therefore, we tend to generate suitable anisotropic meshes for computation. It means a mesh with several element layers everywhere through the thickness, even for thin and curved geometries which captures precisely the interfaces between subdomains as fluid-structure interface for example.

In order to follow this issue, the level-set method is coupled to an anisotropic mesh adaptation as described in [9]. Let us introduce to a metric notion which is a *d*-rowed and *d*-columned, real, symmetrical, positive definite matrix representing a local base that modifies the distance computation, such that:

$$\|x\|_M = \sqrt{{}^T x.M.x} \ , \ \langle x, y \rangle_M = {}^T y.M.x \tag{3.60}$$

Note first that if M is constant (that is to say *M* doesn't depend of x), then we end up with a Euclidean space. In addition if *M* is identity, the distance corresponds to the usual one in the Euclidean space. In our case, the metric *M* isn't constant (Riemannian space) which can be regarded as a tensor whose eigenvalues are related to the mesh sizes, and whose eigenvectors define the directions for which these sizes are applied. At this point, we want to put enough elements where it is necessary (i.e. through the thickness). For that purpose, we propose to take advantage of the anisotropic adaptation driven by a metric field *M*, built in such a way that the direction of mesh refinement is given by the unit normal to the interface, which corresponds to the gradient of the level-set function:

$$x = \frac{\nabla \alpha(x)}{\|\nabla \alpha(x)\|} \tag{3.61}$$

In order to define the mesh size *h*, we introduced a characteristic thickness *e* that will determine its distribution in the space following the interface function $\alpha(x)$:

$$h = \begin{cases} h_d & \text{if } |\alpha(x)| > e/2 \\ \dfrac{2h_d(m-1)}{m \times e}|\alpha(x)| + \dfrac{h_d}{m} & \text{if } |\alpha(x)| \le e/2 \end{cases} \tag{3.62}$$

where h_d is the default mesh size far from the interface ($|\alpha(x)| > e/2$), and it's reduced in the direction perpendicular to the interface in the ways related with a factor m.

Therefore, we can introduce the corresponding metric M as follows:

$$M = C(x \otimes x) + \frac{1}{h_d} I \text{ with } C = \begin{cases} 0 & if\ |\alpha(x)| \geq e/2 \\ \frac{1}{h^2} - \frac{1}{h_d^2} & if\ |\alpha(x)| < e/2 \end{cases} \quad (3.63)$$

Practically, the mesh is generated in several steps using the MTC mesher and remesher [102] [103] for which the metric can then be corrected by a solver and a posteriori anisotropic estimator error [9] [104].

As shown in Figure 3-26 which presents a close-up on the interface zone at the end of the anisotropic adaptation process, the mesh has been refined near the interface. Consequently, only additional nodes are locally added in this region, whereas the rest of domain has maintained the same background size.

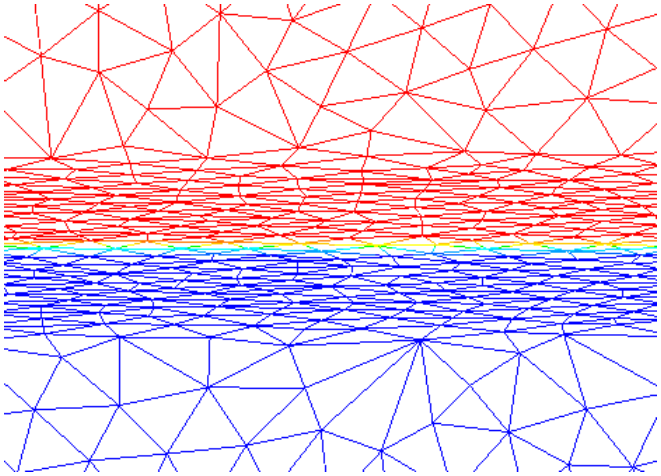


Figure 3-26: Interface refinement using anisotropic mesh adaptation: a zoom at the interface region.

Let us introduce and summarize the resulting method in the modeling of the tensile test with regard of the Eulerian approach.

3.4.2 Eulerian method for the incompressible elastic tensile test

We consider the same case but in an Eulerian context, described in Figure 3-1 (right). We define three different regions with different viscosities which determine three fields:

- the solid field, representing the grip of the traction machine (grey), fixed in the top and mobile in the bottom, we introduce a viscosity η_{rig} for the behavior of the solid to ensure the non-deformability,
- the fluid (blue), with a viscosity η_f to guarantee that it will not influence the behavior of the specimen,

- the specimen (red) with an elastic behavior and a Young's Modulus E and Poisson's coefficient ν_e. As explained in the section 2.3 and equation (2.72), we can introduce a viscosity $\eta_e = \mu_e \Delta t = \frac{E\Delta t}{2(1+\nu_e)}$ to represent the elastic behavior of the specimen,

As we have three different fields, thus three interface functions are usually defined. In our case, we have splitted the solid in two sub regions, leading to three functions:

- α_{ve} represents the distance to interface of the specimen,
- $\alpha_{s-\sup}$ represents the distance to interface of the upper part of the solid which is fixed,
- $\alpha_{s-\inf}$ represents the distance to interface of the lower part of the solid which is mobile,

Therefore, a mixture function of the three fields (solid/fluid/specimen) as the Heaviside function is used to compute the material properties:

$$\eta_1 = \eta_e H(\alpha_{ve}) + \eta_f (1 - H(\alpha_{ve})) \tag{3.64}$$

$$\eta_2 = \eta_{rig} H(\alpha_{s-\sup}) + \eta_1 (1 - H(\alpha_{s-\sup})) \tag{3.65}$$

$$\eta_{ve} = \eta_{rig} H(\alpha_{s-\inf}) + \eta_2 (1 - H(\alpha_{s-\inf})) \tag{3.66}$$

For the numerical simulations, interpolation P0 was used.

As shown in Figure 3-27, illustrates the interface zone of three subdomains, grip(solid)/fluid/specimen, the mesh has been refined when approaching the interface, whereas the rest of the subdomains remain at the same background size.

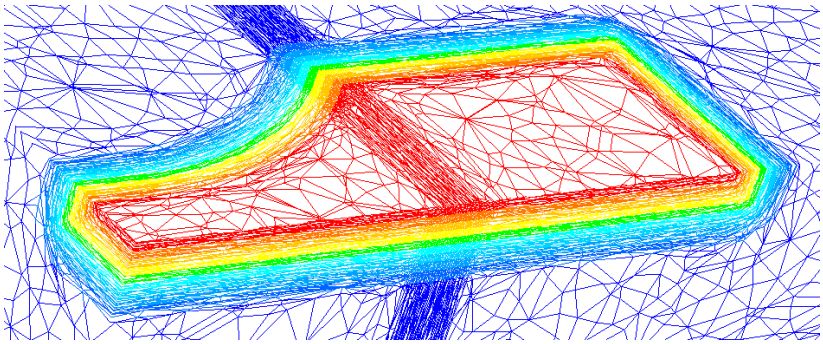


Figure 3-27: Zoom on the specimen/fluid interface after anisotropic adaptation in 3D.

Due to the flow complexity, the velocity is strongly sheared, thus the transport of the interface can deteriorate rapidly. The gradient of α, the phase function, can become steep and unstable, and $|\nabla \alpha| = 1$ is not ensured.

So a reinitialization step is necessary [95]. A new Level-Set formulation method to follow the

interface motion was proposed by Coupez [88]. To resume, the transport or convective reinitialization is solved through the following equation:

$$\begin{cases} \dfrac{\partial \alpha}{\partial t} + v\nabla\alpha + \lambda s\left(|\nabla\alpha| - \sqrt{1-\left(\dfrac{\pi}{2e}\alpha\right)^2} \right) = 0 \\ \alpha(t=0,x) = \alpha_0(x) \end{cases} \tag{3.67}$$

where a modified Level-Set function is given first as follows [88]:

$$\begin{cases} \alpha = \dfrac{2e}{\pi}\sin\left(\dfrac{\pi}{2e}\alpha\right) & |\alpha| < e \\ \alpha = \dfrac{2e}{\pi} & \alpha > e \\ \alpha = -\dfrac{2e}{\pi} & \alpha < -e \end{cases} \tag{3.68}$$

s the sign of β (initially α), $\lambda = \dfrac{d\tau}{dt}$ where t and τ is the time and the fictitious time, e is the mixture thickness.

The Level-Set formulation offers a certain freedom in modeling heterogeneous media. The choice of the mixing function $H(\alpha)$ determines the characteristic of the mixture of different subdomains, and thus affects the interface. In fact, the more abrupt the function is, the less the diffusion of interface we have.

Finally, the system of equations to resolve is illustrated as follows:

$$\begin{cases} \nabla\cdot 2\eta_{ve}\varepsilon(v) - \nabla p = -H(\alpha_{ve})\nabla\cdot\tau \\ \tau = 2\mu_e\varepsilon(u) \\ -\nabla\cdot v = 0 \\ \dfrac{du}{dt} = \dfrac{\partial u}{\partial t} + v\nabla u = v \\ v = v_{imposed} \ in\ \Gamma_{\inf} \ and\ v = 0 \ in\ \Gamma_{\sup} \end{cases} \tag{3.69}$$

We remark that the "extra-stress" τ is only applied in the specimen domain and is neglected in others domains.

To resume, the resolution algorithm by the Eulerian method is quite complex. First, the conservation of momentum and the conservation of volume must be solved. Then, it requires a robust solver to transport the interface, following the choice of mixing function to minimize the diffusion of interface. After, the resolution of the 3rd solution field *u* will be computed [95] which provides the "extra-stress". During the simulation, the remeshing may be sequentially interposed to ensure the good representation of interface and the advantages of anisotropic mesh mentioned in the above section, essential in 3D applications.

For more details in the numerical calculation, the time scheme of resolution may be explained as follows:

Algorithm for *loading* and *unloading*:

For each time step $\left[t^n, t^{n+1}\right]$ for *loading* **do**

Knowing τ^n

1) Compute $\left(v^{n+1}, p'^{n+1}\right)$ such that

$$\begin{cases} \nabla\cdot 2\eta_{ve}\varepsilon\left(v^{n+1}\right) - \nabla p'^{n+1} = -\nabla\cdot\tau^n \\ \tau^n = 2\mu_e\varepsilon\left(u^n\right) \\ -\nabla\cdot\left(v^{n+1}\right) = 0 \\ v = v_{imposed} \ in\ \Gamma_{\inf} \ and\ v = 0 \ in\ \Gamma_{\sup} \end{cases} \tag{3.70}$$

2) Transport the interface by solving

$$\begin{cases} \dfrac{\alpha^{n+1} - \alpha^n}{\Delta t} + v^{n+1}\nabla\alpha^{n+1} + \lambda s\left|\nabla\alpha^{n+1}\right| = \lambda s\sqrt{1 - \left(\dfrac{\pi}{2e}\alpha^n\right)^2} \\ \alpha\left(t=0,x\right) = \alpha_0\left(x\right) \end{cases} \tag{3.71}$$

3) Find u^{n+1} by solving

$$\frac{u^{n+1} - u^n}{\Delta t} + v^{n+1}\nabla u^{n+1} = v^{n+1} \tag{3.72}$$

4) Compute the extra-stress tensor

$$\tau^{n+1} = 2\mu_e\varepsilon\left(u^{n+1}\right) \tag{3.73}$$

5) Remesh if necessary

End for *loading*

For each time step $\left[t^n, t^{n+1}\right]$ for *unloading* **do**

Knowing τ^n

1) Compute $\left(v^{n+1}, p'^{n+1}\right)$ such that

$$\begin{cases} \nabla\cdot 2\eta_{ve}\varepsilon\left(v^{n+1}\right) - \nabla p'^{n+1} = -\nabla\cdot\tau^n \\ \tau^n = 2\mu_e\varepsilon\left(u^n\right) \\ -\nabla\cdot\left(v^{n+1}\right) = 0 \\ v = -v_{imposed} \ in\ \Gamma_{\inf} \ and\ v = 0 \ in\ \Gamma_{\sup} \end{cases} \tag{3.74}$$

2) Transport the interface by solving

$$\begin{cases} \dfrac{\alpha^{n+1} - \alpha^n}{\Delta t} + v^{n+1}\nabla\alpha^{n+1} + \lambda s\left|\nabla\alpha^{n+1}\right| = \lambda s\sqrt{1 - \left(\dfrac{\pi}{2e}\alpha^n\right)^2} \\ \alpha\left(t=0,x\right) = \alpha_0\left(x\right) \end{cases} \tag{3.75}$$

3) Find u^{n+1} by solving

$$\frac{u^{n+1} - u^n}{\Delta t} + v^{n+1}\nabla u^{n+1} = v^{n+1} \tag{3.76}$$

4) Compute the extra-stress tensor

$$\tau^{n+1} = 2\mu_e \varepsilon\left(u^{n+1}\right) \tag{3.77}$$

5) Remesh if necessary

End for *unloading*

We highlight that the convected term in equation (3.78) is neglected in the stress tensor calculation:

$$\begin{cases} \varepsilon\left(u^{n+1}\right) = \varepsilon\left(u^{n}\right) + \varepsilon\left(du^{n+1}\right) \\ \varepsilon\left(du^{n+1}\right) = \varepsilon\left(v^{n+1} - v^{n+1}\nabla u^{n+1}\right)dt \approx \varepsilon\left(v^{n+1}\right)\Delta t \end{cases} \tag{3.78}$$

3.4.3 Numerical results

Material parameters and the specimen form are chosen in order to satisfy the experimental parameters of PMMA which will be presented in chapter 5:

	E	ν_e	η_{rig}	η_f
Value	$70e^6$ *(Pa)*	0.5	$3e^6$ *(Pas)*	10 *(Pas)*

Table 3-2: Material parameters used.

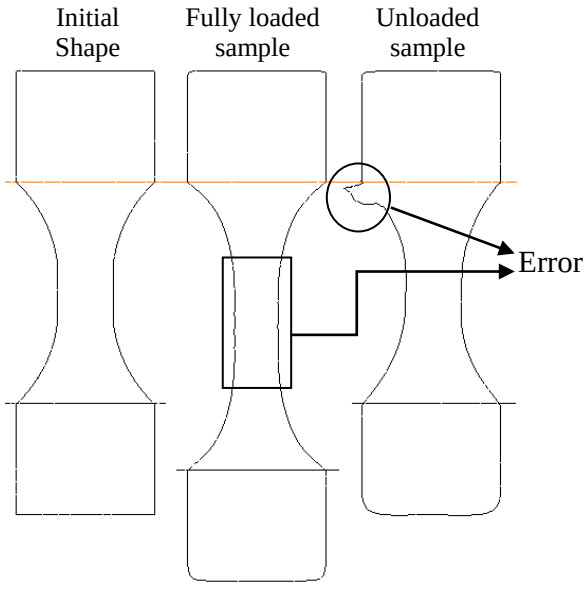


Figure 3-28: Tensile test by an Eulerian approach. Schematic representation of the specimen interface shape by an Eulerian method. Please note that the specimen interface is represented by the zero iso-value of the distance function α which is transported by the Level-Set method.

The interface of the specimen, represented by the zero iso-value of the Level-set function (Figure 3-28), is distorted at large deformations, mainly on the corners because of the high distortion of elements in this zone. In fact, we are then face to a multiphase problem similar to the flow between two rigid particles case which will be treated just below, in which these oscillations on pressure appear as displayed in the follow figure:

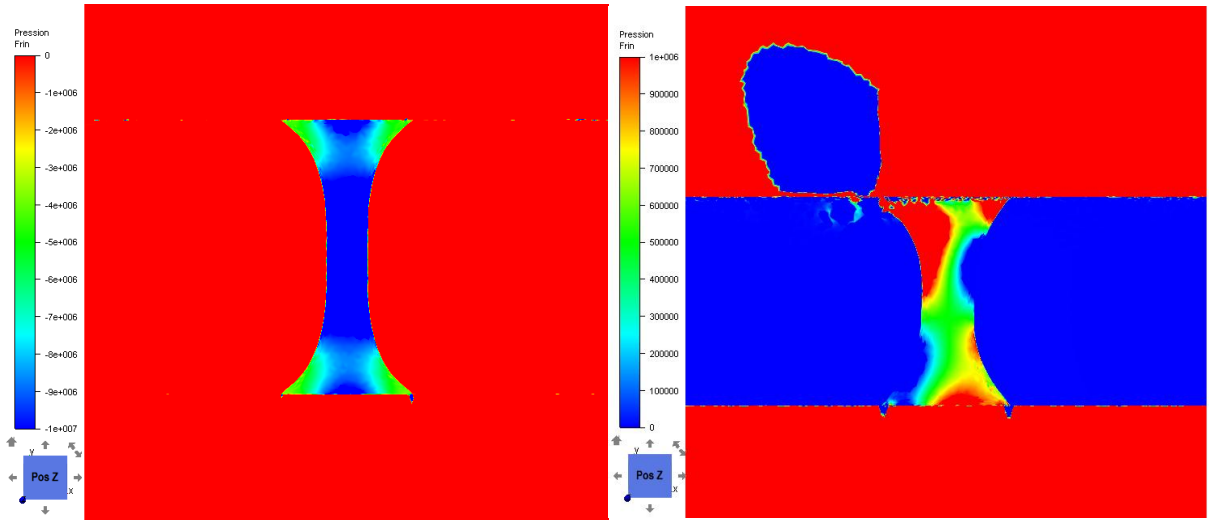


Figure 3-29: Pressure field under loading (left) and unloading (right).

Strong oscillations of the pressure field exist that can be extremely problematic to later calculation of the stress inside the specimen. As displayed in Figure 3-29, the pressure oscillations appear strongly in the mixed zone of viscosity, i.e. near the interface. This indicates that stabilization is not good in the area where the solid viscosity is much greater than in the fluid. In fact, the difference of viscosity between two phases causes a steep change of viscosity in the mixed zone which engenders big difficulties in stabilization.

Numerically, modeling of a multiphase problem where a solid as a strong viscosity generates important viscosities not only in the solid domain, but also in the element containing the interface. As detailed in the previous section, in the bubble space of FE resolution, we find a term, called the sub-matrix C, to stabilize the system. This sub-matrix C is directly dependent on the inverse of viscosity. Thus, when the viscosity increases, the stabilization term decreases. For strong values of the viscosity as those that we impose in the solid, the stabilization term tends to zero. We find ourselves that with a non-stabilized formulation, close to a P1/P1 formulation in the solid zone. A more detail can be found in the following chapter devoted to the stabilization problem.

In the following, we will look at the case where the solid is no longer elastic or viscoelastic, but rigid, and the fluid flows around it, the flow between two rigid solid particles to take a deep look into this stabilization problem.

3.5 Application in flow between two rigid particles

3.5.1 Formulation for a rigid solid

Practically, to model the undeformable solid, an equivalent non-deformability condition is used:

$$\varepsilon(u)=0 \quad \forall x\in\Omega_s \quad \Leftrightarrow \quad \begin{cases} \nabla\cdot\varepsilon(u)=0 & \forall x\in\Omega_s \\ \varepsilon(u)\cdot\vec{n}=0 & sur\ \partial\Omega_s \end{cases} \tag{3.79}$$

The weak form of this condition is then expressed by using a Lagrangian multipliers vector λ:

$$\int_{\Omega_s}\lambda\nabla\cdot\varepsilon(u)d\Omega=-\int_{\Omega_s}\nabla\lambda:\varepsilon(u)d\Omega+\underbrace{\int_{\partial\Omega_s}\lambda\left(\varepsilon(u)\cdot\vec{n}\right)d\Gamma}_{=0} \tag{3.80}$$

Due to the symmetric property of gradient of λ, the above equation can be written as:

$$\int_{\Omega_s}\nabla\lambda:\varepsilon(u)d\Omega=\int_{\Omega_s}\varepsilon(\lambda):\varepsilon(u)d\Omega \tag{3.81}$$

Therefore, we can express the stress inside the rigid solid:

$$\sigma=\varepsilon(\lambda)-pI \tag{3.82}$$

Finally, the variational formulation for the problem can be deduced:

Find $(v,\lambda,p)\in(V,V,P)$ such that $\forall(w,\varsigma,q)\in(V_0,V_0,P)$:

$$\begin{cases} 2\eta_f\int_{\Omega}\varepsilon(v):\varepsilon(w)d\Omega-\int_{\Omega}p\nabla\cdot wd\Omega+\int_{\Omega_s}\varepsilon(\lambda):\varepsilon(w)d\Omega=0 \\ \int_{\Omega}q\nabla\cdot vd\Omega=0 \\ \int_{\Omega_s}\varepsilon(\varsigma):\varepsilon(\lambda)d\Omega=0 \\ +boundary\ conditions \end{cases} \tag{3.83}$$

We can consider that the Lagrangian multiplier λ contributes to the necessary applied stress to ensure the undeformability of the solid field within the multiphase problem.

The resolution of the above system may be done directly, which leads to a linear system consisting of 7N unknowns instead of 4N due to the additional 3N unknowns of the Lagrange multipliers, equivalent to those used for the velocity field. To avoid this increase in the number of unknowns, i.e. the computing cost, two approximate methods may be used to impose the rigidity constraint: the first method is the Lagrangian penalization method, and the second one, more precise, is the augmented Lagrangian method coupling with an iterative method, the so-called the Uzawa algorithm.

3.5.1.1 Lagrangian penalization method

Naturally, the penalty method replaces a constrained optimization problem by a series of unconstrained problems whose approximate solutions converge to the solution of the original constrained problem [105]. In our case, this is achieved by adding a term to the objective function which forms the unconstrained problem:

$$L_{\eta_s}(v,q) = L(v,q) + \int_{\Omega_s} \eta_s \varepsilon(v) : \varepsilon(w) d\Omega \tag{3.84}$$

where L_{η_s} is the Lagrangian penalization of the problem. The approximated solution (v_{η_s}, p_{η_s}) which minimize L_{η_s} is closer to the exact solution when the penalization factor η_s is high. The variational formulation can be resumed as:

Find $(v,p) \in (V,P)$ such that $\forall (w,q) \in (V_0,P)$:

$$\begin{cases} 2\eta_f \int_{\Omega} \varepsilon(v) : \varepsilon(w) d\Omega - \int_{\Omega} p \nabla \cdot w d\Omega + \int_{\Omega_s} 2\eta_s \varepsilon(v) : \varepsilon(w) d\Omega = 0 \\ \int_{\Omega} q \nabla \cdot v d\Omega = 0 \\ + \textit{boundary conditions} \end{cases} \tag{3.85}$$

The penalization factor η_s can be interpreted as a solid viscosity and the problem is simply to solve a Stokes incompressible multi-domain problem. Basically, in this approach a solid domain is considered as a viscous fluid with high viscosity which is usually 1000 times greater than the fluid viscosity [106] [107]. However, the use of a high penalization factor deteriorates the conditioning of discrete system, and the resulting solution may become too far from the solution of constrained problem. To overcome this problem, the formulation with Lagrange multiplier, coupled with an iterative method should be used: the augmented Lagrangian method with Uzawa algorithm.

3.5.1.2 Augmented Lagrangian method with Uzawa algorithm

The standard augmented Lagrangian method was first introduced by Fortin and Glowinski [108]. It consists in solving an optimization problem by solving a velocity–pressure saddle point with an Uzawa algorithm [109].

To find a Lagrangian saddle point of our problem, we can use the iterative method to calculate the multiplier, and thus to reduce, at each iteration, to the resolution of a standard problem in velocity-pressure. Note that in Uzawa algorithm first increment returns to the resolution by the Lagrangian penalization method.

Algorithm:

Initiation τ^0, practically we impose $\tau^0 = 0$
For each time step $\left[t^n, t^{n+1}\right]$ **do**

Knowing τ^{n+1}, find $\left(v^{n+1}, p^{n+1}\right)$ such that

$$\begin{cases} 2\eta\int_{\Omega}\left(\alpha_{f/s}\right)\varepsilon\left(v^{n+1}\right):\varepsilon\left(w\right)d\Omega-\int_{\Omega}p^{n+1}\nabla\cdot w d\Omega=-\int_{\Omega_s}\tau^{n+1}:\varepsilon\left(w\right)d\Omega \\ \int_{\Omega}q\nabla\cdot v^{n+1}d\Omega=0 \\ +\textit{boundary conditions} \end{cases} \tag{3.86}$$

And τ^{n+2} is found by solving

$$\begin{cases} \tau^{n+2}=\tau^{n+1}+r_s\varepsilon\left(v^{n+1}\right) \\ r_s=rH\left(\alpha_{f/s}\right) \end{cases} \tag{3.87}$$

with r is the multiplier factor, and the mixed law for viscosity is described as:

$$\eta\left(\alpha_{f/s}\right)=H\left(\alpha_{f/s}\right)\eta_f+\left(1-H\left(\alpha_{f/s}\right)\right)\eta_s \tag{3.88}$$

Condition to stop the loop on n

$$\int_{\Omega_s}\varepsilon\left(v^{n+1}\right):\varepsilon\left(v^{n+1}\right)d\Omega<\varepsilon \quad with \quad \varepsilon\ll 1 \tag{3.89}$$

End for

3.5.2 Numerical results

In the above section, some resolution methods were proposed to solve this problem. However, due to some missing terms in the resolution, revealed in the previous section as the "bubble extra-stress" B_{v_b} in the fine-scales resolution (equation (3.24)) which has a significant influence in the resolution by the augmented Lagrangian method with Uzawa algorithm. Thus, this section will only be devoted to resolution by the penalization method, for the other methods, lector can refer to the next chapter 4.

Modeling of the flow between the two rigid particles can be performed by a monophasic simulation as showed in Figure 3-30. The results display a perfect pressure distribution through the channel between two rigid bodies, representing two fibers. Please note that this simulation is the resolution of a simple classical Stokes problem.

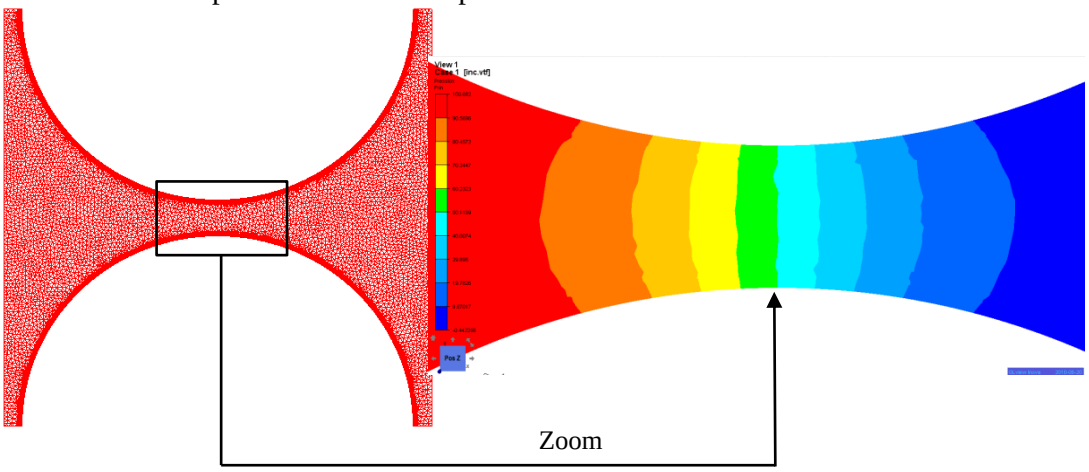


Figure 3-30: Monophasic case for the modeling the two phase flow of a fluid around a rigid body (*reference solution*).

Now we numerically solve this case by a two phase approach where viscosities for the fluid phase and for the solid phase are chosen as:

	η_s	η_f
Value	$1e^4\ (Pas)$	$1e^2\ (Pas)$

Table 3-3: Material parameters used for the flow between two rigid solid particles case by the penalization method.

In this case, we find a flow such as illustrated by the velocity field in Figure 3-31 (left) by the monophasic resolution and in Figure 3-31 (right) by the penalization method for an anisotropic mesh. The velocity field is quite acceptable for these simulations. However, we observe strong oscillations of the pressure field (Figure 3-32).

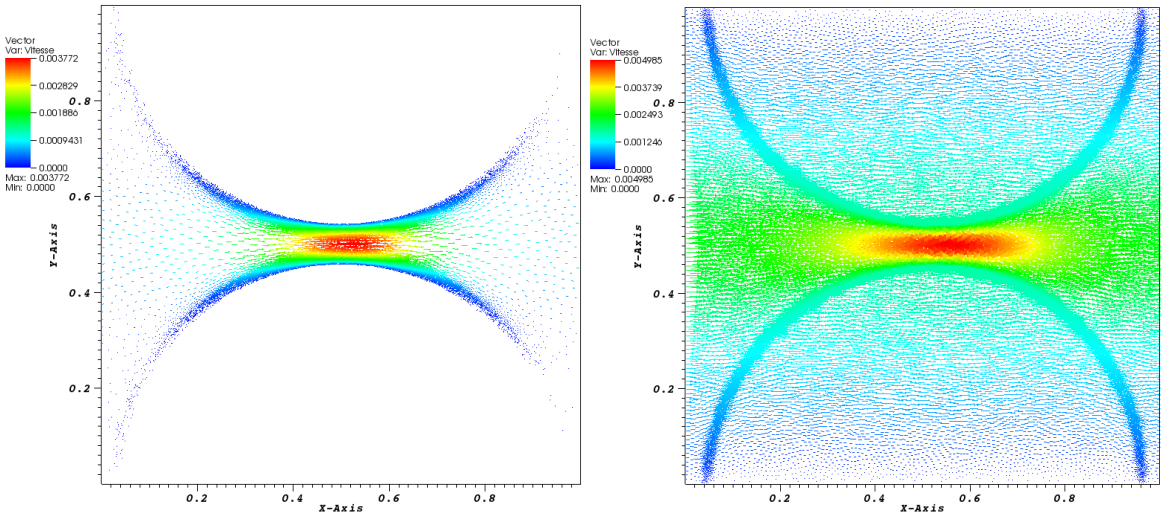


Figure 3-31: Velocity field. In the first row, on the left velocity by the one phase modeling, on the right velocity by the penalization method is displayed.

Strong oscillations of the pressure field (Figure 3-32) exist that can be extremely problematic to later calculation such as the permeability of the equivalent media [91] which directly dependent on its gradient, or in dynamic problem.

Figure 3-32 showed that the pressure field inside the fluid domain is smooth, but it appears strongly oscillations near the interface. As explained previously in the resolution of the tensile test by the Eulerian approach, for strong values of the viscosity as those that we impose in the solid which engenders big difficulties in stabilization. Let move to the following chapter which will be devoted to the stabilization problem to find the answer.

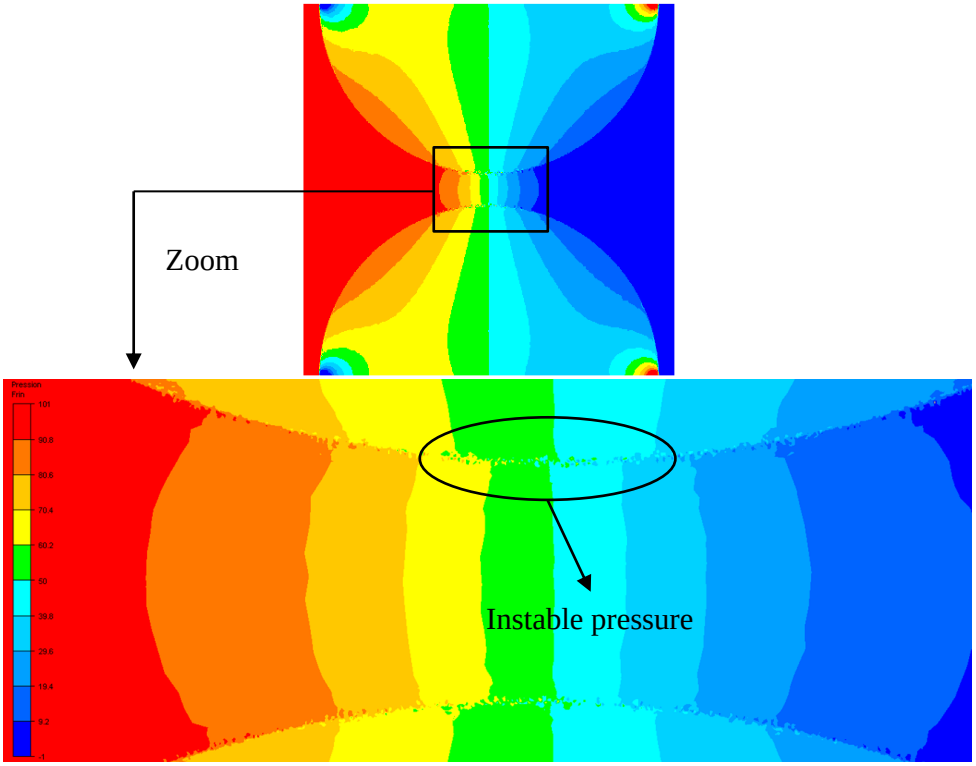


Figure 3-32: Pressure oscillation on the interface solid-fluid.

3.5.3 Concluding remarks

In this chapter, our preliminary study demonstrates the ability of the existing solver, based on the finite element library CimLib®. Therefore, two different benchmarks was proposed et performed to simulate the two phase flows problem where resolution by the monolithic approach can be performed as mixed phases (the tensile test case) or two separated phase (the flow between rigid particles case). For the first one, classical loading as tension, shearing, compression, and bending in 2D and 3D was achieved with the satisfactory results in the Lagrangian framework which give us a good indication for the following work as part of our project. However, some instability problems appeared in the incremental time step resolution in the Lagrangian framework, especially at large deformations. Indeed, the origin of this problem is related to the magnitude of the elastic stress. If the latter is too large, the extra-stress in the right-hand side members of the equilibrium equation causes an ellipticity problem in the resolution by the mixed method. Moreover, some missing terms cited could also cause the unstable problem of resolution.

With regard to the Eulerian framework, the similar instability problem also appeared due to the strong oscillations of the pressure field. In fact, modeling of a multiphase problem with a solid with a strong viscosity may cause a steep change of viscosity in the mixed zone which engenders big difficulties in stabilization. Regarding the second case, strong oscillations of the pressure field were also observed in the simulation. Thus, our next work is to accomplish a numerical stabilized solution to treat these problems which will be developed in the next chapter.

3.6 Résumé du chapitre en français

La robustesse de notre approche décrite au chapitre 2 est confrontée au problème dit de Stokes avec “extra-contrainte”. Deux benchmarks sont proposés : un cas purement élastique et le cas d’écoulement visqueux entre deux particules rigides. La formulation mixte vitesse-déplacement utilisée pour résoudre ces équations différentielles par la méthode des éléments finis est détaillée

Le cas du corps purement élastique représente une limite du comportement viscoélastique dont notre formalisme doit rendre compte précisément. Dans cet objectif, des résolutions incrémentale et directe sont discutée dans le cadre Lagrangien pour des sollicitations de traction, flexion, torsion et compression. La méthode incrémentale semble plus pertinente dans tous les cas. Une étude de sensibilité au maillage est entreprise.

Cependant, certains problèmes d’instabilité sont apparus même lors d’une résolution incrémentale, principalement aux grandes déformations lorsque la contrainte élastique devient prédominante. Ceux-ci conduisent à des résultats non physiques. L’origine est un problème d’ellipticité dans la résolution par la méthode mixte, lié au calcul explicite de “l'extra-contrainte”, quand l’ordre de grandeur de la contrainte élastique devient trop grand.

Une formulation implicite, toujours possible ferait appel à des développements complexes et resterait sans doute très coûteuse en temps de calcul. De plus, les hypothèses de petites transformations, qui sont abusives dans ce contexte, mériteraient d’être levées avant d’aller plus loin dans l’écriture numérique.

Dans le cas d’une approche Eulérienne la méthode d'immersion de domaine, largement utilisé pour modéliser les problèmes multiphasiques, est utilisée. Elle donne lieu à de fortes oscillations non physiques dans le champ de pression que nous nous sommes attachés à supprimer. Le chapitre 4 détaille ce travail de stabilisation.

Chapter 4

4 Stabilized Mixed Finite Elements

4 Stabilized Mixed Finite Elements 91

4.1 Improvement on the mixed velocity-pressure-displacement formulation through a complete solver 93

4.1.1 Stabilized mixed finite elements 95

4.1.2 Comparison between the old solver NSTC and the new SMC 103

4.1.3 Application in the elasticity case: comparison with the old solver 105

4.1.4 Application: flow between two rigid solid particles 115

4.2 Improving stabilization through the bubble viscosity modification 121

4.2.1 A novel formulation with modification of bubble's viscosity 121

4.2.2 Application 123

4.2.3 Concluding remarks 132

4.3 Improving stabilization through Elastic Viscous Split Stress (EVSS) 133

4.3.1 Short review on computational methods used in viscoelastic flow 133

4.4 Résumé du chapitre en français 136

The objective of this chapter is to define the main features of our solver which allow treating a general mechanical problem where the behavior can go from a Newtonian fluid to an elastic or rigid solid, being the main purpose the treatment of a viscoelastic one. Since the description of the numerical methods used at the beginning of this work to solve the extended Navier-Stokes equation with an extra-stress tensor showed, in chapter 3, the requirement of an improvement to overcome some instability problems, this chapter will focus on implementing missing terms in the actual solver and stabilizing the numerical resolution method. Three stabilization methods will be exploited to improve the results obtained in the previous chapter, being the first one based on the stabilized mixed finite element, the second related to the modification of bubble viscosity and the last one based on the Elastic Viscous Stress Splitting (EVSS).

The first part of this chapter presents the resolution of the extended compressible-incompressible Navier-Stokes equation with an extra-stress tensor in the context of the stabilized mixed finite element framework, where we will put in evidence terms missing in the formulation shown in the previous chapter. Furthermore, it will lead to the construction of a new solver, that instead of being specifically enriched in velocity is built in such a way that it is generic to the bubble enrichment we wish to add to whatever variable (for example, P1+/P1+), in particular for the extra stress tensor. The implementation in CimLib® is detailed and applied to quasi static loadings, which reduces to a compressible-incompressible Stokes like system. Improvement of the solver is then discussed.

The second part of the chapter describes one other approach of stabilization based on the modification of the viscosity for the bubble enrichment equation in the mixed finite element. Several applications are analyzed by using this stabilization method. A study on the stabilization influence and improvement in the numerical simulation of viscoelastic behavior is then investigated.

Finally, in the last section, a short review on computational methods for viscoelasticity in 3D in which the mixed method, the EVSS and the DEVSS will be detailed to measure the efficiency.

4.1 Improvement on the mixed velocity-pressure-displacement formulation through a complete solver

Since the results shown in chapter 3 revealed some instability problems and demonstrated the requirement of the stabilization resolution, this section will be devoted to the first stabilized method based on the complete mixed FE resolution. In this case, the complete formulation will be taken into account, meaning that bubble terms that have been neglected will be included. Furthermore, we have decided to implement a new mixed finite element solver in the CimLib library, that will allow the introduction of *n* variables that can or cannot be all enriched.

Regarding a general dynamic test, resolution of an incompressible as well as compressible viscoelastic Kelvin-Voigt model by our monolithic approach is simple enough whilst it will enlighten all potential difficulties and allow an objective validation of the approach.

The system equations to solve in the more general viscoelastic (Kelvin-Voigt model) compressible case are, as detailed previously:

$$\begin{cases} \rho\left(\dfrac{\partial v}{\partial t} + v\cdot\nabla v\right) - \nabla\cdot 2\eta_{ve}\varepsilon(v) + \nabla\left(p_e + p_v\right) = f - \nabla\cdot\tau \\ \tau = 2\mu_e\varepsilon\left(u - vdt\right) \\ \nabla\cdot u + \dfrac{1}{\lambda_e}p_e = 0 \\ \nabla\cdot v + \chi_{p_v}\left(\dfrac{\partial p_v}{\partial t} + v\nabla p_v\right) = 0 \\ \dfrac{du}{dt} = \dfrac{\partial u}{\partial t} + v\nabla u = v \end{cases} \tag{4.1}$$

The Finite Element Method is a good choice for solving those differential equations. However, within a numerical framework, severe points and difficulties can be encountered: approximation spaces must respect the *inf-sup* condition (Brezzi-Babuska) [92] [93] [94] in the case of a resolution by a mixed finite element method; predominance of the nonlinear convective terms in the momentum conservation in a Navier-Stokes flow problem or in the displacement advection equation. Both this points have been treated by appropriate stabilization techniques [95] [110]. However, one other primordial difficulty is induced by the "extra-stress τ" in the right-hand member of conservation of momentum which necessarily depends on the behavior model. Unfortunately, instabilities were observed when this extra-stress becomes important when compared with the viscous terms. The main reason behind this lack of stability could be related with the fact that, velocity (or displacement) bubble enrichment has not been considered in the formulation for this extra-stress tensor. Thus, it will be our first objective, detailed in this chapter.

During the three last decades, several papers have been done on the subject of stabilization of finite element methods in the field of computational fluid dynamics (CFD) to deal with the advection dominated phenomena and mixed field problems. Straightforward application of the Galerkin version of the finite element method to certain problems of mathematical physics and engineering yields to numerical approximations does not ensure the stability properties of the continuous problem [100]. This is the basic reason for introducing stabilized methods. Generally,

all stabilized method have the similar fundamental contribution for the advection operator on keeping the compromising accuracy, and circumventing the Babuska–Brezzi condition.

Among the full collection of stabilized finite methods, two approaches have achieved particular success. The first very popular method was firstly proposed by Arnold, Brezzi and Fortin [96] for the Stokes problem. Basically, it introduced the MINI-element where discrete finite element space for velocity V_h is enriched with space of so-called "bubble" functions V_h^b. With this philosophy, stabilized problems still have been enhanced where the bubbles from certain element-level boundary-value problems were derived. These are referred to the development in the residual-free bubble (RFB) method, presented in the works of Brezzi and colleagues [111] [100], following the so-called unusual stabilized methods by Franca et al. [112].

Another approach for the construction of stabilized methods is the variational multiscale method (VMS), introduced later by Hughes and co-workers [113] which has been widely used. Several study was investigated in VMS method as the work of Masud et al. [114] [115], a two-level variational multiscale method [116] [117], or also a three-level finite element method of Gravemeier [118]. Recent developments of residual based stabilization methods using orthogonal subscales and time dependent subscales which present promising results could be found in the works of Codina et al. [119] [120] or Hachem [121].

In principle, the philosophy of this method is different from the previous one. In fact, in the first approach, even if the fine-scales are numerically unresolvable, or uninterested in resolving, their effect on the coarse-scales, i.e. resolvable scales, must be accounted for in order to accurately calculate the coarse-scales. And, the variational multiscale method consists of two fundamental steps: the first is purely non-numerical, the original problem is decomposed into two sub-problems: the fine-scales is first solved in terms of the coarse scales, its results are then substituted into the second sub-problem which involves a modified problem only in the coarse scales. This is sometimes referred to as a subgrid-scale model. The second or final step of the VMS approach is then related to application of the Galerkin method to the modified problem as illustrated on the following diagram.

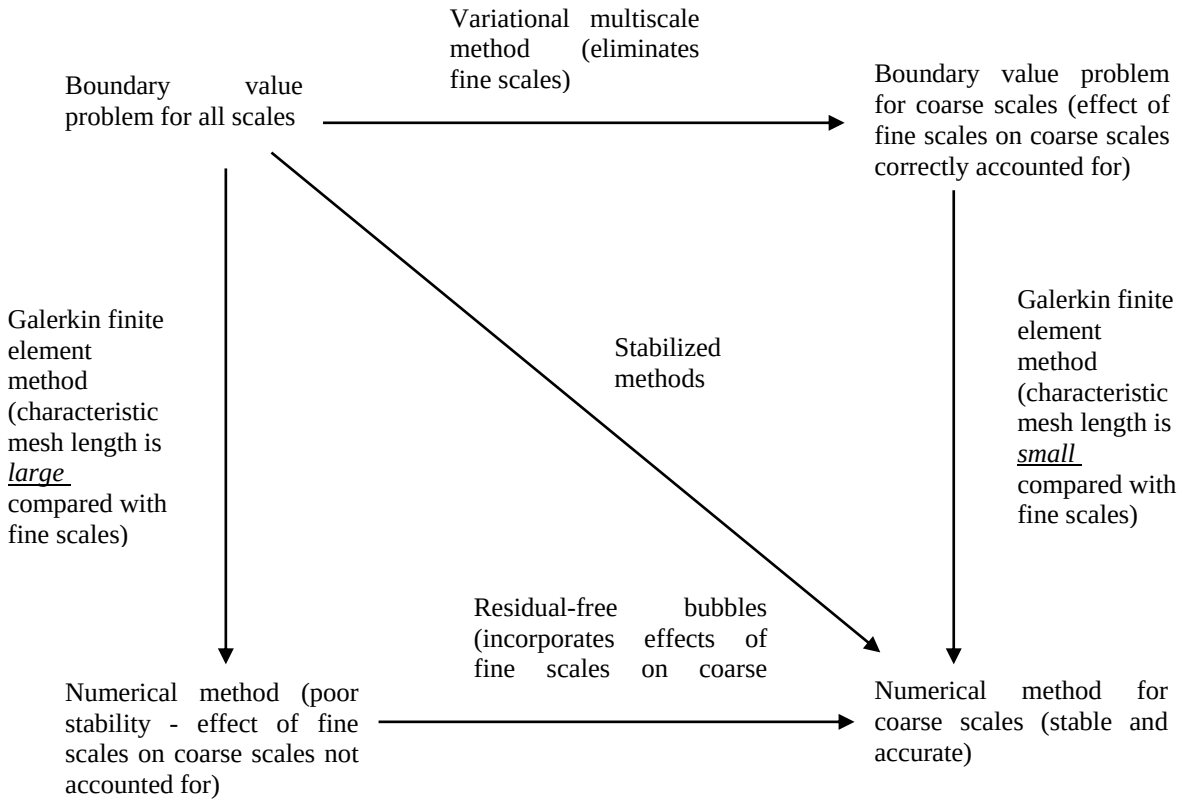


Figure 4-1: Commutative diagram of stabilized methods (after Brezzi et al [100]).

The situation can be summarized in a commutative diagram (Figure 4-1) where Brezzi and co-workers [100] showed the equivalence between these two methodologies. Note that stabilized methods interestingly may be viewed as a short-cut, diagonal path through the diagram.

The main interest of this chapter will focus on the stabilization of the solver based on the MINI element P1+/P1, where the strong form is presented in equation (4.1). The 2D finite element solver using this approach was developed by Coupez [97] [98] and [99]. The work was later accomplished for the 3D Stokes problem with the implementation in Cimlib [12], followed by an extension to transient Navier-Stokes [95]. Recently, the stabilized results for turbulent flows in the study of Hachem [110] [121], inspired by the work of Codina et al. [119] [120], have been shown as promising. This is considered as a combination of a stable MINI-element/stabilizing formulation strategy. In this sense, the present work can be considered as a manner to continue and complete those references.

4.1.1 Stabilized mixed finite elements

With the aim to build a general solver which allow resolving an incompressible as well as compressible viscoelastic Kelvin-Voigt, the equation (4.1) is simplified as described in the below equation:

$$\begin{cases} \rho\left(\frac{\partial v}{\partial t}+v\cdot\nabla v\right)-\nabla\cdot 2\eta_{ve}\varepsilon(v)+\nabla p'=f-\nabla\cdot\tau \\ \tau=2\mu_e\varepsilon\left(u-vdt\right) \\ \nabla\cdot v+\chi_{p'}\left(\frac{\partial p'}{\partial t}+v\nabla p'\right)=0 \\ \frac{du}{dt}=\frac{\partial u}{\partial t}+v\nabla u=v \end{cases} \tag{4.2}$$

where $\chi_{p'}$ represent $\chi_{p_e}=\frac{1}{\lambda_e}$ as in the compressible elastic behavior or χ_{p_v} in the compressible viscous fluid, thus the "pressure" is replaced by p'.

The discrete Galerkin problem consists therefore in solving the mixed problem (4.3):

Find $\left(u_h,v_h,p_h\right)\in\left(V_h,V_h,P_h\right)$ such that $\forall\left(\varsigma_h,w_h,q_h\right)\in\left(V_h^0,V_h^0,P_h\right)$:

$$\begin{cases} \rho\left(\frac{\partial v_h}{\partial t}+v_h\nabla v_h,w_h\right)-\left(p'_h,\nabla\cdot w_h\right)+2\eta_{ve}\varepsilon\left(v_h\right):\varepsilon\left(w_h\right)=-\tau_h:\varepsilon\left(w_h\right)+\left(f_h,w_h\right) \\ \tau_h=2\mu_e\varepsilon\left(u_h-v_hdt\right) \\ \left(-\nabla\cdot v_h,q_h\right)-\left(\chi_{p'}\left(\frac{\partial p'_h}{\partial t}+v_h\nabla p'_h\right),q_h\right)=0 \\ \left(\frac{\partial u_h}{\partial t}+v_h\nabla u_h,\varsigma_h\right)=v_h \end{cases} \tag{4.3}$$

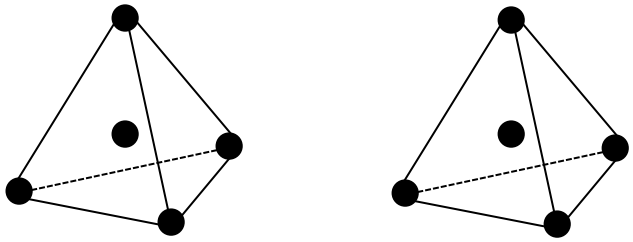
Finite element approximation (4.3) can generate instabilities because of two mains reasons:

- the first one was cited in chapter 3 which related to the compatibility of the *inf-sup* condition (Brezzi-Babuska)
- the dominance of the convective term as $v_h\nabla v_h$ in dynamic problem or $v_h\nabla u_h$, in our case where the resolution by a mixed formulation in *(u, v, p) (displacement, velocity, pressure)* is developed, in that oscillations will appear that influence the whole numerical solution

Moreover, as mentioned in chapter 3, the missing terms as the "bubble extra-stress" τ_b in the fine-scales resolution which did not allows completing a full resolution as the augmented Lagrangian method with Uzawa algorithm for the flow between two rigid particles case. Therefore, our first idea is to build a solver which completes the missing terms, i.e. a solver where the extra-stress is also enriched by a bubble function.

Furthermore, to deal with a generic problem as for example highly dynamics, not only the velocity (displacement) is enriched by addition of a degree of freedom (called bubble function) in the center of elements [98] [97], but also the pressure is enriched by a bubble function that will cure the spurious oscillations in the convection-dominated regime as well as the pressure instability. Thus, a mixed generic solver where we have the flexibility to enrich the velocity, the pressure as well as the extra-stress or the displacement will be developed.

For a better comprehension, this means that the standard finite element approximation using equal-order-linear-continuous velocity–pressure-displacement (extra-stress) variables is enriched with velocity-pressure-displacement (or extra-stress) bubble functions, i.e. the P1+/P1+ element (Figure 4-2).



Velocity interpolation Pressure interpolation

Figure 4-2: Element P1+/P1+ for velocity-pressure.

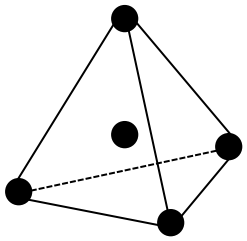


Figure 4-3: Displacement interpolation.

In this context, we consider an overlapping sum decomposition of the displacement, velocity and the pressure fields into coarse-scales and fine-scales, $u = u_h + u_h^b$, $v = v_h + v_h^b$, and $p' = p'_h + p'^b_h$ where u_h, v_h and p'_h are the linear part of the displacement, velocity and pressure; u_h^b, v_h^b and p'^b_h are the bubble displacement, velocity and pressure. Likewise, we keep the same decomposition for the weighting functions $\varsigma = \varsigma_h + \varsigma_h^b$, $w = w_h + w_h^b$ and $q = q_h + q_h^b$.

We can perform the enrichment of the functional spaces as follows:

$$V = V_h \oplus V_h^b,\ V_0 = V_{h,0} \oplus V_{h,0}^b \text{ and } P = P_h \oplus P_h^b \tag{4.4}$$

where the finite element space P_h^b has been added at what was shown in chapter 3, defined as:

$$P_h^b = \left\{ p_h^b, p_{h|K}^b \in P_k\left(K_i\right) \bigcap H_0^1(K_i), i = 1,...D \quad \forall K \in \Omega_K \right\} \tag{4.5}$$

Find $\left(u_h, v_h, p_h\right) \in \left(V_h, V_h, P_h\right)$ such that $\forall \left(\varsigma_h, w_h, q_h\right) \in \left(V_h^0, V_h^0, P_h\right)$:

$$\begin{cases} \rho\left(\dfrac{\partial\left(v_h+v_h^b\right)}{\partial t}+\left(v_h+v_h^b\right)\nabla\left(v_h+v_h^b\right),w_h+w_h^b\right)-\left(p_h'+p_h'^b,\nabla\cdot\left(w_h+w_h^b\right)\right) \\ +2\eta_{ve}\varepsilon\left(v_h+v_h^b\right):\varepsilon(w_h+w_h^b)=-\left(\tau_h+\tau_h^b\right):\varepsilon\left(w_h+w_h^b\right)+\left(f_h,w_h+w_h^b\right) \\ \tau_h=2\mu_e\varepsilon\left(u_h-v_h dt\right)\quad and\quad \tau_h^b=2\mu_e\varepsilon\left(u_h^b-v_h^b dt\right) \\ \left(-\nabla\cdot\left(v_h+v_h^b\right),q_h+q_h^b\right)-\left(\chi_{p'}\left(\dfrac{\partial p_h'}{\partial t}+\left(v_h+v_h^b\right)\nabla\left(p_h'+p_h'^b\right)\right),q_h+q_h^b\right)=0 \\ \left(\dfrac{\partial\left(u_h+u_h^b\right)u_h}{\partial t}+\left(v_h+v_h^b\right)\nabla\left(u_h+u_h^b\right),\varsigma_h+\varsigma_h^b\right)=\left(v_h+v_h^b\right) \end{cases} \tag{4.6}$$

Thus, we obtain the system equations which can be split into two sub-problems by separating the two scales, called the coarse-scale problem:

$$\begin{cases} \rho\left(\dfrac{\partial\left(v_h+v_h^b\right)}{\partial t},w_h\right)+\rho\left(\left(v_h+v_h^b\right)\nabla\left(v_h+v_h^b\right),w_h\right)-\left(p_h'+p_h'^b,\nabla.w_h\right) \\ +2\eta_{ve}\varepsilon\left(v_h\right):\varepsilon\left(w_h\right)=\left(f_h,w_h\right)-\tau_h:\varepsilon\left(w_h\right) \\ \tau_h=2\mu_e\varepsilon\left(u_h-v_h dt\right) \\ \left(-\nabla\cdot\left(v_h+v_h^b\right),q_h\right)-\left(\chi_{p'}\left(\dfrac{\partial(p_h'+p_h'^b)}{\partial t}+\left(v_h+v_h^b\right)\nabla\left(p_h'+p_h'^b\right)\right),q_h\right)=0 \\ \left(\dfrac{\partial\left(u_h+u_h^b\right)}{\partial t}+\left(v_h+v_h^b\right)\nabla\left(u_h+u_h^b\right),\varsigma_h\right)=v_h \end{cases} \tag{4.7}$$

and the fine-scale problem:

$$\begin{cases} \rho\left(\dfrac{\partial\left(v_h+v_h^b\right)}{\partial t},w_h^b\right)+\rho\left(\left(v_h+v_h^b\right)\nabla\left(v_h+v_h^b\right),w_h^b\right)-\left(p_h'+p_h'^b,\nabla.w_h^b\right) \\ +2\eta_{ve}\varepsilon\left(v_h^b\right):\varepsilon\left(w_h^b\right)=\left(f_h,w_h^b\right)-\tau_h^b:\varepsilon\left(w_h^b\right) \\ \tau_h^b=2\mu_e\varepsilon\left(u_h^b-v_h^b dt\right) \\ \left(-\nabla\cdot(v_h+v_h^b),q_h^b\right)-\left(\chi_{p'}\left(\dfrac{\partial(p_h'+p_h'^b)}{\partial t}+(v_h+v_h^b)\nabla\left(p_h'+p_h'^b\right)\right),q_h^b\right)=0 \\ \left(\dfrac{\partial\left(u_h+u_h^b\right)}{\partial t}+\left(v_h+v_h^b\right)\nabla\left(u_h+u_h^b\right),\varsigma_h^b\right)=v_h^b \end{cases} \tag{4.8}$$

4.1.1.1 Time scheme

As previously, we introduce a coupling resolution scheme in which the resolution of displacement (see equations (4.17)) was separated from the resolution of velocity and pressure.

$$\begin{cases} \rho\left(\dfrac{v_{h.i+1}+v^b_{h,i+1}}{\Delta t},w_h\right)^{n+1}+\rho\left(v_{h.i}\nabla v_{h.i+1}+v_{h.i+1}\nabla v_{h.i}+v^b_{h,i}\nabla v^b_{h,i+1}+v^b_{h,i+1}\nabla v^b_{h,i},w_h\right)^{n+1} \\ +\rho\left(v_{h,i}\nabla v^b_{h,i+1}+v_{h,i+1}\nabla v^b_{h,i}+v^b_{h,i+1}\nabla v_{h,i}+v^b_{h,i}\nabla v_{h,i+1},w_h\right)^{n+1} \\ -\left(p'_{h,i+1}+p'^b_{h,i+1},\nabla.w_h\right)^{n+1}+2\eta_{ve}\varepsilon\left(v_{h.i+1}\right)^{n+1}:\varepsilon\left(w_h\right)=\left(f_h,w_h\right)^{n+1}+\rho\left(\dfrac{v_h+v^b_h}{\Delta t},w_h\right)^{n} \\ +\rho\left(v_{h.i}\nabla v_{h.i}+v^b_{h,i}\nabla v^b_{h,i}+v_{h,i}\nabla v^b_{h,i}+v^b_{h,i}\nabla v_{h,i},w_h\right)^{n+1}-2\mu\varepsilon\left(u_h\right)^{n}:\varepsilon\left(w_h\right) \\ \left(-\nabla\cdot\left(v_{h.i+1}+v^b_{h,i+1}\right)^{n+1},q_h\right)-\left(\dfrac{\chi_{p'}}{\Delta t}\left(p'_{h,i+1}+p'^b_{h,i+1}\right)^{n+1},q_h\right)=-\left(\dfrac{\chi_{p'}}{\Delta t}\left(p'_h+p'^b_h\right)^{n},q_h\right) \\ -\left(\left(v_h+v^b_h\right)^{n}\nabla\left(p'_h+p'^b_h\right)^{n},q_h\right) \end{cases} \tag{4.9}$$

and the fine-scale

$$\begin{cases} \rho\left(\dfrac{v_{h.i+1}+v^b_{h,i+1}}{\Delta t},w^b_h\right)^{n+1}+\rho\left(v_{h.i}\nabla v_{h.i+1}+v_{h.i+1}\nabla v_{h.i}+v^b_{h,i}\nabla v^b_{h,i+1}+v^b_{h,i+1}\nabla v^b_{h,i},w^b_h\right)^{n+1} \\ +\rho\left(v_{h,i}\nabla v^b_{h,i+1}+v_{h,i+1}\nabla v^b_{h,i}+v^b_{h,i+1}\nabla v_{h,i}+v^b_{h,i}\nabla v_{h,i+1},w^b_h\right)^{n+1}-\left(p'_{h,i+1}+p'^b_{h,i+1},\nabla.w^b_h\right)^{n+1} \\ +2\eta_{ve}\varepsilon\left(v^b_{h.i+1}\right)^{n+1}:\varepsilon\left(w^b_h\right)=\left(f_h,w^b_h\right)^{n+1}+\rho\left(\dfrac{v_h+v^b_h}{\Delta t},w^b_h\right)^{n} \\ +\rho\left(v_{h.i}\nabla v_{h.i}+v^b_{h,i}\nabla v^b_{h,i}+v_{h,i}\nabla v^b_{h,i}+v^b_{h,i}\nabla v_{h,i},w^b_h\right)^{n+1}-2\mu\varepsilon\left(u^b_h\right)^{n}:\varepsilon\left(w^b_h\right) \\ \left(-\nabla\cdot\left(v_{h.i+1}+v^b_{h,i+1}\right)^{n+1},q^b_h\right)-\left(\dfrac{\chi_{p'}}{\Delta t}\left(p'_{h,i+1}+p'^b_{h,i+1}\right)^{n+1},q^b_h\right)=-\left(\dfrac{\chi_{p'}}{\Delta t}\left(p'_h+p'^b_h\right)^{n},q^b_h\right) \\ -\left(\left(v_h+v^b_h\right)^{n}\nabla\left(p'_h+p'^b_h\right)^{n},q^b_h\right) \end{cases} \tag{4.10}$$

We remark that the convective term $v\nabla v$ is calculated implicitly through a Newton-Raphson procedure, which uses the solution at the previous iteration through the following equation:

$$v^{n+1}_{h,i+1}=v^{n+1}_{h,i}+\left(v^{n+1}_{h,i+1}-v^{n+1}_{h,i}\right) \tag{4.11}$$

$$v^{b,n+1}_{h,i+1}=v^{b,n+1}_{h,i}+\left(v^{b,n+1}_{h,i+1}-v^{b,n+1}_{h,i}\right) \tag{4.12}$$

where $v_{h,i}$ and $v^b_{h,i}$ are a known velocity and known bubble velocity, calculated by the previous iteration of the Newton-Raphson scheme.

To linearize the nonlinear terms $v_h\nabla v_h$, we apply a Newton method that consists in neglecting terms of second order, and to iterate the linear system thus obtained until convergence:

$$\begin{aligned} v_{h,i+1}^{n+1}\nabla v_{h,i+1}^{n+1} &= \left(v_{h,i}+\left(v_{h,i+1}-v_{h,i}\right)\right)^{n+1}\nabla\left(v_{h,i}+\left(v_{h,i+1}-v_{h,i}\right)\right)^{n+1} \\ &= \left(v_{h,i}\nabla v_{h,i+1}+v_{h,i+1}\nabla v_{h,i}-v_{h,i}\nabla v_{h,i}+\left(v_{h,i+1}-v_{h,i}\right)\nabla\left(v_{h,i+1}-v_{h,i}\right)\right)^{n+1} \\ &\approx v_{h,i}^{n+1}\nabla v_{h,i+1}^{n+1}+v_{h,i+1}^{n+1}\nabla v_{h,i}^{n+1}-v_{h,i}^{n+1}\nabla v_{h,i}^{n+1} \end{aligned} \tag{4.13}$$

$$\left(v_{h,i+1}^{b}\nabla v_{h,i+1}^{b}\right)^{n+1} \approx \left(v_{h,i}^{b}\nabla v_{h,i+1}^{b}+v_{h,i+1}^{b}\nabla v_{h,i}^{b}-v_{h,i}^{b}\nabla v_{h,i}^{b}\right)^{n+1} \tag{4.14}$$

$$\begin{aligned} \left(v_{h,i+1}\nabla v_{h,i+1}^{b}\right)^{n+1} &= \left(v_{h,i}+\left(v_{h,i+1}-v_{h,i}\right)\right)^{n+1}\nabla\left(v_{h,i}^{b}+\left(v_{h,i+1}^{b}-v_{h,i}^{b}\right)\right)^{n+1} \\ &\approx \left(v_{h,i}\nabla v_{h,i+1}^{b}+v_{h,i+1}\nabla v_{h,i}^{b}-v_{h,i}\nabla v_{h,i}^{b}\right)^{n+1} \end{aligned} \tag{4.15}$$

$$\left(v_{h,i+1}^{b}\nabla v_{h,i+1}\right)^{n+1} \approx \left(v_{h,i+1}^{b}\nabla v_{h,i}+v_{h,i}^{b}\nabla v_{h,i+1}-v_{h,i}^{b}\nabla v_{h,i}\right)^{n+1} \tag{4.16}$$

Concerning the resolution of the displacement which was separated from the resolution of velocity and pressure, standard Galerkin method is not suitable for solving a convection dominated problem as our problem, where the relation between displacement-velocity is solved thorough the convected equations (4.21) and (4.22). The main reason comes from the property centered difference of the standard Galerkin method: oscillations appear in the solution when the problem has a dominant hyperbolic character. Therefore, the need of a stabilization method is essential, and we can find SUPG or Residual-Free Bubbles (RFB) [111] [122].

With regard to the linear hyperbolic problem, the weak form of an implicit scheme for the convected problem in the displacement resolution is as follows:

$$\left(\frac{u_h}{\Delta t},w_h\right)^{n+1}+\left(v_h\nabla u_h,w_h\right)^{n+1}=\left(\frac{u_h}{\Delta t},w_h\right)^{n}+\left(v_h,w_h\right)^{n+1} \tag{4.17}$$

Using SUPG, one of the most popular stabilization method introduced by Brooks [123], the implicit weak form (4.17) can be developed as:

$$\begin{aligned} &\left(\frac{u_h}{\Delta t},w_h\right)^{n+1}+\left(v_h\nabla u_h,w_h\right)^{n+1}+\tau_k^{SUPG}\left(\frac{u_h}{\Delta t},v_h\nabla w_h\right)^{n+1}+\tau_k^{SUPG}\left(v_h\nabla u_h,v_h\nabla w_h\right)^{n+1} \\ &=\left(\frac{u_h}{\Delta t},w_h\right)^{n}+\tau_k^{SUPG}\left(\frac{u_{h,t-\Delta t}}{\Delta t},v_h\nabla w_h\right)^{n+1}+\left(v_h,w_h\right)^{n+1} \end{aligned} \tag{4.18}$$

where the test function is constructed as following:

$$\tilde{w}_h = w_h+\tau_k^{SUPG}v_h\nabla w_h \tag{4.19}$$

This substitution adds a numerical diffusion, but only in the upwind direction, that is the axis of the convected velocity. The stabilization parameter τ_k^{SUPG} (constant by element) depends on the mesh size and the velocity norm, generally we take [123]:

$$\tau_k^{SUPG} = \frac{1}{2}\frac{h_\kappa}{|v_{|\kappa}|} \tag{4.20}$$

where $v_{|\kappa}$ is a constant velocity on the element κ by taking the average velocity of all nodes of this element.

Furthemore, displacement resolution can also done through the resolution in the coarse-scale (4.21) and in the fine-scale (4.22):

$$\left(\frac{u_h + u_h^b}{\Delta t}, w_h\right)^{n+1} + \left(\left(v_h + v_h^b\right)\nabla\left(u_h + u_h^b\right), w_h\right)^{n+1} = \left(\frac{u_h + u_h^b}{\Delta t}, w_h\right)^{n} + \left(v_h + v_h^b, w_h\right)^{n+1} \tag{4.21}$$

$$\left(\frac{u_h + u_h^b}{\Delta t}, w_h^b\right)^{n+1} + \left(\left(v_h + v_h^b\right)\nabla\left(u_h + u_h^b\right), w_h^b\right)^{n+1} = \left(\frac{u_h + u_h^b}{\Delta t}, w_h^b\right)^{n} + \left(v_h + v_h^b, w_h^b\right)^{n+1} \tag{4.22}$$

This method reduces to the RFB method, a more detailed description can be found in [95] [110].

As described in the above section, a complete formulation on which the velocity and the pressure are resolved in both the fine-scale and the coarse-scale, is coupled with the resolution of the displacement advection equation. In spite of significantly increasing computational cost, our methodology presents several advantages. In the literature, the fine-scale is often unresolved because the coupled resolution in the coarse-scale and the fine-scale for both the velocity and the pressure is quite complicated. Therefore, the static condensation step is used to substitute the fine-scale solution into the large-scale problem providing additional terms [124] [125]. However, due to the complexity of substituting the complete fine-scale solution into the large-scale, some terms in the fine-scale must be neglected. Thanks to our solver, we have the flexibility to solve a complex problem where a complete formulation without neglecting any terms or returning to classical methods where the static condensation is performed.

4.1.1.2 Matrix formulation

Let us summarize and rewrite the resulting variational stabilized formulation for the resolution of velocity and pressure in the usual matrix scheme (4.23) where the previous scheme in (4.9) and (4.10) can be put naturally under the matrix form that remains to be solved:

$$\begin{pmatrix} A_{vv} & A^t_{vv_b} & A^t_{vp} & A^t_{vp_b} \\ A_{vv_b} & A_{v_b v_b} & A^t_{v_b p} & A^t_{v_b p_b} \\ A_{vp} & A_{v_b p} & A_{pp} & A^t_{pp_b} \\ A_{vp_b} & A_{v_b p_b} & A_{pp_b} & A_{p_b p_b} \end{pmatrix} \begin{pmatrix} v \\ v_b \\ p \\ p_b \end{pmatrix} = \begin{pmatrix} B_v \\ B_{v_b} \\ B_p \\ B_{p_b} \end{pmatrix} \tag{4.23}$$

where:

$$A_{vv} = \rho\left(\frac{v_{h.i+1}}{\Delta t}, w_h\right)^{n+1} + \rho\left(v_{h.i}\nabla v_{h.i+1} + v_{h.i+1}\nabla v_{h.i}, w_h\right)^{n+1} + \left(2\eta_{ve}\varepsilon(v_{h,i+1}) : \varepsilon(w_h)\right)^{n+1}$$

$$
\begin{aligned}
&A_{v_b v_b} = \rho\left(\frac{v^b_{h,i+1}}{\Delta t}, w_h\right)^{n+1} + \rho\left(v^b_{h,i}\nabla v^b_{h,i+1} + v^b_{h,i+1}\nabla v^b_{h,i}, w_h\right)^{n+1} + 2\eta_{ve}\varepsilon\left(v^b_{h.i+1}\right)^{n+1} : \varepsilon\left(w^b_h\right)\\
&A^t_{vv_b} = \rho\left(\frac{v^b_{h,i+1}}{\Delta t}, w_h\right)^{n+1} + \rho\left(v^b_{h,i}\nabla v^b_{h,i+1} + v^b_{h,i+1}\nabla v^b_{h,i}, w_h\right)^{n+1}\\
&+\rho\left(v_{h,i}\nabla v^b_{h,i+1} + v_{h,i+1}\nabla v^b_{h,i} + v^b_{h,i+1}\nabla v_{h,i} + v^b_{h,i}\nabla v_{h,i+1}, w_h\right)^{n+1}\\
&A_{vv_b} = \rho\left(\frac{v_{h.i+1}}{\Delta t}, w^b_h\right)^{n+1} + \rho\left(v_{h.i}\nabla v_{h.i+1} + v_{h.i+1}\nabla v_{h.i}, w^b_h\right)^{n+1}\\
&+\rho\left(v_{h,i}\nabla v^b_{h,i+1} + v_{h,i+1}\nabla v^b_{h,i} + v^b_{h,i+1}\nabla v_{h,i} + v^b_{h,i}\nabla v_{h,i+1}, w^b_h\right)^{n+1}\\
&A_{pp} = -\left(\frac{\chi_{p'}}{\Delta t}p'_{h,i+1}, q_h\right)^{n+1} \quad A^t_{pp_b} = -\left(\frac{\chi_{p'}}{\Delta t}p'^b_{h,i+1}, q_h\right)^{n+1} \quad A_{p_b p_b} = -\left(\frac{\chi_{p'}}{\Delta t}p'^b_{h,i+1}, q^b_h\right)^{n+1}\\
&A^t_{vp} = -\left(p'_{h,i+1}, \nabla\cdot w_h\right)^{n+1} \quad A^t_{vp_b} = -\left(p'^b_{h,i+1}, \nabla\cdot w_h\right)^{n+1} \quad A^t_{v_b p_b} = -\left(p'^b_{h,i+1}, \nabla\cdot w^b_h\right)^{n+1} \quad A^t_{v_b p} = -\left(p'_{h,i+1}, \nabla\cdot w^b_h\right)^{n+1}
\end{aligned}
\tag{4.24}
$$

and

$$
\begin{aligned}
&B_v = \left(f_h, w_h\right)^{n+1} + \rho\left(\frac{v_{h,t-\Delta t} + v^b_{h,t-\Delta t}}{\Delta t}, w_h\right)^n + \rho\left(v_{h.i}\nabla v_{h.i} + v^b_{h,i}\nabla v^b_{h,i} + v_{h,i}\nabla v^b_{h,i} + v^b_{h,i}\nabla v_{h,i}, w_h\right)^{n+1}\\
&-2\mu\varepsilon\left(u_h\right)^n : \varepsilon\left(w_h\right)\\
&B_{v_b} = \left(f_h, w^b_h\right)^{n+1} + \rho\left(\frac{v_{h,t-\Delta t} + v^b_{h,t-\Delta t}}{\Delta t}, w^b_h\right)^n + \rho\left(v_{h.i}\nabla v_{h.i} + v^b_{h,i}\nabla v^b_{h,i}, w^b_h\right)^{n+1} - 2\mu\varepsilon\left(u_h\right)^n : \varepsilon\left(w^b_h\right)\\
&B_p = -\left(\frac{\chi_{p'}}{\Delta t}\left(p'_h + p'^b_h\right), q_h\right)^n - \left(\left(v_h + v^b_h\right)\nabla\left(p'_h + p'^b_h\right), q_h\right)^n\\
&B_{p_b} = -\left(\frac{\chi_{p'}}{\Delta t}\left(p'_h + p'^b_h\right), q^b_h\right)^n + \left(\left(v_h + v^b_h\right)\nabla\left(p'_h + p'^b_h\right), q^b_h\right)^n
\end{aligned}
\tag{4.25}
$$

Please note that the resolution of the displacement was separated from the resolution of velocity-pressure.

With the mixed developed solver, both the velocity and the pressure spaces are enriched by a bubble space that eliminates the spurious oscillations in the convection-dominated regime as well as the pressure instability which may appear in dynamic problems [111] [119] [123] [124]. It is clear that taking into account the resolution of both fine scales and large scales allows introducing all stabilizing terms in the matrices. The effect of the fine-scale pressure is implicitly taken into account on the resolution by mixed FE with P1+/P1+ element.

Furthermore, using this solver we may adopt the most convenient method of resolution: the resolution with both the velocity and pressure enriched; or use of the MINI-element; or flexibility to choose between the full resolution in fine-scales and coarse-scales, with also the condensation of fine-scales. Later on, several numerical applications will be performed to verify the benefits of the proposed scheme.

4.1.2 Comparison between the old solver NSTC and the new SMC

This section is devoted to the evaluation of our new solver, named "Stokes-Mixte-Complet" (SMC) and its implementation in the library FE CimLib®, mainly in terms of efficiency (in what concerns the quality of the results, the subsequent sections will summarize it). The study focuses on the assembly time, the resolution time, the number of iterations compared to the old solver, named "Navier-Stokes-Test-Compressible" (NSTC).

Performance tests are done using the tensile test case. We highlight that, in this test case, the resolution formulation of the tensile test was modified then compared with the previous one showed in chapter 3.

One has to note that the resolution algorithms of the mass conservation equation can be written:

$$-\nabla_{x^{n+1}}\cdot\left(v^{n+1}\right)=\boxed{\frac{\nabla_{x^{n+1}}\cdot\left(u^{n}\right)}{\Delta t}}\rightarrow \text{Missing term in the tensile test in chapter 3} \tag{4.26}$$

For better comprehension, the above equation can be developed as following:

$$-\nabla_{x^{n+1}}\cdot\left(v^{n+1}\right)=\frac{\nabla_{x^{n+1}}\cdot\left(u^{n}\right)}{\Delta t}$$

$$\Leftrightarrow \nabla_{x^{n+1}}\cdot\left(u^{n}\right)-\nabla_{x^{n+1}}\cdot\left(v^{n+1}\right)\Delta t=0 \tag{4.27}$$

$$\Leftrightarrow \nabla_{x^{n+1}}\cdot\left(u^{n+1}\right)=0$$

which returns to the full formulation of the mass conservation equation for the incompressible problem where the mass conservation equation is well described for the resolution of the displacement and not that of the resolution of the velocity as showed previously.

Thus, in an incremental Lagrangian context, we solve at each increment the equation:

$$\begin{cases}\nabla_{x^{n+1}}\cdot 2\mu_e\Delta t\varepsilon\left(v^{n+1}\right)-\nabla_{x^{n+1}}p'^{n+1}=-\nabla_{x^{n+1}}\cdot 2\mu_e\varepsilon\left(u^{n}\right)\\ \nabla\cdot\left(v^{n+1}\right)=-\dfrac{\nabla_{x^{n+1}}\cdot\left(u^{n}\right)}{\Delta t}\\ u^{n+1}=u^{n}+v^{n+1}\Delta t\\ v=v_{imposed}\ in\ \Gamma_{\inf}\ and\ v=0\ in\ \Gamma_{\sup}\end{cases} \tag{4.28}$$

Meshes of the samples used are displayed in Figure 4-4.

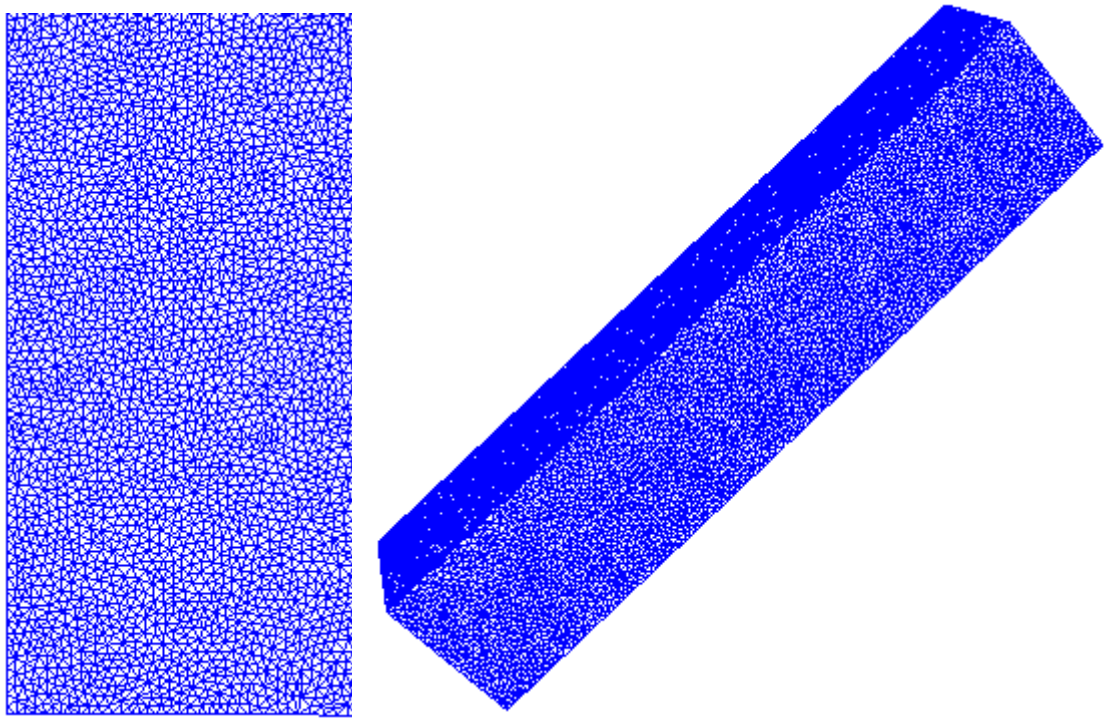


Figure 4-4: Mesh representation of the sample in the tensile test in 2D (zoom of a part of the sample) and 3D. The sample in 2D contains 142.130 nodes/282.472 elements, and that in 3D contains 142.522 nodes/783.324 elements.

Inertia effects were neglected and the enriched pressure is not necessary. Thus, we can put easily the "bubble pressure" p_b' at zero for the simulations, leading to the mixed finite element method with the Mini-element P1+/P1, where only the velocity is enriched by a bubble function. The mixed formulation in three fields *(u, v, p)* was separated by a weak coupling between the resolution of the two fields *(v, p)* with the P1+/P1 interpolation and that of the displacement *(u)* (or extra-stress).

	New (StokesMixteComplet)				Old (NavierStokesTestCompressible)			
Assembly time	1.22	2.37	4.59	7.18	1.52	3.08	7.14	9.99
Resolution time	319.9	463.96	728.9	1071	126.46	195.49	303.54	461.96
Number of iterations	2659	2087	1874	1673	2260	2066	1873	1627
Cost time/iterations	0.12	0.22	0.39	0.64	0.056	0.095	0.16	0.28
Number of processors	8	4	2	1	8	4	2	1
Number of nodes/elements	142.130 Nodes/282.472 Elements							

Table 4-1: Comparison between the NSTC and the SMC solvers in 2D.

	New (SMC)				Old (NSTC)			
Assembly time	7.06	13.89	27.57	44	8.32	14.44	28.45	55.85
Resolution time	1189.2	1507.9	2757.2	2999	336.11	537.21	1025.95	1430.6
Number of iterations	1503	1024	792	482	1019	782	687	478
Cost time/iterations	0.79	1.47	3.48	6.22	0.33	0.69	1.49	2.99
Number of processors	8	4	2	1	8	4	2	1
Number of nodes/elements	142.522 Nodes/783.324 Element							

Table 4-2: Comparison between the NSTC and the SMC solvers in 3D.

Tables 4-1 and 4-2 summarize the results of simulations using from one processor to eight processors in parallel, in two dimensions as well as in three dimensions.

Firstly, with regard to the assembly time, it is clear that the new solver (SMC) is quicker than the old one (NSTC), since it skips the condensation step mentioned previous in the chapter 3 (see equation (3.24)). In fact, this step concerns a matrix product and its inverse which generates a considerable CPU time compared to the direct resolution with the new SMC solver.

However, assembly time represents a low weight compared with the resolution time. In this late case, the new solver is about two times in 2D and three times in 3D slower than the old solver. That is justified by the fact that, in the new solver, the fine-scales are also solved, which consists in a considerable number of added unknowns in the system of resolution.

An important factor is related to the number of iterations which is relative to the preconditioning used. In consequence, the number of iterations in two dimensions is quasi-identical for the new solver SMC and the old solver NSTC, which justifies our theory and methodology. And the slight difference between the old solver and the new in 2D (or 3D) in parallel is also acceptable. This can be explained by the fact that the resolution system by the new solver is more complex than that of the new solver. In fact, the fine-scales are resolved in the new SMC solver, thus we need to treat more on the neighborhood nodes and elements interfaces which cause more difficulty for the preconditioning resolution.

4.1.3 Application in the elasticity case: comparison with the old solver

4.1.3.1 Incompressible elastic tensile test case by the single time step resolution

As mentioned in the above section, a perfect elastic recovery requires the full resolution of the incompressible elastic tensile test by completing the solver with the missing term shown previously. For a better comprehension, please follow the demonstration below. First, if we consider an incompressible recovery modeling as detailed in chapter 3, the resolution matrix is written:

$$\begin{pmatrix} A^1_{vv} & 0 & {}^tA^1_{vp} \\ 0 & A^1_{v_bv_b} & {}^tA^1_{v_bp} \\ A^1_{vp} & A^1_{v_bp} & 0 \end{pmatrix} \begin{pmatrix} u^1 \\ u^1_b \\ p^1 \end{pmatrix} = \begin{pmatrix} -A^1_{vv} \times u^0 \\ -A^1_{v_bv_b} \times u^0_b \\ 0 \end{pmatrix} \tag{4.29}$$

In order to keep the presentation and demonstration simple, we show only the resolution by one time step resolution which returns to the resolution in displacement-pressure *(u-p).* Consequently, the resolution of the matrix returns to find $\left(u^1, u^1_b, p^1\right)$ which satisfies:

$$\begin{cases} A^1_{vv} \times u^1 + {}^tA^1_{vp} \times p^1 = -A^1_{vv} \times u^0 \\ A^1_{v_bv_b} \times u^1_b + {}^tA^1_{v_bp} \times p^1 = -A^1_{v_bv_b} \times u^0_b \\ A^1_{vp} \times u^1 + A^1_{v_bp} \times u^1_b = 0 \end{cases} \tag{4.30}$$

with u^1, u^1_b and p are the displacement, bubble displacement and the pressure in recovery. This can be deduced from the following system by the condensation u^1_b in the second equation:

$$\begin{cases} u^1 = -u^0 - \left(A^1_{vv}\right)^{-1} \times {}^tA^1_{vp} \times p^1 \\ u^1_b = -u^0_b - \left(A^1_{v_bv_b}\right)^{-1} \times {}^tA^1_{v_bp} \times p^1 \\ A^1_{vp} \times \left[-u^0 - \left(A^1_{vv}\right)^{-1} \times {}^tA^1_{vp} \times p^1\right] - A^1_{v_bp} \times \left[-u^0_b - \left(A^1_{v_bv_b}\right)^{-1} \times {}^tA^1_{v_bp} \times p^1\right] = 0 \end{cases} \tag{4.31}$$

Finally, we can easily find the solution displayed in system (4.32) where $u^1 \neq -u^0$, meaning there is no reason for the deformed objet to go back to its original position.

$$\begin{cases} u^1 = -u^0 - \left(A^1_{vv}\right)^{-1} \times {}^tA^1_{vp} \times p^1 \\ u^1_b = -u^0_b - \left(A^1_{v_bv_b}\right)^{-1} \times {}^tA^1_{v_bp} \times p^1 \\ p^1 = -\left[A^1_{vp} \times \left(A^1_{vv}\right)^{-1} \times {}^tA^1_{vp} + A^1_{vp} \times \left(A^1_{v_bv_b}\right)^{-1} \times {}^tA^1_{v_bp}\right]^{-1} \left(A^1_{vp} \times u^0 + A^1_{v_bp} \times u^0_b\right) \end{cases} \tag{4.32}$$

Therefore, the missing term is numerically required to get a perfect recovery process which will be demonstrated immediately in the section below.

We remind the algorithm under loading is as follows:

$$\begin{cases} \nabla_{x^0} \cdot 2\mu_e \varepsilon\left(u^0\right) - \nabla_{x^0} p'^0 = 0 \\ -\nabla_{x^0} \cdot \left(u^0\right) = 0 \\ u = u^0 \\ u = u_{imposed} \text{ in } \Gamma_{\inf} \text{ and } u = 0 \text{ in } \Gamma_{\sup} \end{cases} \tag{4.33}$$

The configuration is updated by moving the mesh:

$$x^0 + u^0 \Rightarrow x^1 \tag{4.34}$$

Then, the recovery process is modeled:

$$\begin{cases} \nabla_{x^1} \cdot 2\mu_e \varepsilon\left(u^1\right) - \nabla_{x^1} p'^1 = -\nabla_{x^1} \cdot 2\mu_e \varepsilon\left(u^0\right) \\ -\nabla_{x^1} \cdot \left(u^1\right) = \nabla_{x^1} \cdot \left(u^0\right) \\ u = u^0 + u^1 \\ u = -u_{imposed} \ in \ \Gamma_{\inf} \ and \ u = 0 \ in \ \Gamma_{\sup} \end{cases} \tag{4.35}$$

with u^0 and u^1 are the displacement solution under loading and unloading. We can summarize the resolution during loading in the usual matrix form:

$$\begin{pmatrix} A^0_{vv} & 0 & {}^tA^0_{vp} \\ 0 & A^0_{v_b v_b} & {}^tA^0_{v_b p} \\ A^0_{vp} & A^0_{v_b p} & 0 \end{pmatrix} \begin{pmatrix} u^0 \\ u^0_b \\ p^0 \end{pmatrix} = \begin{pmatrix} 0 \\ 0 \\ 0 \end{pmatrix} \tag{4.36}$$

Now, if we add the missing term, the resolution matrix in unloading can be rewritten as:

$$\begin{pmatrix} A^1_{vv} & 0 & {}^tA^1_{vp} \\ 0 & A^1_{v_b v_b} & {}^tA^1_{v_b p} \\ A^1_{vp} & A^1_{v_b p} & 0 \end{pmatrix} \begin{pmatrix} u^1 \\ u^1_b \\ p^1 \end{pmatrix} = \begin{pmatrix} -A^1_{vv} \times u^0 \\ -A^1_{v_b v_b} \times u^0_b \\ -A^1_{vp} \times u^0 - A^1_{v_b p} \times u^0_b \end{pmatrix} \tag{4.37}$$

Bubble extra-stress

Missing term in coarse-scale

Missing term in fine-scale

Since the fine-scales are unresolved in our previously implemented solver (NSTC), their effects are remained only in the coarse-scales. Therefore the appearance of the "bubble extra-stress" and the "missing term" generates a true difficulty with respect to the implementation, since it obliges the storage or the recalculation of the bubble values (of velocity or displacement, for example). Thanks to our development, this is avoided, since there is no condensation of the bubble terms and their values are directly computed. Furthermore, expansion of our methodology to modeling of a complex behavior (like the viscoelastic one, with even one other equation on the extra-stress tensor) would imply to add, as a separate degree of freedom, the bubble extra-stress to the NSTC solver. Fortunately, this work is implicit using the new solver (SMC).

Therefore, in the following section, in order to justify the influence of the missing terms (bubble extra-stress and missing term in fine-scales) to the stabilization of the numerical simulation, we will compare the results obtained by the two solvers in the incompressible tensile test.

First, let us demonstrate why the deformed incompressible elastic specimen can come back to its original shape in spite of the resolution by the old solver NSTC where the bubble extra-stress and the missing term in fine-scales was put to zero:

$$\begin{cases} A_{vv}^1 \times u^1 + {}^t A_{vp}^1 \times p^1 = -A_{vv}^1 \times u^0 \\ A_{v_b v_b}^1 \times u_b^1 + {}^t A_{v_b p}^1 \times p^1 = 0 \\ A_{vp}^1 \times u^1 + A_{v_b p}^1 \times u_b^1 = -A_{vp}^1 \times u^0 \end{cases} \tag{4.38}$$

By replacing the u^1 and u_b^1 from two first equations to the last equation, the system can be rewritten:

$$\begin{cases} u^1 = -u^0 - \left(A_{vv}^1\right)^{-1} \times {}^t A_{vp}^1 \times p^1 \\ u_b^1 = -\left(A_{v_b v_b}^1\right)^{-1} \times {}^t A_{v_b p}^1 \times p^1 \\ -A_{vp}^1 \times \left[u^0 + \left(A_{vv}^1\right)^{-1} \times {}^t A_{vp}^1 \times p^1\right] - A_{v_b p}^1 \times \left[\left(A_{v_b v_b}^1\right)^{-1} \times {}^t A_{v_b p}^1 \times p^1\right] = -A_{vp}^1 \times u^0 \end{cases} \tag{4.39}$$

We obtain the following system:

$$\begin{cases} u^1 = -u^0 - \left(A_{vv}^1\right)^{-1} \times {}^t A_{vp}^1 \times p^1 \\ u_b^1 = -\left(A_{v_b v_b}^1\right)^{-1} \times {}^t A_{v_b p}^1 \times p^1 \\ \left[A_{vp}^1 \times \left(A_{vv}^1\right)^{-1} \times {}^t A_{vp}^1 + A_{v_b p}^1 \times \left(A_{v_b v_b}^1\right)^{-1} \times {}^t A_{v_b p}^1\right] \times p^1 = 0 \end{cases} \tag{4.40}$$

this allows deducing the solutions:

$$\begin{cases} u^1 = -u^0 \\ u_b^1 = 0 \\ p^1 = 0 \end{cases} \tag{4.41}$$

This means bubble displacement stabilization is not present in this case.

From the algebra point of view, we have shown that, in the incompressible elastic case, a perfect recovery is possible, even with the resolution by one increment or several increments. And this was confirmed by the results displayed in Figure 4-5 for the single time step resolution by displacement-pressure or later for the incremental time step resolution by velocity-pressure (Figure 4-10). However, we remind one more time that because of the condensation step in the old NSTC solver, the fine-scales are unresolved, only their effects are remained in the coarse-scales. Thus we did not have the possibility to verify the solution of the bubble velocity with this solver. This will be confirmed later with the new SMC solver (see Figure 4-9).

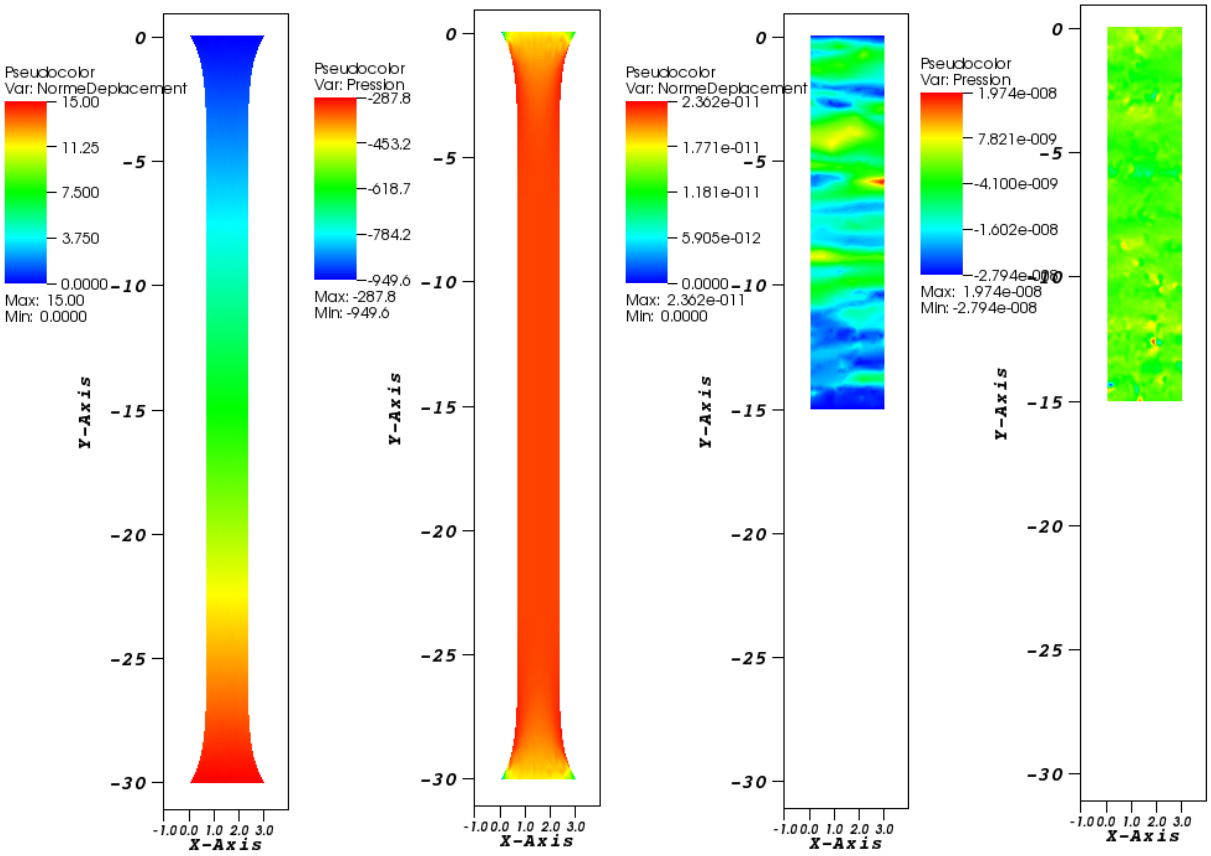


Figure 4-5: Displacement norm and pressure under loading-unloading with the old NSTC solver. Errors in recovery are of the order of the asked precision for the iterative solver ($1e^{-11}$) for the displacement norm and $1e^{-8}$ for pressure.

Now, let us demonstrate the similar problem by using the new SMC solver where a full resolution with all missing terms mentioned above is completed:

$$\begin{cases} A^1_{vv} \times u^1 + {}^t A^1_{vp} \times p^1 = -A^1_{vv} \times u^0 \\ A^1_{v_b v_b} \times u^1_b + {}^t A^1_{v_b p} \times p^1 = -A^1_{v_b v_b} \times u^0_b \\ A^1_{vp} \times u^1 + A^1_{v_b p} \times u^1_b = -A^1_{vp} \times u^0 - A^1_{v_b p} \times u^0_b \end{cases} \tag{4.42}$$

By replacing the u^1 and u^1_b from two first equations to the last equation, the system can be rewritten:

$$\begin{cases} u^1 = -u^0 - \left(A^1_{vv}\right)^{-1} \times {}^t A^1_{vp} \times p^1 \\ u^1_b = -\left(A^1_{v_b v_b}\right)^{-1} \times {}^t A^1_{v_b p} \times p^1 - u^0_b \\ -A^1_{vp} \times \left[u^0 + \left(A^1_{vv}\right)^{-1} \times {}^t A^1_{vp} \times p^1\right] - A^1_{v_b p} \times \left[\left(A^1_{v_b v_b}\right)^{-1} \times {}^t A^1_{v_b p} \times p^1 + u^0_b\right] = -A^1_{vp} \times u^0 - A^1_{v_b p} \times u^0_b \end{cases} \tag{4.43}$$

We obtain the following system:

$$\begin{cases} u^1 = -u^0 - \left(A^1_{vv}\right)^{-1} \times {}^tA^1_{vp} \times p^1 \\ u^1_b = -\left(A^1_{v_bv_b}\right)^{-1} \times {}^tA^1_{v_bp} \times p^1 - u^0_b \\ \left[A^1_{vp} \times \left(A^1_{vv}\right)^{-1} \times {}^tA^1_{vp} + A^1_{v_bp} \times \left(A^1_{v_bv_b}\right)^{-1} \times {}^tA^1_{v_bp}\right] \times p^1 = 0 \end{cases} \tag{4.44}$$

this allows deducing the solutions:

$$\begin{cases} u^1 = -u^0 \\ u^1_b = -u^0_b \\ p^1 = 0 \end{cases} \Leftrightarrow \begin{cases} u = u^1 + u^0 = 0 \\ u_b = u^1_b + u^0_b = 0 \\ p = 0 \end{cases} \tag{4.45}$$

with u and u_b are the displacement and bubble displacement, p is the pressure in recovery.

Accounting for results in Figure 4-6 enables us to confirm that the solution of our algorithm quoted in equations (4.45) is exact.

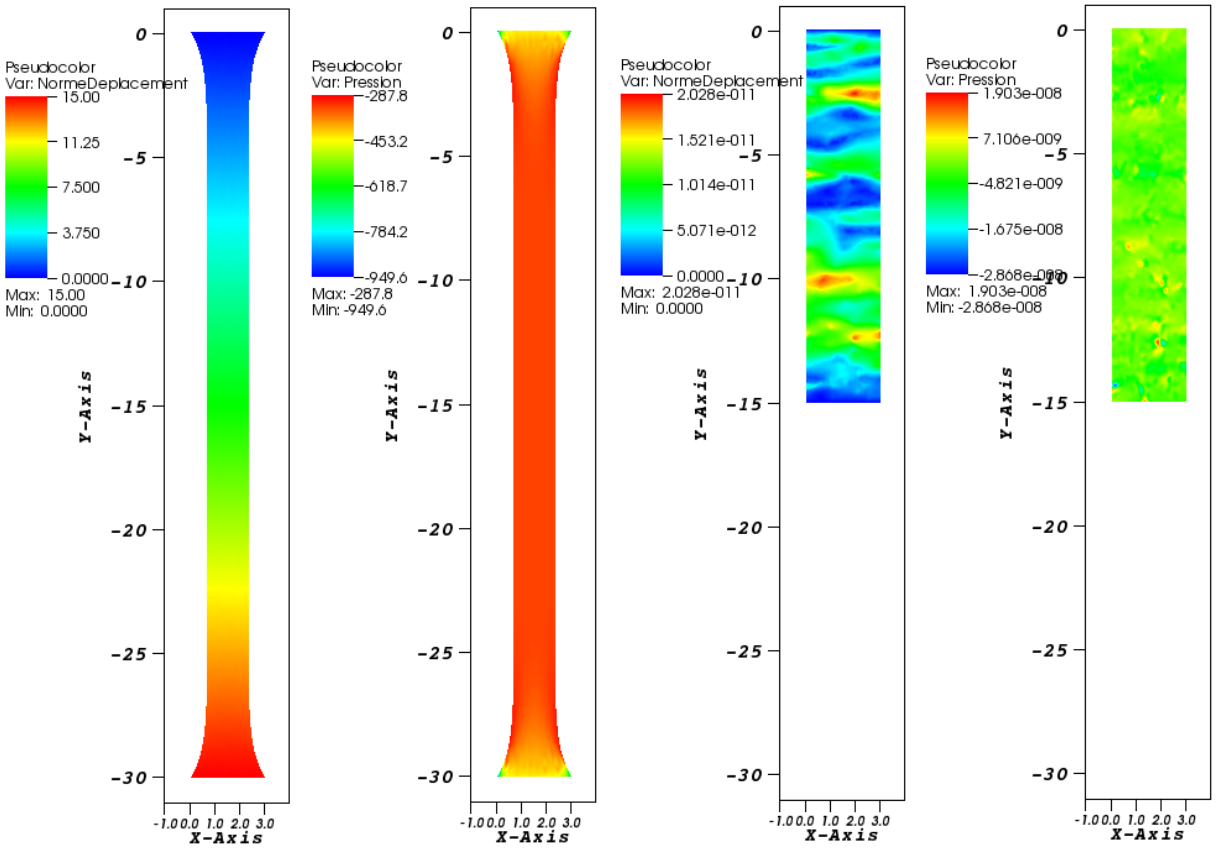


Figure 4-6: Displacement norm and pressure under loading-unloading with the new SMC solver. Errors in recovery are of the order of the asked precision for the iterative solver ($1e^{-11}$) for the displacement norm and $1e^{-8}$ for pressure.

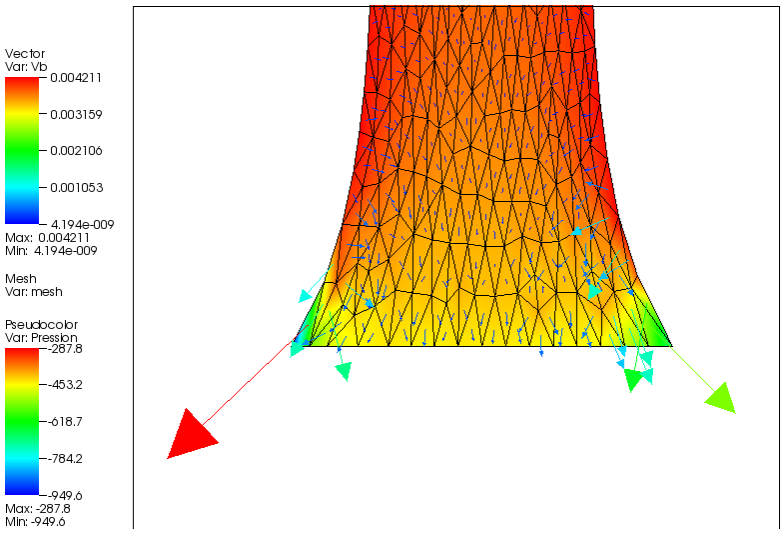


Figure 4-7: Schematic representation of the bubble velocity field in the specimen under loading with the mesh geometry and the pressure field. Since the bubble velocity is computed on elements, these vectors are illustrated on elements. Note that the pressure field is colored as its displayed scale.

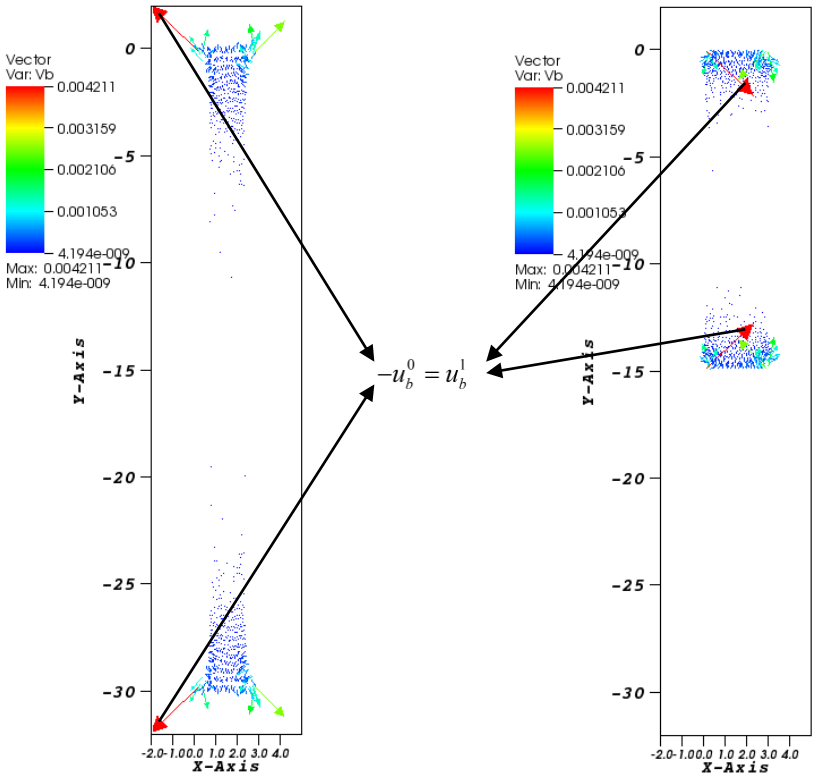


Figure 4-8: Bubble displacement under loading u_b^0 (left) and under unloading u_b^1 (right) with the full resolution by the new SMC solver. First, we can see the unstable pressure zone in the borders where the intensity of the bubble displacement is strong. Secondly, this shows a perfect recovery in which the obtained bubble displacements are perfectly opposite to traction and during spring back.

Interestingly, with our new solver (SMC), it is possible to display the computed bubble displacement as shown on Figure 4-7 (or in the later application illustrated on Figure 4-26). We can retrieve more information in the stabilization problem and understand how the enriched bubble function can improve the quality of resolution compared to the standard method without

the full stabilization. As demonstrated in Figure 4-7 (or in Figure 4-26), the bubble displacement tends to compensate the strong jump of pressure inside the unstable zone. This will probably help us to investigate and develop other stabilization methods in the future.

As presented in Figure 4-7 and Figure 4-8, the bubble displacement is interestingly illustrated inside the elements. When the formulation is fully enriched with the bubble velocity (we compute all the missing terms), obtained bubble displacements are perfectly opposite to traction and during spring back, i.e. in recovery, we find:

$$u_b^1 = -u_b^0 \tag{4.46}$$

which is different with the obtained bubble displacements by using the old NSTC solver. In this case, the bubble displacements are zero $u_b^1 = 0$ during spring back, i.e. in recovery, we find as well demonstrated previously.

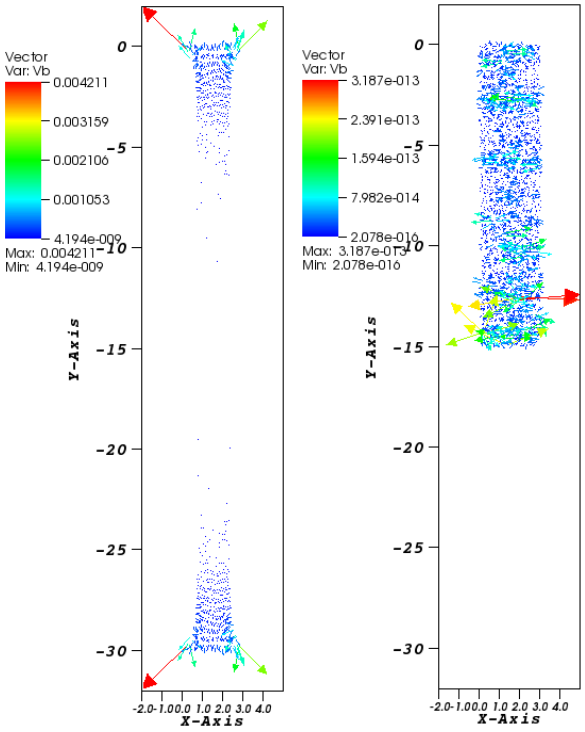


Figure 4-9: Bubble displacement under loading u_b^0 (left) and under unloading u_b^1 (right) with the resolution by the old NSTC solver. This shows that the obtained bubble displacements are zero during spring back as theoretically demonstrated.

4.1.3.2 Incompressible elasticity case by an incremental time step resolution

In the previous section, for the single time step resolution, we have shown that the perfect recovery of the tensile test case can be performed by the incompressible elastic behavior where the missing term was completed in the test case presented in the preliminary work in chapter 3. However, as mentioned in chapter 3, some instabilities problems occurred in the incremental method for the viscoelastic as well as the elastic case. The main reasons proposed were related to the fact that, when the elastic part dominates in the viscoelastic case or when strain is higher than 35% in the elastic case, the elastic stress become very important. This effect may be due to some missing terms in the resolution as mentioned previously (non-linear terms in large deformations or

"bubble extra-stress"). Therefore, with our new development of the mixed solver SMC, we will first verify the influence of the bubble extra-stress in the resolution of the tensile test by the incremental time step method.

As detailed previous in chapter 3 for the incompressible elastic tensile test, we reintroduce rapidly the full resolution of the tensile test. The general split algorithm in the incremental approach is shortly described below:

Algorithm for *loading* and *unloading*:

For each time step $\left[t^n, t^{n+1}\right]$ for *loading* **do**

Knowing τ^n

1) Compute $\left(v^{n+1}, p'^{n+1}\right)$ such that

$$\begin{cases} \nabla_{x^{n+1}} \cdot 2\eta_{ve}\varepsilon\left(v^{n+1}\right) - \nabla_{x^{n+1}} p'^{n+1} = -\nabla_{x^{n+1}} \cdot \tau^n \\ \tau^n = 2\mu_e \varepsilon\left(u^n\right) \\ -\nabla_{x^{n+1}} \cdot \left(v^{n+1}\right) = \dfrac{\nabla_{x^{n+1}} \cdot \left(u^n\right)}{\Delta t} \\ v = v_{imposed} \ \textit{in} \ \Gamma_{\inf} \ \textit{and} \ v = 0 \ \textit{in} \ \Gamma_{\sup} \end{cases} \tag{4.47}$$

2) Find u^{n+1} by solving

$$u^{n+1} = u^n + v^{n+1}\Delta t \tag{4.48}$$

3) Update the configuration by moving the mesh

$$x^{n+1} + u^{n+1} \Rightarrow x^{n+2} \tag{4.49}$$

4) Compute the extra-stress tensor

$$\tau^{n+1} = 2\mu_e \varepsilon\left(u^{n+1}\right) \tag{4.50}$$

End for *loading*

For each time step $\left[t^n, t^{n+1}\right]$ for *unloading* **do**

Knowing τ^n

1) Compute $\left(v^{n+1}, p^{n+1}\right)$ such that

$$\begin{cases} \nabla_{x^{n+1}} \cdot 2\eta_{ve}\varepsilon\left(v^{n+1}\right) - \nabla_{x^{n+1}} p'^{n+1} = -\nabla_{x^{n+1}} \cdot \tau^n \\ \tau^n = 2\mu_e \varepsilon\left(u^n\right) \\ -\nabla_{x^{n+1}} \cdot \left(v^{n+1}\right) = \dfrac{\nabla_{x^{n+1}} \cdot \left(u^n\right)}{\Delta t} \\ v = -v_{imposed} \ \textit{in} \ \Gamma_{\inf} \ \textit{and} \ v = 0 \ \textit{in} \ \Gamma_{\sup} \end{cases} \tag{4.51}$$

2) Find u^{n+1} by solving

$$u^{n+1} = u^n + v^{n+1}\Delta t \tag{4.52}$$

3) Update the configuration by moving the mesh

$$x^{n+1} + u^{n+1} \Rightarrow x^{n+2} \tag{4.53}$$

4) Compute the extra-stress tensor

$$\tau^{n+1} = 2\mu_e \varepsilon\left(u^{n+1}\right) \tag{4.54}$$

End for *unloading*

The material parameters (see Table 3-2) and the specimen form are chosen in order to satisfy the experimental tensile test of PMMA (see Figure 3-1) which will be presented later in the chapter 5.

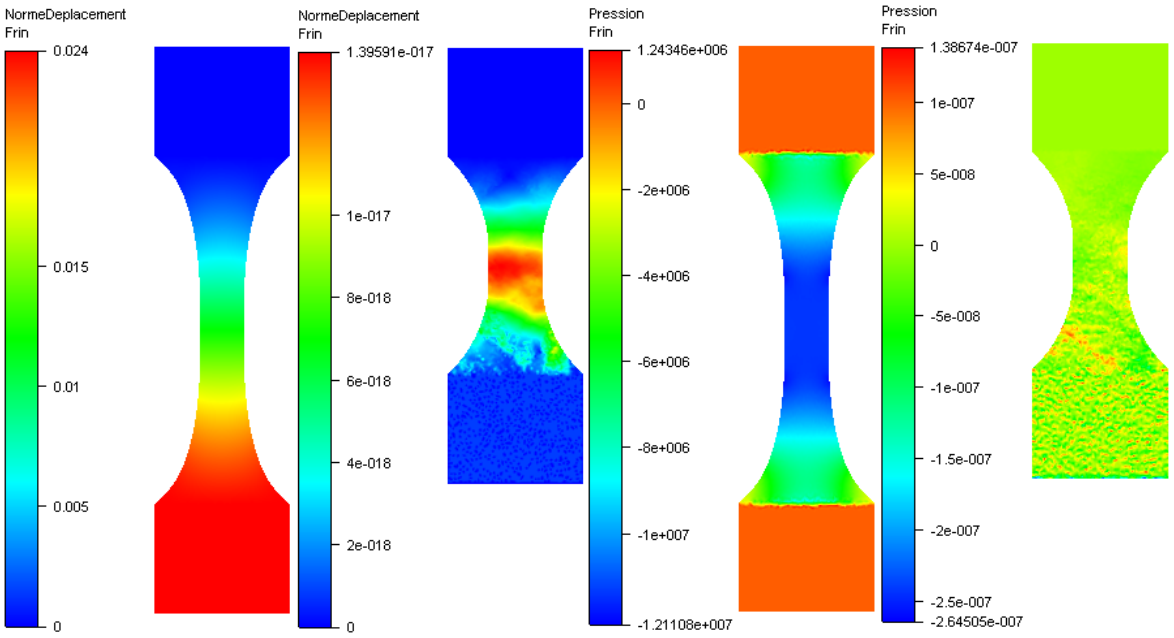


Figure 4-10: Displacement norm (mm) and pressure (Pa) in traction and return by the incremental time step resolution *(velocity-pressure "v-p") (*40% of strain for 100 time steps). Note that the errors introduced in recovery are of the order of the asked precision for the iterative solver ($1e^{-17}$), for the displacement norm and ($1e^{-7}$) for the pressure with the new SMC solver with different.

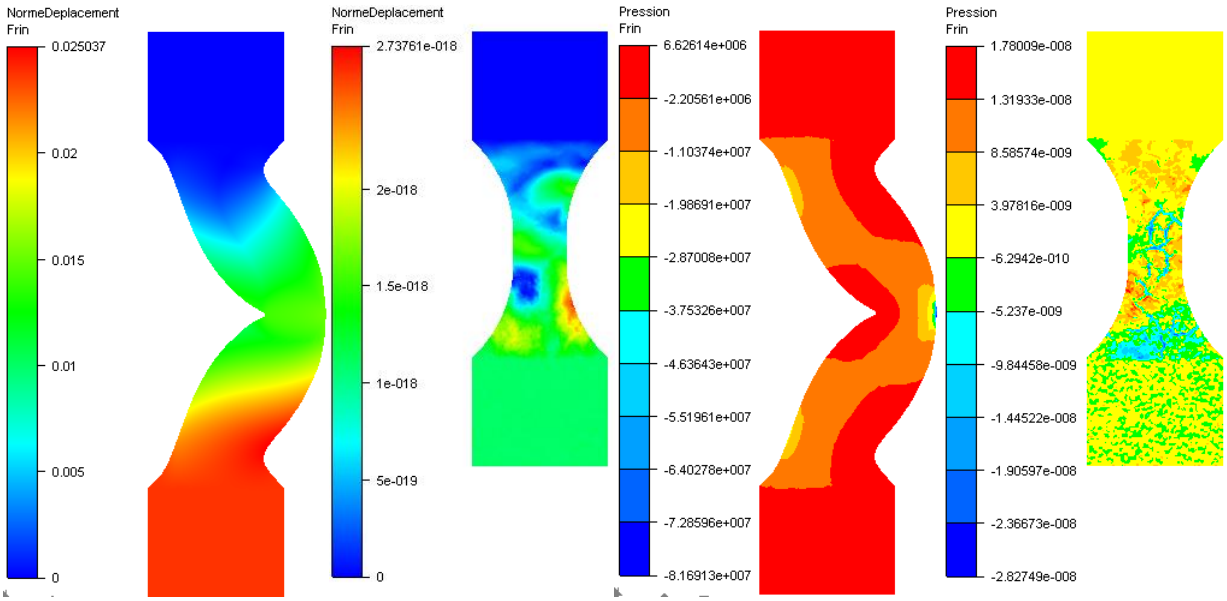


Figure 4-11: Displacement norm (mm) and pressure (Pa) in traction and return by the incremental time step resolution *(velocity-pressure "v-p") (*60% of strain for 100 time steps).

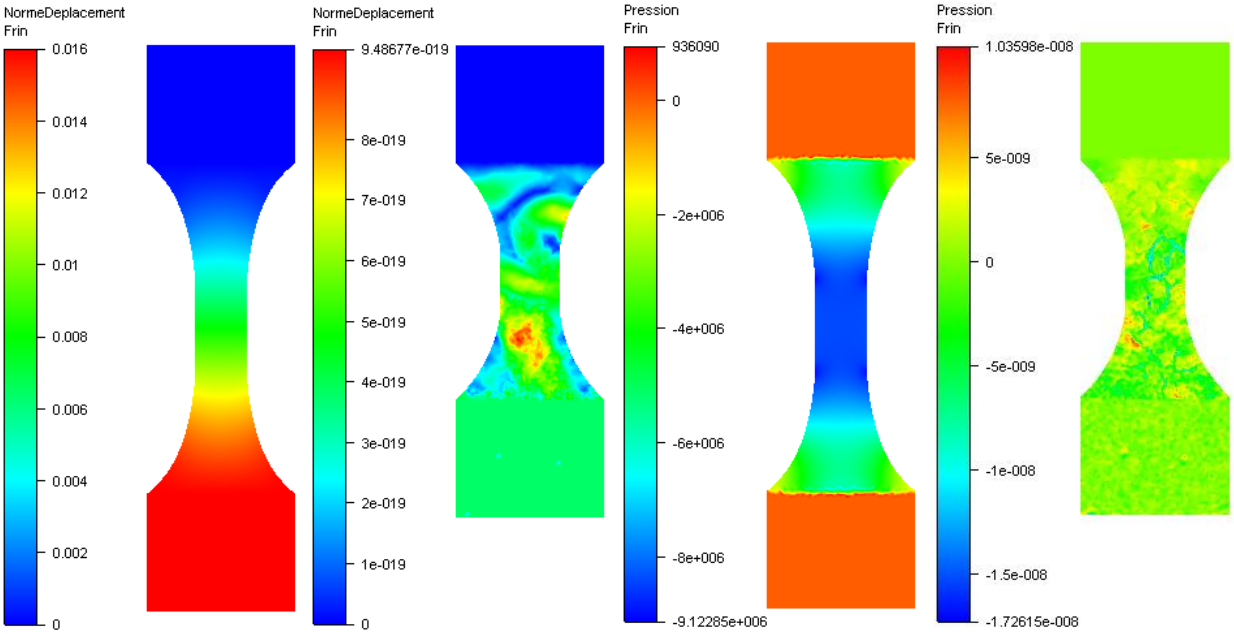


Figure 4-12: Displacement norm (mm) and pressure (Pa) in traction and return by the incremental time step resolution *(velocity-pressure "v-p") (*60% of strain for 10 time steps).

As displayed from Figure 4-10 to Figure 4-12, the results illustrate some points concerning incremental resolution: the result obtained is perfect in which the strain can attain 40% (Figure 4-10). However, the instabilities problems have still appeared when the strain is more than 50% of strain (Figure 4-11) whatever the solver used (the SMC and the NSTC solver). The full resolution by the new SMC solver did not help us to stabilize the problem. To overcome the problem, one technical method is to optimize the time step of resolution. We can see that we can decrease this phenomenon by decreasing the time step (see Figure 4-12). An open issue remains concerning these instabilities, one solution should be to complete the formulation with linear terms issuing from large deformations, as shown in chapter 2.

Furthermore, an Eulerian approach has shown to be more "complete". But since in this case, we have seen the appearance of other type of instabilities (in the pressure at the interface regions), we will now look at the improvement of the stabilization to try to eliminate this oscillations. In a first time, we will look at the test case of flow between rigid particles.

4.1.4 Application: flow between two rigid solid particles

In the latter case of a fluid that flows between rigid particles, results with the penalization method showed an instability on the pressure problem, which is not good enough to model the efforts on the solid phase (rigid or elastic), even if the velocity appears as well computed. Thus, the augmented Lagrangian method with Uzawa algorithm can be applied thanks to its robustness and accuracy compared to those of the Lagrangian penalization method [106] [107], since the penalization coefficient of the solid phase can be decreased, lowering the amplitude of the instabilities. Application of the augmented Lagrangian algorithm is equivalent, in our solver, to the introduction of an extra-stress in the formulation from the weak formulation (3.86). The discrete form can be described as:

$$\begin{cases} 2\eta_f \varepsilon\left(v_h^{n+1}\right) : \varepsilon\left(w_h\right) - \left(p_h, \nabla . w_h\right) = -\tau_h^{n+1} : \varepsilon\left(w_h\right) \\ 2\eta_f \varepsilon\left(v_h^{b,n+1}\right) : \varepsilon\left(w_h^b\right) - \left(p_h, \nabla \cdot w_h^b\right) = -\tau_h^{b,n+1} : \varepsilon\left(w_h^b\right) \\ -\left(\nabla \cdot \left(v_h^{n+1} + v_h^{b,n+1}\right), q_h\right) = 0 \end{cases} \quad (4.55)$$

where the penalization stress τ is computed by:

$$\begin{cases} \tau^{n+2} = \tau^{n+1} + r_s \varepsilon\left(v^{n+1}\right) \\ \tau_b^{n+2} = \tau_b^{n+1} + r_s \varepsilon\left(v_b^{n+1}\right) \\ r_s = rH\left(\alpha\right) \end{cases} \quad (4.56)$$

Please note that the τ in this case is not the "extra-stress" in the physical sense as that of the tensile test. This represents the Lagrangian penalization stress. In chapter 3, only the resolution by the penalization method was performed due to the missing penalization stress τ_b in the fine-scales resolution (see equation (4.55)) which appears in the resolution by the augmented Lagrangian method with Uzawa algorithm. Thus, thanks to our new SMC solver, we can complete this one in the fine-scales resolution.

Laure and co-workers [126] studied the influence of penalization factors and the number increment *n* of Uzawa loop on the rigidity condition. The results showed that for each penalization factor, the norm of rigidity constraint decreases quickly until a certain increment number *n*, and then the reduction is slower. In fact, reaching a defined value of *n;* the norm of rigidity stress is uniformly small inside the solid domain whereas it remains more important in the transition area. Therefore, the next Uzawa iterations only decrease the norm inside this transition area [126]. Thus, for our simulation, an optimized value of *n* was used to obtain a good agreement between the quality of results and the computational time cost.

We highlight that with the old solver (NSTC), the augmented Lagrangian method with Uzawa algorithm was performed by neglecting these terms in the right-hand side members in the fine-scales resolution due to the complexity in programming, and thus the applied resolution was not exact. Thanks to our new solver, we will achieve the missing work by using the exact formulation and compare with the old results, and also with the results in the monophasic case, the so-called reference results.

Figure 4-13 represents the velocity fields in the simulation by different methods: the penalization method, the incomplete augmented Lagrangian method with Uzawa algorithm (the NSTC solver) and the complete augmented Lagrangian method with Uzawa algorithm (the SMC solver) (see system of equations (4.55)).

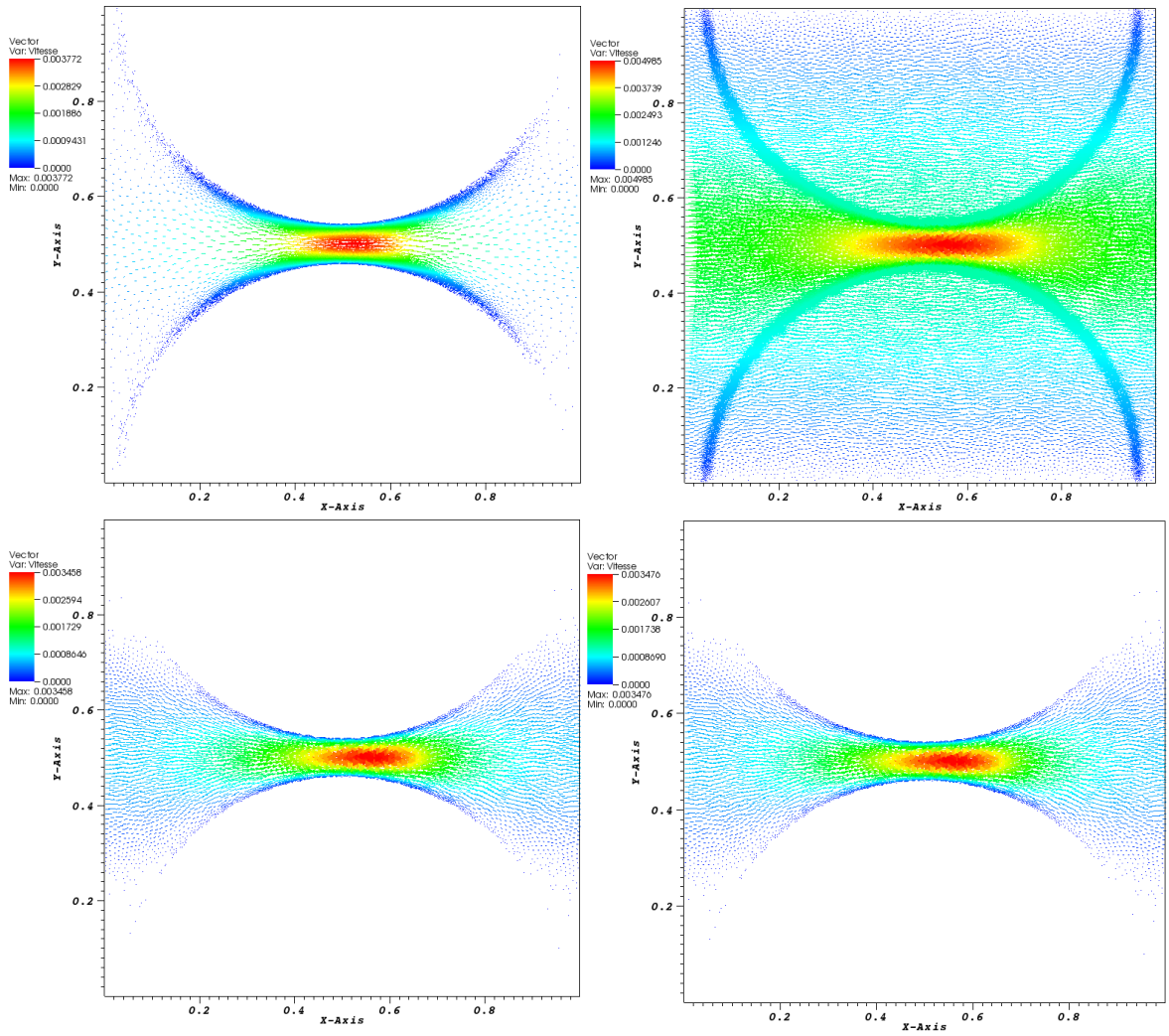


Figure 4-13: Velocity field (linear part) for the test case of flow around rigid particles. In the first row, on the left, velocity by the one phase modeling (reference results), on the right velocity by the penalization method; in the second row, on the left, velocity by the augmented Lagrangian method with Uzawa algorithm (the old solver NSTC) and on the right the new solver SMC (augmented Lagrangian method with Uzawa algorithm with a bubble's extra stress).

With the standard penalization method, the modeling of the solid part has no physical sense due to the appearance of velocity fields inside the solid domain. On the other hand, this velocity is perfectly avoided inside the solid by the incomplete as well as by the complete augmented Lagrangian method with Uzawa algorithm. Despite the missing term "bubble extra-stress" in the incomplete Uzawa formulation, the effect of the augmented Lagrangian method clearly improves the resolution in large-scales. This explains the different velocity fields on the solid, but with regard to the bubble velocity, the difference is considerable (see Figure 4-14). The bubble velocity totally disappeared inside the solid domain when the "bubble extra-stress" is added in the Uzawa formulation which is not the case with the incomplete formulation.

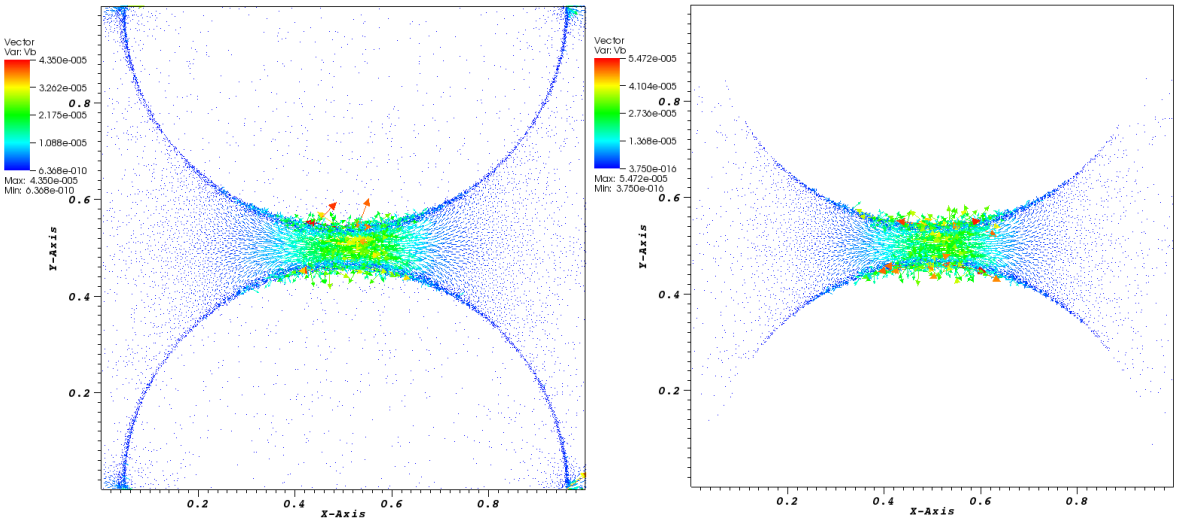


Figure 4-14: Bubble velocity field for the test case of flow around rigid particles using an augmented Lagrangian resolution; of flows in the pore space; on the left, the bubble velocity with the old solver NSTC (recomputed after resolution) and on the right the new solver SMC (directly computed by the solver).

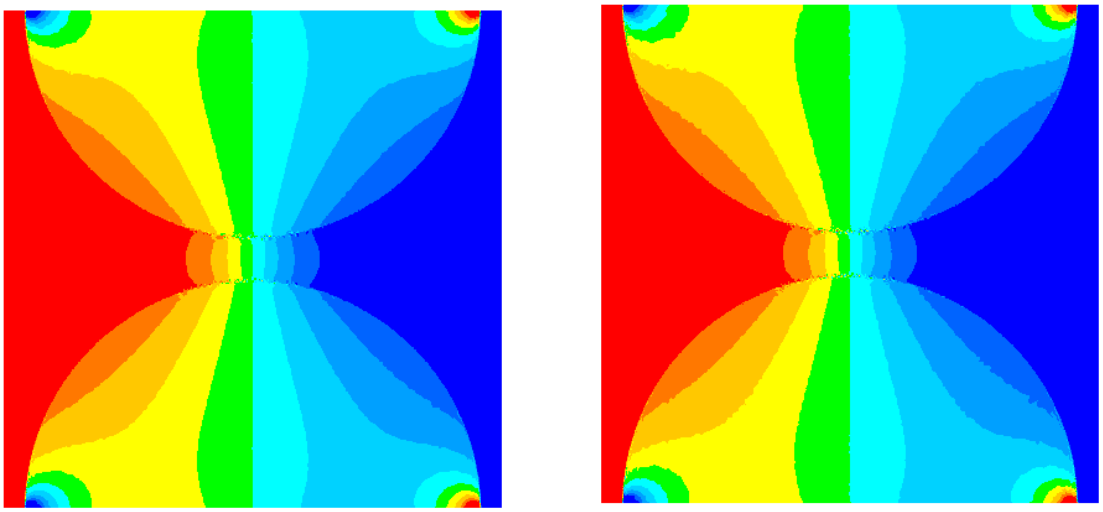


Figure 4-15: Pressure field resolution by the NSTC solver on the left and the SMC solver on the right.

In spite of the added stabilization term in the fine-scales, Figure 4-15 does not evidence a better result on the pressure distribution with a simple penalization. To explain this lack in efficiency let us remind that the weak formulation for the resolution by a monolithic approach can be written as:

$$\begin{cases} 2\eta_f \int_\Omega \varepsilon(v) : \varepsilon(w) d\Omega - \int_\Omega p \nabla \cdot w d\Omega + \int_{\Omega_s} \tau_s : \varepsilon(w) d\Omega = 0 \\ \int_\Omega q \nabla \cdot v d\Omega = 0 \\ \int_{\Omega_s} \varepsilon(v) : \tau_s d\Omega = 0 \\ + boundary\ conditions \end{cases} \tag{4.57}$$

The distribution of fluid and solid inside an element cut by the interface may be represented as the below figure:

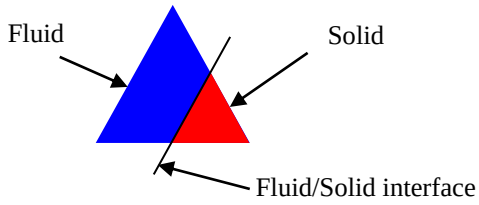


Figure 4-16: Distribution of fluid/solid inside an element

In the previous results, we have considered a viscosity constant per element and proportional to the volume occupied by each domain, which will be a source of error due to the high contrast in viscosities (solid vs. liquid). Assuming that a fluid represents 99% of the filling of an element, its viscosity will be:

$$\eta = \frac{1000\eta_f \times 0.01 + \eta_f \times 0.99}{|\kappa|}|\kappa| \approx 11\eta_f \tag{4.58}$$

that is, far from the liquid viscosity. That is why the penalization, where the viscosity in the solid is chosen very high, is inaccurate as technique. Even if we decrease the viscosity by using an augmented Lagrangian method with an Uzawa algorithm, the same problem appears, due to an inconsistence in the formulation. The "extra-stress" representing the solid stress is supposed P0, constant for element, and is calculated as:

$$\begin{cases} \tau^{n+2} = \tau^{n+1} + r_s \varepsilon\left(v^{n+1}\right) \\ r_s = rH\left(\alpha_{f/s}\right) \end{cases} \tag{4.59}$$

In the solid, the rigidity condition is thus:

$$\varepsilon(v) = 0 \tag{4.60}$$

That is:

$$tr\,\varepsilon(v) = 0 \tag{4.61}$$

$$\Rightarrow \nabla \cdot v = 0 \tag{4.62}$$

being, as the extra-stress, $\varepsilon(v)$ P0. Thus, the weak formulation of the deduced equation may be then understood as:

$$\begin{gathered} \forall q^* \in P^0(\kappa) \text{ find } v \in P^1(\kappa): \\ \left(q^*, \nabla \cdot v\right) = 0 \end{gathered} \tag{4.63}$$

where $P^i(\kappa)$ is the space of polynomials defined on element κ of degree less than or equal to *i*, compared to all variables. But, in the presented (*v*, *p*) formulation, the volume conservation equation is written:

$$\begin{gathered} \forall q \in P^1(\kappa) \text{ find } v \in P^1(\kappa): \\ \left(q, \nabla \cdot v\right) = 0 \end{gathered} \tag{4.64}$$

and thus q and q^* are not in the same functional space, meaning that $\nabla \cdot v = 0$ is not really respected for the solid. Unfortunately, the conflict that appears between the continuous interpolations in equation (4.64) with the discontinuous interpolations in equation (4.63) induces unstable problems in the numerical resolution, mainly when the solid viscosity becomes too important compared with the fluid viscosity. The introduced penalization Lagrangian factor cannot ensure the $\nabla \cdot v = 0$ in the solid domain.

To overcome this stabilization problem, the discontinuous extra-stress τ_s may be replaced by another continuous terms $\tilde{\tau}_s$ using a "stress extrapolation" like method. The idea is to project the extra-stress, calculated on elements, on nodes by an average summation of each neighbor element, called the element package as illustrated in the following figure:

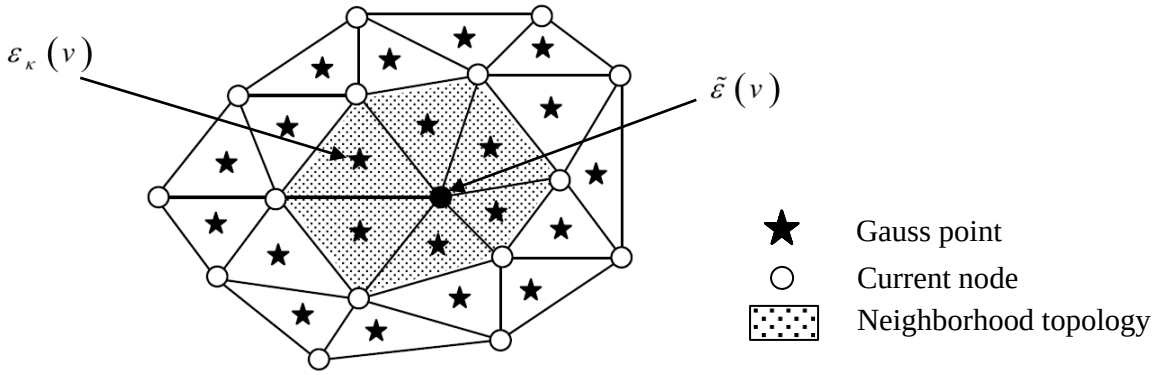


Figure 4-17: Stress projection on node [127].

The stress projection on nodes can be expressed as:

$$\tilde{\varepsilon}(v) = \frac{1}{\sum_{\kappa} |V_\kappa|} \sum_{\kappa} \varepsilon_\kappa(v) |V_\kappa| \tag{4.65}$$

where $|V_\kappa|$ is the volume norm of element.

Therefore, $\tilde{\tau}_s$ is found by solving

$$\begin{cases} \tilde{\tau}^{n+2} = \tilde{\tau}^{n+1} + r_s \tilde{\varepsilon}\left(v^{n+1}\right) \\ r_s = rH\left(\alpha_{f/s}\right) \end{cases} \tag{4.66}$$

Unfortunately, the implementation and validation of this technique was not possible within this thesis, and is a part of the perspective work to follow. In the following, we will introduce another stabilized resolution method based on the EVSS method [17] [18] in which we will apply something close to this stress projection to the Kelvin-Voigt viscoelastic, the Neo-Hookean hyper-elastic and the visco-hyper-elastic behaviors.

To try to decrease the pressure oscillations, we can also modify the equation in the coarse-scales by optimizing the bubble viscosity in the mixed finite element method. This way is investigated in the following.

4.2 Improving stabilization through the bubble viscosity modification

4.2.1 A novel formulation with modification of bubble's viscosity

We will try to improve the previous results through the modification of the bubble stabilization term (either in the old solver or in the new one). If we come back to the weak formulation of, for example, the Stokes problem, it can be described as follows as seen previously:

$$\begin{cases} \int_\Omega 2\eta\varepsilon(v):\varepsilon(w)d\Omega - \int_\Omega p\nabla\cdot w d\Omega = 0 \\ -\int_\Omega q\nabla\cdot v d\Omega = 0 \\ +boundary\ conditions \end{cases} \tag{4.67}$$

The discrete formulation using the MINI-element P1+/P1 can be written:

$$\begin{cases} \int_\Omega 2\eta\varepsilon(v_h):\varepsilon(w_h)d\Omega - \int_\Omega p_h\nabla\cdot w_h d\Omega = 0 \\ \int_\Omega 2\eta\varepsilon(v_h^b):\varepsilon(w_h^b)d\Omega - \int_\Omega p_h\nabla\cdot w_h^b d\Omega = 0 \\ -\int_\Omega q_h\left(\nabla\cdot v_h + \nabla\cdot v_h^b\right)d\Omega = 0 \\ +boundary\ conditions \end{cases} \tag{4.68}$$

The resolution in fine-scales of the system (4.68) is detailed on an element κ as:

$$\forall\kappa\in\Omega_h \quad \int_\kappa 2\eta\varepsilon\left(v_{h,\kappa}^b\phi^b\right):\varepsilon\left(\phi^b\right)d\Omega = \int_\kappa p_{h,\kappa}\phi^b d\Omega \tag{4.69}$$

with $v_{h,\kappa}^b$ is the bubble velocity on the element κ, and ϕ^b is the bubble shape function. According to the fact that the test function is arbitrary chosen [128], we resume:

$$v_{h,\kappa}^b = \left[\int_\kappa 2\eta\nabla\phi_\kappa^b\cdot\nabla\phi_\kappa^b d\Omega + 2\eta\int_\kappa\nabla\phi_\kappa^b\otimes\nabla\phi_\kappa^b d\Omega\right]^{-1}\times\int_\kappa p_{h,\kappa}\phi_\kappa^b d\Omega \tag{4.70}$$

Replacing the bubble velocity v_h^b in the volume conservation equation, i.e. the last equation of the system (4.68):

$$\begin{cases} \int_\Omega q_h\nabla\cdot v_h d\Omega + \sum_\kappa\int_\Omega\Psi_{h,\kappa}\nabla q_h\cdot\nabla p_h d\Omega = 0 \\ \Psi_{h,\kappa} = \left[\int_\kappa 2\eta\nabla\phi_\kappa^b\cdot\nabla\phi_\kappa^b d\Omega + \int_\kappa 2\eta\nabla\phi_\kappa^b\otimes\nabla\phi_\kappa^b d\Omega\right]^{-1}\times\phi_\kappa^b\int_\kappa\phi_\kappa^b d\Omega \end{cases} \tag{4.71}$$

In such approach, the stabilization terms that appeared in the mixed FE with MINI-element (P1+/P1), have similar property as the global stabilization form in the classical mixed FE (P1/P1) [129]:

$$\begin{cases} \Psi_\kappa = \beta^2 \times C_h(p,q) \\ C_h(p,q) = \sum_\kappa h_\kappa^2 \int_\kappa \nabla q_h \cdot \nabla p_h d\Omega \end{cases} \tag{4.72}$$

In fact, the classical stabilized mixed FE introduces a second order term, named the stabilization term, which consists of disrupting or relaxing the incompressibility equation without changing the order of the method. Thus, the stabilization of this problem returns to allow a small numerical local compressibility.

In the stabilized term (4.72), h_κ is the mesh size of the element κ. It was demonstrated that the choice of β is essential and need to be adjusted to control the accuracy and efficiency of the stabilization [129]. Usually, this value $\beta = 1/10$ is chosen to optimize the problem. Practically, it was observed that pressure oscillations become negligible when the tensor Ψ_k was divided by V_κ^2, the square of the volume of the element *k* [91] [99].

In our case, resolution of the system (4.68) is similar with that given previously in chapter 3 (see the matrix form (3.22)). Therefore, the appearance of matrix *C* represents the stabilization formulation in the mixed FE P1+/P1. As the detailed formulation in chapter 3 (the old solver NSTC) or chapter 4 (the new solver SMC), we highlight that the matrix *C* directly depends on the inverse of the viscosity η^{-1}. However, for a multiphase approach, the viscosity in the mixed zone is highly different from the solid phase to liquid phase, which causes some problems to the stabilized method. Since the viscosity near the solid phase is very high (penalization method), the stabilization matrix *C* may vanish, meaning that the effect of the stabilization term tends to zero, thus the problem becomes unstable. The proposed solution to overcome this obstacle is to optimize the viscosity in this mixed zone, mainly in the fine-scales resolution. Therefore, the bubble viscosity η_b in fine-scales, which may be different of that in the coarse-scales, was introduced to control the stabilization effect.

The weak formulation of the problem is now rewritten:

$$\begin{cases} \text{Viscosity} \rightarrow \int_\Omega 2\eta \varepsilon(v_h) : \varepsilon(w_h) d\Omega - \int_\Omega p_h \nabla \cdot w_h d\Omega = 0 \\ \text{Bubble Viscosity} \rightarrow \int_\Omega 2\eta_b \varepsilon(v_h^b) : \varepsilon(w_h^b) d\Omega - \int_\Omega p_h \nabla \cdot w_h^b d\Omega = 0 \\ -\int_\Omega q_h (\nabla \cdot v_h + \nabla \cdot v_h^b) d\Omega = 0 \\ +\textit{boundary conditions} \end{cases} \tag{4.73}$$

The next session is devoted to the analysis of the modification of the bubble viscosity compared to the classical stabilization method.

4.2.2 Application

4.2.2.1 Simple two phase test case

Our first analysis test case is a simple two-phase solid-liquid test, illustrated on Figure 4-18. In the upper edge, we impose a velocity V_x and we observe the distribution of velocity and of pressure inside the domain.

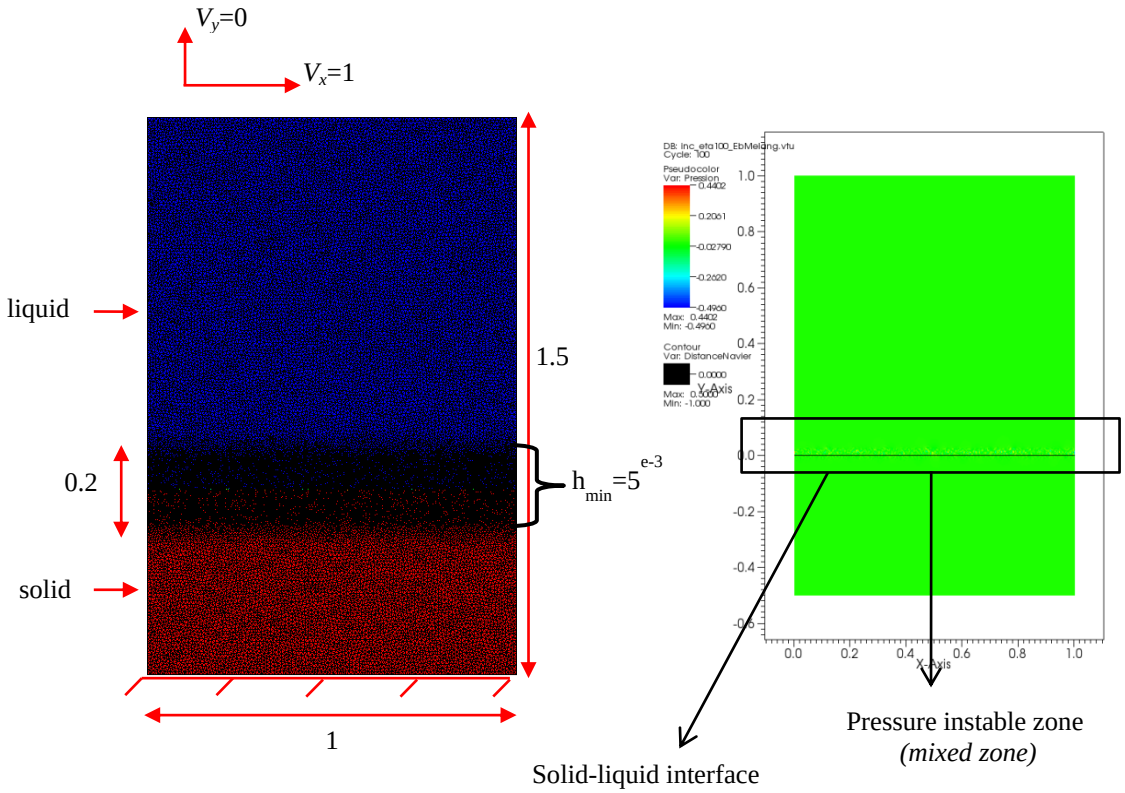


Figure 4-18: Two phase test case.

The domain consisted of two fields: a solid field (red) and a fluid field (blue). This problem is solved by the mixed finite element method with MINI-element P1+/P1 which was described above as the NSTC solver.

In fact, in the incompressible case, the pressure must be a constant everywhere. However, in the iterative resolution method, the initial solution starts at zero, thus the obtained pressure should be zero everywhere inside the domain. However, results indicate non zero pressures, mainly near the interface between the fluid and the solid, the same instabilities as observed previously.

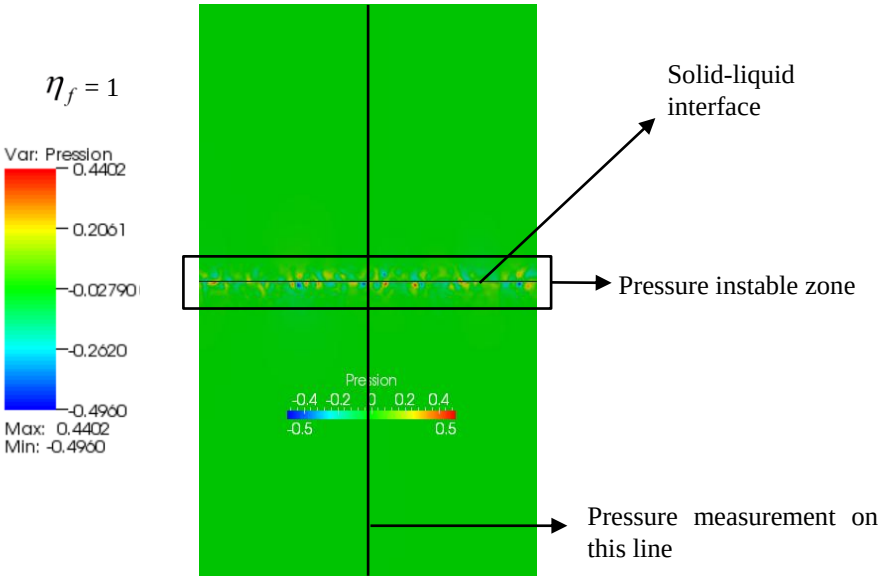
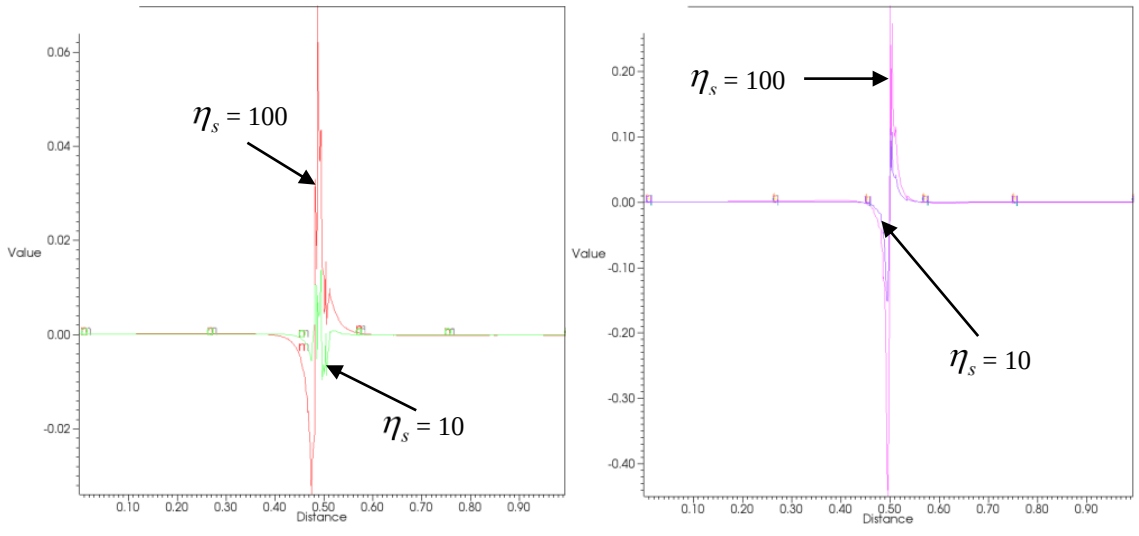


Figure 4-19: Analysis of the pressure unstable zone.

In order to optimize the effect of changing the viscosity on the fine scales equation, two different mixture laws as seen in chapter 3 (Figure 3-24) for viscosity were applied to model the solid and liquid phase. The first is the discontinue law based on elements (P0) where the change occurs only in the elements crossed by the interface. The second is the continuous linear law (P1) that consists in a considering a continuous signed function around a thickness *e* at the interface (at the nodes).

The fluid viscosity is fixed at $\eta_f = 1$ *Pas*, the solid viscosity varies from 1 to 100 *Pas* for both the two mixture laws, P1 and P0. For the results on pressure, with modifying the bubble stabilization, we obtained the following graphs Figure 4-20, for the vertical distribution line drawn in Figure 4-19.



P1 mixture law P0 mixture law

Figure 4-20: Pressure values through a vertical line crossing both domains for different solid viscosities using two different mixture laws. Please note that we did not synchronize the scales of the two curves due to the strong difference between them.

In Figure 4-20, a decrease, then a peak of pressure appears near the interface, demonstrating that the more important difference between the solid and the liquid viscosities is, the more unstable the pressure will appear in the interface solid/liquid, whatever the mixture laws. Moreover, the results showed that the pressure in P1 mixture law is more stable than the mixed P0 due to the smooth change of viscosity at the interface.

Remark that in the test case where the solid viscosity equals the liquid viscosity $\eta_s = \eta_f = 1$, in other words one phase in the simulation, the pressure is zero which logically agrees with the theory.

The pressure becomes more stable when the bubble viscosity decreases (Figure 4-21), which confirms the hypothesis concerning the lack of stabilization for the penalization technique in the above description.

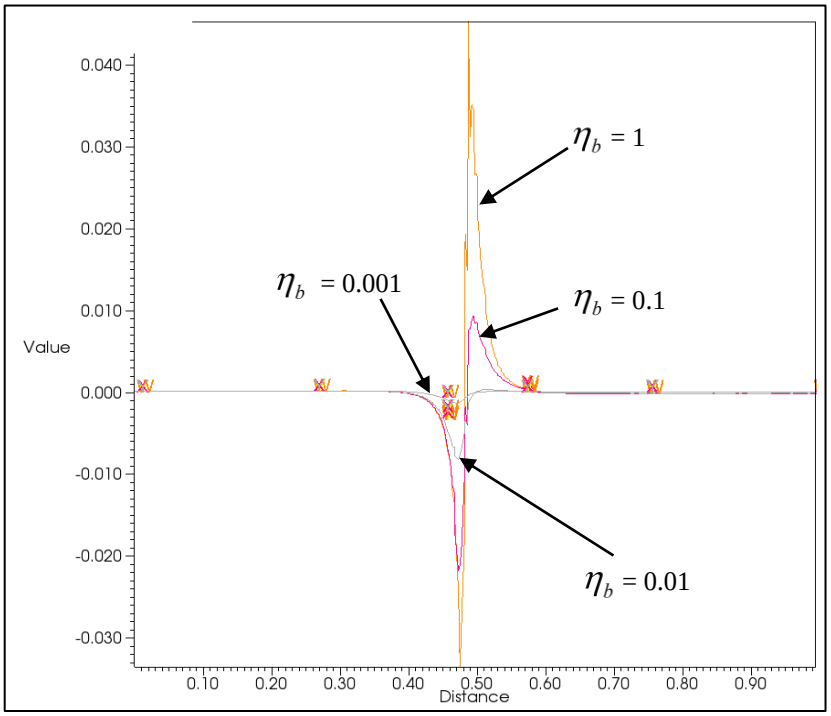


Figure 4-21: Pressure for different bubble viscosities, from 0.001 to 1 Pas by P1 mixture law.

Modifying the bubble viscosity also optimizes the effect of the stabilized term in the resolution. However, the over-stabilization can distort the result when the bubble velocity is too small. Furthermore, it is not necessary to stabilize the whole domain and only stabilization on the unstable zone is required. In our case, this represents the zone close to the interface. Therefore, we used two different methods to describe the needed stabilization zone with the mixed laws as following:

The first one is based on the rectangular function type:

$$\eta_b = \Omega_\alpha \eta_{ref} + (1 - \Omega_\alpha)\eta_f \tag{4.74}$$

And the second is based on the smoothed function:

$$\eta_b = \eta_{ref} + \left(\frac{|\alpha|}{e}\right)^2 \left(\eta_f - \eta_{ref}\right) \tag{4.75}$$

where η_{ref} is called the reference viscosity, in this case we chose $\eta_{ref} = 1e^{-3}$, Ω_α is the modified bubble viscosity zone. Schematic representation of the two methods is illustrated on Figure 4-22.

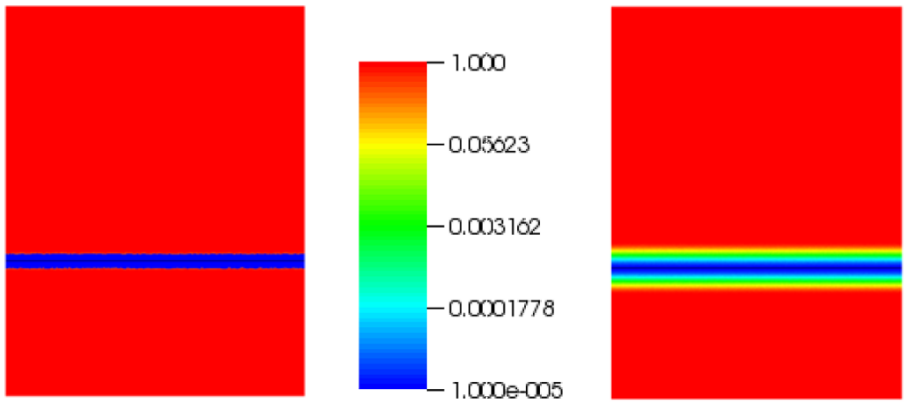


Figure 4-22: Bubble viscosity by two laws for the distribution of the bubble viscosity. On the left the rectangular function, and on the right the smoothed function.

The results shown in Figure 4-23 confirm the significant improvement on the pressure field. The modification effect of bubble viscosity decreases strongly the unstable phenomena near the interface where the maximum pressure can be divided by a factor of 70 times. For a more detailed numerical simulation and comparison, results are summarized in Table 4-3 where several configuration tests were simulated to measure the influence of the bubble viscosity modification on the pressure stabilization. Remark that the results in this case are performed with a P1 mixture law of viscosity for the coarse scale resolution.

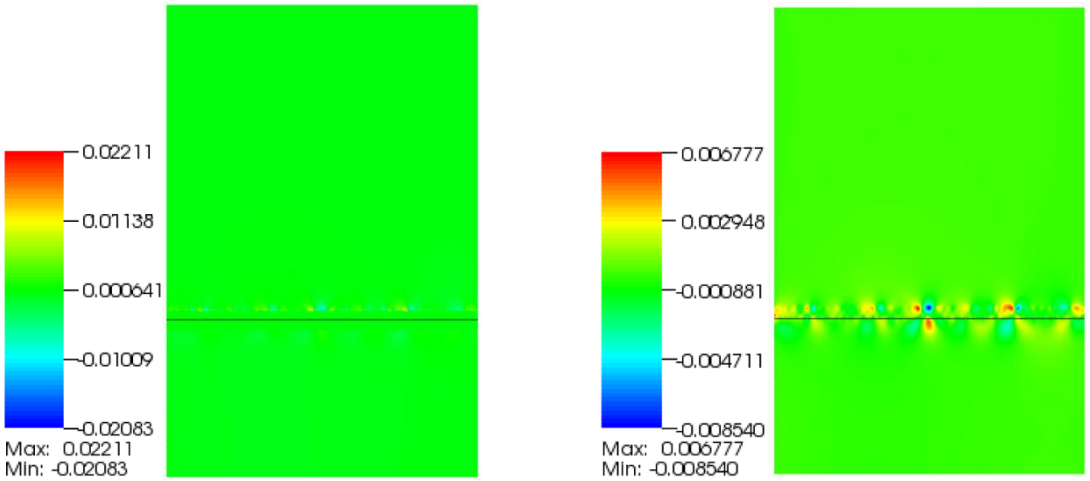


Figure 4-23: Pressure by two mixture laws of bubble viscosity. Maximum pressure decreases from 0.44 to 0.022 (reduces above 20 times). Maximum pressure decreases from 0.44 to 0.0067 (reduces above 70 times the error committed). Please note that we did not synchronize the scale of the two figures due to the strong difference between them.

With this stabilized method that concentrates the modification of bubble velocity in the unstable zone, we can improve the pressure field in the whole domain, and ensure that the velocity field is not disturbed. Indeed, as shown on Figure 4-24 and Figure 4-25, the norm L^2 of errors on the

velocity with the modified bubble viscosity is quasi-identical to that observed with the regular method.

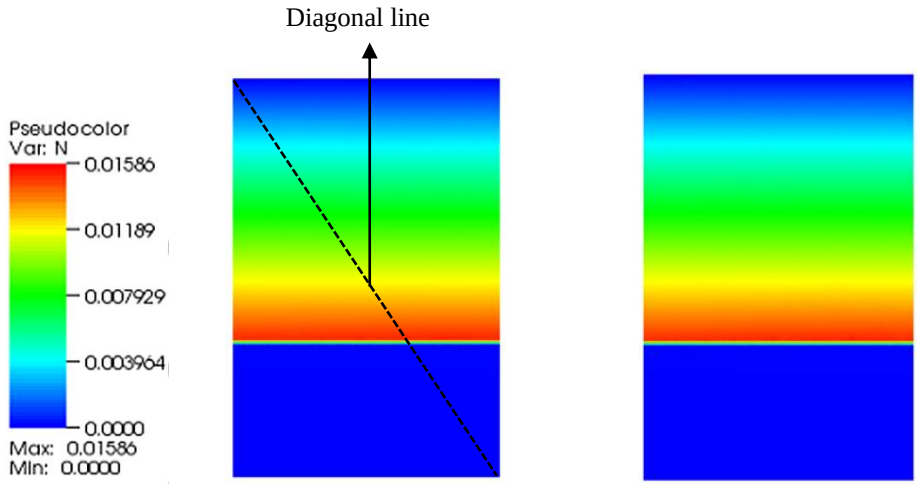


Figure 4-24: Norm L^2 of errors on the velocity using the standard bubble viscosity (left) and the modification of bubble viscosity (right).

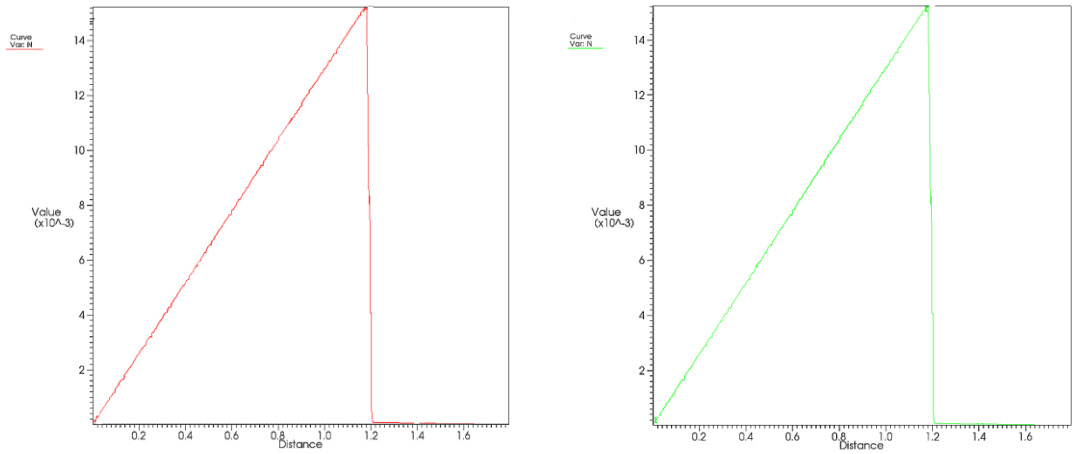


Figure 4-25: Norm L^2 of errors on the velocity using the standard bubble viscosity (left) and the modification of bubble viscosity (right). Measurement is taken on the diagonal line of the simulation domain as illustrated in Figure 4-24.

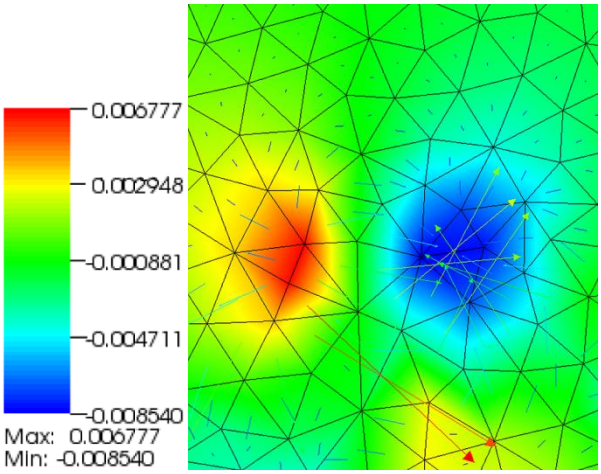


Figure 4-26: Bubble velocity on the unstable pressure zone.

Mixed law		P1		P0	
Solid viscosity (*Pas*)		10	100	10	100
Bubble viscosity= mixed viscosity (normal)		0,13	0,44	1,11	3,29
Bubble viscosity = fluid viscosity			0,18		0,77
2nd method to modify bubble viscosity (smoothed function)			0,022		0,024
1st method to modify bubble viscosity (rectangular function)			0,0067		0,065
Gain in the accuracy of the result (times)	mixture law P1		70		7
	mixture law P0		500		50

Table 4-3: Maximum pressure obtained for different configuration tests (the fluid viscosity is 1 *Pas* for all the tests). The gain in the accuracy of the result is compared between the 1st method to modify bubble viscosity and the result performed with the mixture laws P1 and P0.

4.2.2.2 Flow between two rigid solid particles

The promising results in the above section by modifying the bubble viscosity will be exploited with the previous test cases. Firstly, we consider the fluid flow between rigid particles presented in the above section, in which the bubble viscosity is changed. In this case, we specify the zone where the bubble viscosity must be modified; it is small in the interface area and equals to the fluid viscosity in the other zones (rectangular function) as follows:

$$\eta_b = \begin{cases} 10^{-3}\eta_f & |\alpha| < e \\ \eta_f & \alpha > e \quad or \quad \alpha < -e \end{cases} \tag{4.76}$$

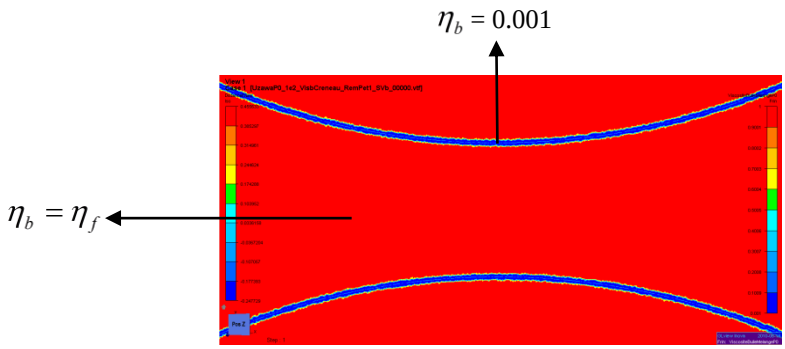


Figure 4-27: Modification of bubble viscosity in the multiphase approach.

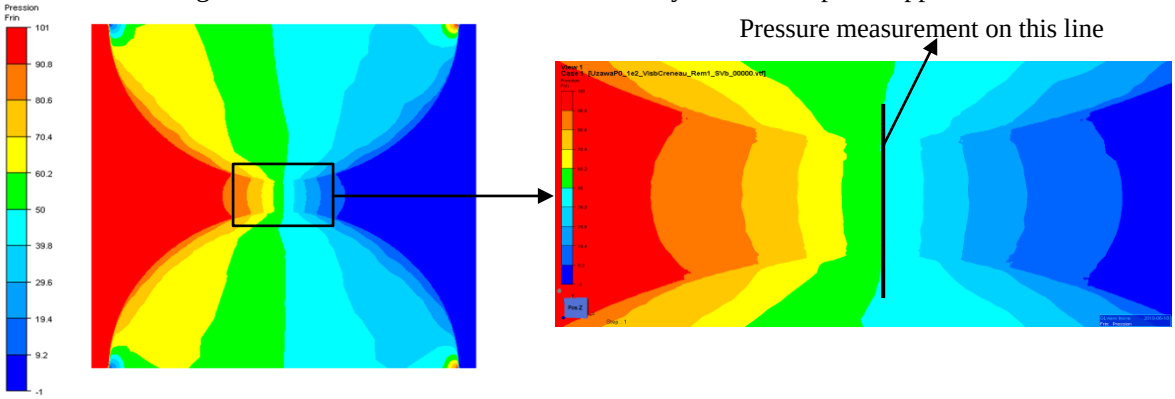


Figure 4-28: Schematic representation of the pressure field.

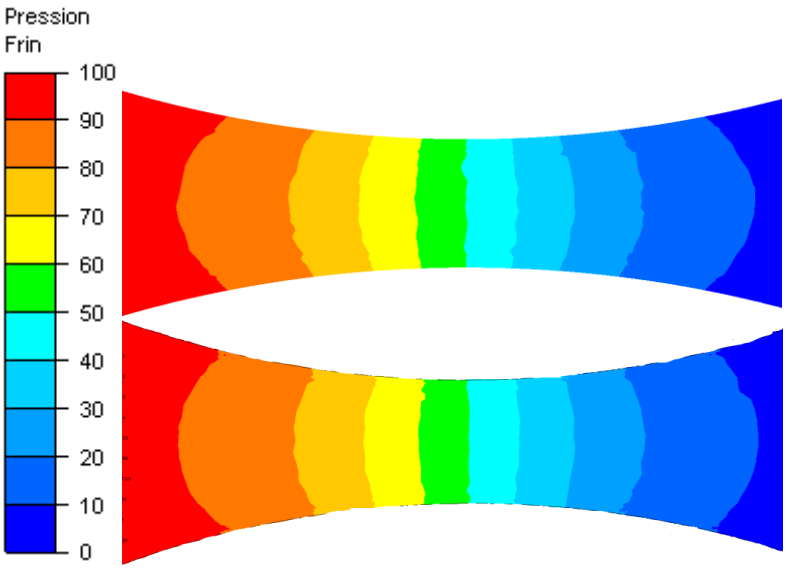


Figure 4-29: Pressure field comparison in the fluid between the monophasic (reference solution) and the multiphase approach after the modification of the bubble viscosity.

The pressure is in very good agreement with the reference monophasic solution (Figure 4-28 and Figure 4-29). We observe that the instability problem disappears at the interface and the pressure is smoothed on the transition zone. A comparison of the augmented Lagrangian with Uzawa algorithm with the "bubble extra-stress" (the new solver SMC) and without the "bubble extra-stress" (the old solver NSTC), called with stabilization and without stabilization method and the modification of bubble viscosity method is depicted in Figure 4-30. As previously, bubble viscosity modification is efficient whereas the added stabilized term on the complete formulation of the augmented Lagrangian method does not improve the lack of stabilization problem.

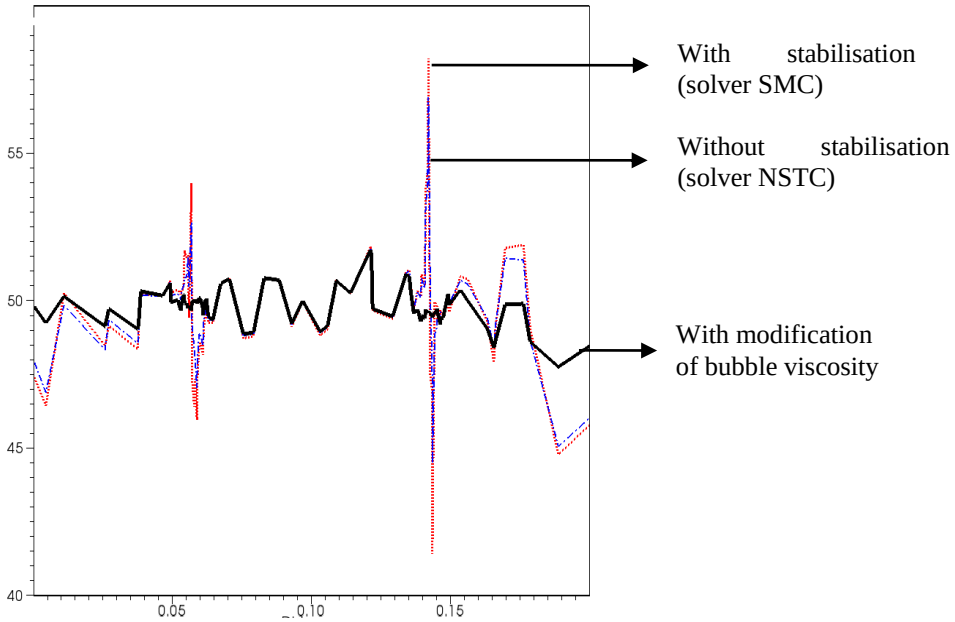


Figure 4-30: Pressure analysis through the thickness with different methods.

4.2.2.3 Tensile test case by an Eulerian approach

The promising results with the modification of bubble viscosity are applied to the resolution of the incompressible elastic test case. In a Lagrangian framework, modification of the bubble viscosity will not avoid oscillations when reaching high deformations. However, these oscillations will only be withdrawn if we consider an Eulerian formulation, on which all the formulation (elastic or viscoelastic) can be expressed correctly. In an Eulerian approach, the fluid surrounding the specimen, as well as the extremities where traction velocities are imposed must be included in the computational domain. We are then face to a multiphase problem similar to the one treated above, where the same oscillation on pressure appear and where we will apply the same stabilization of the viscosity. In this case, we specify the zone where the bubble viscosity must be modified; it is small in the interface area and equals to the fluid viscosity in the other zone (rectangular function) as follows:

$$\eta_b = \begin{cases} 10^{-3}\eta_f & |\alpha| < e \\ \eta_f & \alpha > e \quad or \quad \alpha < -e \end{cases} \tag{4.77}$$

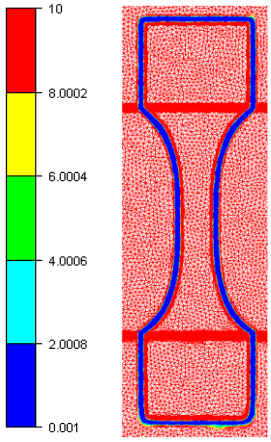


Figure 4-31: Modification of bubble viscosity in the mixture zone in the tensile test by an Eulerian approach.

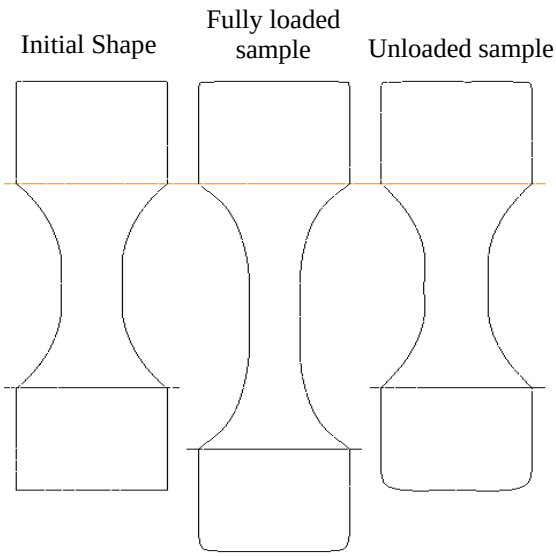


Figure 4-32: Tensile test by an Eulerian method, deformed shape represented by the zero iso-value of the Level-Set function.

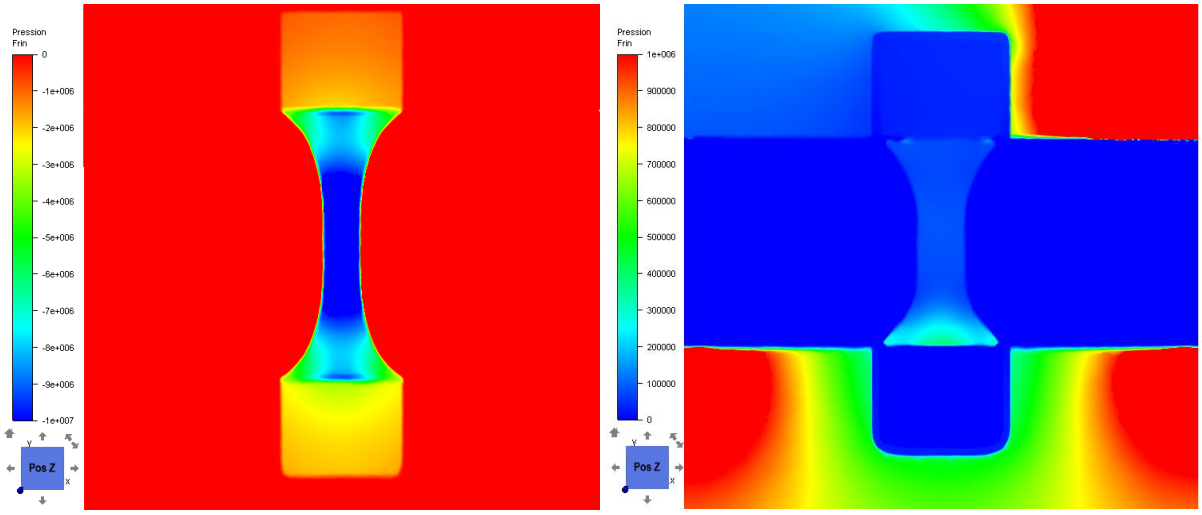


Figure 4-33: Pressure field under loading (left) and unloading (right) with stabilization by modification of the bubble viscosity.

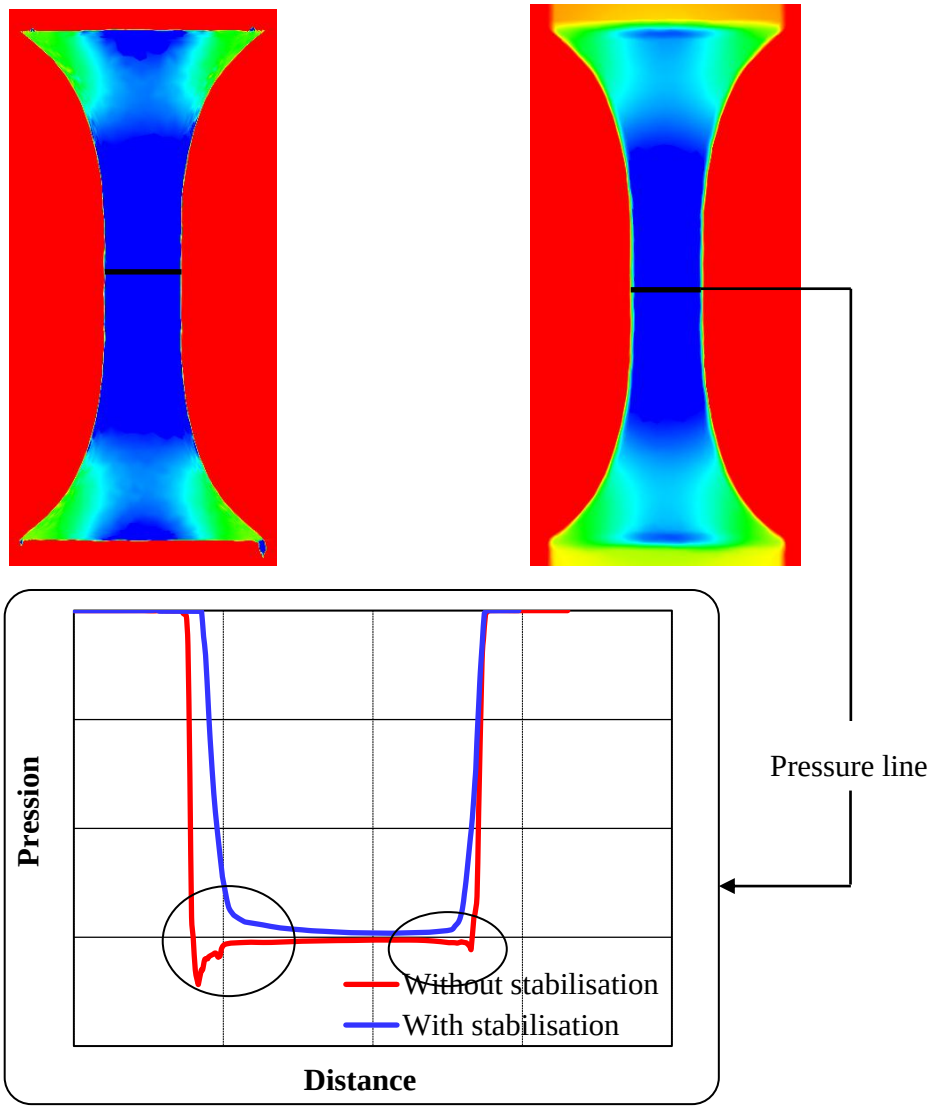


Figure 4-34: Pressure curve without stabilization (red - without modification of the bubble viscosity – left image) and with stabilization (blue - with modification of the bubble viscosity – right image).

Figure 4-32 displays the specimen shape under uploading/unloading in tension, represented by the zero iso-value of the Level-set function. The improvement in the case of the Eulerian method is visible compared to that without stabilization represented previously in chapter 3 (see Figure 3-28). By modifying the bubble viscosity in the unstable zone, we obtained a good representation of the specimen interface. The pressure is also measured in the section, represented in Figure 4-33 and Figure 4-34, which shows to be more stable.

Results are less accurate than those obtained by the incremental technique as a small difference between the initial shape and the shape after recovery appears. There are many factors which may influence the quality of the results, among which the convected Level-Set method, the mesh size and the time step. In fact, Ville and co-workers [90], inspired by the work of Basset et al [95], show the mesh dependency of the accuracy of the convected Level-Set method by a severe test with regards to the diffusion errors. To have a better precision with this method, a good agreement between the mesh and the time step is primordial. Nevertheless, note that the deformation reaches values up to 30%, which is relatively large. The satisfactory results obtained up to now allow us to a more clear regard on future improvement.

4.2.3 Concluding remarks

Two stabilization methods were proposed to improve the results obtained in chapter 3. In spite of the weak effect of the first one on the stabilization problem, the development of the new SMC solver showed several interesting advantages. First, it is possible to display the computed bubble velocity which can help us to retrieve more information in the stabilization problem and understand how the enriched bubble function can improve the quality of resolution. This will probably help us to investigate and develop other stabilization methods in the future. Secondly, thanks to our development, expansion of our methodology to modeling of a complex behavior (like the viscoelastic one, with even one other equation on the extra-stress tensor) would imply to add, as a separate degree of freedom, the bubble extra-stress to the NSTC solver. Fortunately, this work is implicit using the new solver (SMC).

With regard to the second related to the modification of bubble viscosity, modifying the bubble viscosity also optimizes the effect of the stabilized term in the resolution. However, it requires concentrating the modification of bubble velocity only in the unstable zone. The improvement in the simple two phase test, the flow between two rigid solid particles and the tensile test by Eulerian method showed the promising results.

Returning to the preliminary work by modeling the tensile test, a comparison between Lagrangian and Eulerian methods was performed with satisfactory numerical results. For the resolution by the single time step, the perfect recovery was verified whatever strain which may be exceeded 100% of strain. The instability problem in the incremental resolution by the Lagrangian and Eulerian method is very constraining. Nevertheless, thanks to modification of stabilization method, we can even when reaches values up to about 50% of strain, which is relatively large. The satisfactory results obtained up to now allow us to conclude on future improvement, but also to use the actual development on the Kelvin-Voigt and to compare it to experimental curves.

Even if interface stabilities have been partially solved, the problem of dealing with high value of the extra-stress tensor remains. Therefore, one other stabilization technique is exploited in this chapter: the EVSS method.

4.3 Improving stabilization through Elastic Viscous Split Stress (EVSS)

Chapter 2 introduced our objective to develop new numerical techniques to treat viscoelastic, hyper-elastic and visco-hyper-elastic behavior using a mixed formulation *(u, v, p) (displacement, velocity, pressure)*, where the two fields *u* and *v* represent the primary variables of a strain and a strain rate formulation. The results detailed later in chapter 5 will demonstrate that our approach is possible by the confrontation between the numerical simulation and the experimental tensile test with a simple viscoelastic Kelvin-Voigt model. This is more complex model (like visco-hyper-elasticity) will lead to high values on extra-stress. To overcome the difficulties on the loss of ellipticity, we can inspire ourselves in classical methods coming from numerical treatment of liquid viscoelasticity like the EVSS method.

Over the last decades, a lot of research on numerical viscoelastic simulation has been performed. The resolution of the governing equations requires an accurate and stable manner and still being adequate to efficiently handle the multitude of stress unknowns. The most commonly used method based on mixed finite element formulation was introduced by Baaijens [16] for viscoelastic flow analysis. Two basic problems needed resolution: i) the presence of convective terms in the constitutive equation whose relative importance, especially at high Weissenberg number (*We*) and ii) the choice of discretization spaces of the independent variables (velocity, pressure, extra-stresses and auxiliary variables). There have been important developments in the numerical modeling to overcome these problems. The lack of ellipticity of the momentum equation is resolved by using several algorithms such as Explicitly Elliptic Momentum Equation (EEME) formulation introduced by King et al. [130], Elastic Viscous Split Stress (EVSS), formulation of Rajagopalan et al. [17], succeed by the work of Beris and Edwards [18]. Guenette and Fortin [19] introduced a modification of the EVSS formulation, known as the Discrete EVSS method (D.E.V.S.S.), one of the most robust formulations currently available due to their simplicity and can be applied to a variety of constitutive equations more easily, while maintaining stability. To overcome the hyperbolic problem linked to the constitutive equation, all these methods may be coupled to SU (Streamline-Upwind), SUPG (Streamline-Upwind–Petrov–Galerkin) or DG (Discontinuous-Galerkin) techniques for FEM [7] [16] [20] [21].

Then, in this section we present first a short review on computational methods for viscoelasticity in 3D. Next we detail the technique used in our work.

4.3.1 Short review on computational methods used in viscoelastic flow

In the following we consider only one mode where the flows equations are:

$$\begin{cases} -\nabla p + \nabla \cdot \tau = 0 \\ \nabla \cdot v = 0 \end{cases} \tag{4.78}$$

Since differential models will be treated, we suppose a general form of the evolution equation of the extra-stress tensor τ :

$$\theta\left(\frac{d\tau}{dt} - \nabla v\tau - \tau\nabla^t v\right) + f\left(\tau, \varepsilon(v)\right) = 2\eta_e \varepsilon(v) \tag{4.79}$$

where θ is the extra-stress relaxation time, $\eta_e = G\theta$ is an "elastic" viscosity, and $f\left(\tau, \varepsilon(v)\right)$ is a function dependent on the constitutive equation.

4.3.1.1 Mixed methods

Marchal and Crochet [131] proposed the mixed formulation of the isothermal incompressible viscoelastic flow problem. Basically, this is the extension of the velocity-pressure problem where the finite element spaces (V_h, P_h, S_h) for the 3-field problem (v, p, τ) was defined, and that respects the *inf-sup* condition on (v_h, p_h) and (v_h, τ_h). Find $(v, p, \tau) \in V \times P \times S$ such that:

$$\begin{cases} \int_\Omega w \cdot \left(-\nabla p + \nabla \cdot \tau\right) = 0 \\ \int_\Omega q \nabla \cdot v = 0 \\ \int_\Omega \phi \left[\theta \left(\frac{d\tau}{dt} - \nabla v \tau - \tau \nabla^t v \right) + f\left(\tau, \varepsilon(v)\right) - 2\eta_e \varepsilon(v) \right] = 0 \end{cases} \tag{4.80}$$

The fundamental difficulty associated to this mixed form is that a solvent viscosity needs to be introduced (to give an elliptic contribution to the system) and it gets computationally prohibitive for elements with higher interpolation order.

4.3.1.2 E.V.S.S. (Elastic Viscous Stress Splitting)

One way to overcome the absence of a viscous term is a change of variable, also known as the Elastic Viscous Stress Splitting (EVSS) formulation which was first proposed by Rajagopalam and co-workers [17]. The method introduces the strain rate tensor as an addition unknown. Naturally, it proposes the replacement of the extra-stress τ by $\sum$:

$$\sum = \tau - 2\eta_s \varepsilon(v) \tag{4.81}$$

where η_s is a solvent viscosity. This is equivalent to a decomposition of the extra-stress in a purely viscous $2\eta_s \varepsilon(v)$ and a viscoelastic $\sum$ parts. The system of resolution may be resumed:

Find $(v, p, \sum) \in V \times P \times S$ such that:

$$\begin{cases} \int_\Omega w \cdot \left(-\nabla p + 2\eta_s \nabla \cdot \varepsilon(v) + \nabla \cdot \sum\right) = 0 \\ \int_\Omega q \nabla \cdot v = 0 \\ \int_\Omega \phi \left[\theta \left(\frac{d\tau}{dt} - \nabla v \sum - \sum \nabla^t v \right) + f\left(\sum, \varepsilon(v)\right) - 2\eta_e \varepsilon(v) \left(\frac{d\varepsilon(v)}{dt} - \nabla v \varepsilon(v) - \varepsilon(v) \nabla^t v \right) \right] = 0 \end{cases} \tag{4.82}$$

Unfortunately, this change of variables does not yield a closed expression for every constitutive equation. Furthermore, depending on the constitutive law, a third order derivative of the velocity field may be required due to the arising of a convective derivative of the strain rate tensor. To circumvent this problem, Rajagopalam and co-workers [17] considered the strain rate tensor as a separate unknown, obtained by an L2-projection of the velocity gradient. Whereas, Szadi et al [132] introduced the EVSS-G/DG methods which computes the instead of the strain rate tensor, a

velocity gradient field in the same space as $\sum$. The authors used also a Discontinuous Galerkin technique rather than Streamline Upwind (SU).

4.3.1.3 D.E.V.S.S. (Discrete Elastic Viscous Stress Splitting)

Guenette and Fortin [19] introduced a variant of the EVSS formulation, known as the Discrete EVSS method (D.E.V.S.S.). This method is one of the most robust formulations currently available and has been used by several authors within the context of viscoelastic fluids, particularly for the numerical treatment of complex rheological models. It introduced a stabilizing elliptic operator in the momentum equation, avoiding the use of the objective derivative of the strain rate tensor:

$$\sum = \tau - 2\eta_{stable}\varepsilon(v) \tag{4.83}$$

where η_{stable} is an arbitrary viscosity to be chosen. If the stabilizing viscosity is chosen as the solvent viscosity, the problem is:

find $(v, p, \tau, H) \in V \times P \times S \times H$ such that:

$$\begin{cases} \int_\Omega w \cdot \left[-\nabla p + \nabla \cdot \tau + \nabla \cdot \left(2\eta_{stab}\varepsilon(v) \right) - \nabla \cdot \left(2\eta_{stab} H \right) \right] = 0 \\ \int_\Omega q \nabla \cdot v = 0 \\ \int_\Omega \phi \left[\theta \left(\frac{d\tau}{dt} - \nabla v \tau - \tau \nabla^t v \right) + f\left(\tau, \varepsilon(v)\right) - 2\eta_e \varepsilon(v) \right] = 0 \\ \int_\Omega \Phi \left(H - \varepsilon(v) \right) = 0 \end{cases} \tag{4.84}$$

In the formulation, an elliptic operator $\left[2\eta_{stable} \left(\varepsilon(v) - H \right) \right]$ is introduced where H is a discrete approximation of the strain rate tensor $\varepsilon(v)$. In analogy with the EVSS-G method, Baaijens et al. [20] proposed the DEVSS-G method in that a projection of the velocity gradient is made instead of the strain rate tensor. All these methods may be coupled to SU, SUPG or DG strategies. An adaptive version of the DEVSS method was also investigated by Sun [133]. The authors proposed the choice of η_{stable} in such a way that the elastic and viscous contributions are of the same amplitude.

In our case, we will follow a classical mixed formulation of the problem on (u, v, p). We rather consider a time step marching scheme allows splitting the system in two subsystems made of the viscoelastic constitutive equation and the flow equations. In what concerns the flow equations, the choice of the P1+/P1 element for the velocity-pressure problem gives rise to a bubble stabilization technique similar to the D.E.V.S.S. method, whereas the evolution equations solved through our methodology mentioned in the previous chapters. The numerical results for the Kelvin-Voigt viscoelastic model, the Neo-Hookean hyper-elastic model and the visco-hyper-elastic model by the EVSS will be later presented in the following chapter.

4.4 Résumé du chapitre en français

Dans le chapitre 2, nous avons décrit notre méthodologie de résolution et démontré la possibilité de résoudre un problème complexe comme la viscoélasticité ou l'interaction fluide-structure par une approche multiphasique. Ensuite, l'étude préliminaire au chapitre 3 a révélé la nécessité des efforts sur la stabilisation du solveur pour surmonter certains problèmes d'instabilité.

Ce chapitre est donc consacré à la mise en œuvre d'un nouveau solveur permettant de stabiliser la méthode de résolution numérique et d'ajouter les termes manquants dans le solveur réel. Trois méthodes de stabilisation sont proposées pour améliorer les résultats du chapitre 3 : la première est basée sur l'élément finis mixtes stabilisés, la seconde est liée l'introduction d'une viscosité bulle et la dernière est basée sur la méthode EVSS.

La première partie de ce chapitre détaille la résolution du problème de Navier-Stokes compressibles avec "extra-contrainte" dans le contexte de la méthode éléments finis mixtes stabilisés P1+/P1+. Avec ce nouveau concept, la pression est aussi enrichie par une fonction d'interpolation dans l'espace des petites échelles, dit "fonction bulle", ce qui n'existe pas pour les éléments classiques "Mini-Eléments P1+/P1". La mise en œuvre dans CimLib® est détaillée, puis appliquée aux deux cas de benchmark cités précédemment.

Grâce à ce développement, l'implémentation des termes supplémentaires comme "l'extra-contrainte bulle" et la "variation de volume" s'avère plus simple qu'avec l'ancien solveur qui pouvait donner lieu à une vraie difficulté de programmation. Par ailleurs, ce développement sera un réel avantage lors de l'extension à un comportement complexe où l'utilisation de ce nouveau solveur sera indispensable.

Concernant le cas élastique pur dans le contexte de l'approche lagrangienne, les bons résultats obtenus avec un unique incrément de résolution confortent notre stratégie de résolution. L'apport sur la stabilisation dans le cas d'une approche Lagrangienne incrémentale ou dans le cas de l'approche Eulérienne est par contre plus faible. Néanmoins, le développement du nouveau solveur SMC a montré plusieurs avantages intéressants. Premièrement, le champ de vitesse bulle qu'il restitue nous fournit plus d'informations pour analyser et comprendre le rôle de l'enrichissement de fonction bulle au sein de la méthode de stabilisation. En effet, la vitesse de bulles tend à compenser le fort saut de pression près de la zone instable. Cela va sans doute aider à développer une nouvelle méthode de stabilisation à l'avenir. Deuxièmement, grâce à notre développement, l'extension de notre méthodologie à la modélisation d'un comportement viscoélastique plus complexe sera facilitée. Elle aurait impliqué d'ajouter, comme un degré de liberté séparé, la extra-contrainte bulle dans le solveur NSTC. Ce travail est implicite dans le nouveau solveur (SMC).

Pour le cas d'écoulement entre deux particules rigides, malgré une résolution complète grâce à ce nouveau solveur SMC, nous n'avons pas obtenu de meilleurs résultats au niveau de la pression. La raison de cet échec est clairement expliquée dans la section 4.1.4. Pour surmonter ce problème de stabilisation, l'extra-contrainte discontinue doit être rendue continue par interpolation dans le cadre de la méthode "d'extrapolation des contraintes". L'idée est de projeter l'extra-contrainte, calculée dans les éléments, sur les nœuds par une somme moyennée des éléments voisins, appelés le paquet des éléments illustrés dans la Figure 4-17.

La deuxième partie du chapitre décrit l'approche novatrice de stabilisation basée sur la viscosité bulle dans l'élément fini mixte. L'étude de cette méthode est liée aux effets de la viscosité bulle

sur les termes de stabilisation. En effet, ces termes de stabilisation peuvent disparaître près de la phase solide ou la viscosité devient très élevée et très différente de la phase solide à la phase liquide, donc le problème devient instable. La solution proposée pour surmonter cet obstacle est d'optimiser la viscosité dans cette zone de mélange, principalement dans la résolution dans les petite-échelles. Par conséquent, la viscosité bulle peut être différente de celle des phases où elle est introduite pour contrôler l'effet de stabilisation.

Plusieurs applications utilisant cette méthode de stabilisation sont analysées. Enfin, l'influence de la viscosité bulle et l'amélioration de la simulation numérique sont détaillées avec des résultats satisfaisant qui vont nous amener plus loin dans la simulation du comportement viscoélastique Kelvin-Voigt dans le chapitre 5.

En conclusion au travail préliminaire modélisant l'essai de traction, une comparaison entre les méthodes lagrangiennes et eulériennes a été réalisée avec des résultats numériques encourageants. Pour la résolution par un incrément unique, l'élasticité parfaite est conservée quelle que soit la déformation qui peut dépasser 100%. Les instabilités dans la résolution incrémentale par la méthode de Lagrange et d'Euler sont réduites, néanmoins, grâce à la méthode de stabilisation, on peut quand même atteindre des valeurs de déformation de 50%, ce qui est relativement important. Les résultats satisfaisants obtenus jusqu'à présent permettent d'espérer une amélioration dans l'avenir. Aussi pouvons-nous envisager les premières confrontations à l’expérience.

Toutefois, la complexité de la résolution dans le cas d’un comportement visco-hyper-élastiques rend un schéma stabilisé numérique nécessaire. Un bref résumé des méthodes stabilisées dans la littérature est présenté. Les résultats numériques pour le modèle viscoélastique de Kelvin-Voigt, le modèle hyper-élastique de Néo-Hookéen et le modèle visco-hyper-élastiques de Billon par la méthode EVSS sera ensuite présenté dans le chapitre suivant.

Chapter 5

5 Modeling of Viscoelastic, Hyperelastic and Visco-Hyper-Elastic Model

5 Modeling of Viscoelastic, Hyperelastic and Visco-Hyper-Elastic Model 139

5.1 Experimental tensile tests....141

5.1.1 Experimental data base....141

5.1.2 Experimental results analysis....145

5.2 Numerical-experimental comparison....151

5.3 Modeling visco-hyper-elastic behavior....154

5.4 Application of the EVSS stabilized solver to viscoelastic, hyperelastic and visco-hyper-elastic behaviors....157

5.4.1 Kelvin-Voigt viscoelastic model....157

5.4.2 Neo-Hookean viscoelastic model....159

5.4.3 Visco-hyper-elastic model....165

5.5 Résumé du chapitre en français....170

Since perfect elasticity by comparison between the two approaches (Eulerian and incremental Lagrangian) was validated in chapter 4, this chapter focuses on the modeling results where more complex behavior is taken into account: the viscoelastic Kelvin-Voigt, the hyper-elastic Neo-Hookean and the visco-hyper-elastic models will be numerically simulated.

First, we show the results on the viscoelastic Kelvin-Voigt behavior. As the behavior of a polymer depends strongly on the temperature, the validation will be performed on PMMA from its solid state to its flowing state. The experimental tensile tests are performed and compared to simulation results. The Lagrangian and Eulerian approaches are also compared.

Although the good promising for the modeling of viscoelastic behavior of polymer with the viscoelastic Kelvin-Voigt model, the enrichment of polymer behavior is required due to the limit of this simple classic model. Thus, the second section will detail the implementation and exploitation of a visco-hyper-elastic behavior in the FE library CimLib®.

After modeling of the visco-hyper-elastic behavior and the validation in the calculation on the material point, because of the complexity of its resolution in mixed finite elements, our study concerns the adaptation of a stabilized method to deal with it in 3D. Thus, application of the EVSS stabilization method [17] [18] will be detailed in the last section to measure the efficiency, followed by its application to the Kelvin-Voigt viscoelastic, Neo-Hookean hyper-elastic and also the visco-hyper-elastic models.

5.1 Experimental tensile tests

With the aim of validating our methodologies, we did experimental tensile tests and compared with the simulation results, to check at least the order of magnitude. The strategy is to move from experimental tests to numerical simulations and to promote the approach in a physical base through three steps:

- first step is to perform and analyze mechanical testing on one polymer from its solid to its liquid state using different temperatures. To make the problem simpler an amorphous PMMA was chosen to avoid drastic changes due to fusion. This will be done through uploading/unloading and uploading/relaxation tensile experiments,
- second step is to fit and validate the modeling of Kelvin-Voigt's viscoelastic behavior compared with the experimental tests. This will impose to evaluate only the low strain behavior,
- third step, numerical simulation are compared to experimental data. Finally, in the long term, it will be possible to introduced a more relevant model for polymer behavior within our general methodology.

5.1.1 Experimental data base

Polymer is a PMMA, Altuglas® V825T, supplied by Arkema. Samples were tooled from the injection molded plate in the direction perpendicular to the flow direction during injection. Dimensions of the samples are specified in Figure 5-1. These samples have a small central zone of reduced width, which aims a localized deformation, with rectilinear walls, which aims at keeping local stress uniaxial.

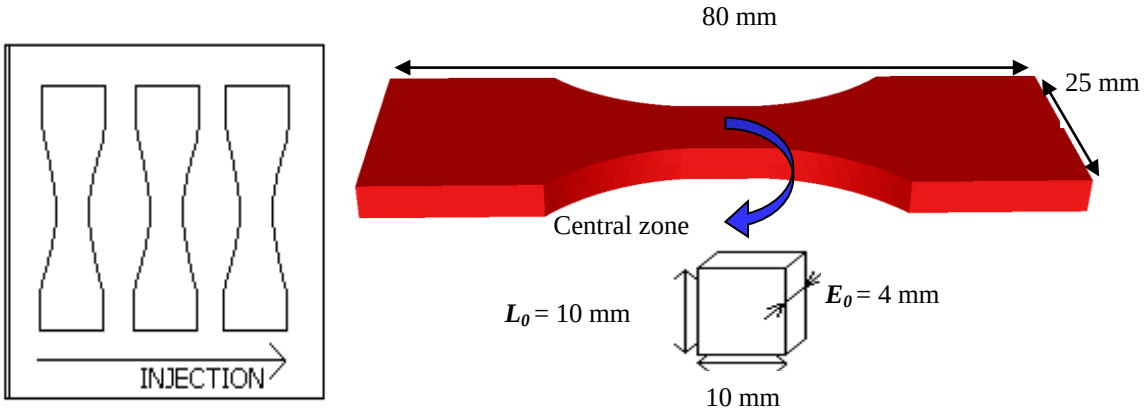


Figure 5-1: Samples tooled from the PMMA plate and its initial form.

The behavior of PMMA drastically depends upon the temperature close to its glass transition temperature (130°C). To gather data representative for both the solid viscoelasticity and the liquid viscoelasticity (to be able to have different set of parameters in our numerical resolution), we performed tests from 90°C to 163°C with two loading types: uploading/unloading and uploading/relaxation (Table 5-1). Strain rate was chosen low, $0.0025s^{-1}$ and $0.1s^{-1}$ to avoid self-heating.

	90°C	110°C	163°C
Rupture loading	x	x	
Loading/unloading	x	x	
Relaxation	x	x	x
Strain rate	$0.0025s^{-1}$	$0.0025s^{-1}$	$0.1s^{-1}$

Table 5-1: Experimental performed tests.

Tests were performed using an exponential crosshead velocity, which should allow strain rate to have low variations during the test. Anyway, for exploitation true instantaneous strain rate is deduced from strain vs. time curves and experiments were referred to using an average strain rate.

Local strain during tension was deduced from the tracking of a random speckle pattern (Figure 5-2) and digital image correlation (DIC) in post processing. DIC was post processed using the commercial software Aramis®.
Pattern was applied on both the front and one lateral faces.

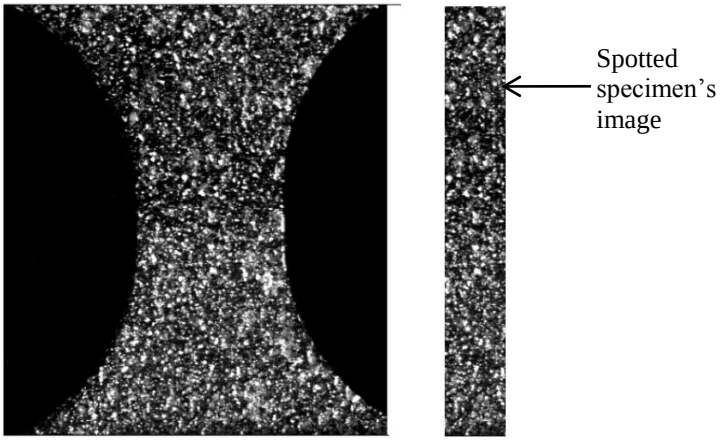


Figure 5-2: Spotted specimen and its image.

Knowing that the quality of this measurement is directly related to the quality of the images let us quote some important points on the experimental tensile tests:

- a random speckle pattern needs to be overlaid on the specimen. Aerosol spray paint black and white is used to make the speckle pattern. The speckle pattern consists of a black base coat which is applied to the entire surface of the specimen. Then, white speckles are laid over the black base coat (see Figure 5-2). This is done as many times as necessary to ensure full recovery,

- to perform 3D measurements patterns were sprayed both on the front and on a lateral face of the samples,

- depending on the level of deformation, we need to ensure that the speckle pattern will not take off during the test or induce artifacts in the measurement of mechanical deformation on the surface of the specimen, especially at high temperatures and large deformation,

- one of the major techniques for optical measuring is the lighting in the specimen area. Indeed, with the rates of 30 frames/second for recording the images, natural light is not sufficient for lighting. Therefore, halogen lamps or high-power projectors could be used. However, halogen lamps or high-power projectors would impact temperature of the

material. Finally, two LED-based spots were chosen to guarantee optimum illumination of the measurements areas. This white light provided optimized grayscale, has no thermal heating,

- another important step is the image focusing. The objective must be perpendicular to the direction of mechanical solicitation, placed in front of the measurement area to avoid optical distortion of the image,

- to follow the evolution of deformation of the specimen we could use a system with two synchronized cameras. This allowed us to record the images of specimens from two different angles, i.e. the specimen front ace and the lateral face. Using the two cameras may avoid the scale problem, e.g. when the dimension of lateral side is too small compared to that of the front side. However, due to the bulky oven that heat up the sample, this does not permit to set up the second camera inside the lateral side. Practically, a prism system inside the oven (see Figure 5-3), which reflect the image of lateral side on the same plane as the front side (Figure 5-2), was used. It is therefore possible to measure the deformations in the three main directions by a single capture image.

At 90 and 110 °C, tensile tests were performed using a universal tensile machine (Figure 5-3) with the above described video extensometer.

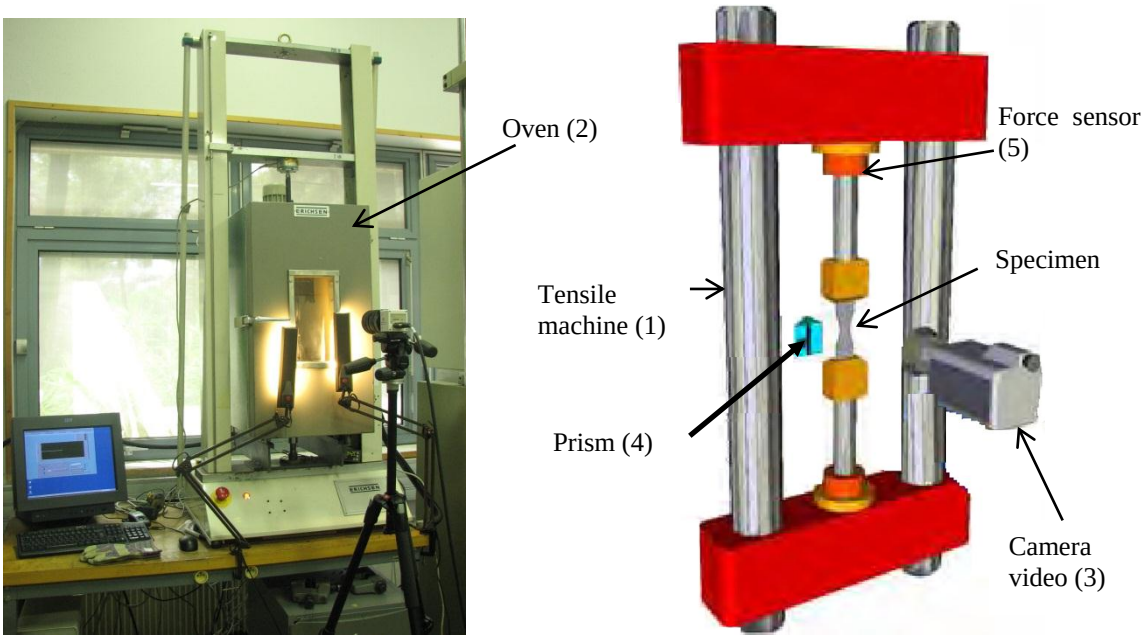


Figure 5-3: Test bench for 90°C and 110°C.

(1) : Tensile machine with the maximum effort to 2000N,

(2) : Oven that heat up the sample,

(3) : Camera helps to capture the sample's image,

(4) : Prism that reflects the sample's image in thickness,

(5) : Force sensor.

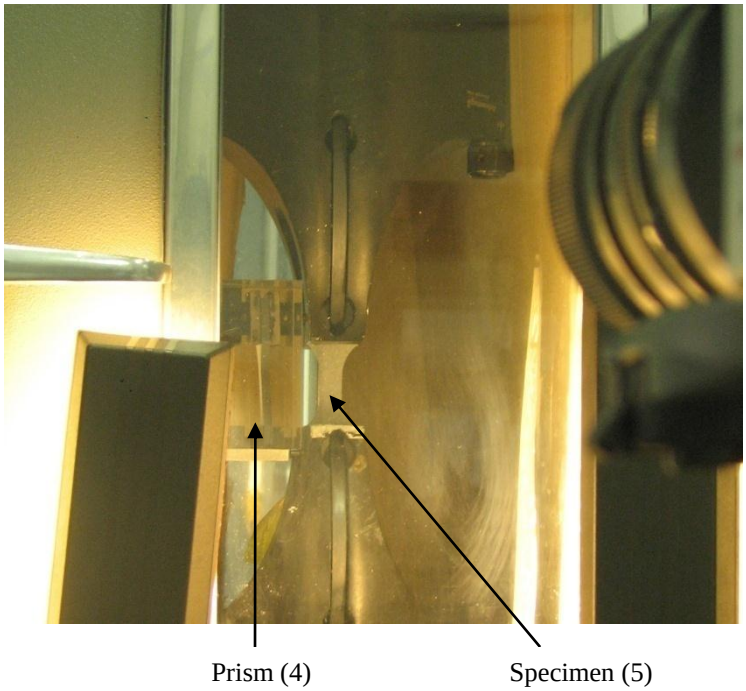


Figure 5-4: Spotted specimen and its image through the prism.

At 163°C, PMMA begins nearly to flow, thus we used an elongationnal rheometer (RME) (Figure 5-6) and other sample geometry (Figure 5-5).

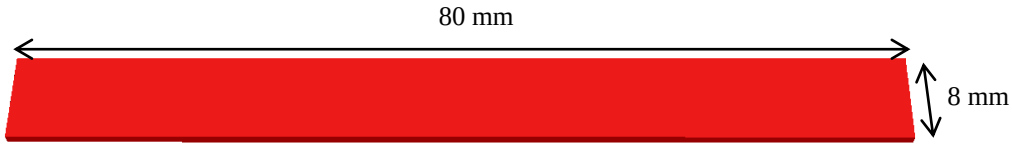


Figure 5-5: Specimen's shape for the relaxation test at 163°C.

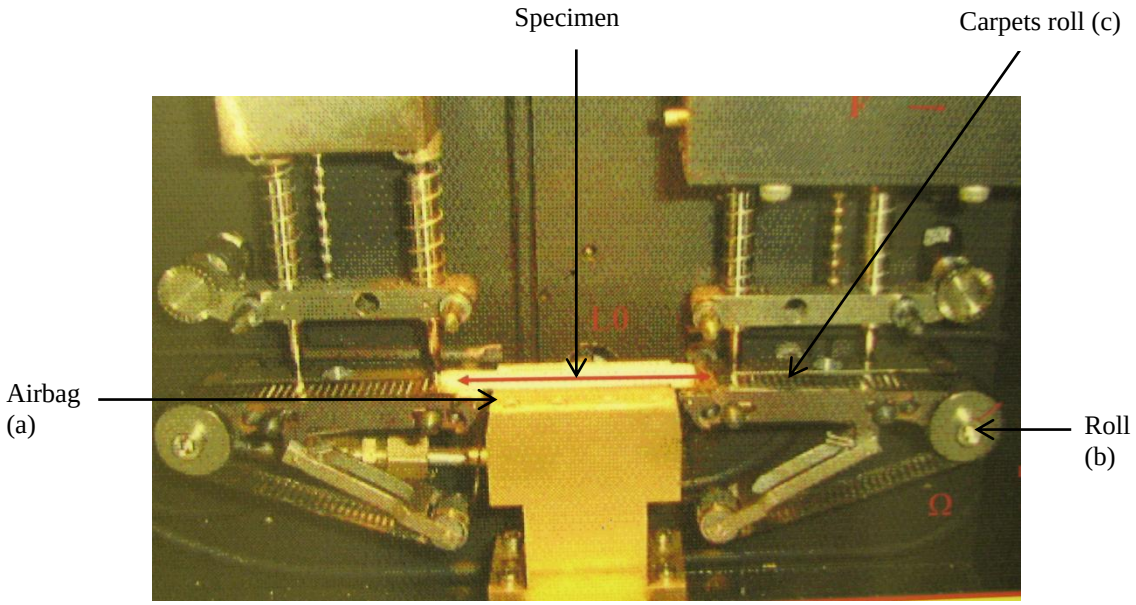


Figure 5-6: Test bench for 163°C.

(a) : It pushes the fluid to avoid the specimen stuck within the bench,

(b) : It rolls which drive the carpet roll,

(c) : Two carpet rolls pull the specimen in two directions with the maximum effort of 1N,

5.1.2 Experimental results analysis

Thanks to the force sensor (Figure 5-3), we can resume the curves which present the evolution of the force under the different solicitations as loading up to rupture, loading/unloading and relaxation at 90°C, 110°C and 163°C.

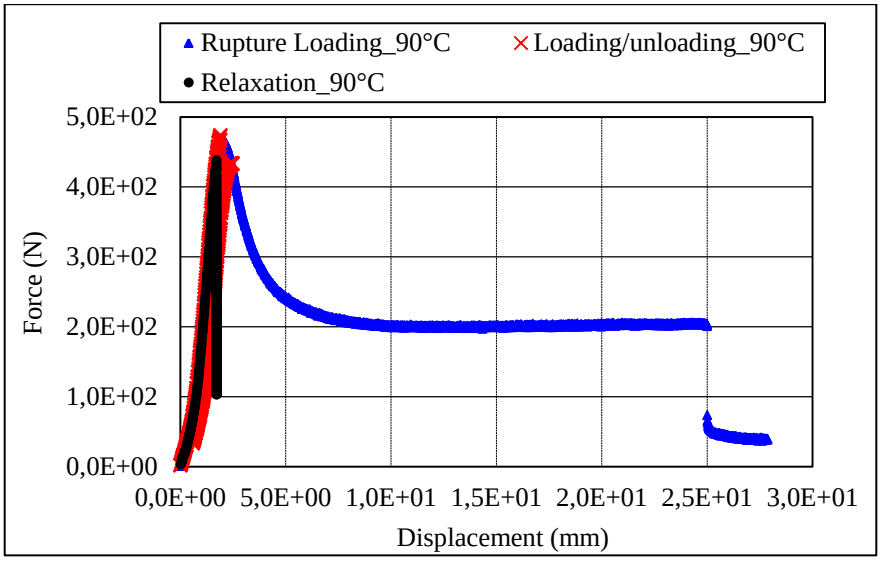


Figure 5-7: Experimental curve force/displacement at 90°C under different solicitations (loading up to rupture, loading/unloading and relaxation).

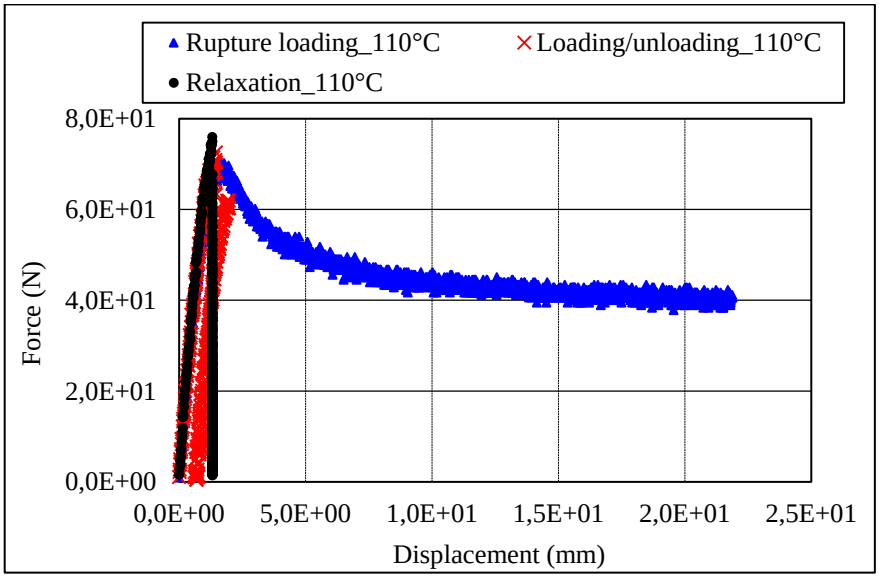


Figure 5-8: Experimental curves force/displacement at 110°C under different solicitations (loading up to rupture, loading/unloading and relaxation).

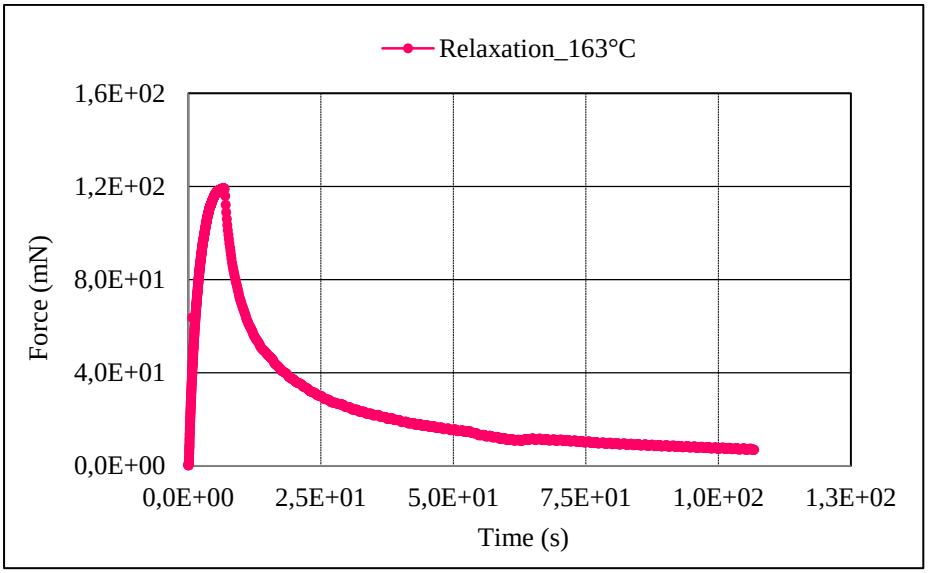


Figure 5-9: Experimental curve force/displacement at 163°C under a relaxation test.

Experimental results analysis is then performed using the industrial software Aramis®. The principle is to compare the digital images and calculate the displacements in an interesting region according to an original image. During the analysis, the software compares the grey patterns of these areas frame by frame, by decomposing the image into small size rectangular sub-images [134] as illustrated in Figure 5-10. Displacements of points are calculated from this comparison.

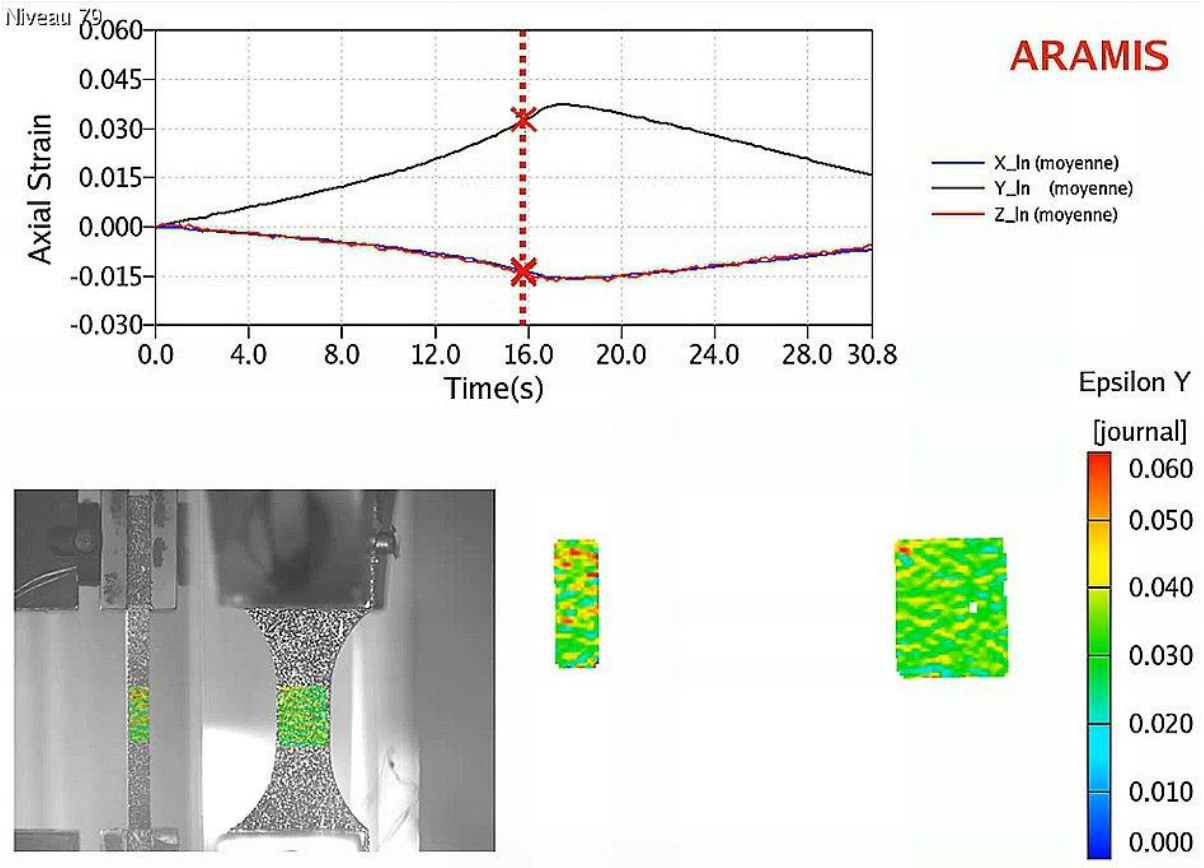


Figure 5-10: Post processing by image correlation analysis.

Despite what is displayed in Figure 5-10, where strain seems quite non-homogeneous because of small deformations and the strain distribution differences remain very small, we may consider that the strain is homogenous. Note that the true strain measurements in the principal direction *I* are the Hencky strain:

$$\varepsilon_i = \ln\left(\frac{l_i}{l_{i0}}\right) \tag{5.1}$$

where l_i and l_{i0} are the current and initial length in the direction *i*. Stress is calculated by:

$$\sigma = \frac{F_0}{E_0 L_0} = \frac{F(t)}{E(t)L(t)} = \frac{F(t)}{E_0 e^{\varepsilon_{xx}} L_0 e^{\varepsilon_{zz}}} = \frac{F(t)}{E_0 L_0 e^{(\varepsilon_{xx}+\varepsilon_{zz})}} \tag{5.2}$$

where F_0, E_0 and L_0 are the force, the initial thickness and the initial length, respectively. ε_{xx} and ε_{zz} are the strain in *x* and *z* direction. Results in Figure 5-11, Figure 5-12, Figure 5-13 and Figure 5-14 display the stress vs. strain during loading/unloading or stress vs. time during relaxation, thanks to the software Aramis® with a local 3D measurement of deformation.

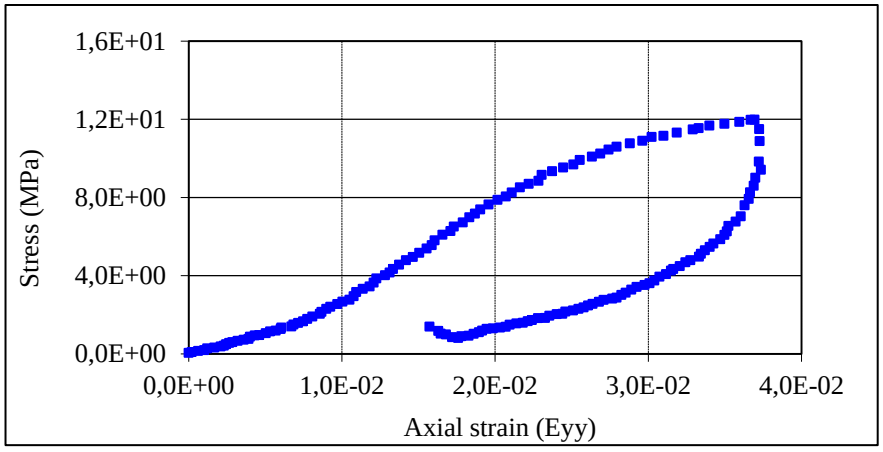


Figure 5-11: Non monotonic tensile tests (loading/unloading) at 90°C.

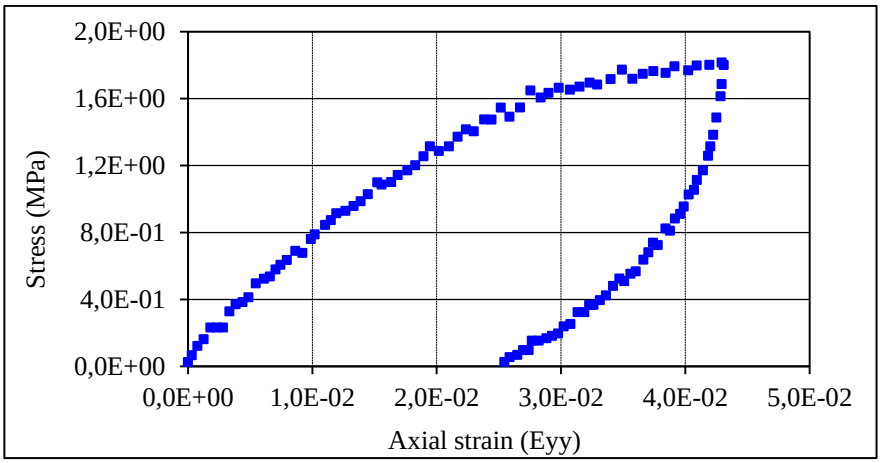


Figure 5-12: Non monotonic tensile tests (loading/unloading) at 110°C.

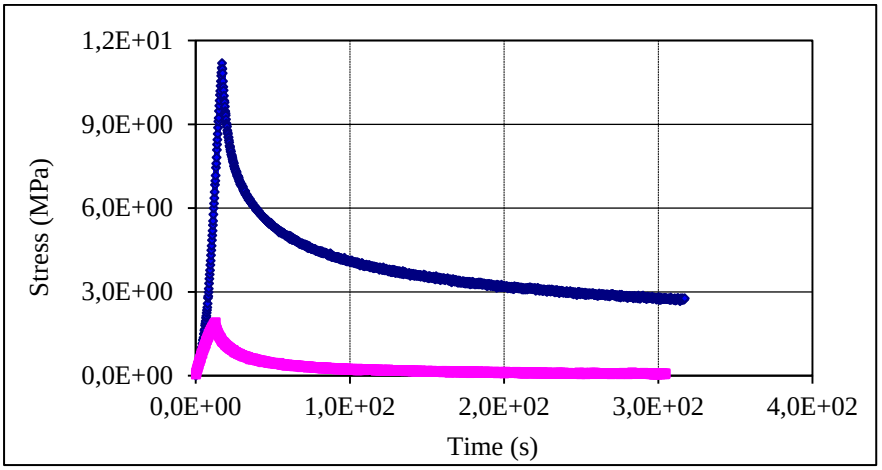


Figure 5-13: Relaxation tests. Comparison between 90°C (blue) and 110°C (pink).

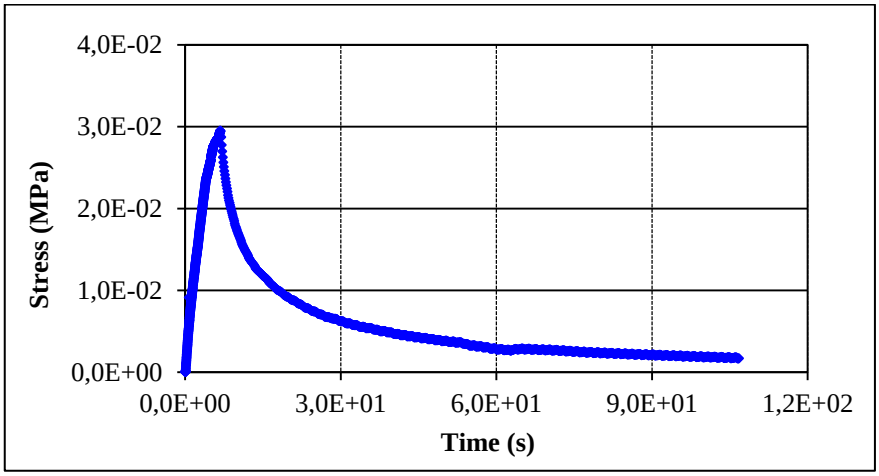


Figure 5-14: Relaxation tests at 163°C.

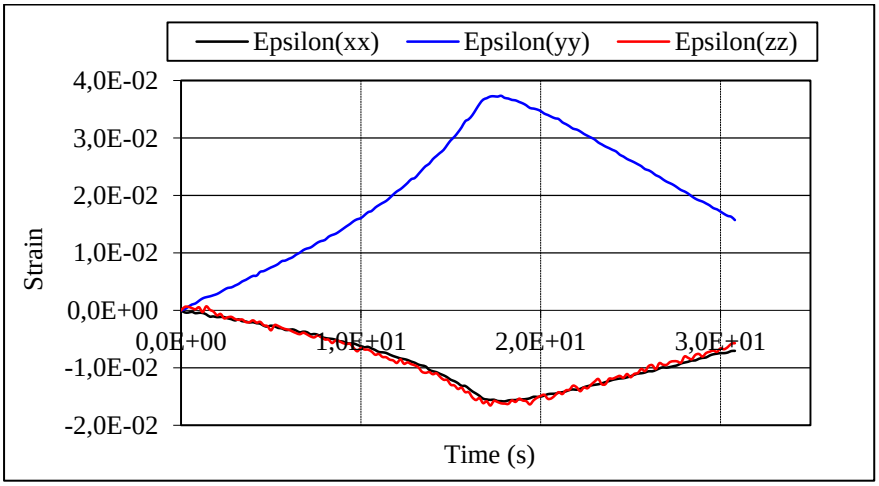


Figure 5-15: Comparison between the strain in the three directions at 90°C.

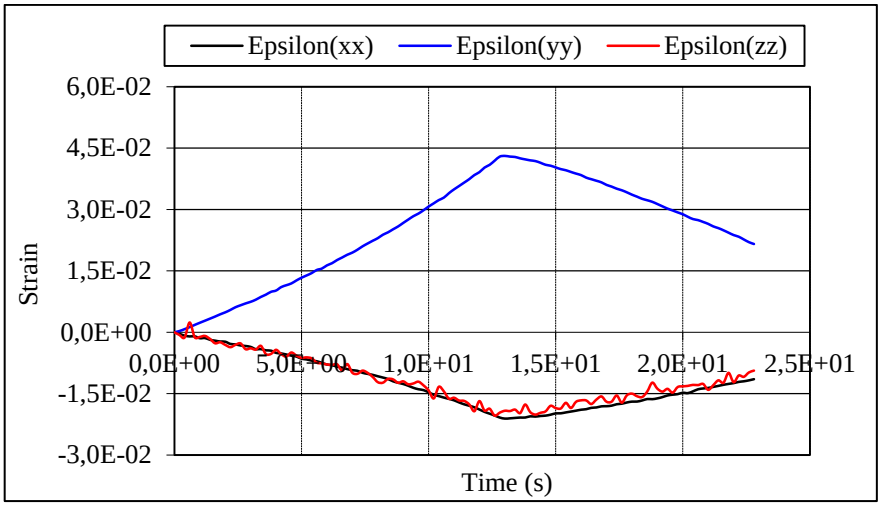


Figure 5-16: Comparison between the strain in the three directions at 110°C.

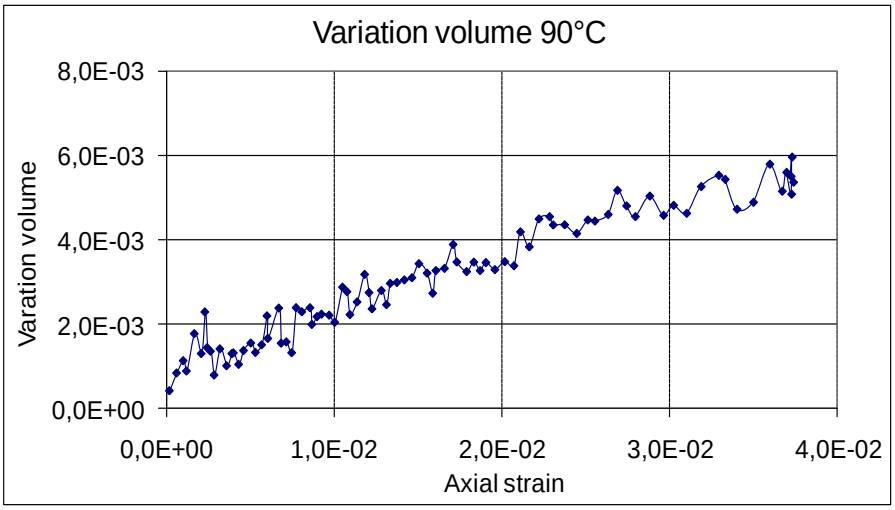


Figure 5-17: Volume variations at 90°C.

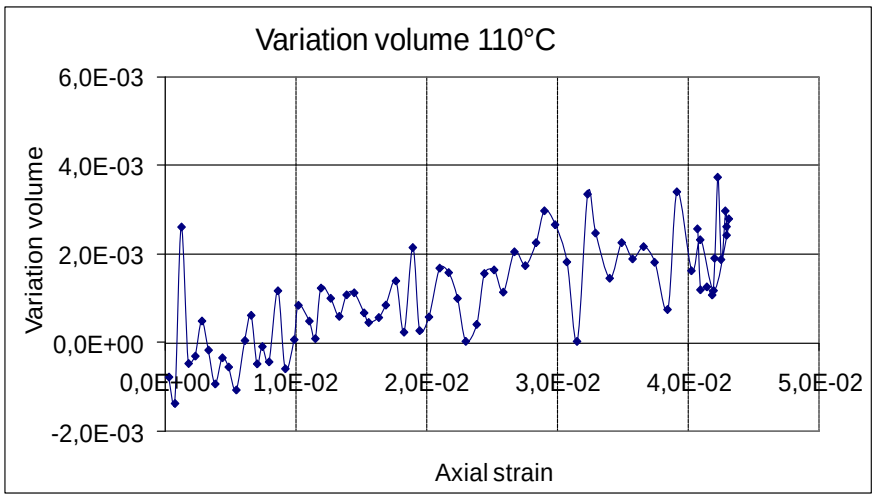


Figure 5-18: Volume variations at 110°C.

Figure 5-15 and Figure 5-16 illustrate that the transversal strain and the strain in the specimen thickness are nearly similar, thus the isotropic hypothesis is verified. In addition, the variation of

volume remains negligible (Figure 5-17 and Figure 5-18), the PMMA can be considered as an incompressible isotropic material.

Moreover, the existence of loading/unloading loops as well as of relaxation validates the viscoelastic nature of the behavior.
Thel Kelvin-Voigt model was used to analyze experimental results. Related parameters were identified by the first linear part of the loading curve. Two methods, incremental Lagrangian and Eulerian were used to illustrate our methodology, in 2D and in 3D, and compared with the experimental results.

Parameters	90°C	110°C	163°C
Young's modulus (*Pa*)	$3e^8$	$7e^7$	$3e^4$
Viscosity (*Pas*)	$1e^4$	$1e^4$	$3e^4$

Table 5-2: Parameters identified for the Kelvin-Voigt model.

5.2 Numerical-experimental comparison

Figure 5-19 displays the longitudinal (σ_{yy}) stress results obtained through simulation in 2D and 3D (incremental Lagrangian and Eulerian) at 110°C. the solver used here is our complete SMC ("Stokes Mixte Complet") with modification with the bubble viscosity to have a more "proper" pressure at the interface. Results show a good repartition of stress inside the specimen, for which the central zone is considered as homogeneous in all directions of deformation.

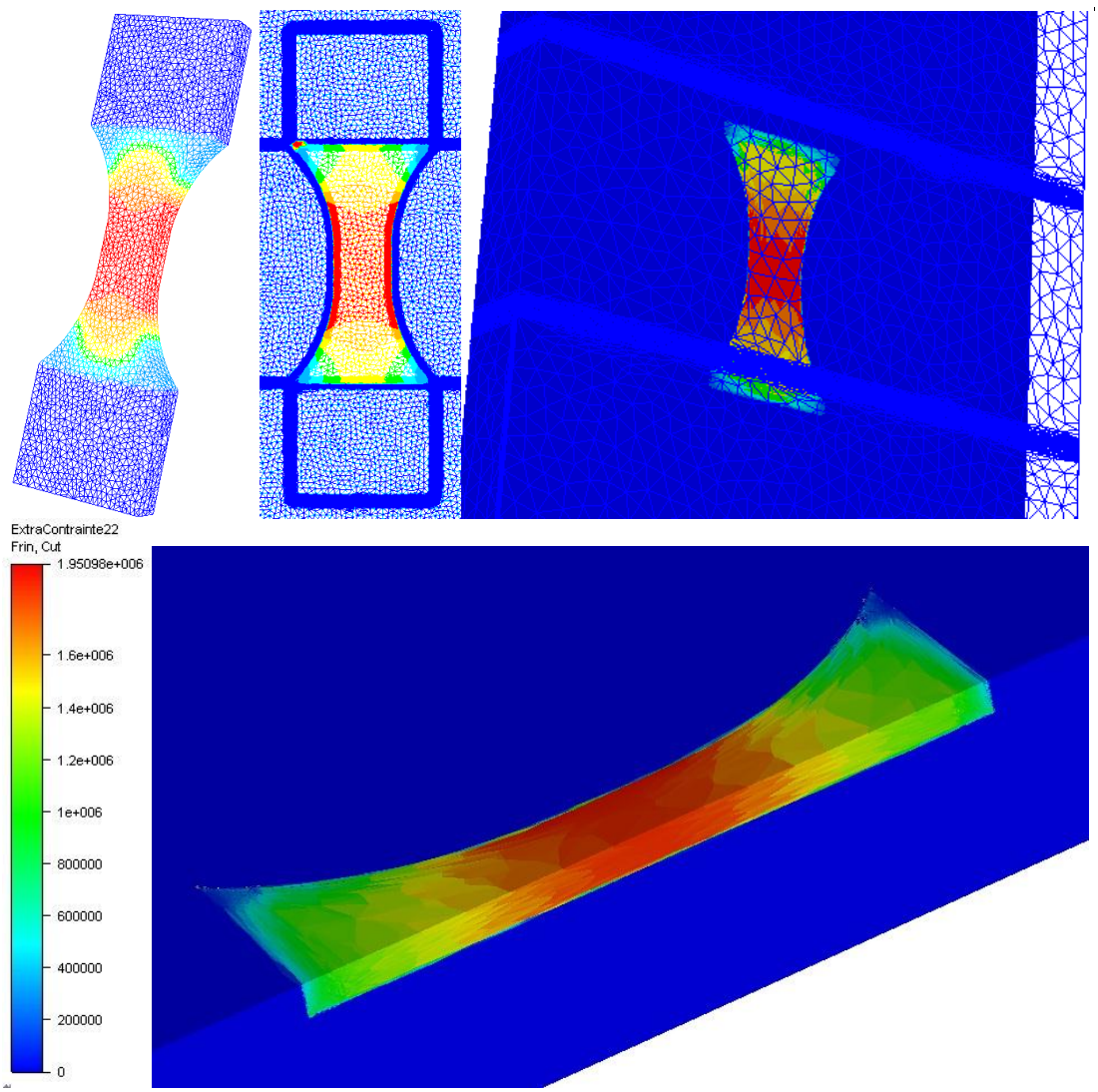


Figure 5-19: σ_{yy} stress at 110°C and loading by the incremental Lagrangian and Eulerian methods in 2D and 3D. In the first row, from left to right, the first image represents the specimen under loading by the incremental Lagrangian approach in 3D, the second describes the 2D Eulerian approach and the last one the 3D Eulerian approach. The image in the second row displays the stress inside of the specimen on two cutting planes, for the 3D Eulerian approach.

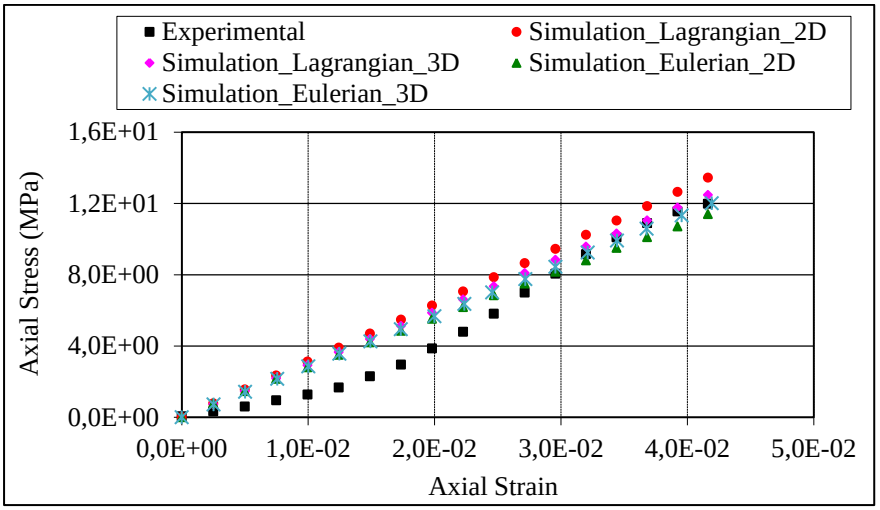


Figure 5-20: Stress vs. Strain curves for loading at 90°C. Curves illustrate the comparison between experimental and simulation by the incremental Lagrangian and Eulerian methods, in 2D and 3D.

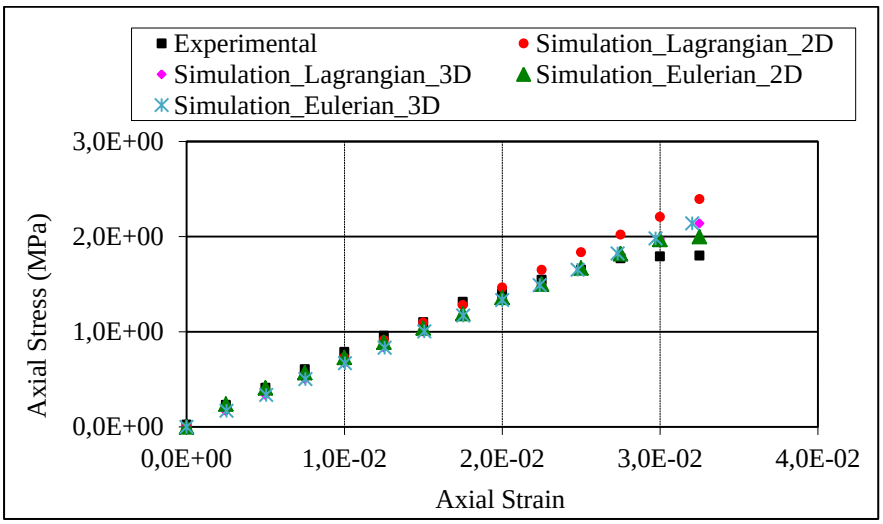


Figure 5-21: Stress vs. Strain curves for loading at 110°C. Curves illustrate the comparison between experimental and simulation by the incremental Lagrangian and Eulerian methods, in 2D and 3D.

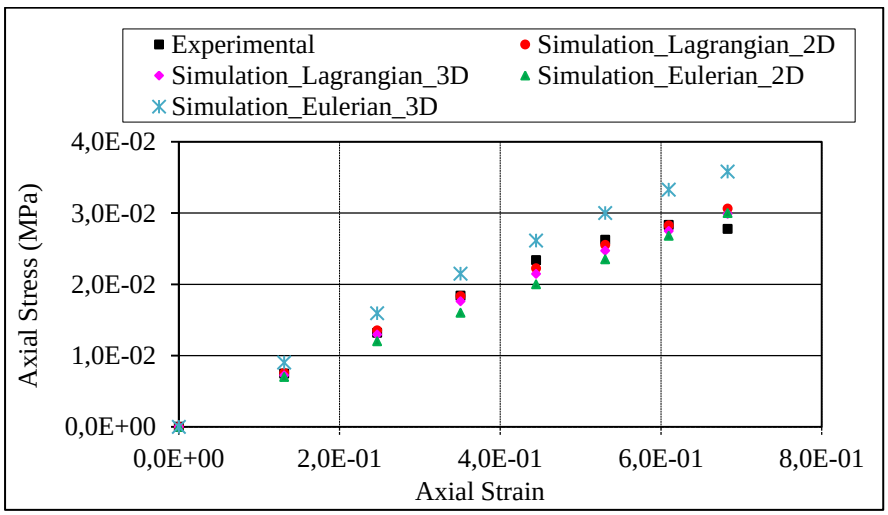


Figure 5-22: Stress vs. Strain curves for loading at 163°C. Curves illustrate the comparison between experimental and simulation by the incremental Lagrangian and Eulerian methods, in 2D and 3D.

Let us remind that we simulated only the phase where the material behavior remains linear. On Figure 5-20, Figure 5-21 and Figure 5-22 we observe a good agreement between the simulations and the experimental tests with an error that remains less than 10% whatever the method is. It is important to highlight the influence of mesh size and time step in the numerical simulation which is the origin of the small differencse between the results in 2D and in 3D.

Nevertheless, this first step demonstrates feasibility. Extension to modeling of viscoelastic behavior is illustrated through several comparisons at different temperatures from the almost solid state to the almost liquid state. It gives a potential measure of our numerical methodology and our future work.

However, a simple Kelvin-Voigt model is not enough to model complex behavior, such as the one of polymers. Therefore, in the next section, we will show the implementation of a more realistic visco-hyper-elastic behavior.

5.3 Modeling visco-hyper-elastic behavior

Kelvin-Voigt viscoelastic model does not represent non-linear effects causing difficulties on well reproducing experimental data, thus a more realistic model is needed.
This section is devoted to the implementation of a visco-hyper-elastic behavior in the library CimLib®. This visco-hyper-elastic model takes into account anelasticity as the result of a change in topology and/or number of entanglements in the material.

5.3.1.1 Validation for the numerical calculation on material point

This visco-hyper-elastic model formalism was detailed in chapter 2 and in the Appendix, and allows reproducing all the thermomechanical behavior of materials on a wide range in strain rate and temperature. It has been implemented in Cimlib by resolution of the set of evolution equations at the material point. The identification and validation of the visco-hyper-elastic model was verified by a series of experimental tests (tensile and shear) for which numerical results are given on the point.

Values for the model parameters are given in Table 5-3, and were taken from Baquet's PhD (Figure 5-23 and Figure 5-24).

	E_c	E_s	α	β	Z_p		
Value	$5.17e^8\,(Pa)$	$3e^8\,(Pa)$	0.088	0	Z_{p1}	Z_{p2}	Z_{p3}
					5.5	5.7	6

Table 5-3: Material parameters used for visco-hyper-elastic model in the tensile and shear tests.

Simulation results show a good agreement with the experimental curves after adjusting the five parameters mentioned in the above section. Observation and sensitivity analysis of the visco-hyper-elastic model compared with the physical behavior can be accomplished by changing the value of these parameters. As illustrated on Figure 5-23 (tensile test) and Figure 5-24 (shear test) where a variation of 10% of Z_p ($Z_{p1} > Z_{p2} > Z_{p3}$), the parameter that controls the slip evolution $\dot{\eta}$, was performed. This demonstrated that the higher this value is, the quicker the slip evolution increases, consequently the slipperiness factor is higher, which imposes a more important stress. This effect is perfectly corresponding with the physical theory, meaning the faster the slip evolution raises, the more significant the entanglement is.

In order to measure the influence of time step in the visco-hyper-elastic model, several numerical simulations were done, illustrated on Figure 5-25, simulation that showed no effects of the time step in the calculation on the material point.

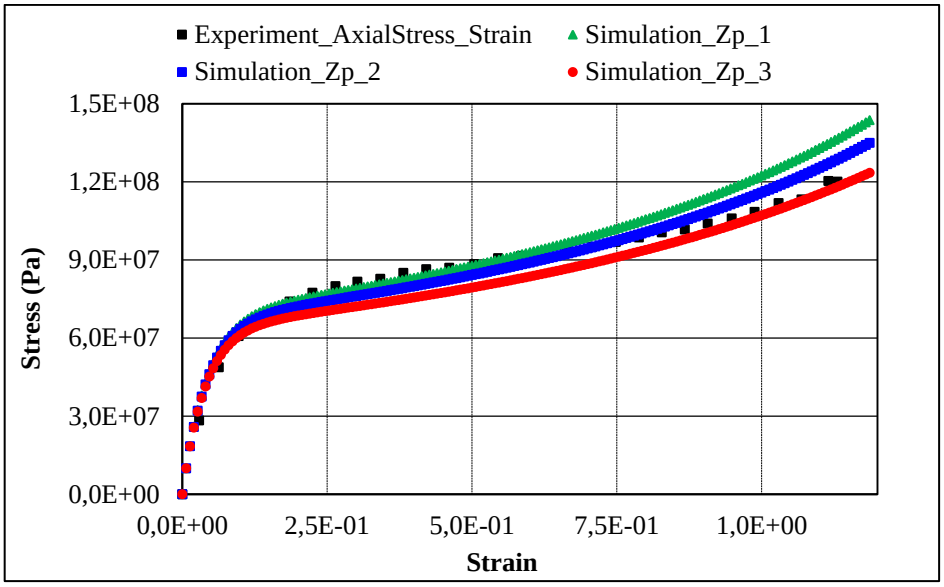


Figure 5-23: Stress vs. Strain curves for the tensile test at 21.6°C and for a strain rate of $1.83e^{-2}$ s^{-1}. The chosen material is a Polyamide 6.6 produced by Rhodia. Curves illustrate the comparison between experimental and simulation by calculation on the material point with different values of Z_p, the parameter that controls the change rate of η.

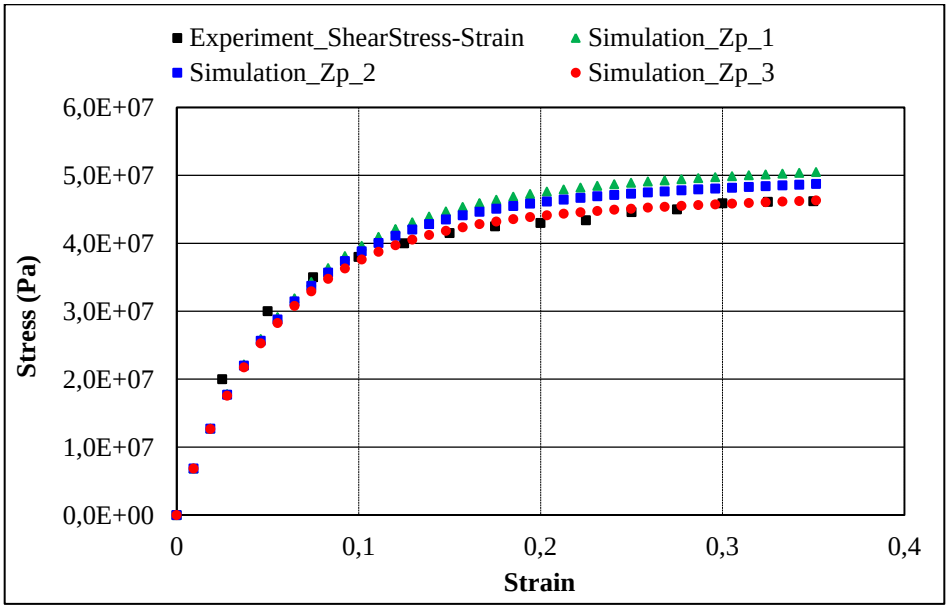


Figure 5-24: Stress vs. Strain curves for the shear test. Curves illustrate the comparison between experimental and simulation by calculation on the material point with different value of Z_p. The value of strain rate is $3.7e^{-2}$ s^{-1}.

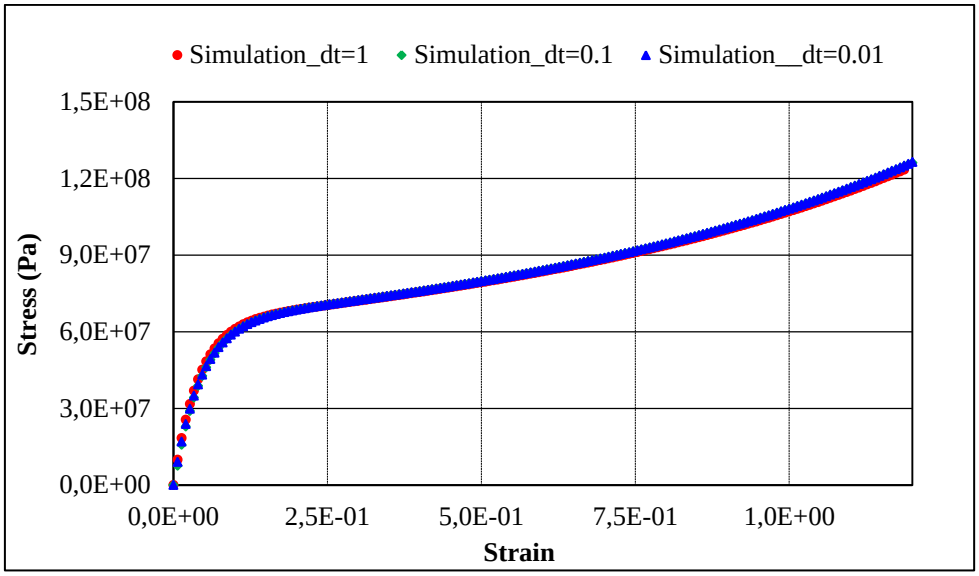


Figure 5-25: Stress vs. Strain curves for the tensile test at 21.6°C and for the strain rate of $1.83e^{-2}$ s^{-1}. Curves illustrate the simulation with different time steps.

We demonstrate here that it is possible to implement a more complex law. However, some specific numerical difficulties can arise that are model-dependent and must be further solved to develop true 3D FEM modeling. Thus, we have considered the following steps: firstly, we apply the built solver with the EVSS technique to a Kelvin Voigt viscoelastic model, then to a Neo-Hookean hyper-elastic model and finally to the visco-hyper-elastic model of Billon.

5.4 Application of the EVSS stabilized solver to viscoelastic, hyperelastic and visco-hyper-elastic behaviors

5.4.1 Kelvin-Voigt viscoelastic model

As detailed in chapter 4, conservation equations to be solved in the whole computational domain are resumed to, when considering a EVSS method and the Kelvin Voigt model:

$$\begin{cases} -\nabla p' + \nabla \cdot 2\left(\eta_s + \eta_v\right)\varepsilon\left(v\right) + \nabla \cdot \Sigma = 0 \\ \Sigma = \tau - 2\eta_s \varepsilon\left(v\right) \\ \tau = 2\mu_e \varepsilon\left(u\right) \\ -\nabla \cdot v = 0 \\ \dfrac{du}{dt} = v \\ + \text{initial and boundary conditions} \end{cases} \tag{5.3}$$

For a matter of simplicity, we do not detail here the variational formulation. However, the basic idea behind this technique is that Σ can be taken P0 (approximated at the elements) or P1 (at the nodes). In the latest case, we have a projection of ε in a different approximation space for the term in the right hand side of conservation of momentum, than the one on the left hand side. Since time steps are considered small in the examples that we have tested, no iterations inside one increment will be done in the following. Application to a tensile test, showing loading/unloading, is performed.

5.4.1.1 Incremental Lagrangian approach

For the sake of simplicity, we start with the incremental Lagrangian approach where the general algorithm is shortly described below.

Algorithm:

For each time step $\left[t^n, t^{n+1}\right]$ **do**

Knowing Σ^n, find $\left(v^{n+1}, p'^{n+1}\right)$ such that

$$\begin{cases} -\nabla_{x^{n+1}} p'^{n+1} + \nabla_{x^{n+1}} \cdot 2\left(\eta_s + \eta_v\right)\varepsilon\left(v^{n+1}\right) = -\nabla_{x^{n+1}} \cdot \Sigma^n \\ -\nabla_{x^{n+1}} \cdot v^{n+1} = 0 \\ + \text{boundary conditions} \end{cases} \tag{5.4}$$

And u^{n+1} is found by solving

$$u^{n+1} = u^n + v^{n+1}\Delta t \tag{5.5}$$

With the recent computed displacement field u^{n+1} and velocity field v^{n+1}, compute the Σ^{n+1} tensor as

$$\Sigma^{n+1} = 2\mu_e \varepsilon\left(u^{n+1}\right) - 2\eta_s \varepsilon\left(v^{n+1}\right) \tag{5.6}$$

End for

Material parameters used are the following:

	E	γ_e	η_s	η_v
Value	$1e^9$ *(Pa)*	0.3	$1e^8$ *(Pas)*	$1e^6$ *(Pas)*

Table 5-4: Material parameters used for the Kelvin-Voigt model.

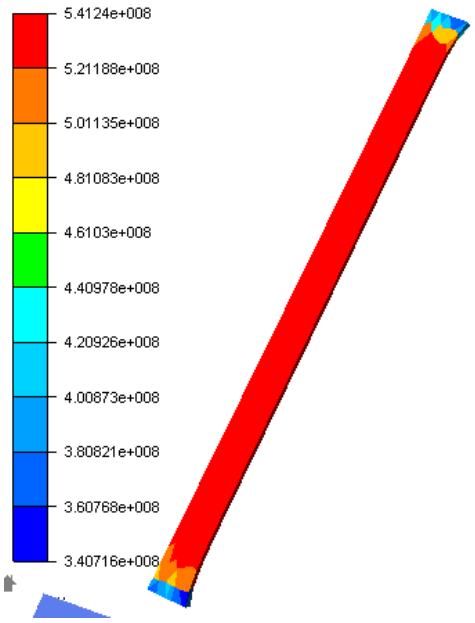


Figure 5-26: Longitudinal stress distribution in the specimen with the Kelvin-Voigt viscoelastic model

Figure 5-26 illustrates a good distribution of stress in the specimen which is enhanced by the stress curve in Figure 5-27, under loading and unloading. The results demonstrate the feasibility of the EVSS method to numerically solve the viscoelastic behavior, and also its conservation. Next section focus on the evolution towards an hyper-elastic model before trying to circumvent the challenge with the visco-hyper-elastic model in the last section.

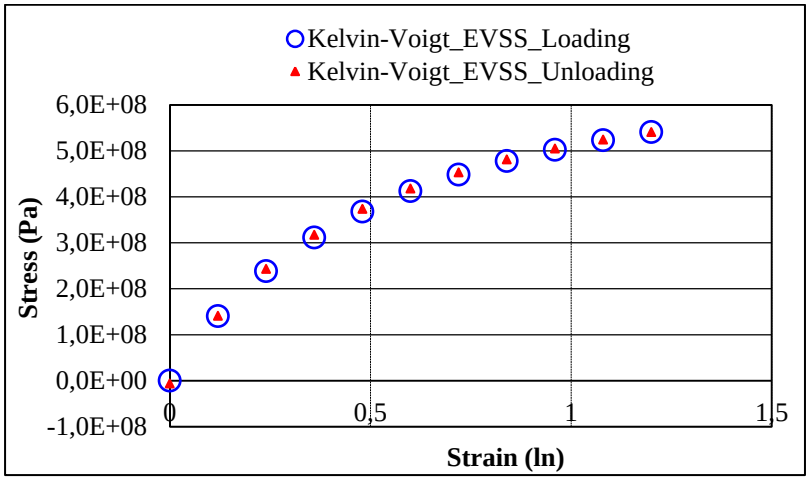


Figure 5-27: Axial stress in the central zone under loading and unloading.

5.4.2 Neo-Hookean viscoelastic model

For the Neo-Hookean combined with the EVSS model, we can resume the conservation equations to be solved in the whole computational domain as:

$$\begin{cases} -\nabla p + \nabla \cdot 2\eta_s \varepsilon(v) + \nabla \cdot \sum = 0 \\ \sum = \tau - 2\eta_s \varepsilon(v) \\ \tau = 2C_{10} B \\ -\nabla \cdot v = 0 \\ \dfrac{du}{dt} = v \\ + \text{initial and boundary conditions} \end{cases} \tag{5.7}$$

5.4.2.1 Lagrangian approach

The algorithm used in an incremental Lagrangian approach is similar to the previous case and I detailed below.

Algorithm:

For each time step $\left[t^n, t^{n+1}\right]$ **do**

Knowing Σ^n, find $\left(v^{n+1}, p^{n+1}\right)$ such that

$$\begin{cases} -\nabla_{x^{n+1}} p^{n+1} + \nabla_{x^{n+1}} \cdot 2\eta_s \varepsilon\left(v^{n+1}\right) = -\nabla_{x^{n+1}} \cdot \sum^n \\ -\nabla_{x^{n+1}} \cdot v^{n+1} = 0 \\ + \text{ boundary conditions} \end{cases} \tag{5.8}$$

And u^{n+1} is found by solving

$$u^{n+1} = u^n + v^{n+1}\Delta t \tag{5.9}$$

With the recent computed displacement field u^{n+1} and velocity field v^{n+1}, compute the Σ^{n+1} tensor as

$$\Sigma^{n+1} = 2C_{10}B^{n+1} - 2\eta_s \varepsilon\left(v^{n+1}\right) \tag{5.10}$$

End for

Material parameters used are the following:

	C_{10}	η_s
Value	$1e^6$ *(Pa)*	$1e^7$ *(Pas)*

Table 5-5: Material parameters used in for the Neo-Hookean model.

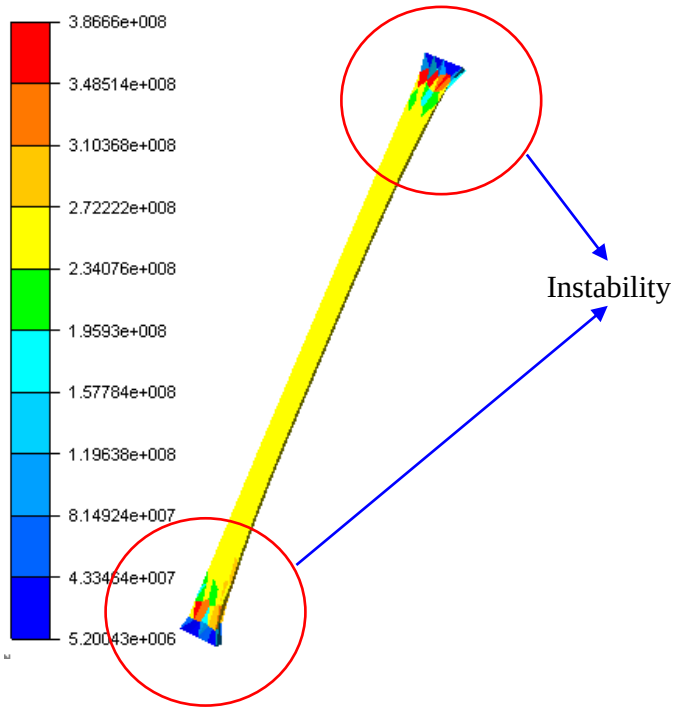


Figure 5-28: Longitudinal stress distribution in the specimen with the Neo-Hookean hyper-elastic model.

In the large deformations, the mesh is largely distorted and lead to inaccurate results as shown in Figure 5-28. We observe instability of the stress distribution, mostly in the border where the mesh is highly deformed, and then remeshing is required. Unfortunately, the left Cauchy-Green tensor B needs to be expressed in the initial configuration, i.e. the original mesh, thus remeshing becomes difficult to perform (difficult to guarantee a good transport of the fields). Consequently, the Eulerian approach will be exploited to overcome the problem.

5.4.2.2 Eulerian approach

The general methodology is similar to the Eulerian cases detailed before. To the mechanical equations we add the transport interfaces, here illustrated by the advection equation for the transport of one interface using the Level Set method. Remeshing can be used in this case, since operators are used in the current configuration. The algorithm below synthetizes the methodology:

Algorithm:

For each time step $\left[t^n, t^{n+1}\right]$ **do**

Knowing Σ^n, find $\left(v^{n+1}, p^{n+1}\right)$ such that

$$\begin{cases} -\nabla p^{n+1} + \nabla \cdot 2\eta_s \varepsilon\left(v^{n+1}\right) = -\nabla \cdot \sum^n \\ -\nabla \cdot v^{n+1} = 0 \\ + \text{ boundary conditions} \end{cases} \tag{5.11}$$

Transport the interface by solving

$$\begin{cases} \dfrac{\alpha^{n+1}-\alpha^{n}}{\Delta t}+v^{n+1}\nabla\alpha^{n+1}+\lambda s\left|\nabla\alpha^{n+1}\right|=\lambda s\sqrt{1-\left(\dfrac{\pi}{2e}\alpha^{n}\right)^{2}} \\ \alpha\left(t=0,x\right)=\alpha_{0}\left(x\right) \end{cases} \tag{5.12}$$

Find u^{n+1} by solving

$$\frac{u^{n+1}-u^{n}}{\Delta t}+v^{n+1}\nabla u^{n+1}=v^{n+1} \tag{5.13}$$

With the recent computed displacement field u^{n+1} and velocity field v^{n+1}, compute the Σ^{n+1} tensor as

$$\Sigma^{n+1}=2C_{10}B^{n+1}-2\eta_{s}\varepsilon\left(v^{n+1}\right) \tag{5.14}$$

Remesh if necessary

End for

To the material parameters given in Table 5-5, we add numerical ones concerning the surrounding fluid and the rigid parts, leading to the following set of values:

	C_k	η_s	η_f	η_{rig}
Value	$1e^6\,(Pa)$	$1e^7\,(Pas)$	$1e^3\,(Pas)$	$3e^6\,(Pas)$

Table 5-6: Material parameters used in Eulerian approach.

We remind that the solid viscosity η_{rig} is chosen to ensure a non-deformable solid; the fluid viscosity is also supposed small enough to optimize the simulation process without influencing the final results.

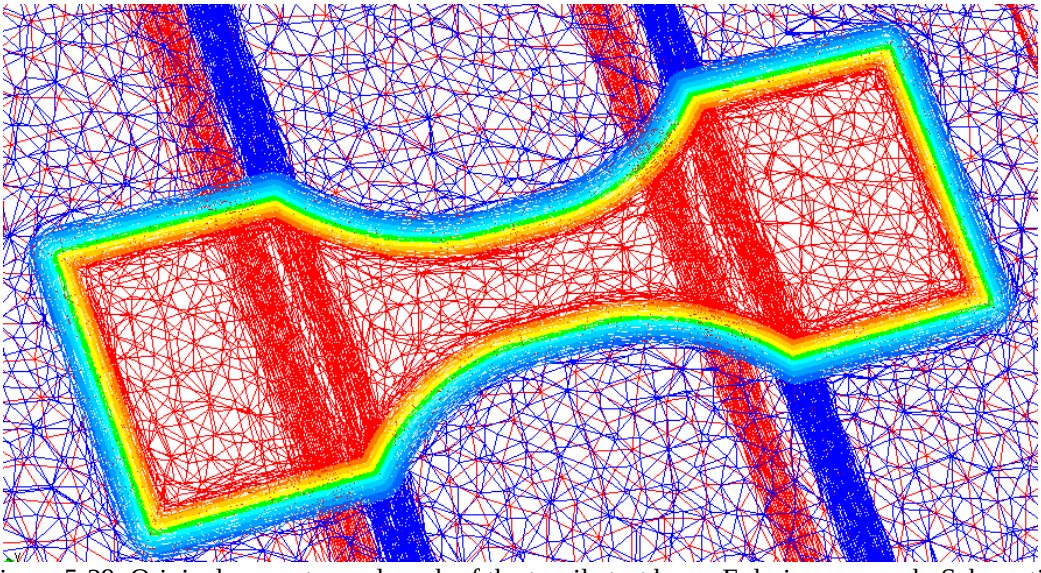


Figure 5-29: Original geometry and mesh of the tensile test by an Eulerian approach. Schematic representation of the mesh in a cutting plane on the thickness of the computational domain.

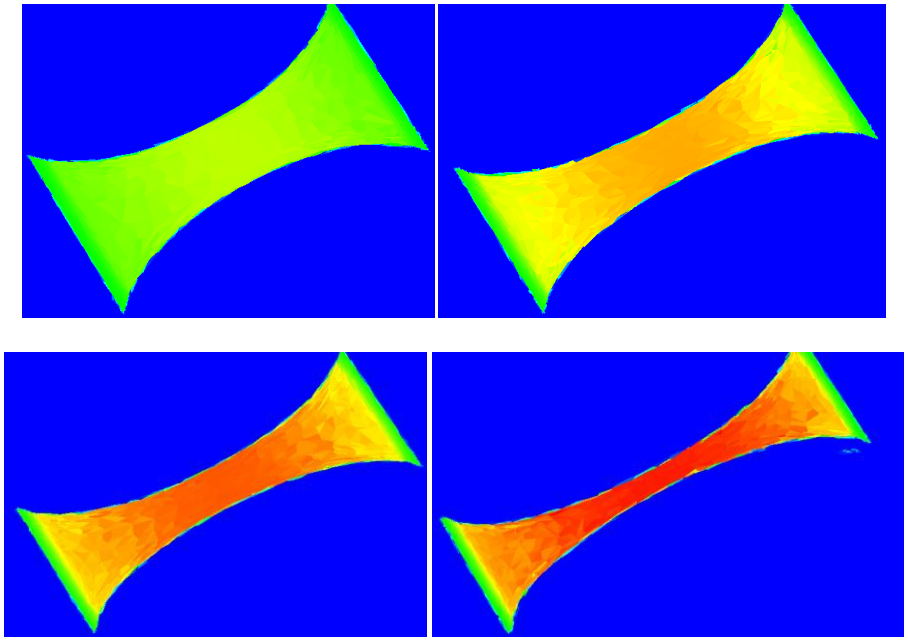


Figure 5-30: Longitudinal stress distribution at 5% (upper left), 15% (upper right), 25% (lower left) and 50% (lower right) of deformation.

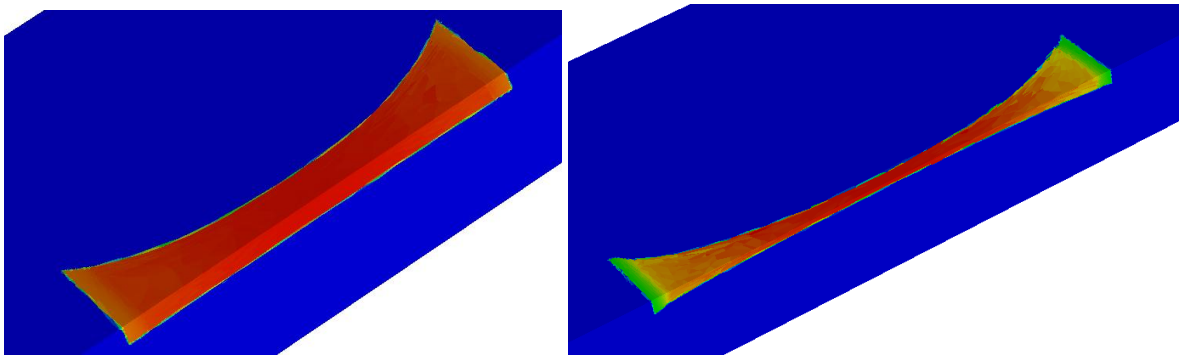


Figure 5-31: Longitudinal stress distribution inside the specimen at 5% (left) and 60% (right) of deformation. Schematic representation is obtained by two symmetric cutting planes following the longitudinal and the thickness direction.

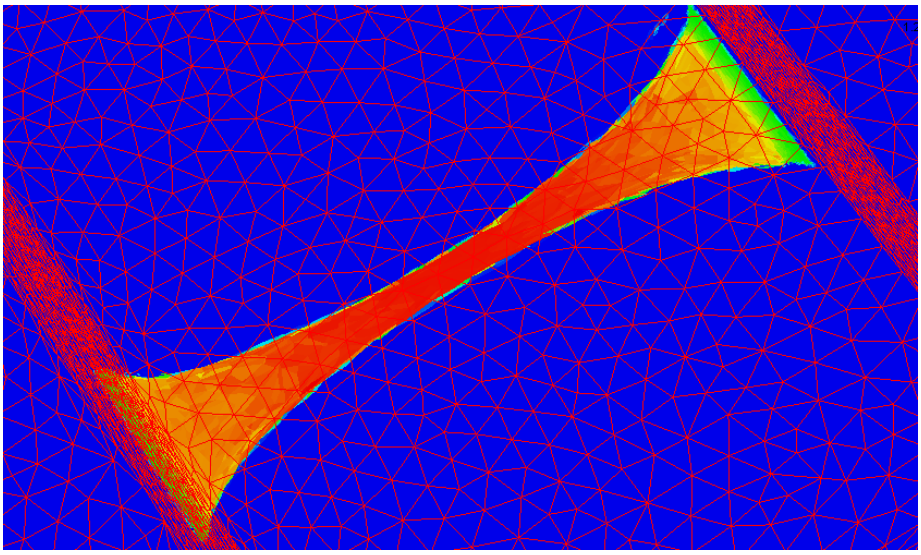


Figure 5-32: Mesh and stress distribution on the cutting plane at 60% strain.

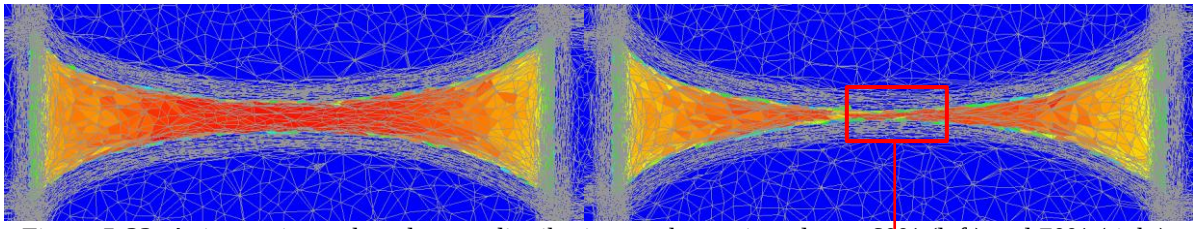


Figure 5-33: Anisotropic mesh and stress distribution on the cutting plan at 60% (left) and 70% (right).

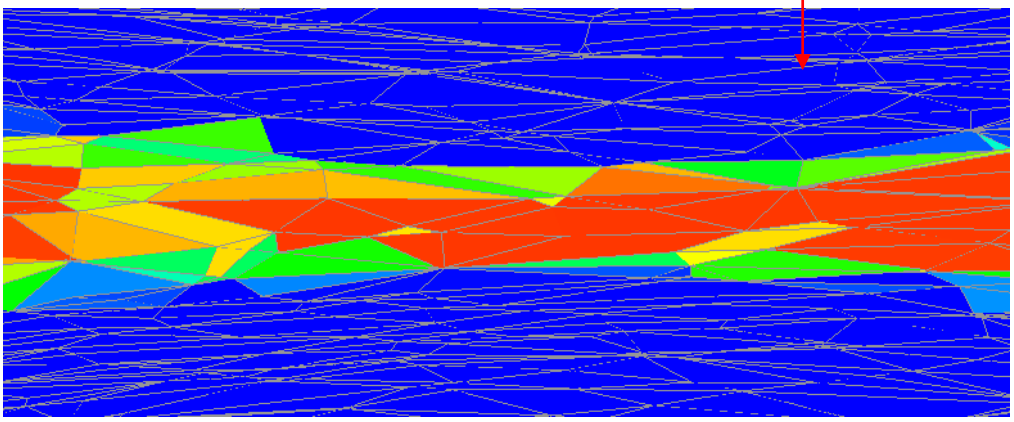


Figure 5-34: Zoom of stress distribution vs. mesh size in the central zone.

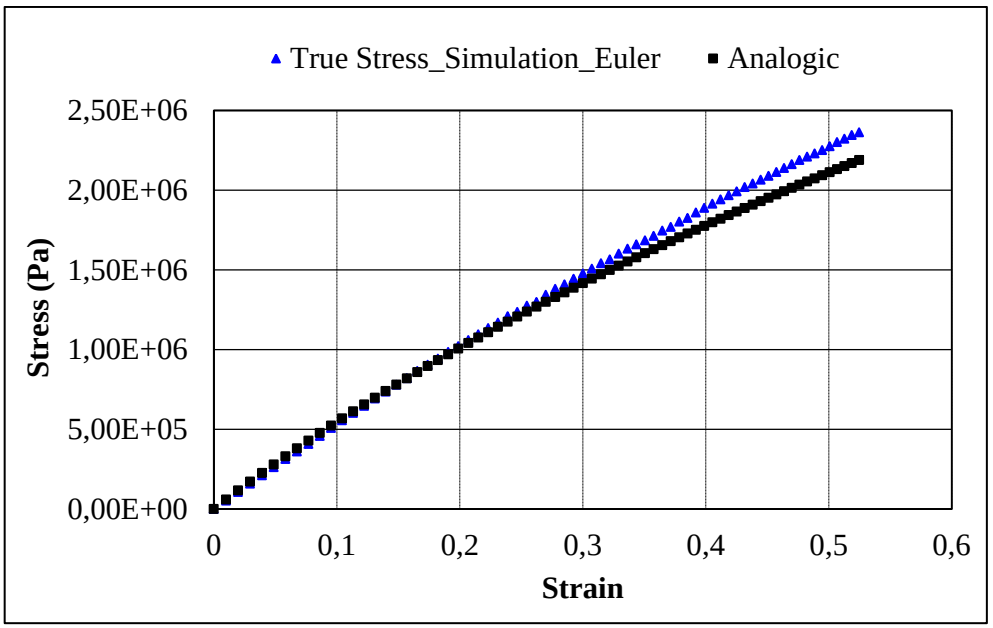


Figure 5-35: A combined numerical/analogic analysis of longitudinal stress with the Neo-Hookean hyper-elastic model.

Computations were performed with the mesh illustrated in Figure 5-29. Results demonstrated that the stress distribution is homogenous (in three dimensions) although the deformation may attain 60% or higher values. Furthermore, we notice the significant reduction of the specimen cross section in the central zone when the deformation is large (Figure 5-33 and Figure 5-34), with an

important error on the determined interface. As explained previously, the error in the interface transport is related with the mesh size, and we can improve the results, mainly in large deformations, by reducing the mesh size which will engender significant consequent simulation times and resources.

Quantitative results shown on Figure 5-35, a combined numerical/analogic analysis of stress with the Neo-Hookean hyper-elastic model, ensuring good perspectives for a future work. Analogic formulation of the incompressible Neo-Hookean behavior in uniaxial extension can be described by:

$$\sigma_{yy} = 2C_{10}\left(\lambda - \frac{1}{\lambda^2}\right) \tag{5.15}$$

Where λ is the elongation in the *y* direction. We remark that the numerical stress displayed on Figure 5-35 is slightly higher than the analogic curve due to the measurement in the central zone where the stress concentration is slighter important than elsewhere. For a better combined result, the average amount of stress throughout the specimen should be given.

5.4.3 Visco-hyper-elastic model

Modeling of the hyper-elastic Neo-Hookean model by the EVSS method showed a good potential to our study, principally in an Eulerian framework. It offered a key point to go on the modeling of the visco-hyper-elastic model, proposed and validated on a material point, mainly on 3D FE numerical simulation.

As a reminder, the stress tensor of the visco-hyper-elastic model is:

$$\sigma' = 2\left[\left(\frac{\partial w}{\partial I_{1e}} + I_{1e}\frac{\partial w}{\partial I_{2e}}\right)C_e - \frac{\partial w}{\partial I_{2e}}C_e^{\,2} + I_{3e}\frac{\partial w}{\partial I_{3e}}I\right] - p^{\#}I \tag{5.16}$$

That allows defining the conservation equation as below:

$$\begin{cases} -\nabla p' + \nabla \cdot 2\eta_s \varepsilon(v) + \nabla \cdot \Sigma = 0 \\ \Sigma = \tau - 2\eta_s \varepsilon(v) \\ \tau = \sigma'(C_e) - \dfrac{1}{3} tr\left(\sigma'(C_e)\right) \\ \sigma'(C_e) = 2\left[\left(\dfrac{\partial w}{\partial I_{1e}} + I_{1e}\dfrac{\partial w}{\partial I_{2e}}\right)C_e - \dfrac{\partial w}{\partial I_{2e}}C_e^{\,2} + I_{3e}\dfrac{\partial w}{\partial I_{3e}}I\right] \\ -\nabla \cdot v = 0 \\ \dfrac{du}{dt} = v \\ + \text{initial and boundary conditions} \end{cases} \tag{5.17}$$

5.4.3.1 Lagrangian approach

Like previously, the numerical schema of resolution in the incremental Lagrangian approach can be shortly written:

Algorithm:

For each time step $\left[t^n, t^{n+1}\right]$ **do**

Knowing Σ^n, find $\left(v^{n+1}, p'^{n+1}\right)$ such that

$$\begin{cases} -\nabla_{x^{n+1}} p'^{n+1} + \nabla_{x^{n+1}} \cdot 2\eta_s \varepsilon\left(v^{n+1}\right) = -\nabla_{x^{n+1}} \cdot \Sigma^n \\ -\nabla_{x^{n+1}} \cdot v^{n+1} = 0 \\ + \text{boundary conditions} \end{cases} \tag{5.18}$$

Find u^{n+1} by solving

$$u^{n+1} = u^n + v^{n+1}\Delta t \tag{5.19}$$

Computation of the evolution variables

With the recent computed displacement field u^{n+1}, velocity field v^{n+1} and the slippage parameters η, compute the Σ^{n+1} tensor as

$$\begin{cases} \Sigma^{n+1} = 2\left(\sigma'\left(C_e^{n+1}\right) - \frac{1}{3}tr\left(\sigma'\left(C_e^{n+1}\right)\right)\right) - 2\eta_s\varepsilon\left(v^{n+1}\right) \\ \sigma'\left(C_e^{n+1}\right) = 2\left[\left(\frac{\partial w}{\partial I_{1e}} + I_{1e}\frac{\partial w}{\partial I_{2e}}\right)C_e^{n+1} - \frac{\partial w}{\partial I_{2e}}\left(C_e^{n+1}\right)^2 + I_{3e}\frac{\partial w}{\partial I_{3e}}I\right] \end{cases} \quad (5.20)$$

End for

Lagrangian resolution within large deformations causes mesh distortions and leads to inaccurate result as for the Neo-Hookean test case. Thus, we will analyze two different configurations of a test bench (Figure 5-36): a perfect tensile test bench where the deformation is homogenous in the whole specimen, avoiding the largely distorted effect in the border; and a normal tensile test bench where a border is fixed and in the other a velocity is imposed.

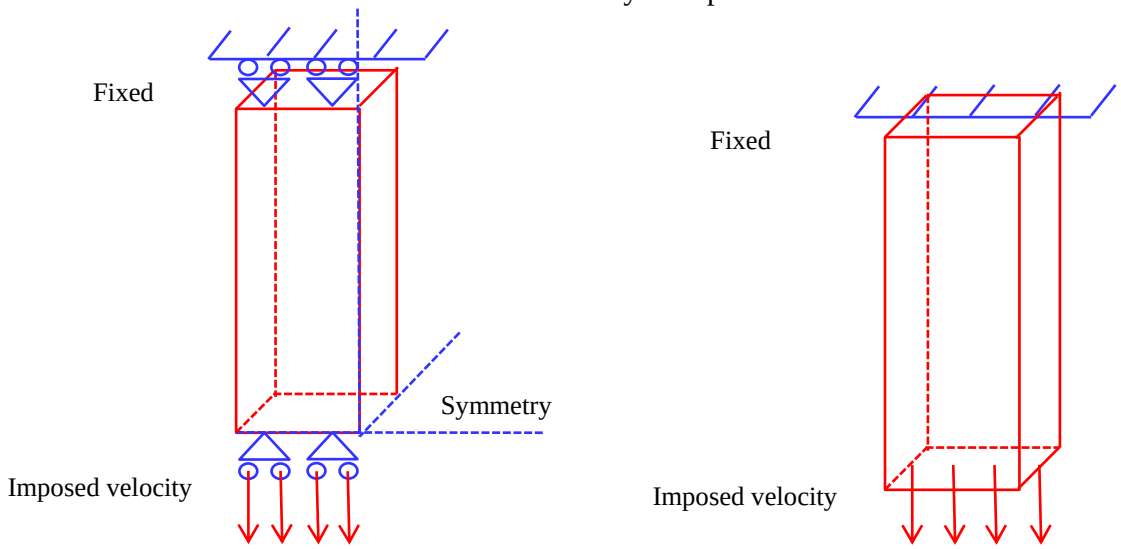


Figure 5-36: A perfect tensile test bench (left) and a normal tensile test bench (right).

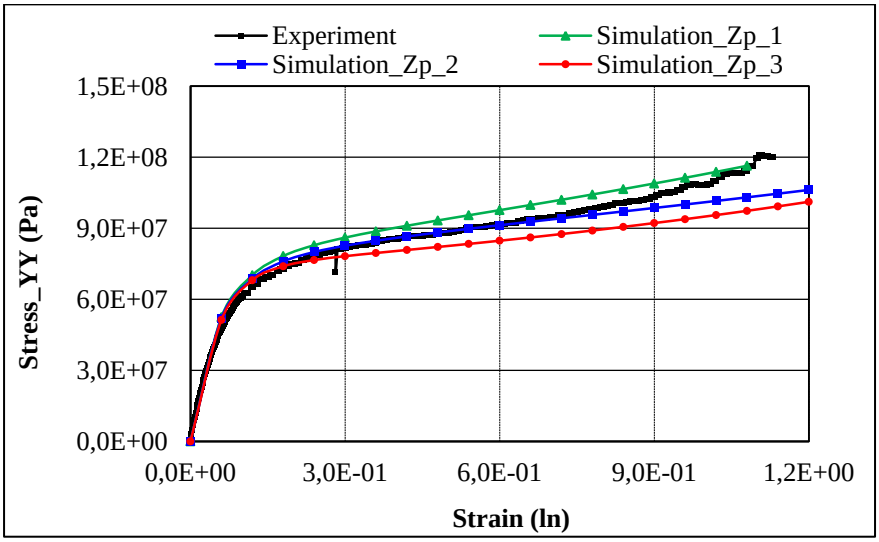


Figure 5-37: Stress evolution comparison between experiment and simulation with different values of Z_p.

Figure 5-37 displays the results in the perfect tensile test showing a good agreement between simulation and experiment curve used in the validation of the implementation of this law in the material point.

For the normal tensile test, the stress becomes instable when the mesh is excessively deformed as illustrated in the figure below. In the central zone, where stress is homogeneous, the numerical curve (Figure 5-39) shows an excellent agreement with the experimental curve, but in the border there is evidence of strong oscillations.

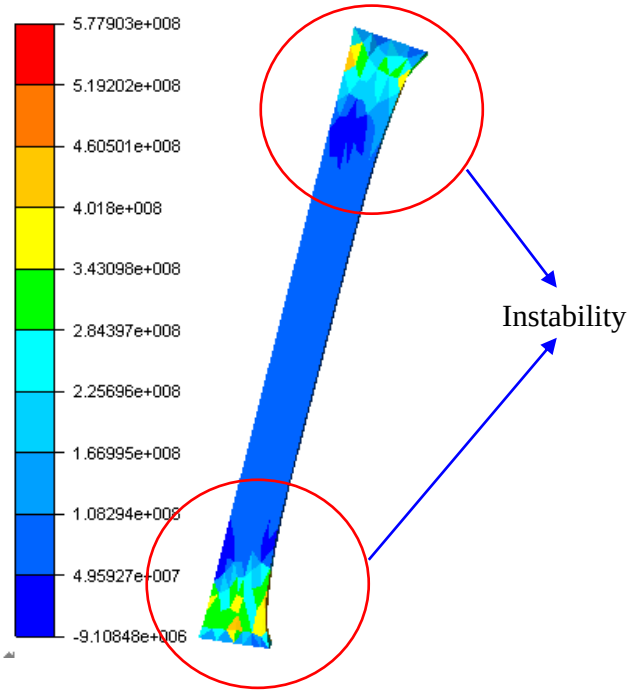


Figure 5-38: Longitudinal stress distribution in the specimen for the visco-hyper-elastic model behavior.

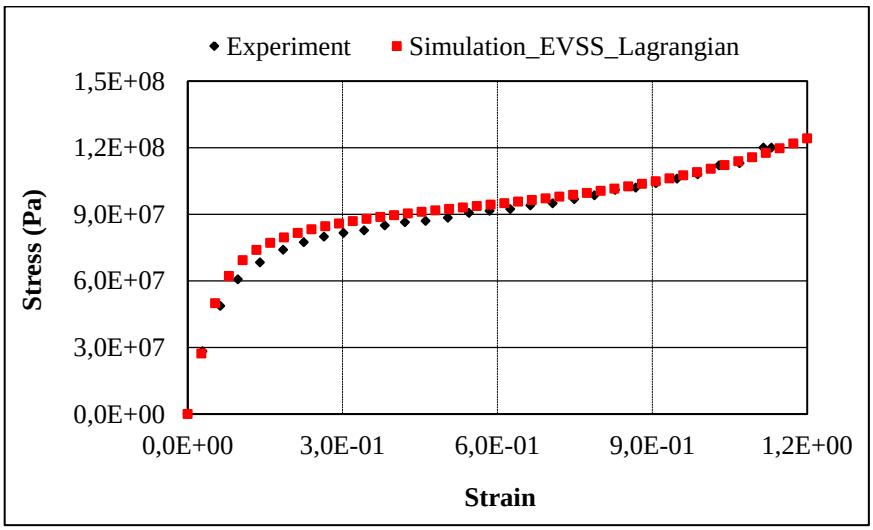


Figure 5-39: A combined numerical/experimental analysis of the longitudinal stress evolution in the central zone with the visco-hyper-elastic model and an incremental Lagrangian approach.

5.4.3.2 Eulerian approach

In the context of our project, due to time limit, we did not investigate the Eulerian approach for this model, despite the promising results on the Kelvin-Voigt or on the hyper-elastic Neo-Hookean models. Anyway, the global methodology is given below.

Algorithm:

For each time step $\left[t^n, t^{n+1}\right]$ **do**

Knowing Σ^n, find $\left(v^{n+1}, p'^{n+1}\right)$ such that

$$\begin{cases} -\nabla p'^{n+1} + \nabla \cdot 2\eta_s \varepsilon\left(v^{n+1}\right) = -\nabla \cdot \Sigma^n \\ -\nabla \cdot v^{n+1} = 0 \\ + \text{ boundary conditions} \end{cases} \tag{5.21}$$

Transport the interface(s) by solving

$$\begin{cases} \dfrac{\alpha^{n+1} - \alpha^n}{\Delta t} + v^{n+1}\nabla\alpha^{n+1} + \lambda s\left|\nabla\alpha^{n+1}\right| = \lambda s\sqrt{1 - \left(\dfrac{\pi}{2e}\alpha^n\right)^2} \\ \alpha\left(t=0, x\right) = \alpha_0\left(x\right) \end{cases} \tag{5.22}$$

Find u^{n+1} by solving

$$\frac{u^{n+1} - u^n}{\Delta t} + v^{n+1}\nabla u^{n+1} = v^{n+1} \tag{5.23}$$

Evolution variables are determined by solving advection equations, for example, $\dot{\eta}^{n+1}$ is known by the equations given previously, then find η^{n+1} by solving

$$\frac{\eta^{n+1} - \eta^n}{\Delta t} + v^{n+1}\nabla\eta^{n+1} = \dot{\eta}^{n+1} \tag{5.24}$$

With the recent computed displacement field u^{n+1}, velocity field v^{n+1} and the slippage parameters η, compute the Σ^{n+1} tensor as

$$\begin{cases} \Sigma^{n+1} = 2\left(\sigma'\left(C_e^{n+1}\right) - \dfrac{1}{3}tr\left(\sigma'\left(C_e^{n+1}\right)\right)\right) - 2\eta_s\varepsilon\left(v^{n+1}\right) \\ \sigma'\left(C_e^{n+1}\right) = 2\left[\left(\dfrac{\partial w}{\partial I_{1e}} + I_{1e}\dfrac{\partial w}{\partial I_{2e}}\right)C_e^{n+1} - \dfrac{\partial w}{\partial I_{2e}}\left(C_e^{n+1}\right)^2 + I_{3e}\dfrac{\partial w}{\partial I_{3e}}I\right] \end{cases} \tag{5.25}$$

Remesh if necessary

End for

5.4.3.3 Conclusions

This section showed the modeling of a visco-hyper-elastic behavior and the implementation in the FE library CimLib® with the validation on a material point. Several comparisons with the experimental mechanical tests, performed by Baquet E. [77], were accomplished.

Due to the complexity of the visco-hyper-elastic behavior, a direct resolution method causes different problems on stabilization. Thus, a classical mixed formulation on (u, v, p) coupling with

the stabilization EVSS method first used to overcome this issue. A time step marching scheme allows splitting the system resolution in two subsystems made of the viscoelastic constitutive equation and the flow equations and was carried out to simplify the numerical resolution. Viscoelastic Kelvin-Voigt model was modeled with success, followed by promising results on the hyper-elastic Neo-Hookean model.

Unfortunately, full FE modeling in 3D and an Eulerian approach of the visco-hyper-elastic behavior was not achieved, needing more investigation. More accurate and complete results can be obtained in a near future, especially with the promising results shown during our study. Furthermore, by using this visco-hyper-elastic model, closer to the real material behavior, we believe that quantitative results can be compared to experimental works.

5.5 Résumé du chapitre en français

La première partie de ce chapitre se concentre sur la modélisation et la simulation du comportement viscoélastique de Kelvin-Voigt. Le comportement des polymères dépend fortement de la température. Proche de sa température de transition vitreuse, un fort changement de comportement, de l'état caoutchoutique à l'état liquide, pourra apparaitre (voir Figure 2-1). Pour recueillir des données représentatives pour la viscoélasticité solide et le liquide viscoélastique, la validation a été effectuée sur un PMMA Altuglas® V825T, fourni par la société Arkema®. Nous avons effectué des tests à différentes températures pour deux modes de chargement: charge/décharge et charge/relaxation (Table 5 1) avec une vitesse de déformation faible, entre $0{,}0025s^{-1}$ et $0{,}1s^{-1}$ pour éviter l'auto-échauffement.

La stratégie de validation de notre méthodologie et de notre résolution numérique est de comparer les tests expérimentaux aux simulations numériques et de promouvoir l'approche physique à travers trois étapes:

- la première étape est d'effectuer et d'analyser les essais mécaniques sur un polymère PMMA dans différents états: du solide au liquide
- la deuxième étape est d'adapter et de valider la modélisation du comportement viscoélastique de Kelvin-Voigt par rapport aux tests expérimentaux
- la troisième étape confronte la simulation numérique aux données expérimentales et justifie la nécessité d'introduire un modèle plus pertinent pour le comportement des polymères

Concernant les simulations numériques, deux méthodes sont utilisées pour valider la méthodologie: la méthode de Lagrange et celle d'Euler, dans lesquelles nous avons utilisé le solveur éléments finis mixtes avec Mini-Elément P1+/P1 développé au chapitre 4.

L'approche lagrangienne est assez simple et facile à mettre en œuvre mais, les problèmes associés aux grandes déformations en limite la validité. L'approche Eulérienne est donc nécessaire. Cette dernière évitera toute distorsion dans les mailles et restera applicale aux problèmes dynamiques comme les cas d'impact, qui représentent des difficultés importantes dans le cadre Lagrangien. Enfin, la comparaison entre les deux approches nous permet de mettre en lumière la capacité de notre solveur et donne un aperçu général des erreurs, des performances et aussi des force et faiblesse de notre solveur et de la méthodologie numérique.

Les essais expérimentaux sont reproduits de manière prometteuse dans la phase linéaire de la déformation, malgré la simplicité du modèle de comportement de Kelvin-Voigt. La robustesse de l'approche étant démontrée on peut désormais envisager d'enrichir la modélisation du comportement.

Dans la dernière section, nous abordons la mise en œuvre d'un modèle de comportement plus réaliste, le modèle visco-hyper-élastiques proposé par Billon [80] [81] [82] [83] [84].

Dérivé du modèle de réseau de Edwards-Vilgis [38] [85] [86], cette nouvelle approche permet de reproduire le comportement thermomécanique des matériaux sur une large gamme de vitesse de déformation et de température. Le calcul au point d'intégration, la modélisation numérique, l'implémentation et la validation du comportement visco-hyper-élastique avec CimLib® sont traité

dans la deuxième section de ce chapitre sur la base des essais mécaniques effectués dans le travail de Baquet E. [77].

Cependant la complexité du comportement visco-hyper-élastique et de sa résolution directe par la méthode des éléments finis mixtes rendent nécessaire un schéma numérique stabilisé, particulièrement en 3D. Notre première tâche est donc d'adapter une formulation mixte classique par un couplage avec la méthode de résolution EVSS pour relever le défi.

En résumé : la méthode de résolution est validée dans le cas du modèle viscoélastique de Kelvin-Voigt et hyper-élastique Néo-Hookéen mais nécessite une étude plus longue pour aller plus loin : modèle de comportement plus complet et application dynamique complexe comme les cas d'impact etc.

Chapter 6

6 Conclusions and Perspectives

6.1 Synthesis and conclusion

Knowing the primordial monitoring and simulating role of injection molding process, one of the most important technologies for forming polymeric material components, the Rem3D® software is focused on this market. The numerical tools can speed up product innovation, reduce the costs, and help us to understand the material behavior all along the process. Before this study, it was possible to predict the mechanical behavior of an injected polymer, where the matrix is thermo elastic or hyper elastic, isotropic or anisotropic. However, polymer processing is more complex where the polymer is transformed under high pressure and temperature and the following cooling process. Nonlinear viscoelastic behavior, crystallization and solidification kinetics, etc. is numerically required during the process. Therefore, to extend the Rem3D® software, the purpose of our research focuses on a more realistic behavior for the matrix. Thus, we consider a matrix of the semi-crystalline polymeric type, which will have viscoelastic behavior (from liquid state to solid state).

The main philosophy is to provide a methodology that enables to account for the viscoelastic behavior of polymers in different states from liquid to solid, which is still an open question. Our idea is to use a mixed formulation in three fields *(u, v, p) (displacement, velocity, pressure)*, with *u* and *v*, represented the primary variables of strain and strain rate formulation to model the viscoelasticity via a multiphase approach, largely used to deal with the fluid structure interaction (FSI) [35]. After a short background and bibliography on viscoelasticity in injection molding and on the numerical computational method to the FSI problem represented in chapter 2, a simple viscoelastic Kelvin-Voigt model was used to explain and validate our approach. Because it can inform the potential difficulties, justify the numerical developments and valid the approach of resolution. In fact, the problem can, in this case, be described as the classical Navier-Stokes problem, in which an "extra-stress" tensor related to the elastic part of deformation is considered (see equation (2.74)). Our approach represents an innovative way to be described and validated in this report.

Elasticity

To strengthen our methodology of resolution, preliminary work is conducted within a framework of a purely elastic case. In fact, the simulation of viscoelastic behavior should be accurate in any case, even for the simple case of a purely elastic body. Despite it is one of the simplest constitutive models that can be imagined, its numerical resolution still has been fascinating. The effectiveness of our calculation was discussed during the simulations with different methods based on the mixed finite element: incremental resolution and single increment of resolution. It was also done on the collection of numerical sources errors by checking the influence of mesh and geometry. At this stage, we can say that the incremental method is more relevant. Finally, verification and validation have been extended to tensile, compression and torsion tests (Figure 3-17 and Figure 3-18).

The numerical simulation achieved the satisfactory results which give us a good indication for the following work as part of my project. However, some unstable problems were appeared, mainly to large deformations more than 35% strain. In fact, these instabilities occurred only with the incremental method when the elastic stress has become important. They lead to a completely non-physical deformation (Figure 3-20 and Figure 3-21). The origin of this problem is related to the magnitude of elastic stress. If the latter is too high, the added stress in the right hand side members of the equilibrium equation causes some ellipticity problem in the resolution by mixed method. Furthermore, the misuse of the assumptions of small deformations for large deformations can lead to instability problems where the nonlinear terms must be added. Thus, numerical stabilized was investigated to overcome this problem.

Stabilization

Three stabilization methods were exploited where the first one is based on the stabilized mixed finite element, the second is related to optimization of bubble viscosity and the last one is based on the Elastic Viscous Stress Splitting (EVSS).

Concerning the first one, stabilizing the numerical resolution method and implementing the missing terms were performed by the development of a new solver based on the mixed finite element method. With objective to handle complex mechanical problems, e.g. dynamic cases, stabilized mixed finite elements was investigated by using the element P1+/P1+ where the pressure is also enriched by an interpolation function in the space of small scales, known as "bubble function". The latter does not exist with respect to the conventional mixed finite elements with Mini-element P1+/P1. Several applications were analyzed by using this stabilization method with the new solver.

First application was performed by the modeling of incompressible elastic case. Good obtained results had strengthened our resolution strategy and shown the ability of this new solver. The representation possibility of the bubble velocity can give us more information to analyze and to better understand the role of the enriched bubble function in the stabilization method.

Regarding on the flow between two rigid particles case, the augmented Lagrangian method coupled with Uzawa's algorithm was applied. However, despite a complete resolution, we had not obtained a better result in terms of pressure. In fact, to overcome this problem, the discontinuous extra-stress in the right hand-side members must be changed by another continuously extra-stress by using an interpolation method, known as "stress extrapolation". The idea is to project the extra-stress, calculated on elements, on nodes by an average summarize of each neighbor element, called “the package element”.

An innovative approach of stabilization based on the modification of bubble viscosity by the mixed finite element was also investigated with several applications such as the two-phase test case, the flow between two rigid particles case and the incompressible elastic by Eulerian resolution. Influence of the bubble viscosity and the improvement of numerical simulation were detailed and demonstrated with satisfactory results. This contributed all necessary elements to lead us further in the simulation of the viscoelastic Kelvin-Voigt behavior.

The third stabilized method was investigated due to the complexity of the visco-hyper-elastic behavior, a direct resolution method will cause divers problems on stabilization. Thus, a classical mixed formulation on (u, v, p) coupling with the stabilization EVSS method was first used to meet the challenge. A time step marching scheme allows splitting the system resolution in two subsystems made of the viscoelastic constitutive equation and the flow equations was carried out to simplify the numerical resolution. Viscoelastic Kelvin-Voigt model was modeled with success, following the promising results on the hyper-elastic Neo-Hookean model. Unfortunately, the full FE modeling in 3D on the visco-hyper-elastic model was not achieved because of the stabilization problem on which needs more investigation.

Viscoelasticity and Visco-hyper-elasticity

As the behavior of polymers depends strongly on the temperature, close to its transition temperature, a strong behavior change from the rubbery state to the liquid state will appear. To obtain representative data for both the viscoelastic in solid phase and liquid phase, the validation was performed at different temperatures on the polymer PMMA Altuglas® V825T, supplied by Arkema®.

Concerning numerical simulations, two methods were used to validate our methodology: the method of Lagrange and Euler, where we used the mixed finite element solver with Mini-element P1+/P1. Although only the linear viscoelastic phase was verified, the results was verified and justified our methodology of resolution whatever applied method, in Lagrangian as well as in Eulerian framework, in 2 dimensions also in 3 dimension with the promising results. This showed and demonstrated the feasibility of viscoelastic modeling by the monolithic approach.

However, a simple classic Kelvin-Voigt model did not allow modeling the real behavior of polymer. Thus, more complex constitutive element of the model can carry away the actual limit. Therefore, the last work in this thesis was devoted to the implementation of a more realistic visco-hyper-elastic model proposed by Billon [80] [81] [82] [83] [84] based on the potential hyper-elasticity of Vilgis Edwards.

This new approach allows reproducing the thermomechanical behavior of materials over a wide range of strain rate and temperature. This model had been successfully implemented and validated by the comparison between the experimental results and the numerical results on integration point.

Concerning the resolution 3D FE modeling, a mixed formulation coupled with the EVSS resolution method was performed where the viscoelastic Kelvin-Voigt and the hyper-elastic Neo-Hookean model have been successfully modeled with the promising results. Unfortunately, the complete modeling 3D FE model of the hyper-visco-elastic model was not reached due to the stabilization problem which needs more investigation. More accurate results could be obtained and completed in the near future, especially with the promising results shown in this study. Using this visco-hyper-elastic model, we believe that the quantitative results could be compared across experimental tests. This is an open door in modeling and simulation in many complex dynamics applications.

6.2 Perspectives

The focus in this work is to develop a new numerical concept for modeling and simulating the complex behavior of polymer as viscoelasticity or visco-hyper-elasticity. Since during our study, some instability problem was appeared, three stabilized methods were presented to overcome this problem. In spite of the considerable amelioration to the numerical result, the study was not accomplished due to the time limit. It opens an interesting way to investigate and to exploit in future works thanks to the promising obtained results.

The modeling of viscoelastic Kelvin-Voigt demonstrated and validated our numerical method of resolution. Also the first work in the visco-hyper-elasticity showed a good potential and it deserves an important investment for the future development.

Clearly, a number of other considerations have to be taken into account for a more robust and stable solver and numerical resolution scheme which may deal with another complex computational simulation as the visco-hyper-elastic behavior, or a dynamic problem as impact case represented in Figure 6-1 and Figure 6-2.

In fact, the response of materials and structures under impact and dynamic contact have actually received a wide attention and investigation due to their important application in many fields such as automobile, aerospace and machinery industry. Conceptually, this is quite complex to numerically model, three different periods may be distinguished: before, during and after contact impact. Several phenomenal regimes may be appeared in space of three periods where low intensity excitation in the first one increases through the second, the material is driven into the other phase, the behavior involves large deformations and heating, finally the response of material constitutes another aspect of behavior after impact.

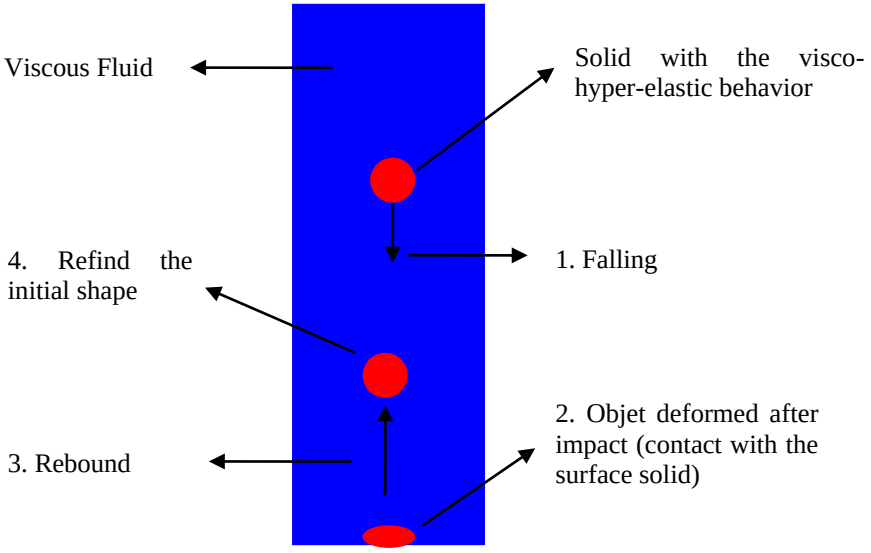


Figure 6-1: Representation of an impact test case 1.

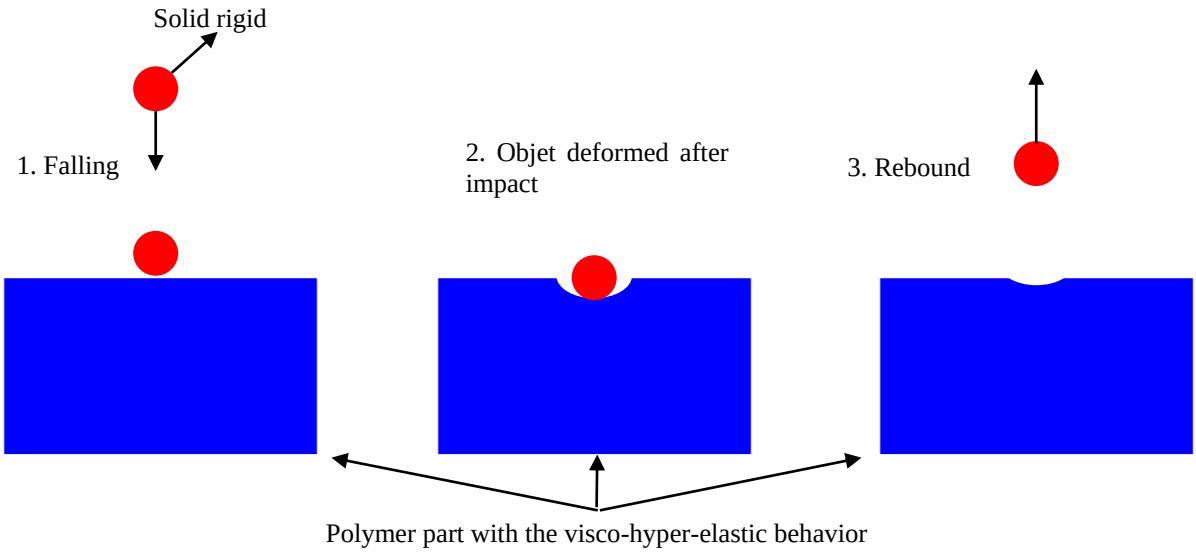


Figure 6-2: Representation of an impact test case 2.

Nomenclature

Abbreviations

ALE	Arbitrary Lagrangian Eulerian
EVSS	Elastic Viscous Stress Splitting
DEVSS	Discrete Elastic Viscous Stress Splitting
FEM	Finite Element Method
FSI	Fluid-Structure Interaction
GLS	Galerkin/Least-Squares
HWNP	High Weissenberg Number Problem
RFB	Residual-Free Bubbles
SUPG	Streamline upwind Petrov-Galerkin
SU	Streamline upwind

Variables and material properties

v	velocity vector
u	displacement vector
$u_{imposed}$	boundary displacement
$v_{imposed}$	boundary velocity
f_s	exterior force applied to solid
p	pressure
τ	extra-stress
χ_p	isothermal compressibility coefficient *Pa-1*
ρ	density kg/m^3
σ	Cauchy stress tensor
σ_i	stress tensor
$\varepsilon(u)$	strain tensor
$\varepsilon(v)$	strain rate tensor
η	dynamical viscosity *Pas*
λ_e	second Lame coefficient
μ_e	first Lame coefficient
ν_e	Poisson's ratio
E	Young's modulus *Pa*
λ	elongation strain in the tensile direction
J	Jacobi
I_i	invariants of right and left Cauchy-Green
F	transformation tensor
C	right Cauchy-Green strain tensor
B	left Cauchy-Green strain tensor
E	Green-Lagrange strain tensor
A	Euler-Almansi tensor
Π	Piola-Kirchhoff tensor
S	second Piola-Kirchhoff tensor
ψ	free energy
w	strain energy density

N_c	density of cross-links
N_s	density of slip-links or the entanglement density
α	inextensibility parameter
η	slipperiness factor

Domains

Γ_i	fluid-structure interface
Ω	spatial computational domain
$\partial\Omega$	special boundary of the computational domain
Ω_i	subdomain *i*
Ω_h	discretized spatial computational domain
κ	element

Temporal and spatial notations

t	time
t_n	instant *n*
a^n	value at time step *n*
$\Delta t = t_{n+1} - t_n$	time element length
x	point coordinates
$H^1(\Omega)$	Hilbert space
$L^2(\Omega)$	Lebesgue space
$[0, \Theta]$	temporal computational domain, Θ is the processus duration
V	function space for velocity (displacement)
P	function space for pressure
S	function space for extra-stress
w	weighting function space for velocity
ς	weighting function space for displacement
q	weighting function space for pressure
ϕ	weighting function space for extra-stress
V_h	discrete finite element space for velocity (displacement)
P_h	discrete finite element space for pressure
V_h^b	discrete finite element space enriched by bubble functions for velocity (displacement)
P_h^b	discrete finite element space enriched by bubble functions for pressure
$V_{h,0}$	discrete weighting finite element space for velocity (displacement)
$V_{h,0}^b$	discrete weighting finite element space enriched by bubble functions for velocity
v_h	discrete solution function space for velocity
u_h	discrete solution function space for displacement
p_h	discrete solution function space for pressure
v_h^b	discrete solution function space for bubble velocity

u_h^b	discrete solution function space for bubble displacement
p_h^b	discrete solution function space for bubble pressure
w_h	discrete weighting function space for velocity
ς_h	discrete weighting function space for displacement
q_h	discrete weighting function space for pressure
w_h^b	discrete weighting function space for bubble velocity
ς_h^b	discrete weighting function space for bubble displacement
q_h^b	discrete weighting function space for bubble pressure

General and Operators

$\nabla_x a$	gradient with respect to the material system x
$\nabla \cdot a$	divergence
$\lvert a \rvert$	Euclidian norm of the vector a
a^t	transposed vector/tensor
$\frac{da}{dt}$	material time derivative
$\frac{\partial a}{\partial t}$	temporal derivative
$\int_a$	integral over the domain of a
$tr(\bullet)$	trace operator

Appendix

A. Modeling visco-hyper-elastic behavior

In this appendix we focus on the modeling of the visco-hyper-elastic from the recent work of Billon N. and co-workers [77] since we have used in the last section.

Deformation invariants

In order to present the visco-hyper-elastic behavior based on the crosslink-sliplink model proposed by Edwards and Vilgis, some mechanical notations will be reminded in the following section. First, we define the right and left Cauchy-Green strain tensor or Cauchy's dilatation tensor as equation (6.1) and (6.2). Note that this strain tensor needs to be expressed in the initial configuration.

$$C = F^t F \tag{6.1}$$

and

$$B = FF^t \tag{6.2}$$

where the gradient tensor of the transformation F is decomposed F_e, the deformation gradient of elastic part and F_{an}, the deformation of anelastic part:

$$F = F_e F_{an} \tag{6.3}$$

We recall the identity of Cayley-Hamilton: a second order tensor is a solution of its characteristic polynomial, i.e.:

$$-C^3 + I_1 C^2 - I_2 C + I_3 = 0 \tag{6.4}$$

Where the invariants of right and left Cauchy-Green is resumed:

$$I_1 = tr(C) = tr(B) \tag{6.5}$$

$$I_2 = \frac{1}{2}\left(I_1^2 - tr\left(C^2\right)\right) \tag{6.6}$$

$$I_3 = \det(C) = \det(B) \tag{6.7}$$

In relation with the deformation ratios tensor $\lambda_{i(i=1,2,3)}$, diagonalized tensor from the strain tensor C and B, the invariants is written:

$$I_1 = \lambda_1^2 + \lambda_2^2 + \lambda_3^2 \tag{6.8}$$

$$I_2 = \lambda_1^2\lambda_2^2 + \lambda_2^2\lambda_3^2 + \lambda_3^2\lambda_1^2 \tag{6.9}$$

$$I_3 = \lambda_1^2 \lambda_2^2 \lambda_3^2 \tag{6.10}$$

where

$$\begin{cases} \dfrac{\partial I_1}{\partial C} = I \\ \dfrac{\partial I_2}{\partial C} = I_1 I - C \\ \dfrac{\partial I_3}{\partial C} = I_3 C^{-1} \end{cases} \tag{6.11}$$

Form of energy

The general framework is based in the crosslink-sliplink model proposed by Edwards and Vilgis [85]. The model is considered as a network which contains two types of junction points: the permanent cross-links where the chains are joined by chemical bonds; and entanglements or slip-links, which allow the chains to slide over one another.

Edwards and Vilgis had derived an express for free energy in the crosslink part, w_c, and the sliplink part, w_s:

$$w = \frac{1}{2} kT \left[\underbrace{N_c \left(\frac{\left(1-\alpha^2\right) I_1^e}{\left(1-\alpha^2 I_1^e\right)} + \ln\left(1-\alpha^2 I_1^e\right) \right)}_{w_c} + \underbrace{N_s \left(\frac{\left(1+\eta\right)\left(1-\alpha^2\right)}{\left(1-\alpha^2 I_1^e\right)} \frac{\partial}{\partial \eta} \left(\ln I_\eta^e \right) + \ln\left[\left(1-\alpha^2 I_1^e\right) I_\eta^e \right] \right)}_{w_s} \right] \tag{6.12}$$

with

$$I_\eta^e = 1 + \eta I_1^e + \eta^2 I_2^e + \eta^3 I_3^e \tag{6.13}$$

By definition of invariants, this potential can be re-written as:

$$w = \left[E_c \left(\frac{\left(1-\alpha^2\right) I_1^e}{\left(1-\alpha^2 I_1^e\right)} + \ln\left(1-\alpha^2 I_1^e\right) \right) + E_s \left(\begin{array}{l} \dfrac{\left(1+\eta\right)\left(1-\alpha^2\right)}{\left(1-\alpha^2 I_1^e\right)} \dfrac{I_1^e + 2\eta I_2^e + 3\eta^2 I_3^e}{1 + \eta I_1^e + \eta^2 I_2^e + \eta^3 I_3^e} \\ + \ln\left(1-\alpha^2 I_1^e\right) + \ln\left(1 + \eta I_1^e + \eta^2 I_2^e + \eta^3 I_3^e\right) \end{array} \right) \right] \tag{6.14}$$

The quantities E_c and E_s have dimensions of stress, being related to the number of crosslinks per unit volume N_c and number of sliplinks per unit volume N_s:

$$E_{c,s} = \frac{1}{2} kTN_{c,s} \tag{6.15}$$

where

- N_c is the concentration of cross-links or the number of crosslinks per unit volume
- N_s is the concentration of slip-links or the entanglement density
- α is the inextensibility parameter, predicted to be inversely proportional to the mean distance. It defines a limit of extensibility corresponding to a singularity in stress
- k is the Boltzmann constant
- T is the absolute temperature
- η is the slippage parameter or the slipperiness factor, a relative measure of the freedom of a link to slide. In principle, it can vary between infinity for perfect sliding and zero for no sliding. If $\eta = 0$ entanglements act as permanent nodes and if $\eta = 1$, they do not contribute to the elasticity of the network; is related to the inextensibility of the network through the maximum draw ratio, i.e. $\lambda_{\max} = \frac{1}{\alpha}$
- I^e is the invariant of right and left Cauchy-Green, related with the Cartesian components of the stretch ratio λ_i

Remark: attention, with respect to the notation in the literature, we kept the notation of slippage parameter as η in this case which is different with the viscosity cited in the above chapters.

Entropic anelasticity

Billon postulates that the basic behavior of the polymer is a tangled hyperelastic network in that the anelasticity is the result of a change in topology and/or number of entanglements most "mobile".

According to Edward Vilgis's model, this produces an increase in the slippage parameter η. However, this change only impacts directly the energy of the system and would not ensure compliance with the thermodynamics principles. To maintain a constant energy to the system, it must be admitted that a physical process takes place in parallel to compensate this change. This process is a relaxation of some elastic energy stored in the network, i.e. a relaxation of the deformation part of the network. This relaxation is the source of anelasticity.

Conceptually, at every moment the solicited material absorbs elastically the applied mechanical energy and returns a part to "re-organize" its entanglements, i.e., increase the slippage parameter η

In a generic way, this is written:

$$N_s \frac{\partial w_s}{\partial \eta} \dot{\eta} + \Delta + \sum_{i=1,3} \left(N_s \frac{\partial w_s}{\partial I_i^e} + N_c \frac{\partial w_c}{\partial I_i^e} \right) \frac{\partial I_i^e}{\partial t} = 0 \tag{6.16}$$

where Δ is the energy consumed to other than the disentanglement (e.g. heating). A 1D model as equation (6.17) may be easier to modeling:

$$N_s \frac{\partial w_s}{\partial \eta}\dot{\eta} + \Delta + \sum_{i=1,3}\left(N_s \frac{\partial w_s}{\partial \varepsilon_e} + N_c \frac{\partial w_c}{\partial \varepsilon_e} \right)\frac{\partial \varepsilon_e}{\partial t} = N_s \frac{\partial w_s}{\partial \eta}\dot{\eta} + \Delta - \sum_{i=1,3}\left(N_s \frac{\partial w_s}{\partial \varepsilon_e} + N_c \frac{\partial w_c}{\partial \varepsilon_e} \right)\frac{\partial \varepsilon_a}{\partial t} = 0 \qquad (6.17)$$

with ε_e and ε_a are respectively elastic and anelastic deformation.

The variation of the slippage parameter η, as a kinetics evolution $\dot{\eta}$, introduces a relaxation capacity of the mechanical solicited network. The proposed kinetics evolution is a function of the stored elastic energy at every moment, in the sense that the more constrained network is, the faster disentanglement is. In addition, the anelasticity is determined by an instantaneous stored elastic energy in the material, and also by the history of the evolution of potential slippage parameter $\dot{\eta}$.

The kinetics evolution $\dot{\eta}$ proposed by Billon as following:

$$\dot{\eta} = Z_p\left(e^{\Delta w} - 1\right) \qquad (6.18)$$

with z_p is a material parameter representing the "entropic force" of entanglement nodes. This parameter controls the slip evolution. In the thermodynamic framework, it is a function of state variables. It is assumed a function of temperature and parameterized by ε :

$$Z_p = f\left(T, \varepsilon\right) \qquad (6.19)$$

where Δw is the elastic energy between two stoked entanglements:

$$\Delta w = w_s\left(I_1^e, I_2^e, \eta\right) - w_s\left(I_1^e = 3, I_2^e = 3, \eta\right) \qquad (6.20)$$

The concept of entropy anelasticity is introduced. We then present the adaptation of statistical reasoning chain in a thermodynamically consistent.

Anelastic behavior

It is possible to assume the anelastic strain rate tensor D_{an} only by the material data without adding other components. The evolution law is defined in the following equation:

$$D_{an} = \frac{3}{2}\frac{1}{(1-\beta)}\frac{(S)^D}{(\sigma_{eq})^2}\frac{\partial w}{\partial \eta}\dot{\eta} \quad \text{with} \quad trace(D_{an}) = 0 \qquad (6.21)$$

this is deduced from the following equation between the thermodynamic forces:

$$(1-\beta)A^{D_{an}} : D_{an} + A^{\eta}\dot{\eta} \geq 0 \qquad (6.22)$$

where $(1-\beta)A^{D_{an}} : D_{an}$ represents the anelastic dissipation, and $A^{\eta}\dot{\eta}$ is the dissipation in the network caused by the degree of freedom evolution of the network nodes. These thermodynamic forces are expressed as:

$$A^{D_{an}} = 2C_e \frac{\partial w}{\partial C_e} - q'I \tag{6.23}$$

and

$$A^{\eta} = -\frac{\partial w}{\partial \eta} \tag{6.24}$$

$(S)^D$ is the stress in the intermediate configuration which can be written:

$$(S)^D = \frac{1}{2}\left(F_e^T \sigma^D F_e^{-T}\right) \tag{6.25}$$

and σ_{eq} is the Von Mises stress:

$$\sigma_{eq} = \sqrt{\frac{3}{2}\sigma^D : \sigma^D} \tag{6.26}$$

Notice that β is the Taylor-Quinney coefficient which represents the proportion of anelastic energy converted into the heating. Two extreme boundaries of β can be defined:

- if $\beta = 1$, the whole dissipation is original thermic, there is no evolution of the network. Anelastic processes are blocked, and the behavior is then the pure hyper-elastic
- if $\beta = 0$, the evolution of the network consumes the entire dissipation anelasticity, then there is no thermal evolution, the behavior is isothermal hyper-visco-elastic.

For example, β is usually close to 1 in the metals, meaning its dissipation from original thermic is strongly important. In the literature, this parameter is commonly, or always, considered as a constant.

Summary

The thermodynamic model presented is based on a description of the energy behavior. We used a potential energy from statistical models of the chain. This choice allowed us to maintain a strong physical sense while minimizing the number of parameters. However, due to the complexity of the global validation with the thermo-mechanic-dynamic model, we are interested only in the weak thermal coupling, meaning the temperature does not change the mechanical behavior.

The constitutive model to be developed relies on the above observations for modeling is therefore explored with some concrete aspects as following:

- the behavior is isotropic and isothermal
- in a first approximation, volume change is neglected, i.e. the polymer is assumed to be incompressible
- to account for the effects of velocity and temperature, both dependence on time and temperature are modeled using dependence upon $a_T \dot{\varepsilon}_{eq}$ by grouping these two variables

into one. It is named the equivalent velocity under the reference temperature. For a better comprehension, lecture may refer to the work of Billon [80].

- entropy is the only source of elasticity
- the model account for hyper-elasticity deformation

And key issues for the model to account for anelasticity and viscous effects are [81]:

- anelasticity and viscous effects results from disentanglement or additional mobility of the slip link. This results in the modification of Edwards Vilgis parameters
- modification induces anelastic strain to reequilibrate free energy
- anelastic strain-rate is controlled by energy balance

The presented thermodynamic model is based on a description of the energy behavior. The potential energy is used from statistical models of the chain. This choice allowed maintaining some physical sense while minimizing the number of parameters. For one condition, five principal parameters of materials ($N_c, N_s, \alpha, Z_p, \beta$) have been introduced which are sufficient to reproduce experimental observation with the good agreement (see Figure 0-4 and Figure 0-3).

Kinetics equations for parameters and dissipation potential based on energy exchanges are combined with initial Edwards-Vilgis's model. This allows reproducing experimental observation in a promising manner [81].

Analytic formulation

Considering that the material is incompressible, the stress tensor is assumed as:

$$\sigma = \sigma' - p'I = \frac{2}{J} F_e \frac{\partial w}{\partial C_e} F_e^t - p^{\#} I \tag{6.27}$$

where σ' is the stress tensor defined by the thermodynamic at an undetermined pressure close to $p^{\#}$ which depends on the initial boundary condition.

For a more detail of the stress tensor, the equation (6.27) can be written as:

$$\sigma = \frac{2}{J} F_e \left(\frac{\partial w}{\partial I_1^e} \frac{\partial I_1^e}{\partial C_e} + \frac{\partial w}{\partial I_2^e} \frac{\partial I_2^e}{\partial C_e} + \frac{\partial w}{\partial I_3^e} \frac{\partial I_3^e}{\partial C_e} \right) F_e^t - p^{\#} I \tag{6.28}$$

with *J* is the Jacobian ratio.

Using the Edwards-Vilgil's model, the analytical expressions of partial derivatives of the elastic energy function are:

$$\frac{\partial w}{\partial I_1^e} = E_c\left(\frac{1-2\alpha^2-\alpha^4 I_1^e}{\left(1-\alpha^2 I_1^e\right)^2}\right) + E_s\left(\begin{array}{l} -\dfrac{\alpha^2(1+\eta)(1-\alpha^2)}{\left(1-\alpha^2 I_1^e\right)^2}\dfrac{I_1^e+2\eta I_2^e+3\eta^2 I_3^e}{1+\eta I_1^e+\eta^2 I_2^e+\eta^3 I_3^e} \\ +\dfrac{(1+\eta)(1-\alpha^2)}{1-\alpha^2 I_1^e}\dfrac{1-\eta^2 I_2^e-2\eta^3 I_3^e}{\left(1+\eta I_1^e+\eta^2 I_2^e+\eta^3 I_3^e\right)^2} \\ +\dfrac{-\alpha^2}{1-\alpha^2 I_1^e}+\dfrac{\eta}{1+\eta I_1^e+\eta^2 I_2^e+\eta^3 I_3^e} \end{array}\right) \tag{6.29}$$

$$\frac{\partial w}{\partial I_2^e} = E_s\left(\frac{(1+\eta)(1-\alpha^2)}{1-\alpha^2 I_1^e}\frac{2\eta\left(1+\eta I_1^e+\eta^2 I_2^e+\eta^3 I_3^e\right)-\eta^2}{\left(1+\eta I_1^e+\eta^2 I_2^e+\eta^3 I_3^e\right)^2}+\frac{\eta^2}{1+\eta I_1^e+\eta^2 I_2^e+\eta^3 I_3^e}\right) \tag{6.30}$$

$$\frac{\partial w}{\partial I_3^e} = E_s\left(\frac{(1+\eta)(1-\alpha^2)}{1-\alpha^2 I_1^e}\frac{\left(3\eta^2+2\eta^3 I_1^e+\eta^4 I_2^e\right)}{\left(1+\eta I_1^e+\eta^2 I_2^e+\eta^3 I_3^e\right)^2}+\frac{\eta^3}{1+\eta I_1^e+\eta^2 I_2^e+\eta^3 I_3^e}\right) \tag{6.31}$$

And that of the degree of freedom of the chains is resumed:

$$\frac{\partial w}{\partial \eta} = E_s\frac{(1-\alpha^2)}{1-\alpha^2 I_1^e}\left(\begin{array}{l} \dfrac{\left(I_1^e+2\eta I_2^e+3\eta^2 I_3^e\right)}{\left(1+\eta I_1^e+\eta^2 I_2^e+\eta^3 I_3^e\right)}+\dfrac{(1+\eta)\left(2I_2^e+6\eta I_3^e\right)}{\left(1+\eta I_1^e+\eta^2 I_2^e+\eta^3 I_3^e\right)} \\ -\dfrac{(1+\eta)\left(I_1^e+2\eta I_2^e+3\eta^2 I_3^e\right)^2}{\left(1+\eta I_1^e+\eta^2 I_2^e+\eta^3 I_3^e\right)^2}+\dfrac{\left(I_1^e+2\eta I_2^e+3\eta^2 I_3^e\right)}{\left(1+\eta I_1^e+\eta^2 I_2^e+\eta^3 I_3^e\right)} \end{array}\right) \tag{6.32}$$

The stress tensor defined by the thermodynamic is written as:

$$\sigma' = \frac{2}{J}\left[\left(\frac{\partial w}{\partial I_{1e}}+I_{1e}\frac{\partial w}{\partial I_{2e}}\right)C_e-\frac{\partial w}{\partial I_{2e}}{C_e}^2+I_{3e}\frac{\partial w}{\partial I_{3e}}I\right] \tag{6.33}$$

General algorithm

As mentioned in the below section, the equivalent velocity under the reference temperature $a_T\dot{\varepsilon}_{eq}$ [80] was defined to account for the effects of velocity and temperature. Knowing the actual temperature, the shift factor is known at every moment. Therefore, the reasoning associates with the temporal equivalence to a reference temperature must also be completed on time discretization:

$$a_T\dot{\varepsilon}_{eq} = a_T\frac{d\varepsilon_{eq}}{dt} = \frac{d\varepsilon_{eq}}{\left(dt/a_T\right)} = \frac{d\varepsilon_{eq}}{d\tau} \tag{6.34}$$

with *dt* is the real time step, $d\tau = \frac{dt}{a_T}$ is the equivalent time step corresponding to the reference temperature.

The expression of the total equivalent time is written as:

$$\tau = \int_0^t \frac{dt}{a_T(t)} \tag{6.35}$$

This equivalent time is based on history because each equivalent time step is directly connected to instant shift factor, or directly connected to the historic evolution of the temperature. This equivalent time is the time "physical" felt by the material.

After the recent work of Billon and co-workers [77], the algorithm of modeling, implemented in Matlab, is illustrated in the following figure:

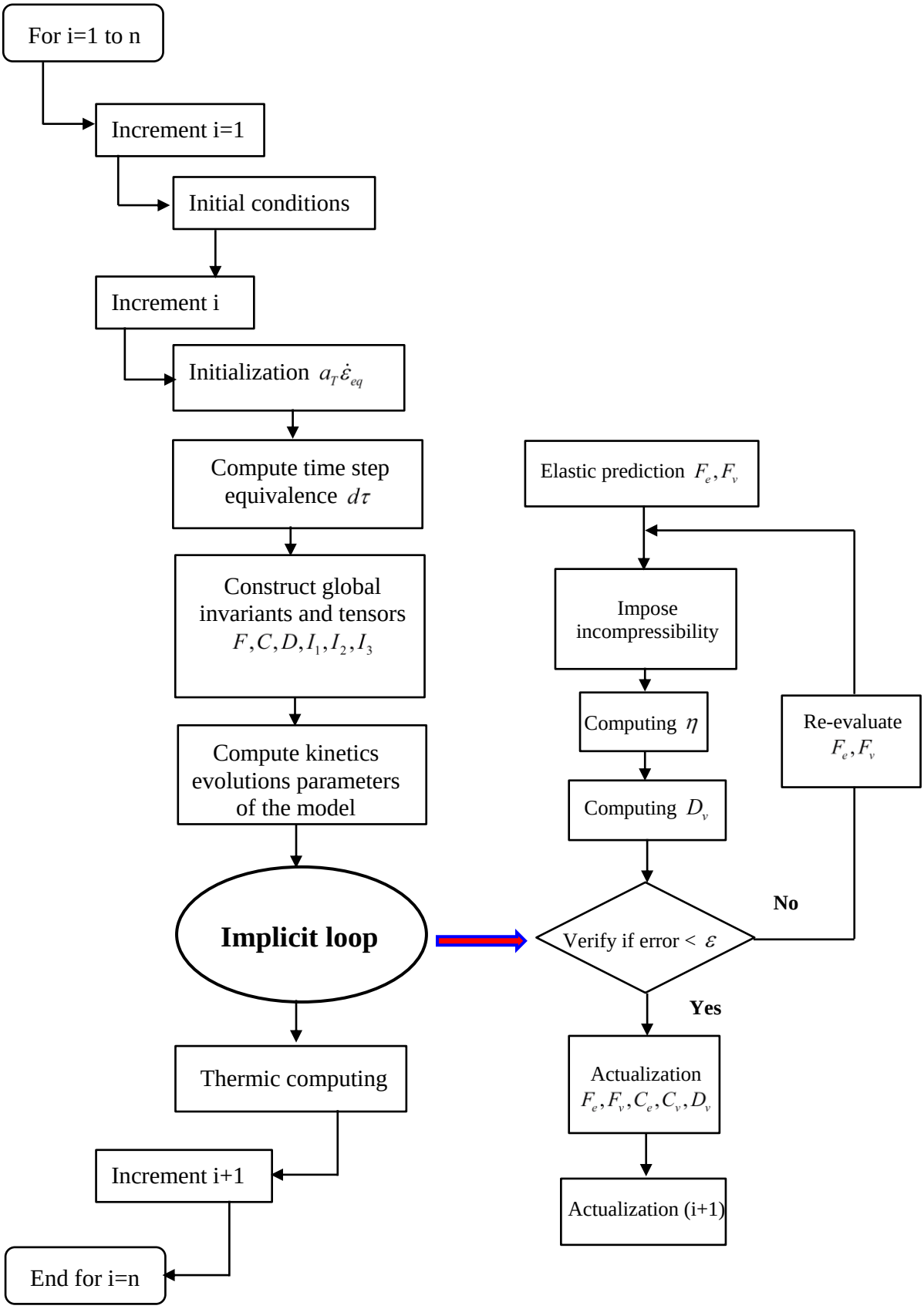


Figure 0-1: Algorithm of resolution

The developed model in its 3D generality is compatible with approaches thermodynamics of irreversible processes and reproduces the behavior of polymers. Its ability to reproduce the anelastic effects, in a uniaxial case, is illustrated in Figure 0-2.

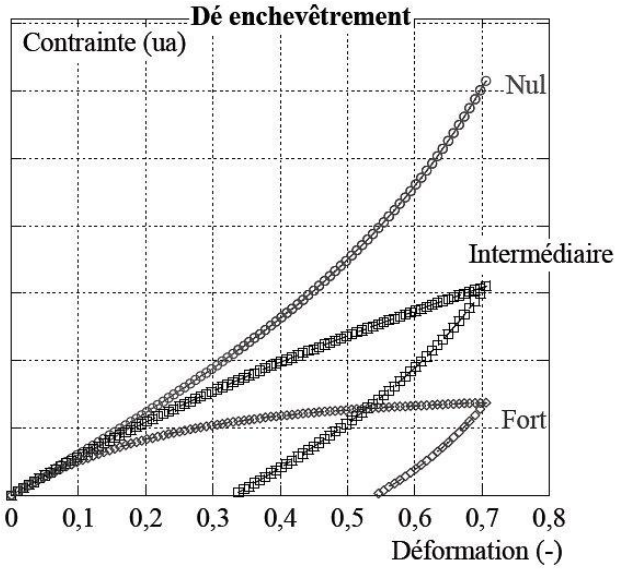


Figure 0-2: Example of obtained results under loading/unloading with the model. Schematic of representation of comparison between the basic hyper-elastic model (no entanglement) and two disentanglement cases [80].

The five basic parameters, cited in the section 0, are sufficient to reproduce the whole hysteresis loop where the application to a PMMA model (Figure 0-4), also a HIPS model (Figure 0-4), gives excellent results.

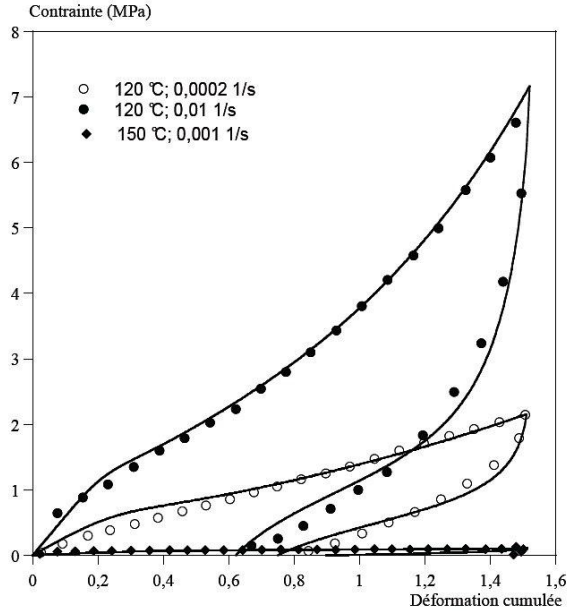


Figure 0-3 : Comparison model (plain line) – experience for PMMA [80].

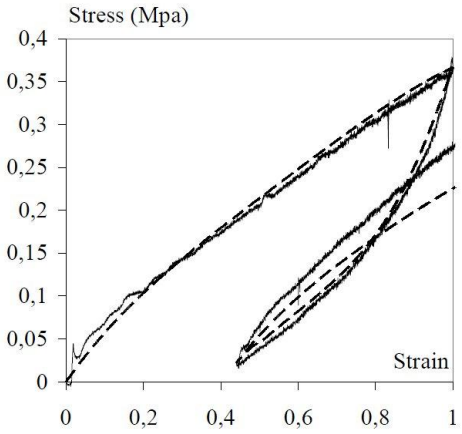


Figure 0-4: Comparison between experimental curve (plain line) and prediction of the model (dotted line) in the case of $10e^{-3}s^{-1}$ tensile test at 115°C [81].

List of Figures

Figure 2-1: E (10 Sec.) for a crystalline polystyrene (A), a lightly cross-linked polystyrene (B), and amorphous polystyrene (C) [15]. 21

Figure 2-2: Schematic representation of Maxwell model. 22

Figure 2-3: Schematic representation of the Kelvin–Voigt model. 23

Figure 2-4: Schematic representation of the Burgers model. 23

Figure 2-5: Generalized Maxwell model. 24

Figure 2-6: Generalized Kelvin-Voigt model. 24

Figure 2-7: The piston problem (interface region expanded for clarity) [46]. 28

Figure 2-8: Referential Lagrangian, Eulerian and ALE [54]. 29

Figure 2-9: Evolution of the mesh following the implemented formulation [58]. 30

Figure 2-10: Pressure drop over a membrane using the fictitious domain method without mesh adaptation (a) and with mesh adaptation (b) (showing the velocity vector field) [68]. 31

Figure 2-11: Illustration of the sharp-interface, and two-phase and mixture diffuse-interface approaches [69]. 32

Figure 2-12: Two-dimensional representation of the displacements [76]. 35

Figure 2-13: Stress description in the different configuration (Lagrangian and Eulerian). 37

Figure 3-1: Simple uploading-unloading tensile test benchmark by the Lagrangian (left) and Eulerian (right) approach. In the left image, schematic of the original deformed and restored specimen. The image represents the initial, loaded and restored configurations. Remark that the specimen dimensions are in agreement with the real dimension of the specimen in the experimental test, which will be later presented in chapter 5. And the right image represents the schematic of the tensile test using an Eulerian method (detailed later in the section 3.4). 53

Figure 3-2: Geometry, boundary conditions and mesh representation for the flow between two rigid particles test case. 54

Figure 3-3: Element P1+/P1 (MINI-element) for velocity-pressure interpolation. 56

Figure 3-4: Displacement interpolation. 57

Figure 3-5: Schematic representation of a reference sub-element (ST_i) in two dimensions. 57

Figure 3-6: Schematic representation of the deformation of specimen, measure of the longitudinal strain. Deformations of the specimen up to two levels of strain are considered: 5 to 10% and 20 to 30% - ε_{yy}. 63

Figure 3-7: Specimen shape under uploading and unloading tensile tests with different levels of strain, for an elastic behavior and resolution on one single step. 63

Figure 3-8: Specimen shape under uploading-unloading tensile with different levels of strain and different meshes (5%, 10%, 20% and 30% strain). 64

Figure 3-9: Specimen shape (with a rectangular/circular hole) under uploading-unloading tensile with different levels of strain and different meshes (5%, 10%, 20% and 30% strain). 65

Figure 3-10: Specimen shape (3D) under uploading-unloading tensile with different levels of strain. 66

Figure 3-11: Specimen shape (3D with a circular hole) under uploading and unloading tensile with different levels of strain and different meshes (5%, 10%, 20% and 30% strain). 66

Figure 3-12: Specimen shape (3D with a rectangular hole) under uploading and unloading tensile with different levels of strain and different meshes (5%, 10%, 20% and 30% strain). 66

Figure 3-13: Specimen shape under uploading-unloading tensile at 30% strain for different time steps. 69

Figure 3-14: Specimen shape (2D with a rectangular hole) under uploading-unloading tensile at 30% strain for different time steps. 69

Figure 3-15: Specimen shape (2D with a circular hole) under uploading-unloading tensile at 30% strain for different time steps. 69

Figure 3-16: Specimen shape (3D with a rectangular/circular hole) under uploading-unloading tensile at 30% strain for a different time steps. 70

Figure 3-17: Specimen shape (3D) under flexion (left image) and torsion (right image) for 100 time steps. 71

Figure 3-18: Specimen shape (3D) under compression for 100 time steps. 71

Figure 3-19: Specimen shape under uploading-unloading tensile at 30% strain for 100 time steps with different viscous and elastic factors. (a, b, c, d) correspond to the different cases of Table 3-1. 73

Figure 3-20: Elastic stress under uploading at 35% strain for 100 time steps in the viscoelastic case. (a, b, c, d) refer to the different cases of Table 3-1 74

Figure 3-21: Viscous stress under uploading at 35% strain for 100 time steps in the viscoelastic case. (a, b, c, d) refer to the different cases of Table 3-1. 74

Figure 3-22: Specimen shape (2D-left image and 3D-right image) under tensile test at 35% strain for 1, 10 and 100 time steps in the elastic case. 75

Figure 3-23: Two phases of a single mesh. The interface $\Gamma_{f/s}$ which separates the two phases through the elements is represented by a distance function α. 76

Figure 3-24: Illustration of the viscosity distribution on the mesh for the two mixture laws: P1 on the left and P0 on the right. 77

Figure 3-25: Vertical section of Figure 3-24. A good intermediate value of the mixed field for the discontinuous law is corresponding to that in the element crossed by the interface. The two variations of slope for the continue law P1 are due to the mesh. 77

Figure 3-26: Interface refinement using anisotropic mesh adaptation: a zoom at the interface region. 79

Figure 3-27: Zoom on the specimen/fluid interface after anisotropic adaptation in 3D. 80

Figure 3-28: Tensile test by an Eulerian approach. Schematic representation of the specimen interface shape by an Eulerian method. Please note that the specimen interface is represented by the zero iso-value of the distance function α which is transported by the Level-Set method. 83

Figure 3-29: Pressure field under loading (left) and unloading (right). 84

Figure 3-30: Monophasic case for the modeling the two phase flow of a fluid around a rigid body (*reference solution*). 87

Figure 3-31: Velocity field. In the first row, on the left velocity by the one phase modeling, on the right velocity by the penalization method is displayed. 88

Figure 3-32: Pressure oscillation on the interface solid-fluid. 89

Figure 4-1: Commutative diagram of stabilized methods (after Brezzi et al [100]). 95

Figure 4-2: Element P1+/P1+ for velocity-pressure. 97

Figure 4-3: Displacement interpolation. 97

Figure 4-4: Mesh representation of the sample in the tensile test in 2D (zoom of a part of the sample) and 3D. The sample in 2D contains 142.130 nodes/282.472 elements, and that in 3D contains 142.522 nodes/783.324 elements. . 104

Figure 4-5: Displacement norm and pressure under loading-unloading with the old NSTC solver. Errors in recovery are of the order of the asked precision for the iterative solver ($1e^{-11}$) for the displacement norm and $1e^{-8}$ for pressure. 109

Figure 4-6: Displacement norm and pressure under loading-unloading with the new SMC solver. Errors in recovery are of the order of the asked precision for the iterative solver ($1e^{-11}$) for the displacement norm and $1e^{-8}$ for pressure. 110

Figure 4-7: Schematic representation of the bubble velocity field in the specimen under loading with the mesh geometry and the pressure field. Since the bubble velocity is computed on elements, these vectors are illustrated on elements. Note that the pressure field is colored as its displayed scale. 111

Figure 4-8: Bubble displacement under loading u_b^0 (left) and under unloading u_b^1 (right) with the full resolution by the new SMC solver. First, we can see the unstable pressure zone in the borders where the intensity of the bubble

displacement is strong. Secondly, this shows a perfect recovery in which the obtained bubble displacements are perfectly opposite to traction and during spring back. 111

Figure 4-9: Bubble displacement under loading u_b^0 (left) and under unloading u_b^1 (right) with the resolution by the old NSTC solver. This shows that the obtained bubble displacements are zero during spring back as theoretically demonstrated. 112

Figure 4-10: Displacement norm (mm) and pressure (Pa) in traction and return by the incremental time step resolution *(velocity-pressure "v-p") (*40% of strain for 100 time steps). Note that the errors introduced in recovery are of the order of the asked precision for the iterative solver ($1e^{-17}$), for the displacement norm and ($1e^{-7}$) for the pressure with the new SMC solver with different. 114

Figure 4-11: Displacement norm (mm) and pressure (Pa) in traction and return by the incremental time step resolution *(velocity-pressure "v-p") (*60% of strain for 100 time steps). 114

Figure 4-12: Displacement norm (mm) and pressure (Pa) in traction and return by the incremental time step resolution *(velocity-pressure "v-p") (*60% of strain for 10 time steps). 115

Figure 4-13: Velocity field (linear part) for the test case of flow around rigid particles. In the first row, on the left, velocity by the one phase modeling (reference results), on the right velocity by the penalization method; in the second row, on the left, velocity by the augmented Lagrangian method with Uzawa algorithm (the old solver NSTC) and on the right the new solver SMC (augmented Lagrangian method with Uzawa algorithm with a bubble's extra stress). . 117

Figure 4-14: Bubble velocity field for the test case of flow around rigid particles using an augmented Lagrangian resolution; of flows in the pore space; on the left, the bubble velocity with the old solver NSTC (recomputed after resolution) and on the right the new solver SMC (directly computed by the solver). 118

Figure 4-15: Pressure field resolution by the NSTC solver on the left and the SMC solver on the right. 118

Figure 4-16: Distribution of fluid/solid inside an element 119

Figure 4-17: Stress projection on node [127]. 120

Figure 4-18: Two phase test case. 123

Figure 4-19: Analysis of the pressure unstable zone. 124

Figure 4-20: Pressure values through a vertical line crossing both domains for different solid viscosities using two different mixture laws. Please note that we did not synchronize the scales of the two curves due to the strong difference between them. 124

Figure 4-21: Pressure for different bubble viscosities, from 0.001 to 1 Pas by P1 mixture law. 125

Figure 4-22: Bubble viscosity by two laws for the distribution of the bubble viscosity. On the left the rectangular function, and on the right the smoothed function. 126

Figure 4-23: Pressure by two mixture laws of bubble viscosity. Maximum pressure decreases from 0.44 to 0.022 (reduces above 20 times). Maximum pressure decreases from 0.44 to 0.0067 (reduces above 70 times the error committed). Please note that we did not synchronize the scale of the two figures due to the strong difference between them. 126

Figure 4-24: Norm L^2 of errors on the velocity using the standard bubble viscosity (left) and the modification of bubble viscosity (right). 127

Figure 4-25: Norm L^2 of errors on the velocity using the standard bubble viscosity (left) and the modification of bubble viscosity (right). Measurement is taken on the diagonal line of the simulation domain as illustrated in Figure 4-24. 127

Figure 4-26: Bubble velocity on the unstable pressure zone. 127

Figure 4-27: Modification of bubble viscosity in the multiphase approach. 128

Figure 4-28: Schematic representation of the pressure field. 128

Figure 4-29: Pressure field comparison in the fluid between the monophasic (reference solution) and the multiphase approach after the modification of the bubble viscosity. 129

Figure 4-30: Pressure analysis through the thickness with different methods. 129

Figure 4-31: Modification of bubble viscosity in the mixture zone in the tensile test by an Eulerian approach. 130

Figure 4-32: Tensile test by an Eulerian method, deformed shape represented by the zero iso-value of the Level-Set function. 130

Figure 4-33: Pressure field under loading (left) and unloading (right) with stabilization by modification of the bubble viscosity. 131

Figure 4-34: Pressure curve without stabilization (red - without modification of the bubble viscosity – left image) and with stabilization (blue - with modification of the bubble viscosity – right image) 131

Figure 5-1: Samples tooled from the PMMA plate and its initial form. 141

Figure 5-2: Spotted specimen and its image. 142

Figure 5-3: Test bench for 90°C and 110°C. 143

Figure 5-4: Spotted specimen and its image through the prism. 144

Figure 5-5: Specimen's shape for the relaxation test at 163°C. 144

Figure 5-6: Test bench for 163°C. 144

Figure 5-7: Experimental curve force/displacement at 90°C under different solicitations (loading up to rupture, loading/unloading and relaxation). 145

Figure 5-8: Experimental curves force/displacement at 110°C under different solicitations (loading up to rupture, loading/unloading and relaxation). 145

Figure 5-9: Experimental curve force/displacement at 163°C under a relaxation test. 146

Figure 5-10: Post processing by image correlation analysis. 146

Figure 5-11: Non monotonic tensile tests (loading/unloading) at 90°C. 147

Figure 5-12: Non monotonic tensile tests (loading/unloading) at 110°C. 147

Figure 5-13: Relaxation tests. Comparison between 90°C (blue) and 110°C (pink). 148

Figure 5-14: Relaxation tests at 163°C. 148

Figure 5-15: Comparison between the strain in the three directions at 90°C. 148

Figure 5-16: Comparison between the strain in the three directions at 110°C. 149

Figure 5-17: Volume variations at 90°C. 149

Figure 5-18: Volume variations at 110°C. 149

Figure 5-19: σ_{yy} stress at 110°C and loading by the incremental Lagrangian and Eulerian methods in 2D and 3D. In the first row, from left to right, the first image represents the specimen under loading by the incremental Lagrangian approach in 3D, the second describes the 2D Eulerian approach and the last one the 3D Eulerian approach. The image in the second row displays the stress inside of the specimen on two cutting planes, for the 3D Eulerian approach. 151

Figure 5-20: Stress vs. Strain curves for loading at 90°C. Curves illustrate the comparison between experimental and simulation by the incremental Lagrangian and Eulerian methods, in 2D and 3D. 152

Figure 5-21: Stress vs. Strain curves for loading at 110°C. Curves illustrate the comparison between experimental and simulation by the incremental Lagrangian and Eulerian methods, in 2D and 3D. 152

Figure 5-22: Stress vs. Strain curves for loading at 163°C. Curves illustrate the comparison between experimental and simulation by the incremental Lagrangian and Eulerian methods, in 2D and 3D. 152

Figure 5-23: Stress vs. Strain curves for the tensile test at 21.6°C and for a strain rate of $1.83e^{-2}$ s^{-1}. The chosen material is a Polyamide 6.6 produced by Rhodia. Curves illustrate the comparison between experimental and simulation by calculation on the material point with different values of Z_p, the parameter that controls the change rate of η 155

Figure 5-24: Stress vs. Strain curves for the shear test. Curves illustrate the comparison between experimental and simulation by calculation on the material point with different value of Z_p. The value of strain rate is $3.7e^{-2}$ s^{-1} 155

Figure 5-25: Stress vs. Strain curves for the tensile test at 21.6°C and for the strain rate of $1.83e^{-2}$ s^{-1}. Curves illustrate the simulation with different time steps. 156

Figure 5-26: Longitudinal stress distribution in the specimen with the Kelvin-Voigt viscoelastic model.....158

Figure 5-27: Axial stress in the central zone under loading and unloading. 158

Figure 5-28: Longitudinal stress distribution in the specimen with the Neo-Hookean hyper-elastic model.....160

Figure 5-29: Original geometry and mesh of the tensile test by an Eulerian approach. Schematic representation of the mesh in a cutting plane on the thickness of the computational domain. 161

Figure 5-30: Longitudinal stress distribution at 5% (upper left), 15% (upper right), 25% (lower left) and 50% (lower right) of deformation.....162

Figure 5-31: Longitudinal stress distribution inside the specimen at 5% (left) and 60% (right) of deformation. Schematic representation is obtained by two symmetric cutting planes following the longitudinal and the thickness direction. 162

Figure 5-32: Mesh and stress distribution on the cutting plane at 60% strain.....162

Figure 5-33: Anisotropic mesh and stress distribution on the cutting plan at 60% (left) and 70% (right). 163

Figure 5-34: Zoom of stress distribution vs. mesh size in the central zone.....163

Figure 5-35: A combined numerical/analogic analysis of longitudinal stress with the Neo-Hookean hyper-elastic model. 163

Figure 5-36: A perfect tensile test bench (left) and a normal tensile test bench (right). 166

Figure 5-37: Stress evolution comparison between experiment and simulation with different values of Z_p 166

Figure 5-38: Longitudinal stress distribution in the specimen for the visco-hyper-elastic model behavior.....167

Figure 5-39: A combined numerical/experimental analysis of the longitudinal stress evolution in the central zone with the visco-hyper-elastic model and an incremental Lagrangian approach.....167

Figure 6-1: Representation of an impact test case 1.....176

Figure 6-2: Representation of an impact test case 2.....177

Figure 0-1: Algorithm of resolution.....190

Figure 0-2: Example of obtained results under loading/unloading with the model. Schematic of representation of comparison between the basic hyper-elastic model (no entanglement) and two disentanglement cases [80].....191

Figure 0-3 : Comparison model (plain line) – experience for PMMA [80]. 191

Figure 0-4: Comparison between experimental curve (plain line) and prediction of the model (dotted line) in the case of $10e^{-3}s^{-1}$ tensile test at 115°C [81]. 192

List of Tables

Table 3-1: Elastic part (σ_e) in relation to a viscous part (σ_v), in what concerns a Kelvin Voigt law. The time step Δt corresponds to a computation of 100 increments. 73

Table 3-2: Material parameters used. 83

Table 3-3: Material parameters used for the flow between two rigid solid particles case by the penalization method. 88

Table 4-1: Comparison between the NSTC and the SMC solvers in 2D. 104

Table 4-2: Comparison between the NSTC and the SMC solvers in 3D. 105

Table 4-3: Maximum pressure obtained for different configuration tests (the fluid viscosity is 1 *Pas* for all the tests). The gain in the accuracy of the result is compared between the 1st method to modify bubble viscosity and the result performed with the mixture laws P1 and P0. 128

Table 5-1: Experimental performed tests. 142

Table 5-2: Parameters identified for the Kelvin-Voigt model. 150

Table 5-3: Material parameters used for visco-hyper-elastic model in the tensile and shear tests. 154

Table 5-4: Material parameters used for the Kelvin-Voigt model. 158

Table 5-5: Material parameters used in for the Neo-Hookean model. 159

Table 5-6: Material parameters used in Eulerian approach. 161

Bibliography

[1] Rong Zheng, Roger I. Tanner, and Xi-Jun Fan, *Injection Molding: Intergarion of Theory and Modeling Mothods*.: Spinger, 2011.

[2] Cardozo D., "Three Models of the 3D Filling Simulation for Injection Molding: Abrief Review," *Journal of Reinforced Plastics and Composites*, no. 27, 2008.

[3] Gao DM, Garcia-Rejon A, Salloum G Hétu JF, "3D finite element method for the simulation of the filling stage in injection molding," *Polym Eng Sci*, no. 38, pp. 223–236, 1998.

[4] F. and Hetu, J.-F. Illinca, "Three dimensional filling and post-filling of polymer injection molding," *International Polymer Processing*, no. 6, pp. 291–301, 2001.

[5] Coupez T Pichelin E, "Finite element solution of the 3D mold filling problem for viscous incompressible fluid," *Comput Methods Appl Mech Eng*, no. 163, pp. 359–371, 1998.

[6] Tie Geng, Dequn Li, and Huamin Zhou, "Three-dimensional finite element method for the filling simulation of injection molding," *Engineering with Computers*, no. 21, pp. 289-295, 2006.

[7] L. Silva, "Viscoelastic compressible flow and application in 3D injection moulding simulation," Mines Paristech, Paris, Phd Thesis 2004.

[8] Luisa Silva, Houssem Miled, Patrice Laure, and Thierry Coupez, "Injection Molding Simulation: Taking into account the process history to predict the anisotropy in the end-use properties," *NUMIFORM, Materials Processing and Design: Modeling, Simulation and Applications*, no. 908, pp. 355-360, 2007.

[9] Coupez T. Gruau C., "3D tetrahedral, unstructured and anisotropic mesh generation with adaptation to natural and multidomain metric," *Comput. Methods Appl. Mech. Engrg.*, no. 194, pp. 4951–4976, 2005.

[10] T. Coupez, "Metric construction by length distribution tensor and edge based error for anisotropic adaptive meshing," *Journal of Computational Physics*, no. 230, pp. 2391–2405, 2011.

[11] Luisa S., Coupez T. Digonnet H., "Cimlib A Fully Parallel Application For Numerical Simulations Based On Components Assembly," in *Numiform*, 2007.

[12] Coupez T. Digonnet H., "Object-oriented programming for fast and easy development of parallel applications in forming processes simulation," in *Second MIT Conference on Computational Fluid and Solid Mechanics*, K.J. Bathe, 2003, pp. 1922-1924.

[13] Digonnet H., Coupez T. Mesri Y., "Advanced parallel computing in material forming with CIMLIB," *European Journal of Computational Mechnanics*, no. 18, pp. 669-694, 2009.

[14] Digonnet H., Ducloux R. Coupez T., "Parallel meshing and remeshing," *Appl. Math. Modelling*, vol. II, no. 25, pp. 83-98, 2000.

[15] Brinson H.F., Brinson L.C., *Polymer Engineering Science and Viscoelasticity, An Introduction*.: Springer edition, 2008.

[16] Baaijens P.T, "Mixed finite element methods for viscoelatic flow analysis: a review," *J. Non-Newtonian Fluid Mech.*, no. 79, pp. 361-385, 1998.

[17] Rajagopalam, D., Armstrong, R., and Brown, R., "Finite element method for steady calculation of viscoelastic flow using constitutive equations with a newtonian viscosity," *Journal of Non-Newtonian Fluid Mechanics*, no. 36, pp. 159–192, 1990.

[18] Beris A., Edwards B., "Thermodynamic of flowing systems," Oxford, New York, 1994.

[19] Guenette R., Fortin M., "A new finite element method for computing viscoelastic flows," *Journal of Non-Newtonian Fluid Mechanics*, no. 60, pp. 275-290, 1995.

[20] Baaijens F., Selen S., Baaijens H., Peters G., "Viscoelastic flow past a confined cylinder of a low density polyethylene," *Journal of Non-Newtonian Fluid Mechanics*, no. 68, pp. 173-203, 1998.

[21] Verbeeten Wilco.M.H, "Computational Polymer Melt," Technische Universiteit Eindhoven, Phd Thesis 2001.

[22] Rasmussen H.K , Hassager O., "Simulation of transient viscoelastic flow with second order time integration," *J. Non-Newtonian Fluid Mech.*, no. 56, pp. 65-84, 1994.

[23] Harlen O.G. , Rallison J.M., Szabo P., "A split Lagrangian-Eulerian method for simulating transient viscoelastic flows," *J. Non-Newtonian Fluid Mech.*, no. 60, pp. 81-104, 1995.

[24] Moresi L., Dufour F. , Muhlhaus H. B., "A Lagrangian integration point finite element method for large deformation modeling of viscoelastic geomaterials," *Journal of Computational Physics*, no. 184, pp. 476-497, 2003.

[25] Etienne J., Hinch E.J., Jie Li, "A Lagrangian-Eulerian approach for the numerical simualtion of free-surface flows of a viscoelastic material," *J. Non-Newtonian Fluid Mech.*, no. 136, pp. 157-166, 2006.

[26] Ganvir V., Lele A., Thaokar R., Gautham B.P., "Simulation of viscoelastic flows of polymer solutions in abrupt contractions using an arbitrary Lagrangian Eulerian (ALE) based finite element method," *J, Non-Newtonian Fluid Mech.*, no. 143, pp. 157-169, 2007.

[27] Hwu C., Chen Y.C., "Analysis of Defects in Viscoelastic Solids by a Transformed Boundary Element Method," *Procedia Engineering*, no. 10, pp. 3038-3043, 2011.

[28] Holzapfel G.A., Reiter G., "Fully coupled thermomechanical behaviour of viscoelastic solids treated with finite elements," *Int. J. Engrng Sci.*, no. 7, pp. 1037-1058, 1995.

[29] Hasampour K., Ziaei-Rad S., Mahzoon M., "A large deformation framework for compressible viscoelastic materials: Constitutive equations and finite element implementation," *International Journal of Plasticity*, no. 29, pp. 1154-1176, 2009.

[30] Huber N., Tsakmakis C., "Finite deformation viscoelasticity laws," *Mech. Mater.*, no. 32, pp. 1-18, 2000.

[31] Assie A.E., Eltaher M.A., Mahmoud F.F., "Modeling of viscoelastic contact-impact problems," *Applied Mathematical Modelling*, no. 34, pp. 2336-2352, 2010.

[32] Assie A.E., Eltaher M.A., Mahmoud F.F., "The response of viscoelastic-frictionless bodies under normal impact," *International Journal of Mechanical Science*, no. 52, pp. 446-454, 2010.

[33] Qian C., Demao Z., "Vibrational analysis theory and application to elastic-viscoelastic composite structures.," *Computer & Structures* , no. 37, pp. 585-595, 1990.

[34] Furuichi M., Kameyama M., Kageyama A., "Three-dimensional Eulerian method for large deformation of viscoelastic fluid: Toward plate-mantle simulation," *Journal of Computational Physics*, no. 227, pp. 4977-4997, 2008.

[35] Milcent T., "Une approche eulérienne du couplage fluide-structure, analys emathématique et applications en biomécanique," l'université Joseph Fourier, Grenoble, PhD Thesis 2009.

[36] Diaz-Calleja R., Prolongo M.G., Masegosa R.M., Calom C. Riande E., *Polymer Viscoelasticity, stress and strain in practice*, Inc Marcel Dekker edition, Ed.

[37] Rosen S.L., *Fundamental Principles of Polymeric Materials*, 2nd ed.: JW.

[38] Sweeney J., Ward I. M., *An Introduction to The Mechanical Properties of Solid Polymers*, 2nd ed.: John Wileys & Sons, 2004.

[39] Van der Vegt A.K., *From Polymers to Plastics*.: VSSD, 2005, ch. 6.

[40] Zrida M., "Simulation du comportement d'un polymère par un modèle d'hyper-visco-hystérésis : application à trois nuances de polypropylène," Université de Bretagne-Sud, Phd Thesis 2009.

[41] Kölke A., Hübner B., Dinkler D. Walhorn E., "Fluid–structure coupling within a monolithic model involving free surface flows," *Computers and Structures*, no. 83, pp. 2100-2111, 2005.

[42] Hübner B., Walhorn E., Dinkler D., "A monolithic approach to fluid–structure interaction using space–time finite elements," *Comput. Methods Appl. Mech. Engrg*, no. 193, pp. 2087–2104, 2004.

[43] Coupez T., Digonnet H., Laure P., Silva L., Valette R., , éditeur M. S, Ed., 2008.

[44] Heil M., Hazel A.L., Boyle J., "Solvers for large-displacement fluid–structure interaction problems: segregated versus monolithic approaches," *Comput Mech*, no. 43, pp. 91–101, 2008.

[45] Heil M., "An efficient solver for the fully coupled solution of large-displacement fluid–structure interaction problems," *Comput. Methods Appl. Mech. Engrg.*, no. 193, pp. 1–23, 2004.

[46] Hulshoff S.J., Brummelen E.H. van, Borst R. de Michler C., "A monolithic approach to fluid–structure interaction," *Computers & Fluids*, no. 33, pp. 839-848, 2004.

[47] Felippa C.A., Ohayon R. Park K.C., "Partitioned formulation of internal fluid-structure interaction problems by localized Lagrange multipliers," *Comput. Methods Appl. Mech. Engrg*, no. 190, pp. 2989-3007, 2001.

[48] Steindorf J. Matthies H.G., "Partitioned strong coupling algorithms for fluid–structure interaction," *Computers and Structures*, no. 81, pp. 805-812, 2003.

[49] Genkinger S., Ramm E. Wall W.A., "A strong coupling partitioned approach for fluid–structure interaction with free surfaces," *Computers & Fluids*, no. 36, pp. 169-183, 2007.

[50] Gingold R.A., Monaghan J.J., "Kernel estimates as a basis for general particle methods in hydrodynamics," *Journal of Computational Physics*, no. 46, pp. 429–453, 1981.

[51] Idelsohn S.R., Marti J., Limache A., Oñate E., "Unified Lagrangian formulation for elastic solids and incompressible fluids: Application to fluid–structure interaction problems via the PFEM," *Comput. Methods Appl. Mech. Engrg*, no. 197, pp. 1762-1776, 2008.

[52] Idelsohn S.R., Oñate E., Pin F. Del, Calvo Nestor, "Fluid–structure interaction using the particle finite element method," *Comput. Methods Appl. Mech. Engrg*, pp. 195, 2100–2123, 2006.

[53] Gerstenberger A., Wolfgang A. Wall., "An eXtended Finite Element Method/Lagrange multiplier based approach for fluid–structure interaction," *Comput. Methods Appl. Mech. Engrg*, no. 197, pp. 1699–1714, 2008.

[54] Donea J., Huerta A., Ponthot J.-Ph., Rodriguez-Ferran A., "Arbitrary Lagrangian-Eulerian Methods," in *Fundamentals*, Ltd John Wiley & Sons, Ed., 2004, ch. 14.

[55] Ouahsine A., Lewin L. Souli M., "ALE formulation for fluide-structure interaction problems," *Comput. Methods Appl. Mech. Engrg*, no. 190, pp. 659-675, 2000.

[56] E. Liberge, "Réduction de modèle par POD-Galerkin pour les problèmes d'intéraction fluide-structure," Université de La Rochelle, Thèse de doctorat 2008.

[57] Huvelin F., "Couplage de codes en interaction fluide-structure et applications aux instabilitées fluide-elastiques," 2008.

[58] Ait Moudid L., "Couplage Fluide-Structure pour la simulation numérique des écoulements fluides dans une conduite à parois rigides ou élastiques, en présence d'obstacles ou non," Université d'Artois, PhD Thesis 2007.

[59] C.S. Peskin, "The immersed boundary method," *Acta Numerica - Cambridge University Press*, pp. 1-39, 2002.

[60] Gay M. Zhang L.T., "Immersed finite element method for fluid-structure interactions," *Journal of Fluids nd Structures*, no. 23, pp. 839-857, 2007.

[61] Liu W.K. Wang X., "Extended immersed boundary method using FEM and RKPM," *Comput. Methods Appl. Mech. Engrg*, no. 193, pp. 1305-1321, 2004.

[62] Wang Z.J. Xu S., "An immersed interface method for simulating the interaction of a fluid with moving boundaries," *Journal of Computational Physics*, no. 216, pp. 454-493, 2006.

[63] Glowinski R., Pan T.W., Hesla T.I., Joseph D.D., Periaux J., "A distributed Lagrange multiplier/Fictitious domain method for the simulation of flow around moving rigid bodies: application to particulate flow," *Comput. Methods Appl. Mech. Engrg*, no. 184, pp. 241-267, 2000.

[64] N.M. Diniz Dos Santos, "Numerical methods for fluid-structure interaction problems with valves," Université Pierre et Marie Curie - Paris VI, Thèse de doctorat 2007.

[65] Hart J. de, Baaijens F., Peters G.W.M., and Schreurs P.J.G., "A computational fluid-structure interaction analysis of a fiber-reinforced stentless aortic valve," *J. Biomech*, pp. 36, 699–712, 2003.

[66] Anderson P.D., Vosse F.N. van de, Sherwin S.J. Loon R. van, "Comparison of various fluid–structure interaction methods for deformable bodies," *Computers and Structures*, no. 85, pp. 833-843, 2007.

[67] Van Loon R., Anderson P.D, Van de Vosse F.N., "A fluid-structure interaction method with solid-rigid contact for heart valve dynamics," *Journal of computational physics*, no. 217, pp. 806-823, 2006.

[68] Van Loon R., Anderson P.D., Hart J., Baaijens F.P.T., "A combined fictious domain/adaptive meshing method for fluid-structure interaction in heart valve dynamics," *Journal of computational physics*, no. 46, pp. 533-544, 2004.

[69] Beckermann C. Sun Y., "A two-phase diffuse-interface model for Hele-Shaw flows with large property contrasts," *Physica D*, no. 237, pp. 3089-3098, 2008.

[70] Beckermann C. Sun Y., "Diffuse interface modeling of two-phase flows based on averaging: Mass and momentum equations," *Physica D*, pp. 281-308, 2004.

[71] Sethian J.A., Osher S., "Fronts propagating with curvature dependent speed: Algorithms based on Hamilton-Jacobi formulations," *Journal of Computational Physics*, no. 79, pp. 12-49, 1988.

[72] Schneider P.J., Eberly D.H., *Geometric Tools for Computer Graphics*, elsevier science inc. édition ed.

New York, NY, U.S.A.: Morgan Kaufmann Series in Computer Graphics, 2002.

[73] Holzapfel G.A., *Nonlinear solid mechanic*.: Wiley, 2000.

[74] Renon N., "Simulation numérique par éléments finis des grandes déformations des sols. Application à la Scarification," Mines ParisTech, Phd Thesis 2002.

[75] Saad P., "Modélisation et identification du comportement non-linéaire des cales en caoutchouc," Ecole Centrale de Lyon, Phd Thesis 2003.

[76] Rappaz M., Bellet M., Deville M., *Numerical Modeling in Materials Science and Engineering*, R.L. Graham, J. Stoer, R. Varga, H. Yserentant R. Bank, Ed.: Spinger, 1998.

[77] Baquet E., "Modélisation thermomécanique visco-hyperélastique du comportement d'un polymère semi-cristallin : application au cas d'une matrice polyamide 6.6," Mines ParisTech, Paris, Phd Thesis 2011.

[78] Chevaugeon N. , "Contribution à l'étude des membranes hyper-élastiques en grandes déformations," Phd Report 2002.

[79] Germain P., *Cours de mécanique des milieux continus*.: MASSON Paris, 1973.

[80] Billon N., "Approche visco hyperélastique basée sur une théorie de réseau," in *Matériaux 2010*, Nantes, France, 2010.

[81] Billon N., "Constitutive model for HIPS in the thermoforming range," in *Int J Mater Form, ESAFORM*, 2008, pp. 679-682.

[82] Billon N., "Visco-hyperelastic modelling for amorphous polymers close to their alpha transition," in *ICR*, 2008.

[83] Billon N., "Visco hyperelastic constitutive model for polymer stretch blow moulding," in *Proc. Computational plasticity X*, Barcelona (Spain), p. 2008.

[84] Billon N. , "Hyperelasticity and strain-rate sensitivity in amorphous pet near alpha transition," in *13th Int. Conf On Deformation Yield and Fracture of Polymers*, Kerkrade (Pays Bas), 2006, pp. 227-229.

[85] Edwards S.F., Vilgis T., "The effect of entanglements in rubber elasticity," *Polymer*, no. 27, pp. 483-492, 1986.

[86] Sweeney J., "A comparison of three polymer network models in current use," *Computational and Theorical Polymer Science*, no. 9, pp. 27-33, 1999.

[87] Lai W. M., Rubin D., Krempl E., *Introduction to continuum mechanics*, 3rd ed.: Butterwort Heinemann, 1993.

[88] Coupez T., "Réinitialisation convective et locale des fonctions Level Set pour le mouvement de surfaces et d'interfaces," in *Journées Activités Universitaires de Mécanique*, La Rochelle, France, 2006.

[89] Legay A., Chessa J., Belytschko T., "An Eulerian-Lagrangian method for fluid-structure interaction based one level sets," *Comput. Methods Appl. Mech. Engrg*, no. 195, pp. 2070-2087, 2006.

[90] Ville L., Silva L. and Coupez T., "Convected Level Set method for the numerical simulation of Fluid Buckling," *Int. J. Numer. Meth. Fluids*, pp. 1–6, 2010.

[91] Puaux G., "Simulation numérique des écoulements aux échelles microscopiques et mésoscopique dans le procédé RTM," Mines ParisTech, Paris, Phd Thesis 2011.

[92] Brezzi F., "On the existence, uniqueness and approximation off saddle point problems arising from Lagragian multipliers," *RAIRO Modélisation Mathematical Analyzes Numerical*, no. 8, pp. 129-151, 1974.

[93] Babuska I., "The finite element method with penalty," *Maths. Comp.*, no. 27, pp. 221-228, 1973.

[94] Fortin M. et al Brezzi F, *Mixed Finite Elements, Compatibility Conditions and Applications*, L. Gastaldi D. Boffi, Ed. Cetraro, Italy: Springer and C.I.M.E. Summer School, 2006.

[95] Basset O., "Simulation numérique d'écoulements multi-fluides sur grille de calcul," Phd Thesis 2006.

[96] Arnold D., Brezzi F., Fortin M., "A stable finite element for Stokes equations," *Calcolo*, no. 21, pp. 337-344, 1984.

[97] Coupez T. and Marie S., "From a direct solver to a parallel iterative solver in 3D forming simulation," *International Journal of Supercomputer and Applications*, no. 11, p. 205, 1997.

[98] Coupez T., "Stable-stabilized finite element for 3D forming calculation," 1996.

[99] Perchat E. , "MINI-élément et factorisations incomplètes pour la parallélisationd'un solveur de Stokes 2D. Application au forgeage," Ecole Nationale supérieure des Mines de Paris, Phd Thesis 2000.

[100] Brezzi F. et al, "b=Integral (g)," *Comput. Methods Appl. Mech. Engrg.*, no. 145, pp. 329-339, 1997.

[101] Paccini A., "Développement d'un modèle éléments finis 3D appliqué à la simulation d'opérations chirurgicales des tissus mous," 2005.

[102] Coupez T., "Génération de maillage et adaptation de maillage par optimisation locale," *Revue européenne des éléments finis*, no. 9, pp. 403-423, 2000.

[103] Coupez T., "3D tetrahedral, unstructured and anisotropic mesh generation with adaptation to natural and multidomain metric," *Computer Methods in Applied Mechanics and Engineering*, no. 194, pp. 4951-4976, 2006.

[104] Gruau C., "Génération de métriques pour adaptations anisotrope de maillage, application à la mise en forme des matériaux," Mines Paristech, Paris, Phd Thesis 2004.

[105] Angot P., Bruneau C.H., Fabrie P., "A penalization method to take into account obstacles in incompressible viscous flows," *Numer. Math.*, no. 81, pp. 497–520, 1999.

[106] Megally A., "Etude et modélisation de l'orientation de fibres dans des thermoplastiques renforcés," Mines ParisTech, PhD Thesis 2005.

[107] Baume G., "Modélisation et simulation numérique directe de l'écoulement d'un fluide complexe," Mines ParisTech, PhD Thesis 2008.

[108] Glowinski R. Fortin M., *Augmented Lagrangian methods: application to the numerical solution of boudary-value problems*, G. PAPANICOLAOU, R. T. ROCKAFELLAR, R. T. ROCKAFELLAR J. L. LIONS, Ed.: Studies in mathematics and its applications, 1983.

[109] Uzawa H., "Iterative method for concave programming," *Studies in linear and nonlinear programming. Stanford University Press*, 1958.

[110] E. Hachem, "Stabilized finite element method for heat transfer and turbulent flows inside industrial furnaces," Mines ParisTech, Paris, Phd Thesis 2009.

[111] Brezzi F., Marini D., Russo A., "Applications of the pseudo residual-free bubbles to the stabilisation of convection-diffusion problems," *Compt. Methods Appl Mech. Engrg.*, pp. 51-63, 1998.

[112] Franca L.P., Farhat C., "Bubble functions prompt unusual stabilized finite element methods," *Comput Methods Appl Mech Eng*, vol. I-IV, no. 123, pp. 299–308, 1995.

[113] Hughes T.J.R., Feijoo G.R., Mazzei L., Quincy J.B., "The variational multiscale method—a paradigm for computational mechanics," *Comput Methods Appl Mech Eng*, vol. I–II, no. 166, pp. 3–24, 1998.

[114] Masud A. , Khurram R.A., "A multiscale/stabilized finite element method for the advection–diffusion equation," *Comput. Methods Appl. Mech. Engrg.*, no. 193, pp. 1997–2018, 2004.

[115] Masud A., Calderer R., "A variational multiscale stabilized formulation for the incompressible Navier–Stokes equations," *Comput Mech*, no. 44, pp. 145–160, 2009.

[116] Franca L.P., Nesliturk A., Stynesb M., "On the stability of residual-free bubbles for convection-diffusion problems and their approximation by the two-level finite element method," *Comput. Methods Appl. Mech. Engrg.*, no. 166, pp. 35-49, 1998.

[117] Volker J., Songul K., William L., "A two-level variational multiscale method for convection-dominated convection-diffusion equations," *Computer Methods. Appl Mech Engr.*, no. 195, pp. 4594-4603, 2006.

[118] Gravemeier V., Wolfgang A. W., Ekkehard R., "A three-level finite element method for the instationary incompressible Navier–Stokes equations," *Comput. Methods Appl. Mech. Engrg.*, no. 193, pp. 1323–1366, 2004.

[119] Codina R., "Stabilization of incompressibility and convection through orthogonal sub-scales in finite element methods," *Computer methods in applied mechanics and engineering*, no. 190, pp. 1579-1599, 2000.

[120] Codina R., "Stabilized finite element approximation of transient incompressible flows using orthogonal subscales," *Comput. Methods Appl. Mech. Engrg.*, no. 191, pp. 4295–4321, 2002.

[121] Hachem E., Rivaux B., Kloczko T., Digonnet H., Coupez T., "Stabilized finite element method for incompressible flows with high Reynolds number," *Journal of Computational Physics*, vol. 229, no. 23, pp. 8643-8665, 2010.

[122] Russo A. Brezzi F., "Choosing bubbles for advection-diffusion problems," *Mathematical models and methods in applied sciences*, no. 4, pp. 571-587, 1994.

[123] Brooks A. N. Hughes T. J. R., "Streamline upwind/Petrov-Galerkin formulations for convective dominated

flows with particular emphasis on the incompressible Navier-Stokes equations," *Comp. Meth. in Appl. Mech. Eng.*, no. 32, pp. 199-259, 1982.

[124] A. Nesliturk Franca L., "On a two-level finite element method fo the incompressible Navier-Stokes equations," *International journal for numerical methods in enginering*, no. 52, pp. 433-453, 2001.

[125] Oilviera S.P. Franca L.P., "Pressure bubbles stabilization fearture in the Stokes problems," *Computer methods in applied mechanics and engineering*, no. 192, pp. 1929-1937, 2003.

[126] Laure P., Beaume G., Basset O., Silva L., Coupez T., "Numerical methods for solid particles in particulate flow simulations," *Fluid structure interaction*, pp. 365-383, 2007.

[127] Boussetta R., "Estimation d'erreur et adaptation," Centre de Mise en Forme des Matériaux, Cours 2006.

[128] Masud A., Khurram R.A., "A multiscale finite element method for the incompressible Navier-Stokes equations," *Computer Methods in Applied Mechanics and Engineering*, no. 195, pp. 1750-1777, 2006.

[129] Norburn S., Silvester D., "Stabilised vs. stable mixed methods for incompressible flow," *Computer Methods in Applied Mechanics and Engineering.*, no. 166, pp. 131-141, 1998.

[130] King R.C., Apelian M.R., Armstrong R.C., Brown R.A., "Numerically stable finite element techniques for viscoelastic calculations in smooth and singular domains," *J. Non-Newtonian Fluid Mech*, no. 29, pp. 147–216, 1988.

[131] Marchal J., Crochet M., "A new mixed finite element for calculating viscoelastic flow," *Journal of Non-Newtonian Fluid Mechanics*, no. 26, pp. 77–114, 1987.

[132] Szadi M., Salmon T., Liu A., Bornside D., Armstrong R., "New mixed finite element method for viscoelastic flows governed by differential constitutive equations," *Journal of Non-Newtonian Fluid Mechanics*, no. 59, pp. 215–243, 1995.

[133] Sun, J., Phan-Thien, N., and Tanner, R., "An adaptive viscoelastic stress splitting scheme and its applications: Avss/si and avss/supg," *Journal of Non-Newtonian Fluid Mechanics*, no. 65, pp. 75–91.

[134] G. mbH, *User Manual software*, 6th ed., GOM, Ed., 2007.

[135] Sahh H. Martin, *Elasticity: Theory, Applications, and Numerics*. Kingston, Rhode Island, USA: Elsevier Inc., 2005.

[136] Hughes T.J.R. , Franca L.P. , Hulbert G.M., "A new finite element formulation for computational fluid dynamics: VIII. The Galerkin/least-squares method for advective–diffusive equations," *Comput. Methods Appl. Mech. Engrg.*, vol. II, no. 73, pp. 173–189, 1989.

Formulation Mixte Vitesse-Déplacement pour La Modélisation du Comportement Complexe des Polymères

RESUME:

Ce travail a été effectué dans le cadre du projet Rem3D® dans lequel participent plusieurs entreprises avec l'objectif de développer un logiciel de simulation 3D par éléments finis du procédé d'injection. L'objectif est de développer une méthode numérique pour modéliser le comportement viscoélastique des polymères de l'état liquide à l'état solide à travers une approche multiphasique qui est normalement utilisée pour traiter les problèmes d'interaction fluide-structure (IFS). La philosophie est d'utiliser une formulation mixte à trois champs *(u, v, p) (déplacement, vitesse, pression)*, où u et v représentent les variables principales de déformation et de vitesse de déformation. Nous sommes ramenés au problème de Navier-Stokes compressible avec présence d'extra-contrainte, qui est résolu en utilisant la méthode des éléments finis mixte. Le présent travail contribue aussi à la mise en place de certains éléments de stabilisation pour la simulation numérique des problèmes multiphasiques par l'approche monolithique.

La pertinence des approches Lagrangienne et Eulérienne est discutée autour de la modélisation d'un corps viscoélastique de Kelvin-Voigt. L'extension de la méthodologie au modèle visco-hyper-élastique abordé, pour l'instant par la modélisation et la validation au point matériel, puis l'implémentation dans la bibliothèque des éléments finis CimLib®. Enfin, un schéma stabilisation de résolution du type EVSS est adopté pour le modèle viscoélastique de Kelvin-Voigt, le modèle visco-hyper-élastique Néo-Hookéen, et aussi un modèle visco-hyper-élastique. Nos résultats laissent entrevoir des perspectives prometteuses dans la simulation et la modélisation, non seulement de la viscoélasticité, mais aussi pour les applications dynamiques complexes.

Mots clés : élasticité, Kelvin-Voigt viscoélastique, hyper-élastique Néo-Hookéen, visco-hyper-élastique, approche multiphasique, éléments finis mixte, formulation mixte vitesse-déplacement.

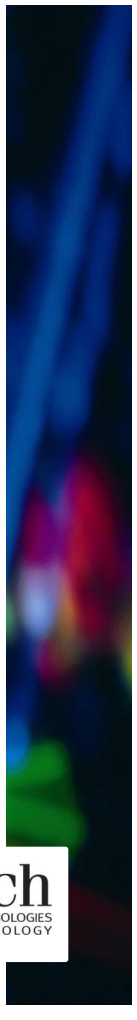
Mixed Velocity-Displacement Formulation for Modeling of Complex Behavior of Polymer

ABSTRACT:

This work concerns the simulation of viscoelastic behavior of polymer at different states. Viscoelastic modeling of polymer was performed from the solid state to the liquid state via a multiphase approach which is largely used to deal with the fluid structure interaction. To ensure the appreciation of the FSI, viscoelasticity is considered in two parts: an elastic one and viscous other where the main idea is to use a mixed formulation in three fields *(u, v, p) (displacement, velocity, pressure)*, with *u* and *v*, represented the primary variables of a strain and a strain rate formulation. We are led to the Navier-Stokes compressible problem with extra-stress, which is solved by using the Mixed Finite Element. The present work contributes some stabilization elements to the numerical simulation of multiphase problem by the monolithic approach.

Comparison between the literature and experiments was performed through the validation of an elastic case and the viscoelastic Kelvin-Voigt model in the context of Lagrangian framework as well as Eulerian framework. The extension of the methodology to a visco-hyper-elastic is given through the modeling and validation on material point on the finite elements library CimLib®. Finally, a stabilization scheme of the EVSS type is adopted for viscoelastic Kelvin-Voigt model, hyper-elastic Neo-Hookean model, and also visco-hyper-elastic model which proposed an open door in computational modeling, not only with viscoelasticity but also complex dynamic application.

Keywords : elasticity, Kelvin-Voigt viscoelastic, multiphase approach, hyper-elastic Neo-Hookean, visco-hyper-elastic, mixed and space-time finite element method, velocity-displacement formulation.



MINES ParisTech

ParisTech
INSTITUT DES SCIENCES ET TECHNOLOGIES
PARIS INSTITUTE OF TECHNOLOGY